Doctoral Dissertation

Studies on Control Schemes of Variable Speed Gas Engine Generation Systems Using Doubly Fed Induction Generator

二次励磁誘導発電機を用いた可変速ガスエンジン発電システムの制御法の研究

ATAJI Ahmad Bashar

January 2016

Division of Electrical, Electronic, and Information Engineering

Graduate School of Engineering

Osaka University

Abstract

This thesis deals with the analysis, modeling, and designing of control systems for generation systems based on the variable speed doubly-fed induction generator (DFIG). Although the initially adopted prime mover is a natural gas-fired internal combustion engine, the control structure should be general that it can be extended to other variable speed generation systems such as wind turbines. The DFIG operates in a distributed generation system and it should guarantee an uninterruptable power supply to a local load which is connected close to the generator.

The control system of the DFIG generation system must guarantee stable power supply to the local load even in the case of grid failure. Thus, the control system must have different modes of operation depending on the status of the grid. The control system must have a grid-connected mode of operation when the generator is connected to the grid, and it must have a stand-alone mode of operation when the generator is disconnected from the grid due to a grid failure. In addition, the control system should guarantee a smooth transition between the different modes of operation. The transition from stand-alone to grid-connected requires a temporary mode of operation where the generator voltage is gradually synchronized with the grid voltage while the generator is still disconnected from the grid; this mode of operation is referred to as synchronization mode.

In this work, a new decoupled control for the grid-connected mode was proposed. The new decoupled control is based on decoupling the stator active and reactive component of the stator current. Compared with the conventional decouple P-Q control method, which is based on decoupling the stator active and reactive power, the proposed decoupled control is more robust and flexible, and it requires less number of machine parameters. The online calculation does not require any parameter, while the controller design requires knowledge of the stator-to-rotor turns ratio only.

The proposed decoupled control requires knowledge of the slip angle which requires a mechanical encoder. To avoid the disadvantages of mechanical encoders, a new slip angle estimator has been proposed. This estimator is based on rotor current

estimation in the synchronous reference frame. Compared with other model-based estimators, the proposed estimator requires the least number of parameters; only one parameter which is the stator inductance. The stator inductance is the inductance measured at the DFIG's stator side; this enables the proposed estimator to use real machine parameters.

For stand-alone mode, the direct voltage control was investigated. The direct voltage control has disadvantages such as absence of slip angle information and inrush currents when connected to the grid. To overcome the limitations of the direct voltage control, we have proposed an estimator of the rotor current angle in the synchronous reference frame. The direct voltage control was modified to include this estimator; this enables the direct voltage control to obtain the slip angle, achieves smooth transition to the grid-connected mode, and guaranteed stable operation of the negative-sequence compensation through the rotor side converter.

Using a 1.1 kW DFIG, the proposed control systems were tested with both simulation and experiments. The simulation was carried out using the PSCAD/EMTDC software. From the obtained results, the proposed control schemes are suitable for variable doubly-fed induction generators-based gas engine generation systems. The control system was general which enables applying the proposed control schemes to other variable speed generation systems.

Acknowledgements

First of all, I thank and praise Almighty Allah. Without Allah's help, I would not have accomplished anything.

I would like to express my heartfelt gratitude towards my supervisor Prof. Toshifumi ISE for his patience, guidance, and support over the course of this project. I would like also to thank Prof. Yushi MIURA for his helpful advice.

I would like to thank Professor Tsuyoshi FUNAKI for his time and effort in reviewing this thesis and the valuable suggestions. I would like also to thank Professor Sigemasa TAKAI, Professor Tetsuzou TANINO and Professor Hiroyuki SHIRAGA for their helpful comments.

I would like to thank all the staff of Graduate School of Engineering of Osaka University who are very kind, supportive and helpful.

I would like to sincerely thank Osaka Gas Co. LTD. for sponsoring this project and providing precious advice and continuous support.

I would like to thank the MASUBUCHI family for their kindness, help, and support. I am grateful to them from the bottom of my heart.

I would like to thank my family for their continuous support and love. They always gave me the energy and confidence to regain determination and enthusiasm. Thanks to them believing in me and thanks to their prayers, I managed to overcome all difficulties that have faced me.

I gratefully acknowledge the Japanese Ministry of Education, Culture, Sports, Science and Technology, who has given me a great opportunity to study in Japan and has granted me the MEXT scholarship, for which I am very grateful from the bottom of my heart.

Studies on Control Schemes of Variable Speed Gas Engine Generation Systems Using a Doubly-Fed Induction Generator

二次励磁誘導発電機を用いた可変速ガスエンジン発電システムの制御法の研究

Chapter 1

Introduction

The global demand for energy, especially electricity, is increasing at an accelerated rate. To fulfill this demand, fossil fuels are being burnt to convert their stored energy into a useful form of energy. Burning fossil fuel releases several greenhouse gases, especially CO_2, which are posing a serious threat to the environment. To cope with the environmental regulations, renewable energy resources are receiving a great amount of interest, and wind turbines and solar cells are being installed worldwide. However, the renewable resources cannot guarantee a stable power supply and depends on the unpredicted nature.

The demand for stable electric power supply is growing, and the internal combustion engines are one important source. The main applications are the stand-by generation, the isolated grid, and the combined operation with renewable resources. In this work, the internal combustion engine running on natural gas is selected as the main prime mover to achieve stable power supply and relatively environment-friendly generation.

Among the internal combustion engines, the gasoline engine can run on natural gas without significant modification to the engine; it only requires special fuel system. The natural gas burns cleaner than other fossil fuel; that is, it releases less greenhouse gases. In addition, natural gas increases the lifetime of the engine and reduces the maintenance requirements.

1.1 Background

The global demand for energy is growing fast as shown in Fig. 1.1 [1]; it is projected to double between 2000 and 2040, where it is growing at an average annual rate of 2.5%. The electric power is one important energy sector.

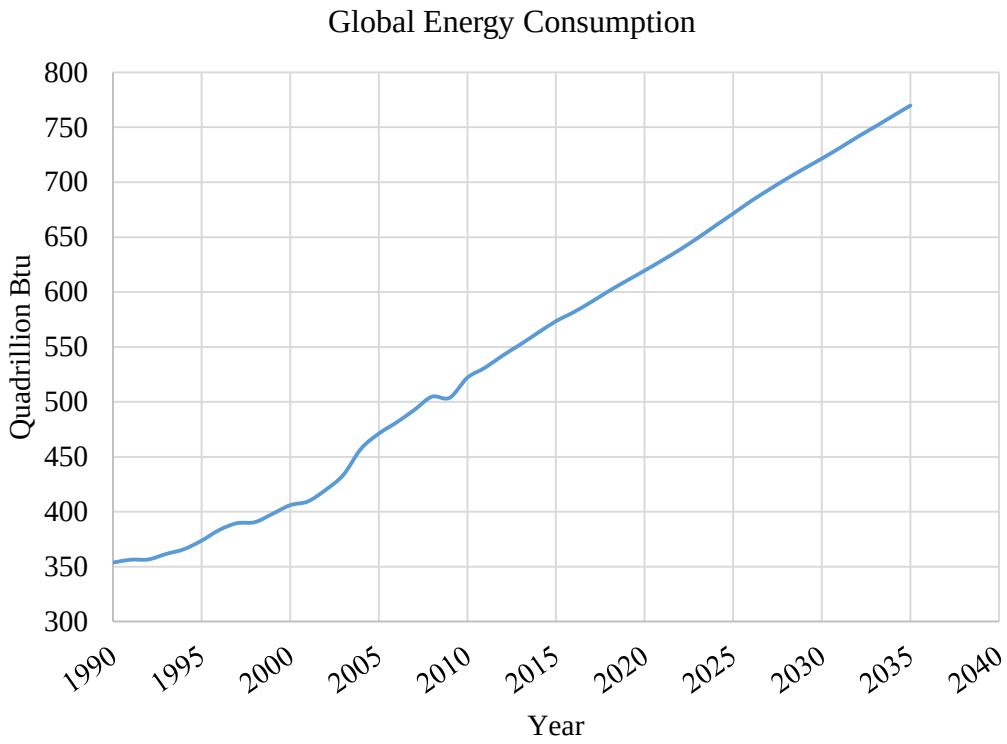

Fig. 1.1: Global energy consumption by quadrillion British thermal unit [1].

The modern society relies greatly on electricity, which is also growing as shown in Fig. 1.2 [2]. To suffice this demand different sources, such as nuclear power, wind power, and fossil fuel, are used.

Currently, the largest source of electricity is from fossil fuel as shown in Fig. 1.3 [2]. Burning fossil fuel is releasing into the atmosphere a worth worrying amount of greenhouse gases, especially CO_2.

Many scientists around the world have related the increase in the CO2 concentration in the atmosphere to the global warming, sea level rise, and global ocean temperature increase as shown in Fig. 1.4 [3]. Consequently, various meetings have been held, and an increased pressure on governments is being placed to regulate the emission of greenhouse gases.

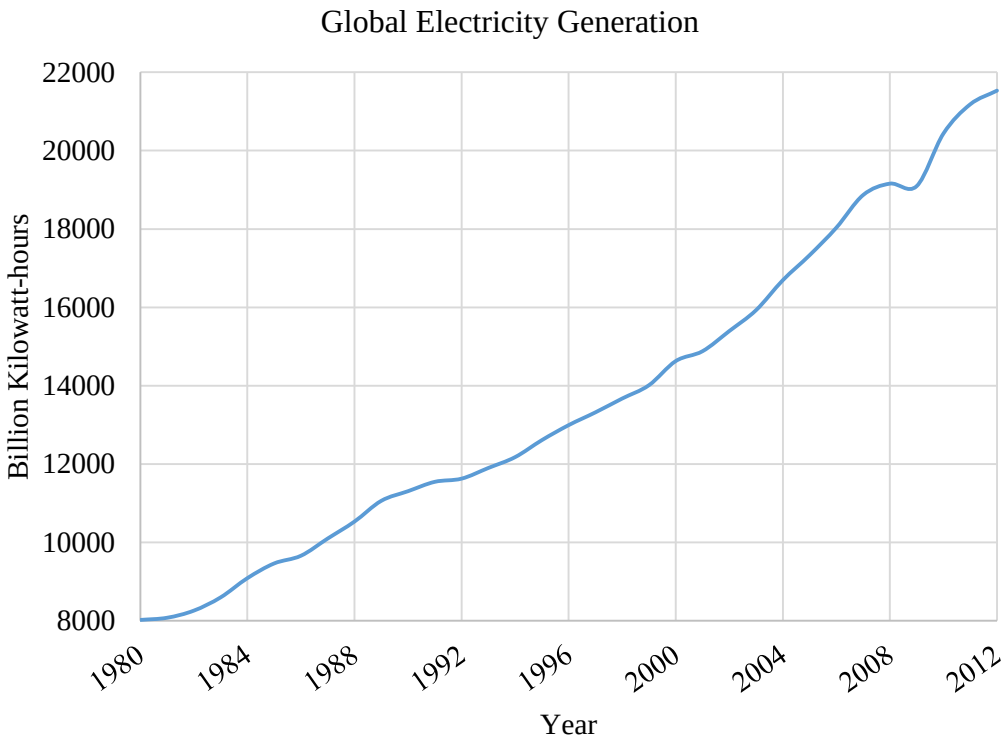

Fig. 1.2: Global electricity generation by billion kilowatt-hour [2].

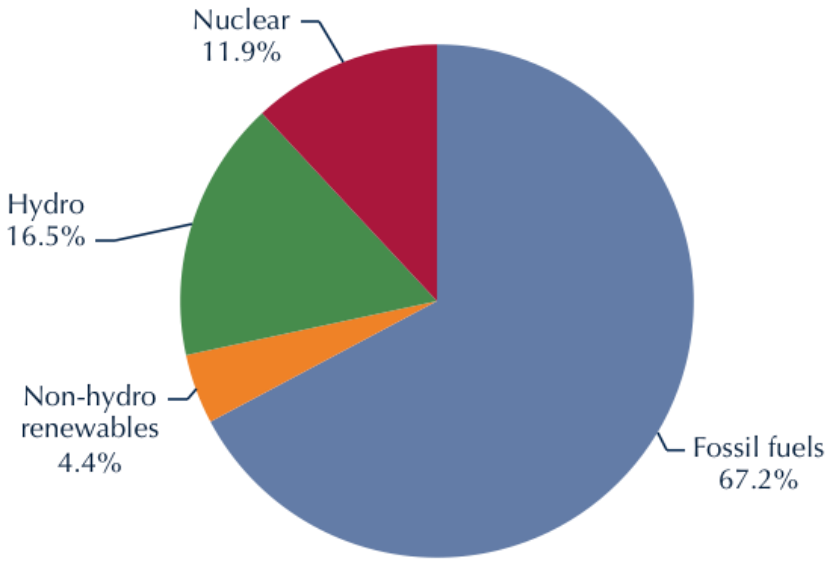

Fig. 1.3: Global electricity generation classified by source in 2014 [2].

The increased worries about environmental issues have encourage the spread of renewable resources especially wind turbines and solar cells. The global capacity of

wind turbines and solar cells are increasing annually as shown in Fig. 1.5 [4] [5].

The main drawbacks of the renewable resources is its dependence on nature, and its high investment costs. Thus, for the time being, the renewable resources cannot completely replace the fossil fuel generation systems. The natural gas can offer a replacement for other fossil fuel especially coal, because it burns cleaner and releases less carbon content for the same amount of generated energy.

For the same amount of generated heat, burning natural gas produces about 30% less CO_2 than burning petroleum, and about 45% less CO_2 than burning coal. Moreover, coal-fired electric power generation releases around 900 kg of CO_2 for every megawatt-hour which is almost double the amount released by natural gas-fired electric power plant [6] [7].

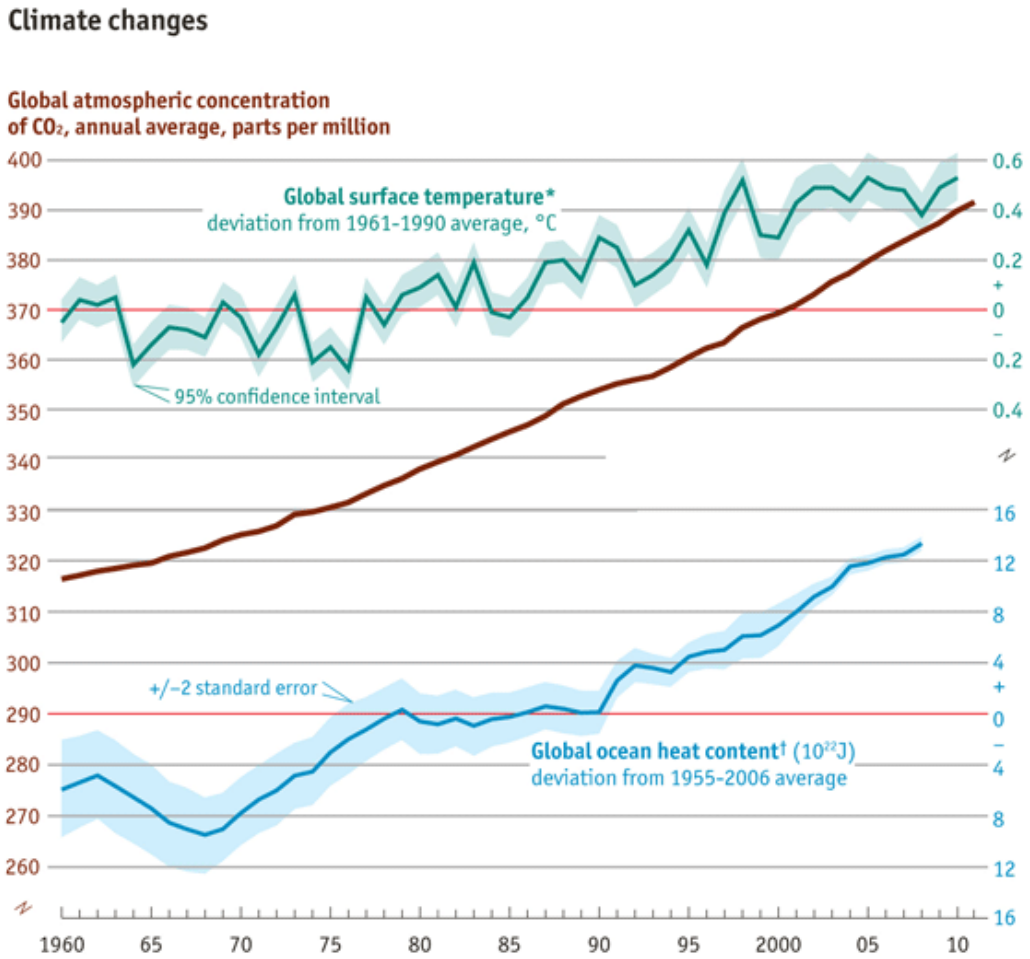

Fig. 1.4: Annual values of the atmospheric average concentration of CO_2, the global surface temperature, and the global ocean heat contents [3].

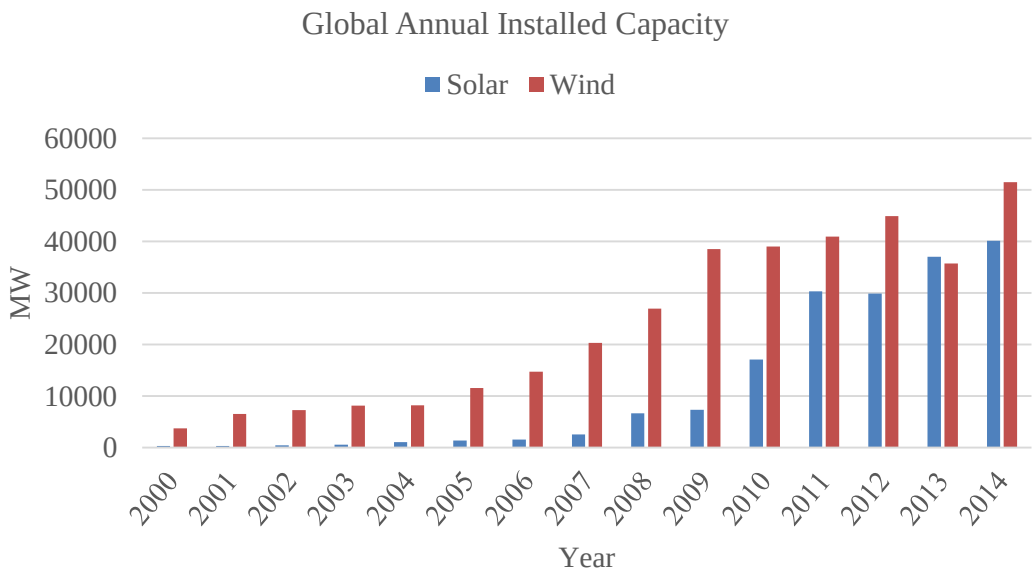

(a) Global annual installed capacity of solar cells (blue) and wind turbines (red).

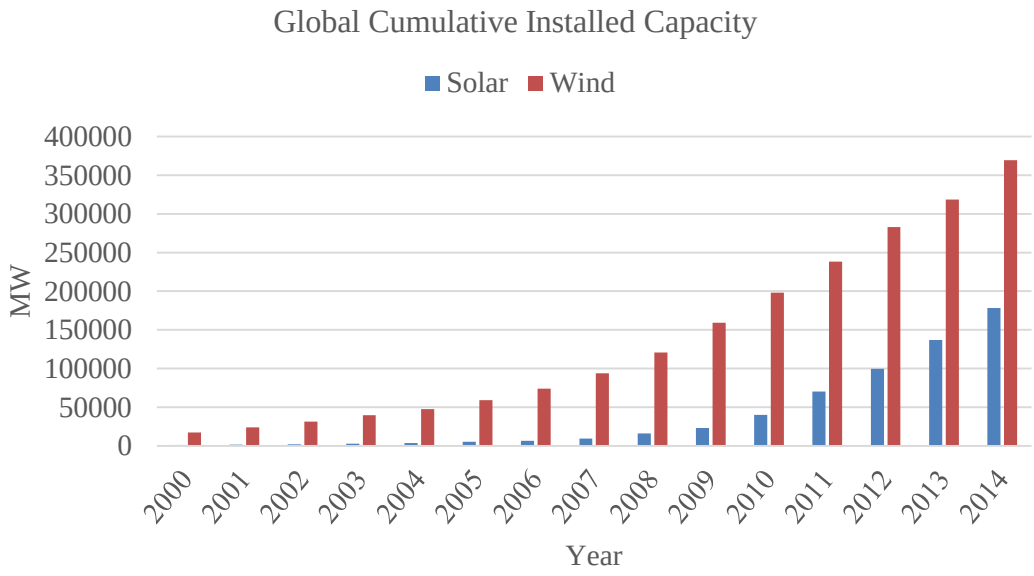

(b) Global cumulative installed capacity of solar cells (blue) and wind turbines (red).

Fig. 1.5: Global annual and cumulative capacity of solar and wind energy [4] [5].

Currently the natural gas is an important source for energy especially electricity and heat. In this work, the variable speed natural gas-fired engine is adopted as the prime mover, and the generator of choice is the doubly-fed induction generator (DFIG).

1.2 Natural Gas Engines

1.2.1 Characteristics of Natural Gas as a Fuel

Most importantly, natural gas significantly reduces the emission of pollutants compared to gasoline. Non-methane hydrocarbons are reduced by approximately 50%, NO_x by 50~87%, CO_2 by 20~30% CO by 70~95%, and the combustion of natural gas produces almost no particulate matter [8].

The natural gas has a relatively high octane number (about 130), meaning that the engine could operate at a compression ratio of 16:1 without any risk of detonation. This allows using engines with higher compression ratios to improve the thermal efficiency by about 10 percent above that of the gasoline engine [8].

Natural gas improves the engine warm-up efficiency, and it mixes easily and evenly in air, which improves the engine performance [8].

The use of natural gas as a vehicle fuel is claimed to provide several benefits to the engine components and to reduce the maintenance requirements. It does not mix with or dilute the lubricating oil. It does not contain any lead, thus it does not produce deposits in the combustion chamber or on the spark plug. This increases the life of the piston's rings and the spark plugs [8].

Natural gas is safer than gasoline and diesel in many aspects. The ignition temperature of natural gas, which is 580 °C, is higher than that of gasoline and diesel which is around 280 °C and 210 °C respectively. Natural gas is lighter than air and evaporate upward rapidly reducing the risk of fire.

1.2.2 Internal Combustion Engines

The internal combustion engines are designed to convert the chemical energy in the fuel into mechanical energy by compressing and burning the fuel. The combustion of the fuel moves pistons in a linear motion. The pistons are connected to a crankshaft which converts the pistons linear motion to a rotary motion.

The internal combustion engines can be classified by the type of ignition into two types: 1) Compression ignition engines, which are also referred to as diesel engines, and 2) spark ignition engines, which are commonly referred to as gasoline or petrol engines.

It is desirable for any alternative fuel to be able to replace the gasoline or diesel without or with minor changes to the engine structure. This would provide great economic savings and would encourage the shift from gasoline or diesel. In this regard, the natural gas is interesting, because most internal combustion engines designed to run on gasoline can run on natural gas without major modification except for the fuel delivery system.

A. Diesel Engine:

The diagram of a four-stroke diesel engine is shown in Fig. 1.6. It has a piston which moves inside a combustion chamber. The piston is connected to the crankshaft by a connecting rod. At the top of the combustion chamber, there is an inlet valve, an exhaust valve, and a fuel injector.

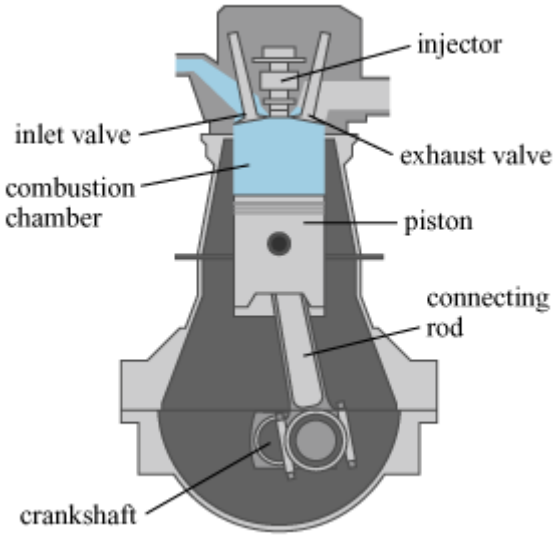

Fig. 1.6: Diagram of the compression ignition engine (the diesel engine) [9].

In a diesel engine, the air is compressed first and, then, the fuel is injected into the combustion chamber. The air compression ratio is high, typically between 15:1 and 22:1, which produces a 40-bar pressure (580 psi). The high compression causes the air temperature to rise to 550 °C. Thus, when the fuel is injected into the cylinder, it is ignited by the heat generated from air compression.

There are four strokes which are the intake, the compression, the power, and the exhaust stroke. During the intake stroke, while the piston is moving down, the inlet valve opens up letting air in the combustion chamber. Then, the compression stroke

starts where the inlet valve closes, and the piston moves up compressing the air. As the piston reaches the top, the power or combustion stroke takes place where the fuel is injected into the combustion chamber at the right moment causing it to ignite and to force the piston downward. During the exhaust stroke, the piston moves up with the exhaust valve being open; this pushes the exhaust created by the combustion of the fuel out of the chamber.

Natural gas is not suitable as an alternative fuel for compression ignition engines, because it has low Cetane number. To modify a diesel engine so that it can run on natural gas, dual fuel is employed as shown in Fig. 1.7.

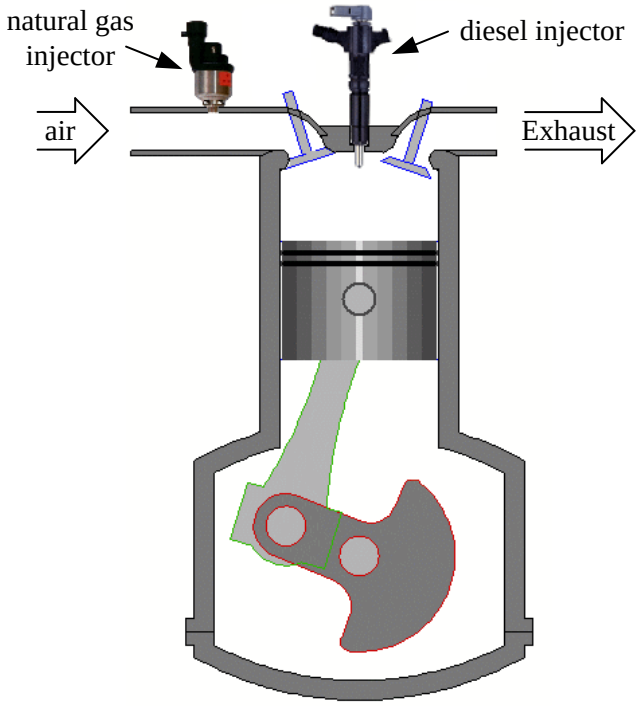

Fig. 1.7: Diagram of the dual-fuel diesel-gas engine [10].

In the dual-fuel engine, between 50% and 75% of the conventional diesel fuel is replaced with natural gas, which is mixed with the intake air. The diesel fuel is injected into the compressed mixture of air and natural gas as in a conventional diesel engine. The ignition of the diesel fuel ignites the natural gas, and generate mechanical energy with much less greenhouse gases.

B. Gasoline Engine:

The gasoline engine has similar structure to a diesel engine, but it has an additional spark plug as shown in Fig. 1.8, which is used to ignite the fuel. Moreover, the fuel

enters the combustion chamber with the air through the inlet valve, and the compression ratio in the spark ignition engine is lower than that in the diesel engine to avoid fuel detonation and engine knocking.

The gasoline engine can operate on natural gas with minor modification except for the fuel delivery and the injection system which needs to be modified. In this work, the natural gas engine refers to the gasoline engine when running on natural gas.

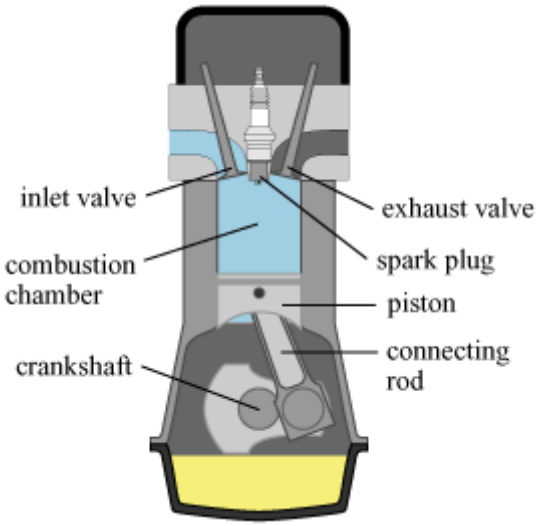

Fig. 1.8: Diagram of the spark ignition engine (the gasoline engine) [9].

1.3 Review of Related Research

The early generation systems were based on fixed speed operation, where a synchronous or asynchronous generator is directly connected to the grid, and it is rotated with a constant speed which correspond to the grid frequency. In the early 1980s, the variable speed operation was commercially introduced to wind turbines, but it was not popular until the 1990s. Since the late 1990s, most wind turbine manufacturers switched to variable speed turbines for power levels in the MW range [11].

The variable speed operation has several advantages compared with fixed speed operation for different generation systems: For internal combustion engine-based generation systems, it reduces the fuel consumption, increases the maximum attainable output power, and achieves a safe operation at low load condition [12] [13]. For wind turbines, it increases the power production, improves the power quality, and reduces mechanical stresses [14] [15]. For hydro-generation systems, it provides remarkable

improvements in energy and hydraulic conditions, improves the efficiency, and increases the turbine lifetime [16] [17].

After few years of introducing the DFIG to variable speed generation systems, it has become very popular, and it occupies around 50% of the wind market [18] [19] due to its advantages. The major advantage of the DFIG, which made it popular, is that the power electronic circuit have to handle a fraction of the generator's power, usually 25% - 30%. This reduces the cost, the losses, and the size of the system [20] [21]. The control system of the power electronic circuit must guarantee a constant output frequency regardless of the speed variations.

Grid-connected operation of the DFIG has received great attention. The early control methods were based on vector control, such in the work of Pena *et al*. (1996) [22] and Datta and Ranganathan (1999) [23], which decouples the rotor current into active and reactive component and controls them separately using a closed-loop configuration which is referred to as rotor current loop. The rotor current references are calculated from the desired active and reactive power using the DFIG model. The vector control has some advantages which are low power ripples and constant switching frequency, but it requires accurate information of the DFIG parameters.

Direct torque [24] [25] and direct power control [26] [27] were proposed to further improve the dynamic response and reduce the dependency on machine parameters. However, these methods produce significant power ripples and variable switching frequency. Several researches proposed new techniques to overcome these issues. For example Zhi and Xu (2007) [28] proposed new direct power control with constant switching frequency, and Abad *et al*. (2008) [29] and Zhi *et al*. (2010) [30] introduced predictive algorithms to the direct power control. These methods have successfully reduced the ripples and have produced constant switching frequency, but they suffer from additional drawbacks such as complicated online calculations and sensitivity to machine parameters.

The decoupled P-Q control was developed from the vector control by introducing an outer loop which generates the rotor current references [31]; this reduces the number of required DFIG parameters while maintaining the advantages of the vector control.

Most of the grid-connected control methods requires the DFIG's rotor position angle which can be measured using a mechanical encoder. The mechanical encoders have several drawbacks: it increases the system cost, increases the wiring complexity,

and reduces the system robustness and reliability. Consequently, considerable research aimed at replacing the mechanical encoder with a software estimator.

Early estimators were based on an open loop structure as in [32]-[35] which are straightforward and easy to realize, but they cannot ensure stable convergence under parameters uncertainty or measurement noise. Closed-loop estimators have better disturbance rejection and better robustness against parameters inaccuracy. Among which, model reference adaptive systems (MRAS) observers are interesting, and they are widely used for speed estimation in cage induction machine drives due to their simplicity [36] [37]. In recent years, several MRAS observers have being proposed and applied to the DFIG; among which, the rotor current-based MRAS observer has very good performance. Some modification to MRAS observers have been proposed to improve them such as reducing the number of machine parameters as in [38] and [39], and improving the transient response as in [40] and [41].

Comparatively, the stand-alone operation of the DFIG has received less attention in the literature compared with grid-connected operation. There are mainly two control methods which are the vector control and the direct voltage control. Vector control [42] controls the generator output voltage indirectly by controlling the magnetizing current; this results in inaccurate output due to the voltage drop on the stator leakage inductance and winding resistance. The vector control was modified in [43] to generate the magnetizing current from the amplitude of the output voltage using a PI (Proportional-integral) controller; this produced accurate output voltage. The vector control methods require some DFIG parameters and the DFIG's rotor position.

The direct voltage control was proposed by Iwanski and Koczara (2004) [44]. It does not require any DFIG parameter, and it achieves sensorless control in terms of the DFIG's rotor speed and angle. However, the direct voltage control cannot correctly estimate the DFIG's rotor position and, consequently, it cannot achieve smooth transition to grid-connected mode, and the negative-sequence compensation through rotor side converter can become unstable for some loads.

1.4 Purpose and Contribution

The purpose of this work is to design a complete control system for the DFIG-based, natural gas engine-driven generation system to operate in a distributed generation system. The control system should be extendable to other variable speed generation

systems such as wind turbines.

In this work, four contribution has been achieved:

1. For grid-connected mode of operation, a new decoupled control was proposed to improve the system robustness. The proposed decoupled control is robust against variation in the grid voltage, variation in DFIG parameters due to saturation, and inaccuracy in the DFIG's rotor position.

2. A new slip angle estimator was proposed for grid-connected operation, which achieves sensorless control in terms of the DFIG's rotor speed and position. The proposed estimator requires the least number of machine parameters compared with other model-based estimators; it requires the stator inductance only. The proposed estimator does not require knowledge of the stator flux linkage, which improves the estimator performance.

3. For stand-alone mode of operation, a new estimator of the rotor current angle was proposed and integrated into the direct voltage control, which enables a smoother connection to the grid by reducing the inrush currents which occurs at the instant of DFIG connection to the grid.

4. The direct voltage control cannot obtain the slip angle which causes the negative-sequence compensation through the rotor side converter to become unstable for some capacitive load. The modified direct voltage control has managed to solve this issue and extended the range of supported linear loads to full range.

1.5 Thesis Outline

In chapter 2, the merits of the variable speed operation of wind turbines and engine generation systems are provided and compared with the fixed speed counterparts. Then, the configuration and the merits of the variable speed doubly-fed induction generator are introduced. The concept of distributed generation systems is briefly introduced and explained. Finally, mathematical modeling of the DFIG and the back-to-back converter is carried out.

In chapter 3, the grid-connected mode of operation is considered. First, the control system for the grid side converter is briefly introduced. Then, the control system for the

rotor side converter is addressed. The proposed decoupled control is introduced and is compared with the conventional decoupled P-Q control. Simulation and experiments are carried out to investigate the proposed decoupled control.

In chapter 4, a new slip angle estimator based on rotor current estimation is introduced. First, a brief review of MRAS observers is provided, and the principle of the rotor current MRAS observer is explained. Then, the concept and design of the proposed estimator is introduced. Sensitivity analysis is provided to investigate the effect of inaccuracy of the DFIG's parameters on the accuracy of the proposed estimator. Simulation and experiments are carried out to investigate the performance of the proposed estimator under different conditions.

In chapter 5, the stand-alone operation is considered. First, the control system for the rotor side converter is addressed, where the conventional direct voltage control is presented with its limitations. Then, the proposed rotor current angle estimator is introduced and integrated into the direct voltage control. Then, the synchronization mode of operation is addressed. Finally, simulation and experiments are carried out to compare the performance of the conventional and the modified direct voltage control during stand-alone and synchronization modes.

In chapter 6, the thesis is concluded with a conclusion.

References

[1] "International Energy Outlook 2011" U.S. Energy Information Administration.

[2] U.S. Energy Information Administration, International Energy Statistics, http://www.eia.gov/cfapps/ipdbproject/IEDIndex3.cfm

[3] Met Office Hadley Centre; NOAA; Scripps Institute of Oceanography; Sydney Levitus et al.

[4] "Global Market Outlook For Solar Power / 2015-2019," Solar Power Europe.

[5] "Global Wind Report Annual Market Update 2014," Global Wind Energy Council.

[6] "Natural Gas and the Environment". Naturalgas.org. Retrieved 2011-02-06.

[7] Rachel Nuwer, "A 20-Year Low in U.S. Carbon Emissions", NY Times, Green Blog, August 17,2012.

[8] Rosli Abu Bakar Semin, "A Technical Review of Compressed Natural Gas as an Alternative Fuel for Internal Combustion Engines," *American Journal of Engineering and Applied Sciences 1 (4)*, pp. 302-311, 2008.

[9] http://www.hk-phy.org/energy/transport/vehicle_phy01_e.html

[10] http://eltcarautomotive.blogspot.jp/2013/04/Dual-fuel-new-technology-for-thesupply.html

[11] M. Mueller and H. Polinder, *Electrical Drives for Direct Drive Renewable Energy Systems*, Woodhead Publishing, 2013, Chap. 6.

[12] G. Iwanski and W. Koczara, "Power Management in an Autonomous Adjustable Speed Large Power Diesel Gensets," in *Proc. EPE-PEMC Power Electronics and Motion Control Conf.*, 2008, Poznan, pp.2164-2169.

[13] R. Pena, R. Cardenas, J. Proboste, J. Clare, and G. Asher, "Wind-Diesel Generation Using Doubly Fed Induction Machines," *IEEE Trans. Energy Conversion*, vol. 23, no. 1, pp. 202-214, Mar. 2008.

[14] H. Jafarnejadsani and J. Pieper, "Gain-Scheduled l_1-Optimal Control of Variable-Speed-Variable-Pitch Wind Turbines," *IEEE Trans. Control Systems Technology*, vol. 23, no. 1, pp. 372-379, Jan. 2015.

[15] B. Singh and N. K. S. Naidu, "Direct Power Control of Single VSC-Based DFIG without Rotor Position Sensor," *IEEE Trans. Industry Applications*, vol. 50, no. 6, pp. 4152-4163, Nov./Dec. 2014.

[16] J. Fraile-Ardanuy, J. R. Wilhelmi, J. J. Fraile-Mora, and J. I. Perez, "Variable-Speed Hydro Generation: Operational Aspects and Control," *IEEE Trans. Energy Conversion*, vol. 21, no. 2, pp. 569-574, Jun. 2006.

[17] L. Belhadji, S. Bacha, I. Munteanu, A. Rumeau, and D. Roye, "Adaptive MPPT Applied to Variable-Speed Microhydropower Plant," *IEEE Trans. Energy Conversion*, vol. 28, no. 1, pp. 34-43, Mar. 2013.

[18] R. Cardenas, R. Pena, S. Alepuz, and G. Asher, "Overview of Control Systems for the Operation of DFIGs in Wind Energy Applications," *IEEE Trans. Industrial Electronics*, vol. 60, no. 7, pp. 2776-2798, Jul. 2013.

[19] J. Mohammadi, S. Vaez-Azdeh, S. Afsharnia, and E. Daryabeigi, "A Combined Vector and Direct Power Control for DFIG-Based Wind Turbines," *IEEE Trans. Sustainable Energy,* vol. 5, no. 3, pp. 767-775, Jul. 2014.

[20] S. Muller, M. Deicke, and R. W. De Doncker, "Doubly Fed Induction Generator Systems for Wind Turbines," *IEEE Industry Applications Magazine*, vol. 8, no. 3, pp. 26-33, May/Jun. 2002.

[21] H. Nian, Y. Song, P. Zhou, and Y. He, "Improved Direct Power Control of a Wind Turbine Driven Doubly Fed Induction Generator During Transient Grid Voltage Unbalance," *IEEE Trans. Energy Conversion,* vol. 26, no. 3, pp. 976-986, Sep. 2011.

[22] R. Pena, J. C. Clare, and G. M. Asher, "Doubly Fed Induction Generator Using Back-to-Back PWM Converters and its Application to Variable-Speed Wind-Energy Generation," in *Proc. IEE Electric Power Applications,* vol. 143, no. 3, pp. 231-241, May 1996.

[23] R. Datta and V. T. Ranganathan, "Decoupled Control of Active and Reactive Power for a Grid-Connected Doubly-Fed Wound Rotor Induction Machine without Position Sensors," in *Proc. IEEE/IAS Annual Meeting Conf.*, 1999, Phoenix, pp. 2623-2630.

[24] S. Arnalite, J. C. Burgos, and J. L. Rodriguez-Amendo, "Direct Torque Control of a Doubly-Fed Induction Generator for Variable Speed Wind Turbines," *Electric Power Components and Systems,* vol. 30, no. 2, pp. 199-216, 2002.

[25] Z. Mahi, C. Serban, and H. Siguerdidjane, "Direct Torque Control of a Doubly-Fed Induction Generator of a Variable Speed Wind Turbine Power Regulation," in *European Wind Energy Conf.,* May 2007, Milan.

[26] R. Datta and V. T. Ranganathan, "Direct Power Control of Grid-Connected Wound Rotor Induction Machine without Rotor Position Sensors," *IEEE Trans. Power Electronics,* vol. 16, no. 3, pp. 390-399, May 2001.

[27] L. Xu, and P. Cartwright, "Direct Active and Reactive Power Control of DFIG for Wind Energy Generation," *IEEE Trans. Energy Conversion*, vol. 21, no. 3, pp. 750-758, Sep. 2006.

[28] D. Zhi and L. Xu, "Direct Power Control of DFIG with Constant Switching Frequency and Improved Transient Performance," *IEEE Trans. Energy Conversion,* vol. 22, no. 1, pp. 110-118, Mar. 2007.

[29] G. Abad, M. A. Rodriguez, and J. Poza, "Two-Level VSC-Based Predictive Direct Power Control of the Doubly Fed Induction Machine with Reduced Power Ripple at Low Constant Switching Frequency," *IEEE Trans. Energy Conversion*, vol. 23, no. 2, pp. 570-580, Jun. 2008.

[30] D. Zhi, L. Xu, and B. W. Williams, "Model-Based Predictive Direct Power Control of Doubly Fed Induction Generators," *IEEE Trans. Power Electronics,* vol. 25, no. 2, pp. 341-351, Feb.

2010.

[31] S. Li, T. A. Haskew, K. A. Williams, and R. P. Swatloski, “Control of DFIG Wind Turbine with Direct-Current Vector Control Configuration,” *IEEE Trans. Sustainable Energy,* vol. 3, no. 1, pp. 1-11, Jan. 2012.

[32] L. Xu and W. Cheng, “Torque and reactive power control of a doubly-fed induction machine by position sensorless scheme,” *IEEE Trans. Ind. Appl.*, vol. 31, no. 3, pp. 636–641, May/Jun. 1995.

[33] M. Abolhassani, P. Niazi, H. Toliyat, and P. Enjeti, “A sensorless integrated Doubly-Fed electric alternator/active filter (IDEA) for variable speed wind energy system,” in *Conf. Rec IEEE IAS Annu. Meeting*, Salt Lake City, UT, 2003, vol. 1, pp. 507–514.

[34] L. Morel, H. Godfroid, A. Mirzaian, and J. M. Kauffmann, “Double-Fed induction machine: Converter optimisation and field oriented control without position sensor,” *Proc. Inst. Electr. Eng.—Power Appl.*, vol. 145, no. 4, pp. 360–368, Jul. 1998.

[35] B. Hopfensperger, D. J. Atkinson, and R. A. Lakin, “Stator-flux oriented control of a doubly-fed induction machine without position encoder,” *Proc. Inst. Electr. Eng.—Power Appl.*, vol. 147, no. 4, pp. 241–250, Jul. 2000.

[36] V. Verma, M. J. Hossain, T. Saha, and C. Chakraborty, “Performance of MRAS Based Speed Estimators for Grid Connected Doubly Fed Induction Machines During Voltage Dips,” in *Proc. IEEE Power and Energy Society General Meeting,* pp. 1-8, Jul. 2012.

[37] I. Benlaloui, S. Drid, L. Chrifi-Alaoui, and M. Ouriagli, “Implementation of a New MRAS Speed Sensorless Vector Control of Induction Machine,” *IEEE Trans. Energy Conversion,* vol. 30, no. 2, pp. 588-595, Jun. 2015.

[38] B. Shen, B. Mwinyiwiwa, Y. Zhang, and B. T. Ooi, “Sensorless Maximum Power Point Tracking of Wind by DFIG Using Rotor Position Phase Locked Loop (PLL),” *IEEE Trans. Power Electronics,* vol. 24, no. 4, pp. 942-951, Apr. 2009

[39] B. Mwinyiwiwa, Y. Zhang, B. Shen, and B. T. Ooi, “Rotor Position Phase-Locked Loop for Decoupled P-Q Control of DFIG for Wind Power Generation,” *IEEE Trans. Energy Conversion,* vol. 24, no. 3, pp. 758-765, Sep. 2009.

[40] D. G. Forchetti, G. O. Garcia, and M. I. Valla, “Adaptive Observer for Sensorless Control of Stand-Alone Doubly-Fed Induction Generator,” *IEEE Trans. Industrial Electronics*, vol. 56, no. 10, pp. 4174-4180, Oct. 2009.

[41] G. Iwanski, M. Szypulski, T. Luszczyk, and P. Pura, “Cross and Dot Product Based MRAS Observer of the Rotor Position of Doubly Fed Induction Machine,” in *Proc. 9th International Conf. EVRE*, Mar. 2014, pp. 1-5.

[42] R. Cardenas, R. Pena, J. Proboste, G. Asher, and J. Clare, “Sensorless Control of a Doubly-Fed Induction Generator for Stand Alone Operation,” in *Proc. 35th Annual IEEE Power Electronics Specialists Conf.,* Aachen, Germany, 2004, vol. 5, pp. 3378-3383.

[43] A. K. Jain and V. T. Ranganathan, “Wound Rotor Induction Generator with Sensorless Control and Integrated Active Filter for Feeding Nonlinear Loads in a Stand-Alone Grid,” *IEEE Trans. Industrial Electronics*, vol. 55, no. 1, pp. 218-228, Jan. 2008.

[44] G. Iwanski and W. Koczara, “Sensorless Stand Alone Variable Speed System for Distributed Generation,” in *Proc. 35th IEEE Power Electronics Specialists Conf.*, Aachen, Germany, 2004, vol. 3, pp. 1915-1921.

Chapter 2

Variable Speed Doubly-Fed Induction Generator in Distributed Generation Systems

In this work, the variable speed natural gas-fired engine is the prime mover, and the generator of choice is the doubly-fed induction generator (DFIG). The target is to build a complete control system for the DFIG generation system to operate correctly in a distributed generation system. The control system should be general so that it can be extended to other variable speed generation systems such as wind turbines.

The variable speed operation is attractive for different generation systems, such as internal combustion engines and wind turbines, because it offers several advantages which will be presented in the following sections. The DFIG is widely adopted in variable speed generation systems because it requires a converter rated at a fraction of the generator's rating (25%~30%); this reduces the system cost and improves the efficiency.

To meet the modern grid requirements, the DFIG should operate in a distributed generation system (DGS). In a DGS, several generation systems are connected to the grid, and a local load is connected near each generation system. The control system is responsible for guaranteeing an uninterruptable power supply to its local load regardless of the grid condition. Normally, the generator is connected to the grid, which is referred to as grid-connected mode, and it supports the grid by supplying active and reactive power. Since the grid-connected control will become unstable in case of grid failure, the control system must disconnect the generator from the grid, and it should regulate the amplitude and frequency of the generated voltage; this mode of operation is referred to as stand-alone mode. Consequently, the control system must support these two modes of operation.

In addition, the control system should achieve a smooth transition between the two modes of operation. The smooth transition from stand-alone to grid-connected mode requires a temporary mode of operation to gradually synchronize the generator's output voltage with that of the grid; this mode of operation is referred to as synchronization mode.

2.1 Variable Speed Generation Systems

Conventional generation systems use a synchronous or asynchronous generator which is rotating with a fixed speed; this configuration is referred to as fixed speed operation. The speed of the generator corresponds to the generated voltage frequency.

If the speed of the generator's rotor is allowed to vary, variable speed operation is obtained. The variable speed operation has several advantages for different generation systems; however, only the internal combustion engine and the wind turbine will be discussed in the following sections.

2.1.1 Internal Combustion Engine-Based Generation Systems

A. Fixed Speed Operation

Internal combustion engine based power generation is conventionally fixed speed, and it employs a synchronous generator. The engine speed corresponds to the frequency of the generated voltage, and it is regulated to guarantee a constant output frequency even with load variation.

If the losses are ignored, the generated electrical power is equal to the engine's mechanical power. The engine's output power characteristics are shown in Fig. 2.1 for four different fuel consumptions. The fixed speed operation corresponds to the red line in Fig. 2.1.

In the engine characteristic graph, there is a forbidden area where operation results in incomplete combustion of hydrocarbons and produces glaze on the engine internal components such as pistons, spark plugs, fuel injectors, etc. This can reduces the lifetime of the engine and increases the maintenance requirement [1].

To avoid operation in the forbidden region a dummy load is needed. The dummy load is normally disconnected; it is only connected in the case of low load condition.

The dummy load increases the power demand above the forbidden region to achieve safe operation of the engine. The dummy load can be rated at up to 40% of the engine power. Consequently, fuel consumption is increased in the case of low load condition.

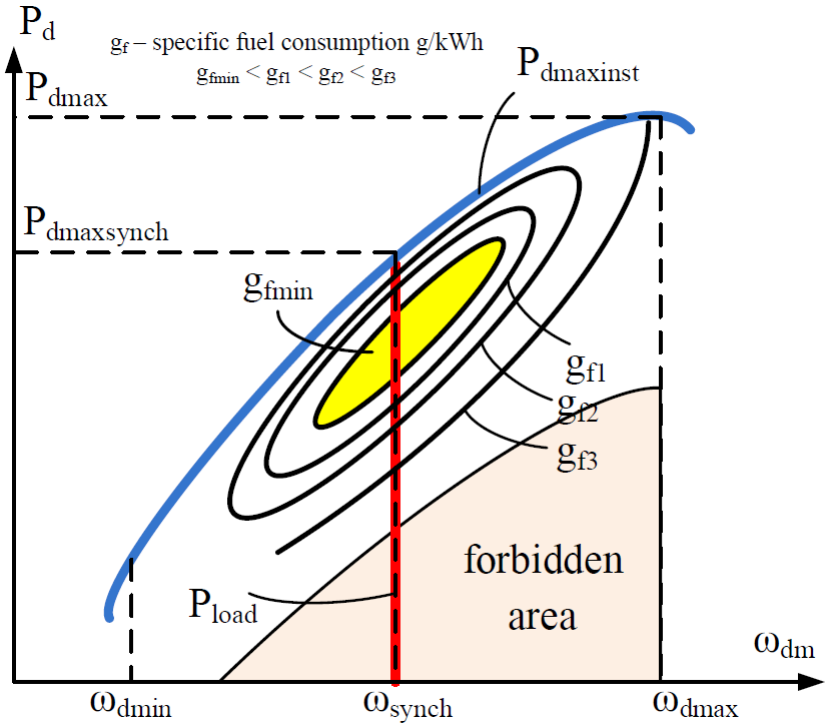

Fig. 2.1: Output power of an internal combustion engine for four different fuel consumption and with fixed speed operation (red) [1].

The maximum attainable power ($P_{dmaxsynch}$) from the internal combustion engine is significantly smaller than the engine maximum power (P_{dmax}) which can be delivered at a higher speed. This means that the engine must be overrated and oversized for fixed speed operation.

In Fig. 2.1, there is a region highlighted by yellow color which is referred to as optimum region. Operation in this region results in the lowest fuel consumption and, consequently, the best efficiency. However, this optimum region occupies a very narrow portion of the fixed speed operation.

B. Variable Speed Operation

In variable speed operation, the speed of the engine and, consequently, of the generator is allowed to vary within limited range. The engine's speed is varied with the output power in order to improve the fuel consumption efficiency. The engine's output power characteristic with variable speed operation is shown in Fig. 2.2, where the red

line corresponds to the variable speed operating.

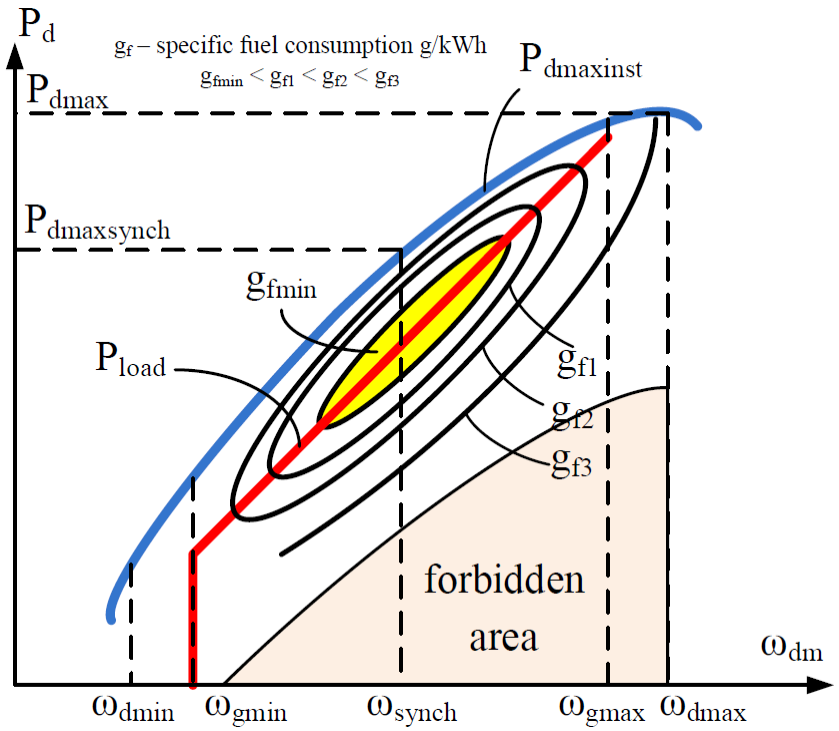

Fig. 2.2: Output power of an internal combustion engine for four different fuel consumption and with variable speed operation (red) [1].

In variable speed operation, the engine avoids the forbidden region by operating at low speed in the case of low load condition. Consequently, there is no need for dummy loads. This improves the efficiency at low load condition, reduces maintenance, and increases the engine's lifetime.

By operating the engine at higher speed, in the case of high load, the maximum output power is increased. Consequently, the maximum attainable output power is much higher than that of a fixed speed; this offers size and cost savings.

The engine speed is varied with the output power to track the minimum fuel consumption. Consequently, the optimum region occupies a wider portion of the operation region, which reduces the fuel consumption. This offers considerable savings and reduces the CO_2 emissions.

These advantages make the variable speed operation very attractive and we can expect, in the near future, that all fixed speed engines will be replaced with variable speed engines.

2.1.2 Wind Turbine-Based Generation Systems

A. Introduction

The wind turbine extracts, in the form of mechanical power, a fraction of the power available in the wind which is, then, converted into an electrical power using a generator. Referring to Fig. 2.3, the power available in the wind P_W that flows through a circle of radius R is given by (2.1), where ρ is the air density and U is the wind speed.

$$P_W = \frac{1}{2}\rho\pi R^2 U^3 \tag{2.1}$$

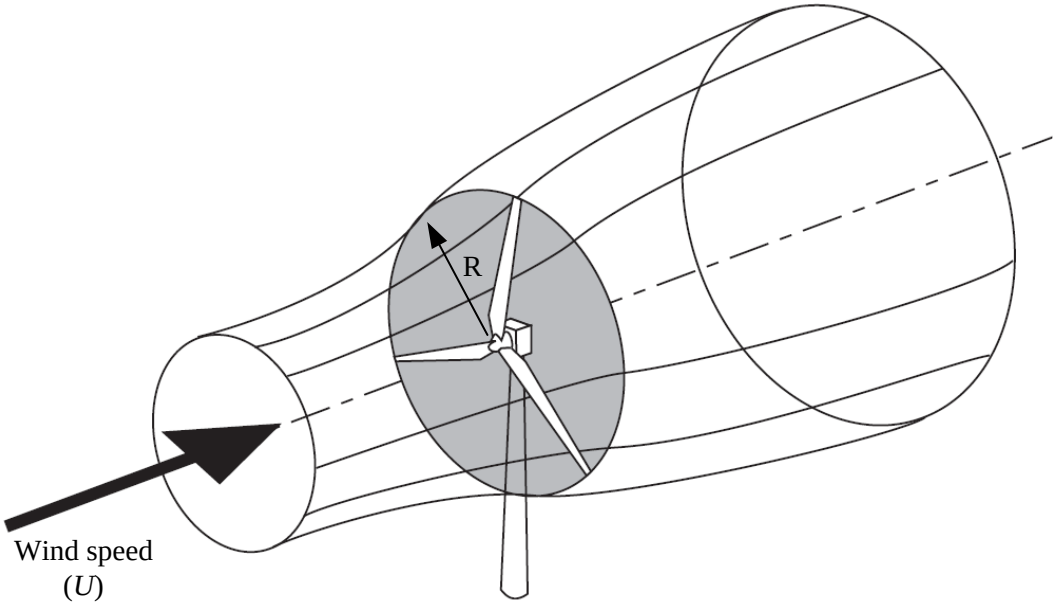

Fig. 2.3: Airstream of a wind turbine [2].

The extracted power by the wind turbine is referred to as turbine power (P_T) and is given by (2.2), where C_P is the power coefficient of the wind turbine.

$$P_T = C_P \cdot P_W \tag{2.2}$$

The power coefficient of a wind turbine is a function of the blade pitch angle (β) and the tip speed ratio (λ) which is defined by (2.3), where ω is the speed of the turbine in (rad/s).

$$\lambda = \frac{\omega R}{U} \tag{2.3}$$

According the wind speed, there are four regions of operation for a wind turbine which are depicted in Fig. 2.4.

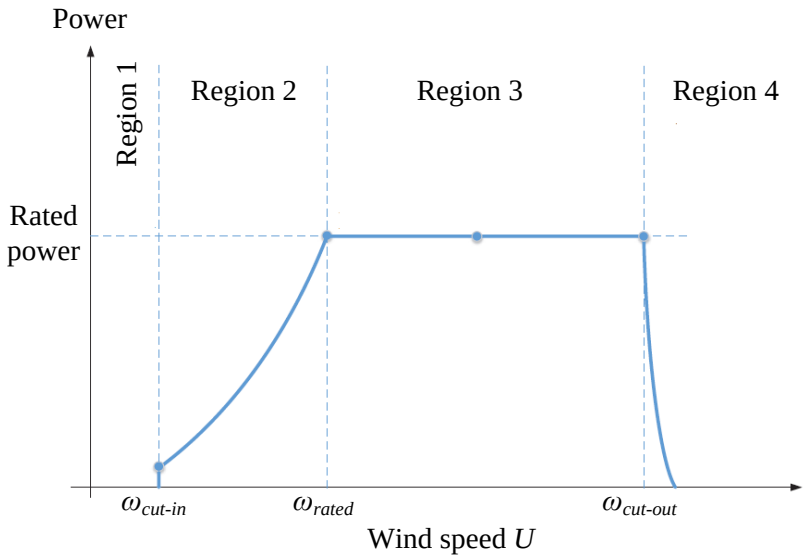

Fig. 2.4: Operating regions of a wind turbine.

In region 1, where the wind speed is low, the wind does not have enough power to rotate the turbine. Once the wind speed is above a lower limit ($\omega_{cut\text{-}in}$), the wind turbine operates in region 2, where it should obtain the maximum power possible until the extracted power reaches the upper limit imposed by the generator's rating. Normally, the wind turbine operates in region 2.

In region 3, the blade pitch angle is commonly employed to limit the extract power to the generator's rating. For higher wind speed above $\omega_{cut\text{-}out}$, the turbine will experience sever centrifugal force which can damage the turbine. Thus, in region 4, the turbine is stopped by making the C_p near zero and engaging mechanical brakes.

B. Fixed Speed Operation

The older wind turbines are mostly fixed speed because they are simple to build and easy to operate. Currently, the fixed speed operation is still in use for small size turbines [3].

The fixed speed wind turbines use an asynchronous or a synchronous generator which are connected directly to the grid. The asynchronous generator operates with very narrow speed range above the synchronous speed, while the synchronous generator operates with a constant speed at the synchronous speed.

The fixed speed wind turbines has several advantages when compared with the variable speed wind turbines: It is cheaper, it is simpler to operate, it is mechanically simpler, it requires less maintenance, and it is more robust [3] [4].

On the other hand, fixed speed wind turbines have several disadvantages, some of which can be observed from Fig. 2.5 which depicts the power output of a fixed speed wind turbine for different wind speeds.

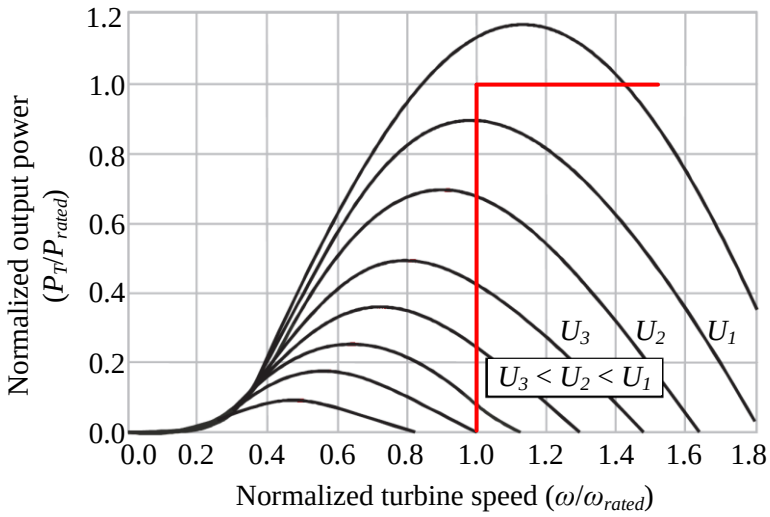

Fig. 2.5: Power characteristic of wind turbine as a function of the turbine speed for different wind speeds with fixed speed operation (red).

The cut-in speed of a fixed speed turbine is higher than that of a variable speed turbine. In other words, the fixed speed turbine has a narrower active region of operation, which reduces the return-on-investment.

The turbine speed is relatively high which can produce acoustic noise and increase the probability of bird collision. In addition, the relatively high speed requires a gearbox with high ratios or requires allowing the turbine to rotate at higher speed which requires the tower to withstand higher structural loads [3]; this increases the mechanical design complexity.

The fixed speed turbine can operate optimally at only one wind speed; in Fig. 2.5, it is U_1. This speed corresponds to the tip speed ratio that gives the maximum value of the power coefficient [5].

Because of fixed speed operation, fluctuation in wind speed as well as gusts

translates into continuous and sudden torsional torques that stresses the drive train shaft and the gearbox [3], and it produces fluctuation in the output power [4].

C. Variable Speed Operation

The variable speed operation of the wind turbines is popular especially with large turbines, because of its advantages. The power characteristic of a variable speed wind turbine is depicted in Fig. 2.6.

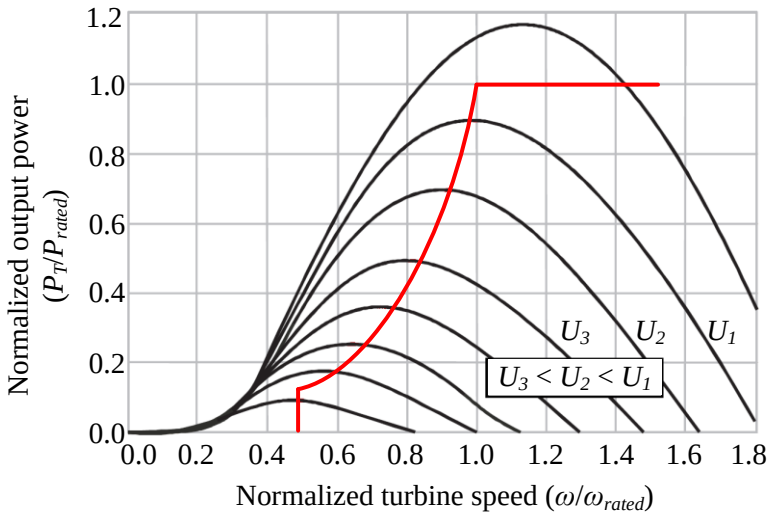

Fig. 2.6: Power characteristic of a wind turbine as a function of the turbine speed for different wind speeds with variable speed operation (red).

From Fig. 2.6, the variable speed wind turbine can produce power at lower wind speeds. Thus, the variable speed turbines has an active region of operation wider than the fixed speed turbines [3]; this increases the return-on-investment. In addition, the rotor speed in region 2 is varied to maintain peak aerodynamic efficiency which increases the extracted power compared with the fixed speed operation [3] [5]; this increases the return-on-investment.

The variable speed operation leads to a reduction in mechanical stresses, because the turbine will act as flywheel whose speed can vary in response to wind turbulence and cyclic torque variations such as those produced by tower shadow [5]. This produces a smoother output power which means higher power quality [5].

The new grid code regulation requires the wind turbines to continue operation and to support the grid in case of grid fault. These requirements are difficult to meet with

fixed speed turbines, but they can be met with variable speed turbines [3] [5].

The power electronic converter in variable speed wind turbines allows controlling the generated active and reactive powers. Furthermore, the converter enables smooth connection of the generator to the grid [5]; this makes variable speed turbines suitable for distributed generation systems [4].

The reduced rotor speed in slow winds significantly reduces the acoustic noise and the chances of bird collision [3].

On the other hand, variable speed wind turbines are more complex and more expensive, and they require more maintenance. The power electronic converter generates electrical noise and harmonics which requires additional filters [3] [5].

2.2 Variable Speed Doubly-Fed Induction Generator

The variable speed operation of an internal combustion engine or a wind turbine has several advantages; however, the varying speed of the generator produces variable output frequency. Thus, special configuration is required to guarantee fixed frequency output. There are two main types of variable speed systems: The broad range and the limited range variable speed.

The broad range variable speed allows the speed of the generator to vary from near zero to the rated speed. This configuration requires a fully rated converter to be inserted between the generator and the grid as shown in Fig. 2.7. This configuration normally uses a synchronous generator whose rotor is either a permanent magnet or a wound rotor.

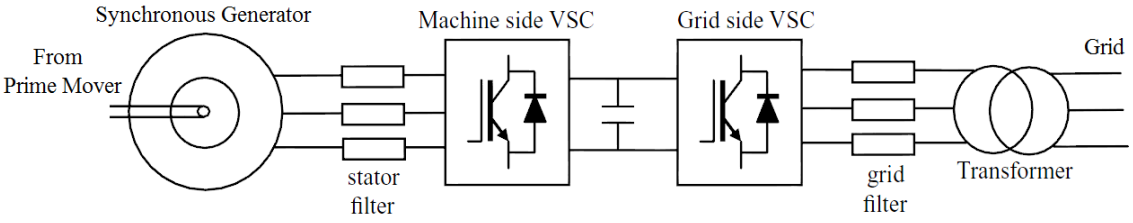

Fig. 2.7: Configuration of the broad range variable speed generation system [6].

The wound rotor synchronous generator allows access to the rotor windings through slip rings and brushes. By controlling the rotor current, the voltage and the reactive power at the generator's stator terminal can be controlled. However, the losses

in the rotor circuit reduces the overall efficiency, and the slip rings reduce the system robustness and increase the maintenance requirements.

The permanent magnet synchronous generator does not have a rotor circuit, which reduces the losses and increases the robustness. However, the absence of rotor circuit reduces the controllability of the output voltage and the reactive power. Moreover, it is made out of rare earth magnetic materials to provide strong magnetic field; thus the cost is higher.

The broad range variable speed has some disadvantages which are:

- The rating of the converter is equal to the generator rating which increases the system cost and size.
- The losses of the converter reduces the system's overall efficiency.
- The converter produces harmonics and electrical noise which needs to go through filters to reduces them. The rating of these filters must be equal to the rating of the converter; this increases the system cost and design complexity.

On the other hand, the limited range variable speed systems allow the speed to vary within a limited range typically 20 ~ 40% on either side of the synchronous speed. This configuration achieves almost all the advantages of the broad band variable speed operation. The limited range variable speed, which is characterized by the use of doubly-fed induction generator (DFIG), is depicted in Fig. 2.8.

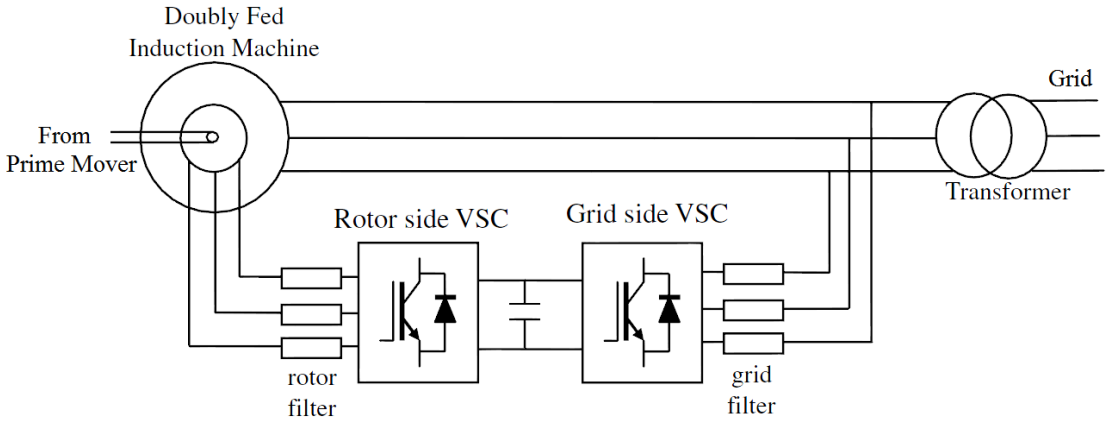

Fig. 2.8: Configuration of the limited range variable speed generation system [6].

The DFIG is an induction machine that has, in addition to the stator windings, rotor windings which are accessible through brushes and slip rings. The converter in a DFIG

generation system is inserted between the stator and rotor terminals, and it supplies the slip power which is a fraction of the generator's power.

The variable speed DFIG system has the following advantages:

- The rating of the converter is a fraction of the generator's rating which is typically 20 ~ 40 %; this significantly reduces the cost and size of the system.
- The system's overall efficiency is improved by approximately 2 ~ 3 % due to reduced power losses of the power electronic converter.
- The rating of the inverter's output filter and EMI filter is reduced, this reduces the design complexity.

The disadvantage of this system is the need for slip rings. The slip rings increases the maintenance cost especially in off-shore turbines. However, the advantages of the DFIG make it popular, where it occupies near 50% of the wind turbine market [7].

2.3 Distributed Generation Systems

A highly civilized and information-oriented society relies greatly on electricity for economic activities and social life. Therefore, high reliability and stability are required for the power supply facilities which sustain social infrastructures [8].

Different types of hazards, such as earthquakes, floods, and typhoons, can cause blackouts; a typical countermeasure to these hazards is to have a back-up power supply near the facility. Originally, diesel engine-driven generators have been used for back-up power supply during islanding condition (stand-alone) because of their capabilities such as fast start-up, durability, and reliability of fuel storage [8].

The search for stable, reliable electricity, resulted in the evolution of distributed generation systems. The distributed generation systems increase the available power, improve the overall reliability, lower the cost, and reduce the emission of greenhouse gases [4].

The concept of a distributed generation system (DGS) assumes that the power network is supplied not only from the central power stations but also from many different local power stations. A local load is connected close to the power station so

that it can supply it during the loss of mains caused by, for example, breaking of the transmission line or permanent short circuit in the grid [9].

A gas engine cogeneration system is one of the promising distributed generation systems; it is regarded as one solution for the environmental problems, because it offer considerable reduction in the emission of greenhouse gases compared with other fossil fuel such as coal or diesel. Fig. 2.9 shows a DFIG based gas engine power system in a distributed generation system.

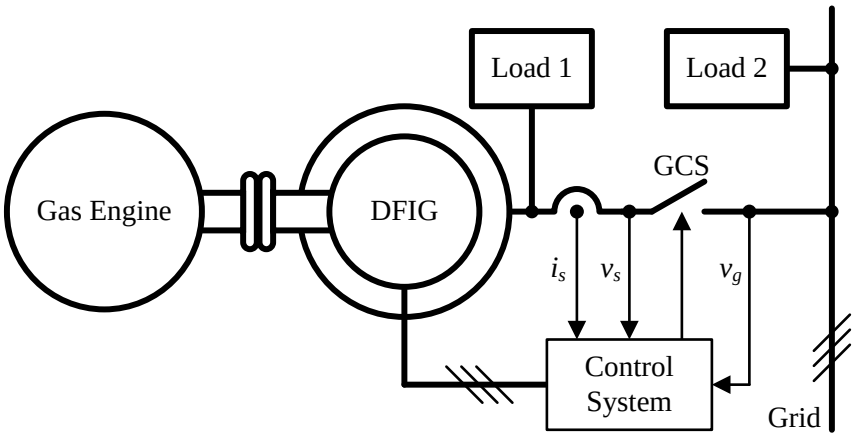

Fig. 2.9: DFIG based generation system in a distributed generation system.

The system is equipped with an intelligent control system to provide all the different modes of operation required for DGS operation, which can be summarized by Fig. 2.10.

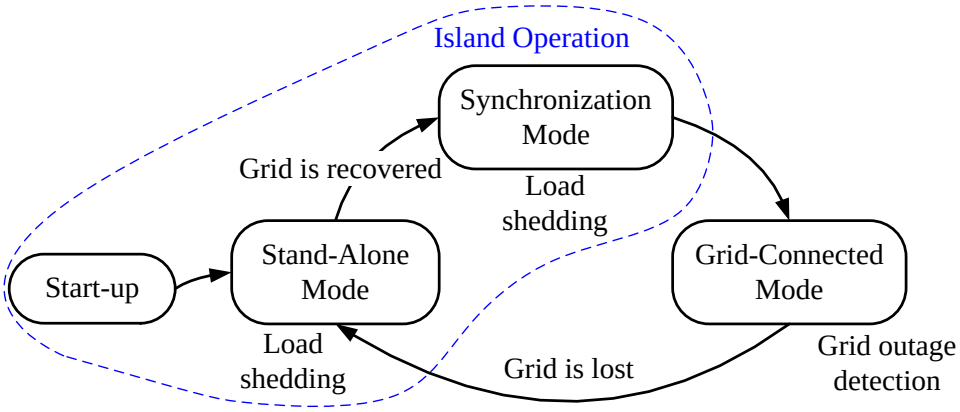

Fig. 2.10: Operation of the DFIG in a distributed generation system.

The control system must be prepared to operate in stand-alone mode of operation during start-up or in the case of grid failure. During stand-alone mode of operation, the

generator supplies all or part of the local load depending on the capacity of the generator, where load shedding is employed to protect the DFIG from overload. The control system, during stand-alone, regulates the amplitude and frequency of the DFIG's output voltage. In addition, the control system continuously checks the grid voltage. When the grid voltage is recovered, the control system must reconnect the DFIG to the grid. The connection must be smooth to protect the DFIG and to maintain an uninterruptable power supply to the local load.

The smooth connection to the grid requires a temporary mode of operation which is the synchronization mode. During this mode, the control system gradually synchronizes the DFIG's output voltage with that of the grid. Once the two voltages are synchronized, the control system reconnects the DFIG by closing the grid-connecting-switch (GCS).

The synchronization mode achieves zero voltage switching of the GCS, it significantly reduces the inrush currents, and it protects the local load and the DFIG from sudden phase change which can cause tripping of electrical equipment and inflect mechanical stresses on the DFIG's shaft. Once the GCS is closed, the control system is switched to grid-connected mode of operation where it supports the grid by controlling the generated active and reactive power.

To ensure an uninterruptable power supply when the DFIG is to be disconnected from the grid due to a grid failure, the control system should be equipped with mains outage detection algorithms based on voltage amplitude and frequency detection [9].

2.4 System Modelling

The electrical circuit of a DFIG system is depicted in Fig. 2.11. It consists of a DFIG, and two converters which are connected to a common dc-link: The grid side converter (GSC) and the rotor side converter (RSC). The GSC operates as an active rectifier which regulates the dc-link voltage by exchanging power with the ac grid.

The RSC controls the angle and amplitude of the DFIG's rotor currents to control the frequency and amplitude of the generated voltage during stand-alone operation or to control the generated active and reactive power during grid-connected operation.

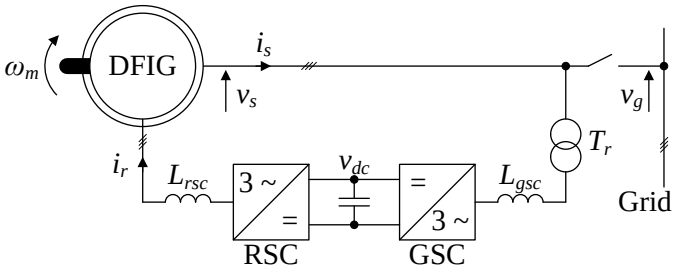

Fig. 2.11: Schematic diagram of the electrical circuit of a DFIG system.

2.4.1 dq-Transformation

In this work, the modeling and the control of the DFIG system are carried out in the synchronous reference frame which requires performing the dq-transformation. The dq-transformation converts the ac voltages and currents into dc quantities; this allows the use of classical control methods which significantly simplifies the control design.

The dq-transformation is a time domain to time domain transformation which converts a three-phase system from the stationary reference frame into a rotating reference frame.

The dq-transformation is defined by a matrix multiplication as in (2.4), where v_o is the zero-sequence component which represents the common mode voltage. The zero-sequence component is zero for three wire systems.

$$\begin{pmatrix} v_d \\ v_q \\ v_0 \end{pmatrix} = T(\theta) \begin{pmatrix} v_a \\ v_b \\ v_c \end{pmatrix} \tag{2.4}$$

There are different definition of the transformation matrix T; in this work we adopt the definition of (2.5), where $\theta = \omega t$ and ω is equal to the voltage angular frequency.

$$T(\theta) = \sqrt{\frac{2}{3}} \begin{pmatrix} \cos(\theta) & \cos\left(\theta - \frac{2\pi}{3}\right) & \cos\left(\theta + \frac{2\pi}{3}\right) \\ -\sin(\theta) & -\sin\left(\theta - \frac{2\pi}{3}\right) & -\sin\left(\theta + \frac{2\pi}{3}\right) \\ \frac{1}{\sqrt{2}} & \frac{1}{\sqrt{2}} & \frac{1}{\sqrt{2}} \end{pmatrix} \tag{2.5}$$

Since three-wire system is adopted in this work, the zero-sequence component is always zero and is dropped; thus, the dq-transformation matrix is redefined by (2.6).

$$T(\theta) = \sqrt{\frac{2}{3}} \begin{pmatrix} \cos(\theta) & \cos\left(\theta - \frac{2\pi}{3}\right) & \cos\left(\theta + \frac{2\pi}{3}\right) \\ -\sin(\theta) & -\sin\left(\theta - \frac{2\pi}{3}\right) & -\sin\left(\theta + \frac{2\pi}{3}\right) \end{pmatrix} \tag{2.6}$$

By using a balanced three-phase voltage which is given by (2.7), the dq-transformation is given by (2.8), where $\varphi = \omega t + \varphi_0$, where φ_0 is the initial voltage angle.

$$\begin{pmatrix} v_a \\ v_b \\ v_c \end{pmatrix} = V \begin{pmatrix} \cos(\varphi) \\ \cos\left(\varphi - \frac{2\pi}{3}\right) \\ \cos\left(\varphi + \frac{2\pi}{3}\right) \end{pmatrix} \tag{2.7}$$

$$\begin{pmatrix} v_d \\ v_q \end{pmatrix} = V \sqrt{\frac{3}{2}} \begin{pmatrix} \cos(\varphi - \theta) \\ \sin(\varphi - \theta) \end{pmatrix} \tag{2.8}$$

The dq-transformation can also be represented in the complex plane using the vector diagram of Fig. 2.12.

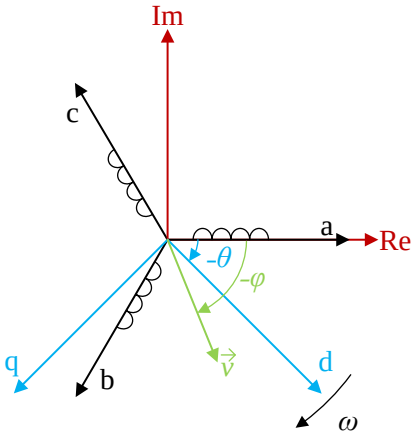

Fig. 2.12: Vector diagram of three-phase system.

The vector representation of the three-phase voltage of (2.7) is given in the stationary reference frame (abc-frame) by (2.9), where V is the voltage amplitude.

$$\vec{v} = \sqrt{\frac{2}{3}}\left(v_a + v_b e^{-j2\pi/3} + v_c e^{j2\pi/3}\right) = V\sqrt{\frac{3}{2}} e^{-j\varphi} \tag{2.9}$$

The vector representation of (2.9) in the dq-frame is given by (2.10)

$$(\vec{v})_{dq} = V\sqrt{\frac{3}{2}}e^{j(\varphi-\theta)} \tag{2.10}$$

Consequently, using the vector representation, the dq-transformation is defined by (2.11), where the star superscript (*) represents the complex conjugate.

$$(\vec{v})_{dq} = e^{-j\theta}\vec{v}^* \tag{2.11}$$

2.4.2 Modeling of the DFIG

Since the DFIG is an induction machine, the mechanical speed can differ from the frequency of the stator voltage. The equivalent mechanical speed of a two-pole machine is denoted as ω_m, and the angular frequency of the generated voltage, which is the synchronous angular frequency, is denoted as ω_s. The mechanical speed is related to the DFIG's rotor speed ω_{rotor} by the number of poles (p) of the DFIG as in (2.12).

$$\omega_m = \frac{p}{2}\omega_{rotor} \tag{2.12}$$

A simplified representation of the cross section of a DFIG is depicted in Fig. 2.13.

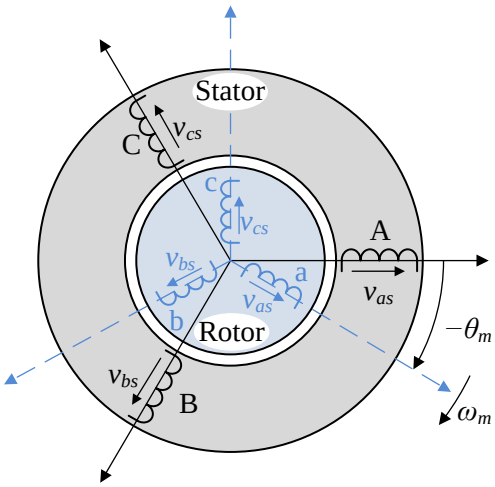

Fig. 2.13: Symbolic representation of the cross section of a DFIG.

The DFIG has two three-phase reference frames: One is the stationary reference frame which is fixed to the stator windings (ABC), and the other is the rotor reference

frame which is fixed to the rotor windings (abc). The mechanical angle θ_m is the angle between the ABC-frame and the abc-frame.

The single phase equivalent circuit of the DFIG is depicted in Fig. 2.14.

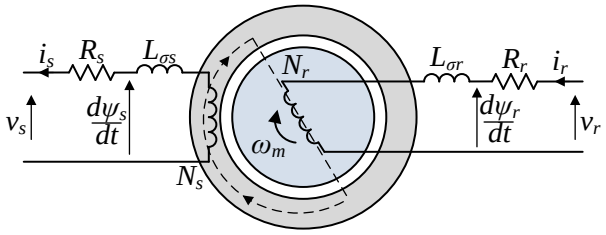

Fig. 2.14: Single-phase equivalent circuit of a DFIG.

The voltage equations across the stator and rotor sides are given by (2.13) and (2.14) respectively.

$$\begin{cases} v_{sa} = -R_s i_{sa} + \dfrac{d\psi_{sa}}{dt} \\ v_{sb} = -R_s i_{sb} + \dfrac{d\psi_{sb}}{dt} \\ v_{sc} = -R_s i_{sc} + \dfrac{d\psi_{sc}}{dt} \end{cases} \tag{2.13}$$

$$\begin{cases} v_{ra} = R_r i_{ra} + \dfrac{d\psi_{ra}}{dt} \\ v_{rb} = R_r i_{rb} + \dfrac{d\psi_{rb}}{dt} \\ v_{rc} = R_r i_{rc} + \dfrac{d\psi_{rc}}{dt} \end{cases} \tag{2.14}$$

Using the vector representation of (2.9), we get (2.15) and (2.16), which are represented in the stationary and the rotor reference frame respectively.

$$\vec{v}_s = -R_s \vec{i}_s + \frac{d\vec{\psi}_s}{dt} \tag{2.15}$$

$$\vec{v}_r = R_r \vec{i}_r + \frac{d\vec{\psi}_r}{dt} \tag{2.16}$$

The rotor currents and voltages can only be measured at the slip rings of the DFIG; that is, they are measured in the rotor reference frame. To write the flux linkage, the rotor and stator currents must be expressed in the same reference frame, which will be

the stator stationary reference frame. Since the rotor reference frame is rotating relative to the stationary reference frame with the mechanical angular frequency ω_m, the rotor current can be expressed in the stationary reference frame, which is denoted by an S subscript, using (2.17).

$$(\vec{\imath}_r)_S = e^{-j\theta_m}\vec{\imath}_r \tag{2.17}$$

Using (2.17), the stator and rotor flux linkage are given by (2.18) and (2.19) respectively, where $L_{\sigma s}$ is the stator leakage inductance, $L_{\sigma r}$ is the rotor leakage inductance, L_m is the mutual inductance, and $L_m = N_r/N_s\, L_s = N_s/N_r\, L_r$.

$$\vec{\psi}_s = -(L_s + L_{\sigma s})\vec{\imath}_s + L_m(\vec{\imath}_r)_S \tag{2.18}$$

$$\left(\vec{\psi}_r\right)_S = -L_m\vec{\imath}_s + (L_r + L_{\sigma r})(\vec{\imath}_r)_S \tag{2.19}$$

The dq-transformation of a rotor quantity is defined by (2.20), where * is the complex conjugate.

$$(\vec{v}_r)_{dq} = e^{-j(\theta_s-\theta_m)}\vec{v}_r{}^* \tag{2.20}$$

Consequently, the mathematical model of the DFIG in the synchronous reference frame is obtained by applying the dq-transformation to (2.15)-(2.19), and it is given by (2.21)-(2.24).

$$(\vec{v}_s)_{dq} = -R_s(\vec{\imath}_s)_{dq} + \frac{d\left(\vec{\psi}_s\right)_{dq}}{dt} + j\omega_s\left(\vec{\psi}_s\right)_{dq} \tag{2.21}$$

$$(\vec{v}_r)_{dq} = R_r(\vec{\imath}_r)_{dq} + \frac{d\left(\vec{\psi}_r\right)_{dq}}{dt} + j(\omega_s - \omega_m)\left(\vec{\psi}_r\right)_{dq} \tag{2.22}$$

$$\left(\vec{\psi}_s\right)_{dq} = -(L_s + L_{\sigma s})(\vec{\imath}_s)_{dq} + L_m(\vec{\imath}_r)_{dq} \tag{2.23}$$

$$\left(\vec{\psi}_r\right)_{dq} = -L_m(\vec{\imath}_s)_{dq} + (L_r + L_{\sigma r})(\vec{\imath}_r)_{dq} \tag{2.24}$$

The equivalent circuit of the DFIG can be obtained from the previous equations, and it is depicted in Fig. 2.15.

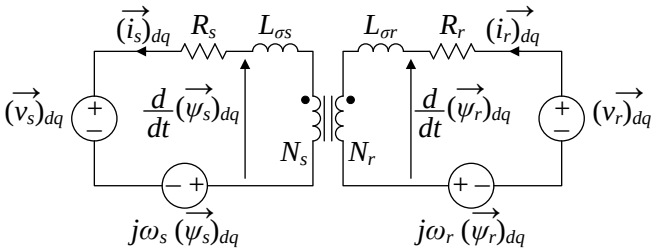

Fig. 2.15: Equivalent circuit of the DFIG in the dq-frame.

It is also important to calculate the active and reactive power and the torque. The stator active and reactive power is calculated in the stationary reference frame using (2.25) and (2.26).

$$p_s = v_{sa} i_{sa} + v_{sb} i_{sb} + v_{sc} i_{sc} \tag{2.25}$$

$$q_s = \frac{1}{\sqrt{3}}[(v_{sb} - v_{sc}) i_{sa} + (v_{sc} - v_{sa}) i_{sb} + (v_{sa} - v_{sb}) i_{sc}] \tag{2.26}$$

Using the vector representation, the active and reactive power are given in the stationary reference frame by (2.27) and (2.28) and in the dq-frame by (2.29) and (2.30).

$$p_s = \mathrm{Re}\{\vec{v}_s^{\,*} \cdot \vec{i}_s\} \tag{2.27}$$

$$q_s = \mathrm{Im}\{\vec{v}_s^{\,*} \cdot \vec{i}_s\} \tag{2.28}$$

$$p_s = \mathrm{Re}\{(\vec{v}_s)_{dq} \cdot (\vec{i}_s)_{dq}^{\,*}\} \tag{2.29}$$

$$q_s = \mathrm{Im}\{(\vec{v}_s)_{dq} \cdot (\vec{i}_s)_{dq}^{\,*}\} \tag{2.30}$$

The electromagnetic torque in the stationary reference frame is given by (2.31) and (2.32).

$$T_e = \frac{p}{2} \cdot \frac{1}{\sqrt{3}}[(\psi_{rc} - \psi_{rb}) i_{ra} + (\psi_{ra} - \psi_{rc}) i_{rb} + (\psi_{rb} - \psi_{ra}) i_{rc}] \tag{2.31}$$

$$T_e = \frac{p}{2} \mathrm{Im}\{\vec{\psi}_r \cdot \vec{i}_r^{\,*}\} \tag{2.32}$$

The electromechanical torque is given in the dq-frame by (2.33).

$$T_e = \frac{p}{2} \mathrm{Im}\left\{(\vec{\psi}_r)_{dq}^{\,*} \cdot (\vec{i}_r)_{dq}\right\} \tag{2.33}$$

Finally, the mechanical dynamics is approximated by (2.34), where J is mechanical inertia and T_d is the prime mover torque (driving torque).

$$J\frac{d}{dt}\omega_{rotor} = T_d - T_e \tag{2.34}$$

2.4.3 Modeling of the RSC's Circuit

In this work the inverter of choice is the simple three-phase three-level inverter as shown in Fig. 2.16 which depicts the RSC circuit.

There are two main methods to generate the gating signals for the inverter's transistors: The sinusoidal pulse width modulation (SPWM) and the space vector modulation (SVM). In this work, we have chosen the SPWM because it is more suitable for use with dq-transformation.

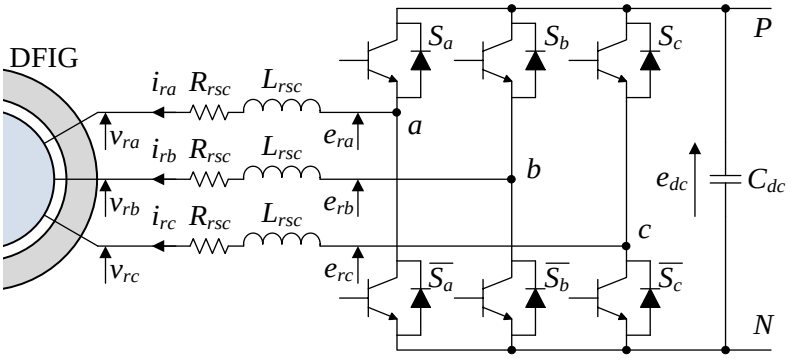

Fig. 2.16: RSC circuit.

The modelling is based on the following assumptions:

1. The transistors turns on and off instantly without delay, rise time or fall time.

2. The effect of the dead-time of the transistor's gating signals is ignored.

3. The RSC circuit is a three-wire circuit; that is $i_{ra} + i_{rb} + i_{rc} = 0$.

4. The dc-link voltage is assumed well-regulated and constant.

The SPWM generates pulses with varying widths which enables controlling the output voltage. The choice of pulse widths enables eliminating and generating certain harmonics. In SPWM, the pulses are generated by comparing a triangular signal at high frequency with three-phase sinusoidal signals at the desired frequency as shown in Fig.

2.17. This generates the desired sine wave signals with additional harmonics at higher frequencies which can be filtered easily.

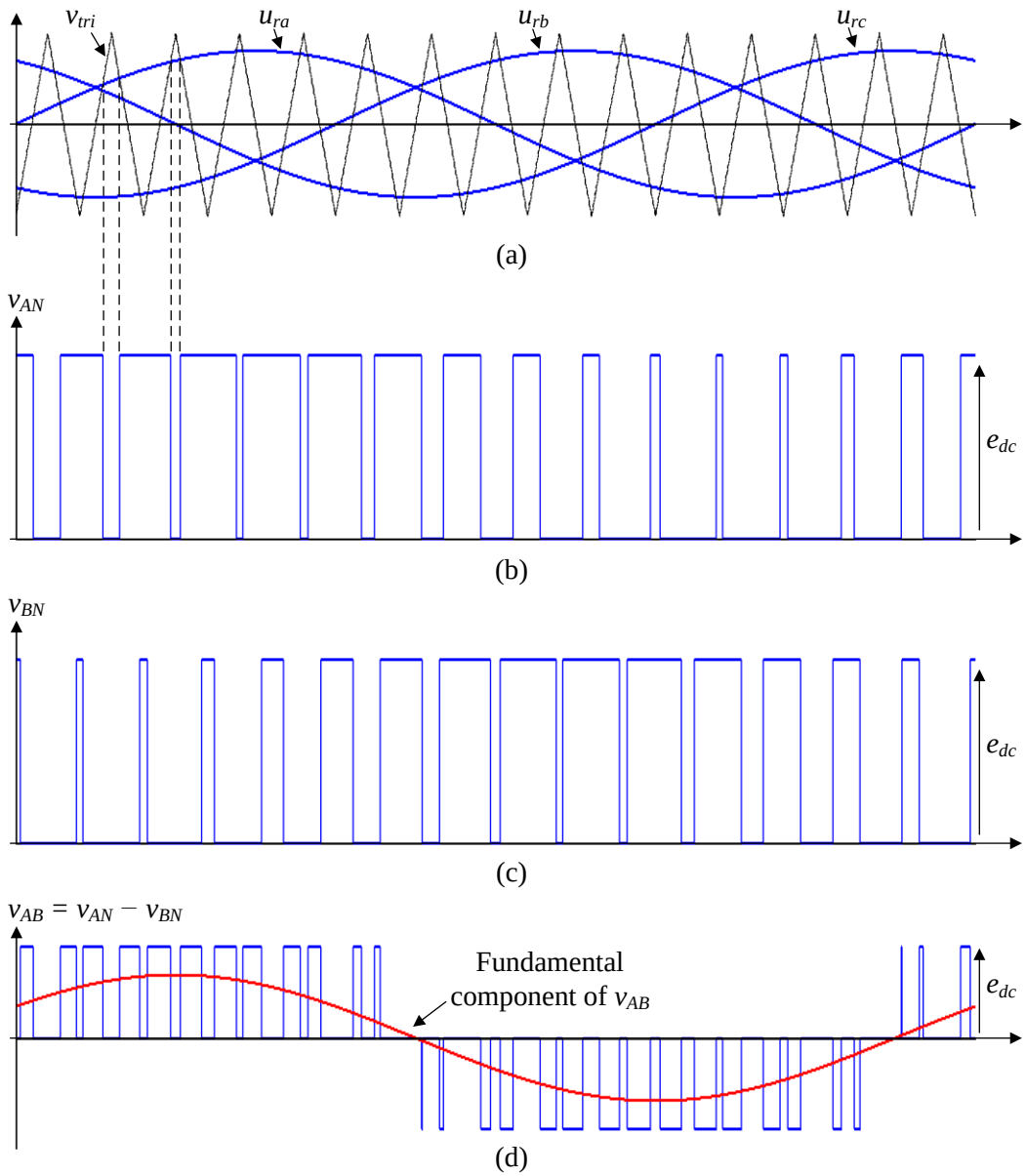

Fig. 2.17: Waveforms of three-phase SPWM.

When the sine signal is higher than the triangular signal the output is connected to the positive rail (P) by turning on the upper transistor, and in the opposite case the output is connected to the negative rail by turning on the lower transistor.

To derive a mathematical model of the RSC, we must define switching functions for each output of the RSC which express their status. Since the dead-time is ignored,

there is only two possible status of an output: being connected to the positive rail (P) or being connected to the negative rail (N). Then, the switching functions are defined mathematically by (2.35)

$$u_{rk} = \begin{cases} 1 & if \quad S_k = On \\ -1 & if \quad S_k = Off \end{cases} \quad for \quad k = \{a, b, c\} \tag{2.35}$$

Using the switching functions, the line-to-line terminal voltages of the RSC can be written as in (2.36).

$$\begin{cases} v_{ab} = v_{aN} - v_{bN} = \dfrac{1}{2}(u_{ra} - u_{rb})e_{dc} \\ v_{bc} = v_{bN} - v_{cN} = \dfrac{1}{2}(u_{rb} - u_{rc})e_{dc} \\ v_{ca} = v_{cN} - v_{aN} = \dfrac{1}{2}(u_{rc} - u_{ra})e_{dc} \end{cases} \tag{2.36}$$

On the other hand, the line (line-to-neutral) voltages of the RSC are given by (2.37).

$$\begin{cases} e_{ra} = \dfrac{1}{3}(2v_{ab} + v_{bc}) \\ e_{ra} = \dfrac{1}{3}(2v_{bc} + v_{ca}) \\ e_{rc} = \dfrac{1}{3}(2v_{ca} + v_{ab}) \end{cases} \tag{2.37}$$

By combining (2.36) and (2.37), the relation between the line-voltages of the RSC and the switching functions is obtained, and it is given in matrix form in (2.38).

$$\begin{pmatrix} e_{ra} \\ e_{rb} \\ e_{rc} \end{pmatrix} = \frac{e_{dc}}{6} \begin{pmatrix} 2 & -1 & -1 \\ -1 & 2 & -1 \\ -1 & -1 & 2 \end{pmatrix} \begin{pmatrix} u_{ra} \\ u_{rb} \\ u_{rc} \end{pmatrix} \tag{2.38}$$

On the other hand, the DFIG's rotor voltages are related to the rotor current and the RSC output voltage as shown in (2.39), which can be rewritten in matrix form as in (2.40).

$$\begin{cases} v_{ra} = -L_{rsc}\dfrac{d}{dt}i_{ra} - R_{rsc}i_{ra} + e_{ra} \\ v_{rb} = -L_{rsc}\dfrac{d}{dt}i_{rb} - R_{rsc}i_{rb} + e_{rb} \\ v_{rc} = -L_{rsc}\dfrac{d}{dt}i_{rc} - R_{rsc}i_{rc} + e_{rc} \end{cases} \tag{2.39}$$

$$\begin{pmatrix} v_{ra} \\ v_{rb} \\ v_{rc} \end{pmatrix} = -L_{rsc}\frac{d}{dt}\begin{pmatrix} i_{ra} \\ i_{rb} \\ i_{rc} \end{pmatrix} - R_{rsc}\begin{pmatrix} i_{ra} \\ i_{rb} \\ i_{rc} \end{pmatrix} + \begin{pmatrix} e_{ra} \\ e_{rb} \\ e_{rc} \end{pmatrix} \tag{2.40}$$

The model of the RSC circuit is described in the rotor reference frame using (2.38) and (2.40).

To obtain this model in the dq-frame, we need to apply the dq-transformation to (2.20) to (2.38) and (2.40). This requires the following definitions, where θ_r is the slip angle which is equal to $\theta_s - \theta_m$:

$$\begin{pmatrix} e_{rd} \\ e_{rq} \end{pmatrix} = T(\theta_r)\begin{pmatrix} e_{ra} \\ e_{rb} \\ e_{rc} \end{pmatrix} \tag{2.41}$$

$$\begin{pmatrix} u_{rd} \\ u_{rq} \end{pmatrix} = T(\theta_r)\begin{pmatrix} u_{ra} \\ u_{rb} \\ u_{rc} \end{pmatrix} \tag{2.42}$$

Then, the mathematical model of the RSC circuit model in the dq-frame is given by the following equations:

$$\begin{pmatrix} e_{rd} \\ e_{rq} \end{pmatrix} = \frac{e_{dc}}{2}\begin{pmatrix} u_{rd} \\ u_{rd} \end{pmatrix} \tag{2.43}$$

$$\begin{pmatrix} v_{rd} \\ v_{rq} \end{pmatrix} = -L_{rsc}\frac{d}{dt}\begin{pmatrix} i_{rd} \\ i_{rq} \end{pmatrix} - R_{rsc}\begin{pmatrix} i_{rd} \\ i_{rq} \end{pmatrix} - \omega_r L_{rsc}\begin{pmatrix} -i_{rq} \\ i_{rd} \end{pmatrix} + \begin{pmatrix} e_{rd} \\ e_{rq} \end{pmatrix} \tag{2.44}$$

2.4.4 Modeling of the GSC's Circuit

The GSC circuit is depicted in Fig. 2.18.

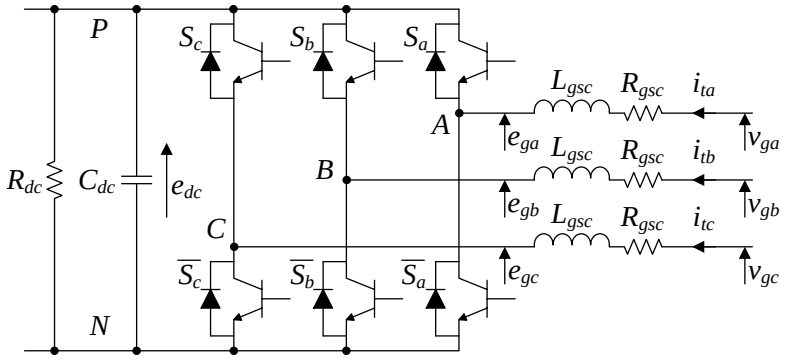

Fig. 2.18: GSC circuit.

The modeling of the GSC circuit is similar to the modeling of the RSC circuit. However, the assumption that the dc-link voltage is constant is dropped and is replaced with the assumption that the RSC can be approximated by a purely resistive load. Since the dc-link is now an RC circuit, there is one more additional equation.

Similar to (2.38) and (2.40), the voltage equations at the GSC inputs are in the stationary reference frame given by (2.45) and (2.46).

$$\begin{pmatrix} e_{ga} \\ e_{gb} \\ e_{gc} \end{pmatrix} = \frac{e_{dc}}{6} \begin{pmatrix} 2 & -1 & -1 \\ -1 & 2 & -1 \\ -1 & -1 & 2 \end{pmatrix} \begin{pmatrix} u_{ga} \\ u_{gb} \\ u_{gc} \end{pmatrix} \tag{2.45}$$

$$\begin{pmatrix} v_{ga} \\ v_{gb} \\ v_{gc} \end{pmatrix} = L_{gsc} \frac{d}{dt} \begin{pmatrix} i_{ta} \\ i_{tb} \\ i_{tc} \end{pmatrix} + R_{gsc} \begin{pmatrix} i_{ta} \\ i_{tb} \\ i_{tc} \end{pmatrix} + \begin{pmatrix} e_{ga} \\ e_{gb} \\ e_{gc} \end{pmatrix} \tag{2.46}$$

The dc-link voltage can be express mathematically by (2.47).

$$\frac{d}{dt} e_{dc} = \frac{1}{2 \cdot C_{dc}} \left(u_{ga} i_{ta} + u_{gb} i_{tc} + u_{gc} i_{tc} \right) - \frac{e_{dc}}{R_{dc} C_{dc}} \tag{2.47}$$

To obtain the mathematical model in the synchronous reference frame, we need the following definitions:

$$\begin{pmatrix} e_{gd} \\ e_{gq} \end{pmatrix} = T(\theta_s) \begin{pmatrix} e_{ga} \\ e_{gb} \\ e_{gc} \end{pmatrix} \tag{2.48}$$

$$\begin{pmatrix} u_{gd} \\ u_{gq} \end{pmatrix} = T(\theta_s) \begin{pmatrix} u_{ga} \\ u_{gb} \\ u_{gc} \end{pmatrix} \tag{2.49}$$

Moreover, with simple mathematical manipulation, (2.50) is derived.

$$u_{ga} i_{ta} + u_{gb} i_{tc} + u_{gc} i_{tc} = u_{gd} i_{td} + u_{gq} i_{tq} \tag{2.50}$$

Then, the mathematical model of the GSC circuit in the synchronous reference frame is given by (2.51)-(2.53).

$$\begin{pmatrix} e_{gd} \\ e_{gq} \end{pmatrix} = \frac{e_{dc}}{2} \begin{pmatrix} u_{gd} \\ u_{gq} \end{pmatrix} \tag{2.51}$$

$$\begin{pmatrix} v_{gd} \\ v_{gq} \end{pmatrix} = L_{gsc} \frac{d}{dt} \begin{pmatrix} i_{td} \\ i_{tq} \end{pmatrix} + R_{gsc} \begin{pmatrix} i_{td} \\ i_{tq} \end{pmatrix} + \omega_s L_{gsc} \begin{pmatrix} -i_{tq} \\ i_{td} \end{pmatrix} + \begin{pmatrix} e_{gd} \\ e_{gq} \end{pmatrix} \tag{2.52}$$

$$\frac{d}{dt} e_{dc} = \frac{1}{2 \cdot C_{dc}} \left(u_{gd} i_{td} + u_{gq} i_{tq} \right) - \frac{e_{dc}}{R_{dc} C_{dc}} \tag{2.53}$$

References

[1] G. Iwanski and W. Koczara, “Power Management in an Autonomous Adjustable Speed Large Power Diesel Gensets,” in *Proc. EPE-PEMC Power Electronics and Motion Control Conf.*, 2008, Poznan, pp. 2164-2169,

[2] T. Burton, D. Sharpe, N. Jenkins, and E. Bossanyi, *Wind Energy Handbook*, John Wiley & Sons, Ltd, ch 3.

[3] M. A. El-Sharkawi, *Wind Energy: An Introduction*, CRC Press, 2015, ch. 4.

[4] M. Rosydai, S. M. Muyeen, R. Takahashi, and J. Tamura, “A Design Fuzzy Logic Controller for a Permanent Magnet Wind Generator to Enhance the Dynamic Stability of Wind Farmes,” *Applied Sciences*, ISSN 2076-3417, pp. 780-800, Feb. 2012

[5] T. Burton, D. Sharpe, N. Jenkins, and E. Bossanyi, *Wind Energy Handbook*, John Wiley & Sons, Ltd, ch 6.

[6] G. Abad, J. López, M. A. Rodríguez, L. Marroyo, and G. Iwanski, *Doubly Fed Induction Machine: Modeling and Control for Wind Energy Generation*. New Jersey: John Wiley, 2011, ch. 1

[7] R. Cardenas, R. Pena, S. Alepuz, and G. Asher, “Overview of Control Systems for the Operation of DFIGs in Wind Energy Applications,” *IEEE Trans. Industrial Electronics*, vol. 60, no. 7, pp. 2776-2798, Jul. 2013.

[8]

[9] G. Iwanski and W. Koczara, “DFIG-Based Power Generation System with UPS Function for Variable-Speed Applications,” *IEEE Trans. Industrial Electronics*, vol. 55, no. 8, pp. 3047-3054, Aug. 2008.

Chapter 3

Grid-Connected Mode of Operation

Normally, the DFIG is connected to the grid and operates in the grid-connected mode, as in Fig. 3.1; this is why this mode had received a great deal of attention and several controllers have been proposed in the literature.

The control system of the grid-connected DFIG is composed of two main controllers; one to generate the gating signals for the RSC and another for the GSC. The controller for the GSC is the same during stand-alone and grid-connected mode, and it has to regulate the dc-link voltage and to supply reactive power. This topic is well-established in the literature, and will be covered briefly in this chapter.

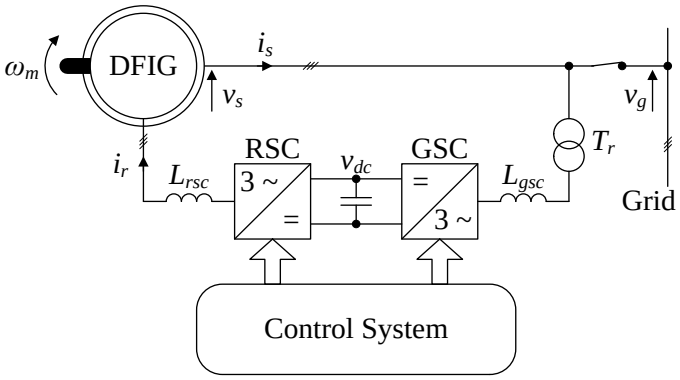

Fig. 3.1: Schematic diagram of the grid-connected DFIG.

The controller for RSC must regulate the generated active and reactive power by controlling the rotor currents. Early techniques are based on vector control [1] [2], which decouples the rotor current into active and reactive components and controls them using a rotor current loop. More recently, direct torque [3] [4], direct power [5] [6], and decoupled P-Q control [7] were introduced and applied in the industry.

In this chapter a new decoupled control is introduced and analyzed. This control is based on the decoupling between the active and reactive components of the stator current in the dq-frame. To appreciate the proposed decoupled control, it will be

compared with the conventional decoupled P-Q control

3.1 Control of the GSC

3.1.1 Phase-Locked Loop (PLL)

Since the stator and rotor quantities are dc-components in the dq-frame, the control system design in this frame is significantly simplified. This, however, requires obtaining the angle of grid voltage which is used in the dq-transformation. This can be accomplished by employing a phase-locked loop (PLL) circuit.

A. Concept

Most applications of static converters, which are connected or to be connected to the utility grid, require knowledge of the angle of the grid voltage which is referred to as the synchronous angle. The PLL circuit allows tracking the synchronous angle continuously and accurately. Normally, the PLL circuit aligns the d- or q-axis with either the grid voltage or the stator flux. In this work, we chose aligning the d-axis with the grid voltage.

The PLL circuit is designed in the dq-frame, which requires performing the dq-transformation on the grid voltage of (3.1), where $\varphi_g = \omega_g t + \varphi_0$.

$$\begin{pmatrix} v_{ga} \\ v_{gb} \\ v_{gc} \end{pmatrix} = V_g \begin{pmatrix} \cos(\varphi_g) \\ \cos\left(\varphi_g - \frac{2\pi}{3}\right) \\ \cos\left(\varphi_g + \frac{2\pi}{3}\right) \end{pmatrix} \tag{3.1}$$

Using the dq-transformation defined by (2.6), we get (3.2) where $\theta_g = \omega_g t + \theta_0$ is the transformation angle.

$$\begin{pmatrix} v_{gd} \\ v_{gq} \end{pmatrix} = \sqrt{\frac{3}{2}} V_g \begin{pmatrix} \cos(\varphi_g - \theta_g) \\ \sin(\varphi_g - \theta_g) \end{pmatrix} \tag{3.2}$$

To align the d-axis with the grid voltage, the q-component must become zero. When the q-component is zero, the two angles are equal, and the PLL circuit will obtain

the synchronous angle.

To force the grid q-voltage to zero, a PI controller followed by an integrator is used. To eliminate the grid voltage amplitude from the transfer function of the PLL circuit, the grid q-voltage is divided by the grid voltage amplitude.

Therefore, the block diagram of the PLL circuit is depicted in Fig. 3.2.

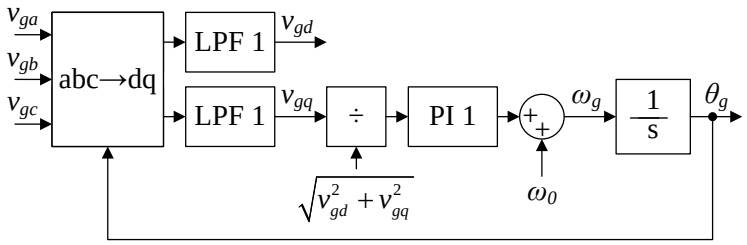

Fig. 3.2: Schematic diagram of the PLL circuit.

Some literatures had addressed some operational issues related to stability of the PLL circuit in the dq-frame and suggested solutions to them [8], which are adopted in this work.

In [8], low pass filters (LPF) for the grid d- and q-voltage are employed to reduce voltage distortion and harmonics. To ensure stability during start up, the PLL circuit has an initial frequency which is equal to the rated grid frequency ($\omega_0 = 2\pi f_0$). It was shown in [8] that with zero initial frequency, the PLL can fail in tracking the synchronous angle during start-up under some adverse conditions.

In addition, the PI controller has an anti-windup, upper and lower saturation limits. The lower saturation limit is needed to avoid instability caused by subharmonics. The oscillations caused by subharmonics can pull the stable point of operation of the PLL to that subharmonic frequency if no limit is employed. The anti-wind up algorithm is needed to avoid oscillation in the output frequency which can take place under adverse conditions [8].

B. Controller Design

The task of controller design involves selecting the parameters of the PI controller which are the proportional K_p and the integral gain K_i, and selecting the order and the cut off frequency of the low pass filters. The low pass filter is a simple first order filter.

The control model of the PLL circuit is derived from (3.2) and Fig. 3.2, and it is depicted in Fig. 3.3. This model is nonlinear, because of the sine function. To simplify the controller design, small signal model is considered.

For small variation around the synchronous angle, the sine function can be approximated by a unity gain, $\sin(x) \approx x$.

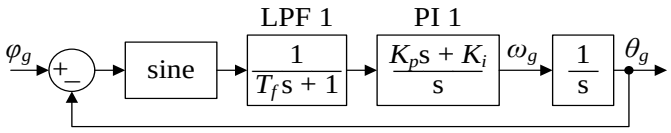

Fig. 3.3: Control model of the PLL circuit.

The cut-off frequency of the filter (LPF 1) should be low to attenuate unwanted noise, but it should not be too low to avoid disturbing the PLL circuit performance. Usually, it is selected ten times higher than the bandwidth of the PLL circuit.

Thus, it can be ignored in the transfer function of the PLL circuit.

Since the cut-off frequency is much smaller than the bandwidth of the PLL circuit, it can be ignored and, consequently, the simplified transfer function of the small signal model of the PLL circuit is given by (3.3).

$$\frac{\theta_g}{\varphi_g - \theta_g} \approx \frac{K_p s + K_i}{s^2} \tag{3.3}$$

To simplify the selection of the PI controller's parameters, we propose introducing new parameters which are related to the PI parameters as in (3.4).

$$\begin{cases} K_i = {\omega_k}^2 \\ K_p = \alpha \cdot \omega_k \end{cases} \tag{3.4}$$

Substituting (3.4) into (3.3), the transfer function is written as in (3.5).

$$\frac{\theta_g}{\varphi_g - \theta_g} \approx \frac{{\omega_k}^2}{s^2}\left(\alpha \frac{s}{\omega_k} + 1\right) \tag{3.5}$$

By normalizing the frequency (s) to ω_k, the different performance criteria, such as the rise time and the overshoot, becomes functions of α only. In this work, we have chosen the bandwidth of (3.5), which is referred to as ω_{bw}, and the output's overshoot as design criteria. The bandwidth should be large to have fast response, but small to

attenuate harmonics of the grid voltage. The first harmonic occurs in the dq-frame at the grid frequency; thus the bandwidth should around ten times smaller than the ω_g.

The variation of the normalized bandwidth and the overshoot are depicted in Fig. 3.4 as functions of α.

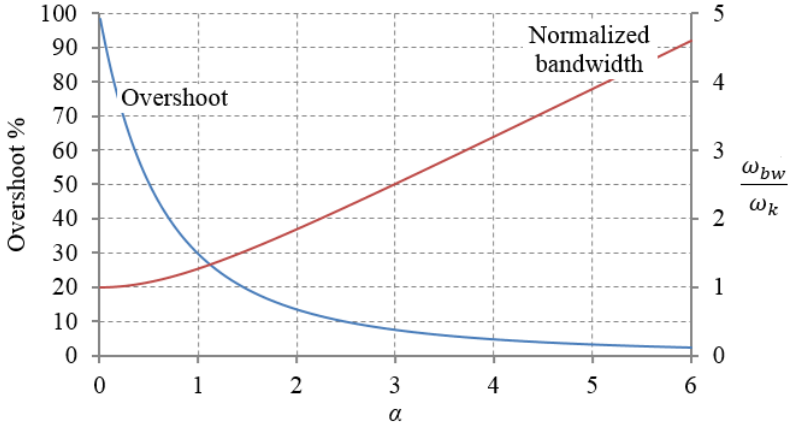

Fig. 3.4: The overshoot and the normalized bandwidth of the PLL circuit as functions of α.

Using the desired overshoot, the value of α and the normalized bandwidth are determined from Fig. 3.4. Then, using the desired bandwidth, the value of ω_k is obtained. Using the values of α and ω_k, the PI parameters are selected.

In this work, the overshoot was selected around 8% only, which corresponds to α equal to 3.5 and a normalized bandwidth equal to around 2.8. The bandwidth ω_{bw} is selected around nine times small than ω_g (ω_{bw} = 40).

Finally, the cut-off frequency of the low pass filter was selected (500 rad/s) slightly more than ten times higher than the ω_{bw} to avoid disturbing the performance of the PLL circuit.

3.1.2 DC-Link Controller

A. Concept

In this work, a transformer, with a turns ratio of N_2/N_1 = 0.5, is inserted between the grid and the GSC, as shown in Fig. 3.5.

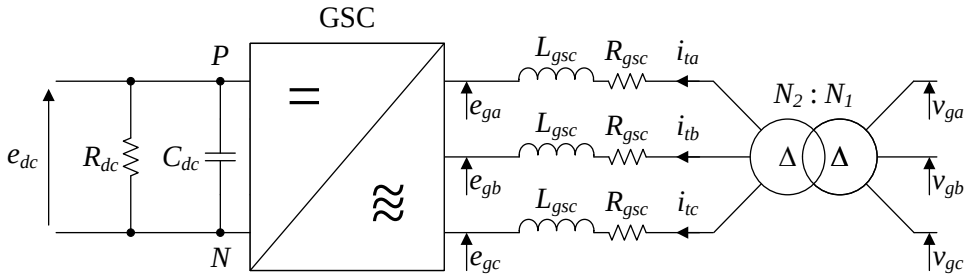

Fig. 3.5: GSC circuit.

To simplify the model, the transformer is assumed ideal, and the voltage at its secondary terminals is equal to the primary voltage multiplied by $a_T = N_2 / N_1$.

Then, based on the study in Chapter 2, the GSC circuit is described, in the stationary frame, by (3.6)-(3.8), where u_g is the sinusoidal PWM signal.

$$\begin{pmatrix} e_{ga} \\ e_{gb} \\ e_{gc} \end{pmatrix} = \frac{e_{dc}}{6} \begin{pmatrix} 2 & -1 & -1 \\ -1 & 2 & -1 \\ -1 & -1 & 2 \end{pmatrix} \begin{pmatrix} u_{ga} \\ u_{gb} \\ u_{gc} \end{pmatrix} \tag{3.6}$$

$$a_T \begin{pmatrix} v_{ga} \\ v_{gb} \\ v_{gc} \end{pmatrix} = L_{gsc} \frac{d}{dt} \begin{pmatrix} i_{ta} \\ i_{tb} \\ i_{tc} \end{pmatrix} + R_{gsc} \begin{pmatrix} i_{ta} \\ i_{tb} \\ i_{tc} \end{pmatrix} + \begin{pmatrix} e_{ga} \\ e_{gb} \\ e_{gc} \end{pmatrix} \tag{3.7}$$

$$\frac{d}{dt} e_{dc} = \frac{1}{2 \cdot C_{dc}} \left(u_{ga} i_{ta} + u_{gb} i_{tc} + u_{gc} i_{tc} \right) - \frac{e_{dc}}{R_{dc} C_{dc}} \tag{3.8}$$

Using dq-transformation, the GSC is modeled by (3.9)-(3.11).

$$\begin{pmatrix} e_{gd} \\ e_{gq} \end{pmatrix} = \frac{e_{dc}}{2} \begin{pmatrix} u_{gd} \\ u_{gq} \end{pmatrix} \tag{3.9}$$

$$a_T \begin{pmatrix} v_{gd} \\ v_{gq} \end{pmatrix} = L_{gsc} \frac{d}{dt} \begin{pmatrix} i_{td} \\ i_{tq} \end{pmatrix} + R_{gsc} \begin{pmatrix} i_{td} \\ i_{tq} \end{pmatrix} + \omega_s L_{gsc} \begin{pmatrix} -i_{tq} \\ i_{td} \end{pmatrix} + \begin{pmatrix} e_{gd} \\ e_{gq} \end{pmatrix} \tag{3.10}$$

$$\frac{d}{dt} e_{dc} = \frac{1}{2 \cdot C_{dc}} \left(u_{gd} i_{td} + u_{gq} i_{tq} \right) - \frac{e_{dc}}{R_{dc} C_{dc}} \tag{3.11}$$

In steady-state, the derivative terms in (3.10) are zero, and the PLL circuit forces v_{gq} to zero. In addition, the R_{gsc} can be ignored compared to $\omega_s L_{gsc}$; thus (3.10) becomes:

$$a_T \begin{pmatrix} v_{gd} \\ 0 \end{pmatrix} \approx \omega_s L_{gsc} \begin{pmatrix} -i_{tq} \\ i_{td} \end{pmatrix} + \begin{pmatrix} e_{gd} \\ e_{gq} \end{pmatrix} \tag{3.12}$$

By combining (3.9) and (3.12), we can write:

$$u_{gd} i_{td} + u_{gq} i_{tq} \approx 2 a_T \frac{v_{gd}}{e_{dc}} i_{td} \tag{3.13}$$

Substituting (3.13) into (3.11), we get (3.14) which is a nonlinear equation.

$$\frac{1}{2} C_{dc} \frac{d}{dt} ({e_{dc}}^2) + \frac{{e_{dc}}^2}{R_{dc}} = a_T v_{gd} i_{td} \tag{3.14}$$

Since (3.14) in nonlinear, small variation model is considered to obtain a linear model, which is given by (3.15).

$$\frac{\Delta e_{dc}}{\Delta i_{td}} \approx \frac{R_{dc}}{2} \cdot \frac{a_T v_{gd}}{{e_{dc}}^*} \cdot \frac{1}{\frac{R_{dc} C_{dc}}{2} s + 1} \tag{3.15}$$

From (3.15), the voltage of the dc-link can be controlled using the GSC's d-current. The GSC's q-current is used to control the reactive power exchanged with the grid using (3.16).

$$Q = -a_T v_{gd} i_{tq} \tag{3.16}$$

The GSC's d- and q-current are controlled by controlling the d- and q-voltages at the GSC's terminal according (3.10). Then, the transfer function can be written as:

$$\begin{pmatrix} i_{td} \\ i_{tq} \end{pmatrix} = \frac{-1}{L_{gsc} \cdot s + R_{gsc}} \begin{pmatrix} e_{gd} - a_T v_{gd} - \omega_s L_{gsc} i_{tq} \\ e_{gq} - a_T v_{gq} + \omega_s L_{gsc} i_{td} \end{pmatrix} \tag{3.17}$$

In the (3.17), there are additional terms that need to be fed-forward to generate the reference terminal d- and q-voltage of the GSC.

B. Controller Design

Since the simplified model in (3.15) is linear, a PI controller can be used to generate the GSC's d-current which is required to regulate the voltage of the dc-link. Similarly, PI controllers are used to generate the required PWM signal to control the

GSC's d- and q-current. Based on the previous study, the control circuit of the GSC is depicted in Fig. 3.6.

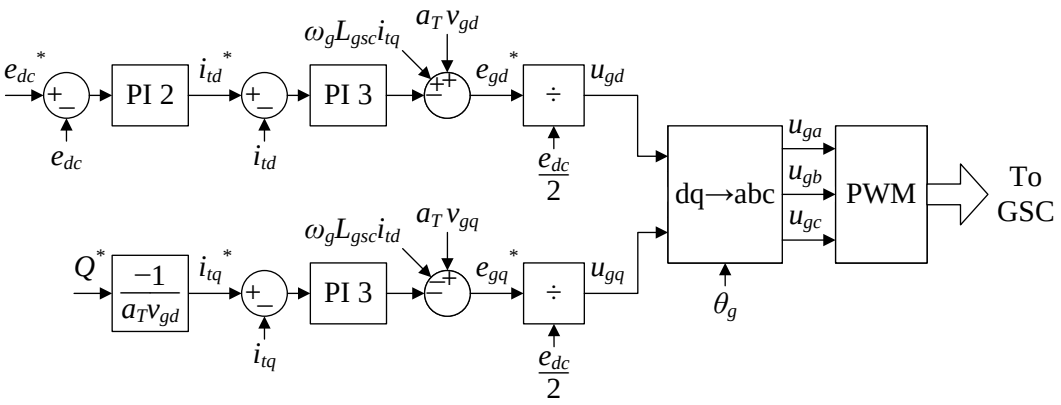

Fig. 3.6: Schematic diagram of the GSC's control.

The simplified control model of the GSC's circuit is depicted in Fig. 3.7.

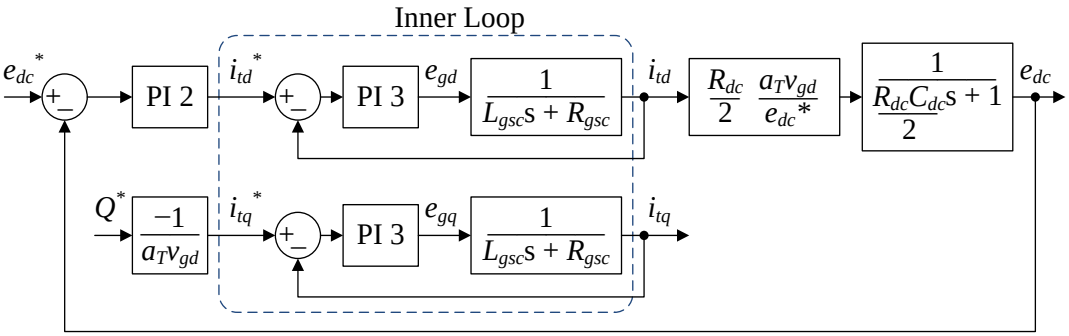

Fig. 3.7: Control model of the GSC's circuit.

The control model of the GSC's circuit contains two loops, the inner loop and the outer loop (dc-link's voltage loop). To ensure stability, the inner loop must be designed at least ten times faster than the outer loop.

The controller design is as follows: First, the inner loop is considered. Its bandwidth is selected faster than the line frequency. The parameters selection for PI 3 to achieve this bandwidth can be easily achieved using, for example, a Bode diagram.

Then, the outer loop is considered. Since the inner loop is much faster, it is approximated by a unity gain. The bandwidth of the outer loop must be smaller than the line frequency to attenuate the ripples at the grid frequency. In this work, it is selected ten times smaller. Then, using Bode diagram, the parameters of PI 2 are determined.

3.2 Control of the RSC

The RSC is connected to the rotor side of the DFIG, and it supplies the slip power. By controlling the amplitude and angle of the rotor current, the stator active and reactive power can be controlled at any speed.

To control the active and reactive power, this paper proposes a new decoupled control, which is an improved version of the conventional decoupled control P-Q control. Before presenting the proposed decoupled control, the conventional decoupled P-Q control is presented.

3.2.1 Conventional Decoupled P-Q Control

The decoupled P-Q control is carried out in the dq-frame, where the active and reactive power are given by (3.18).

$$\begin{cases} P_s = v_{sd} i_{sd} + v_{sq} i_{sq} \\ Q_s = v_{sq} i_{sd} - v_{sd} i_{sq} \end{cases} \tag{3.18}$$

Since the PLL circuit of Fig. 3.2 forces the stator q-voltage to zero, the active and reactive power become decoupled, and they are given by (3.19).

$$\begin{cases} P_s = \quad v_{sd} i_{sd} \\ Q_s = -v_{sd} i_{sq} \end{cases} \tag{3.19}$$

Since the relation between the power and the current in (3.19) is linear, PI controllers can be used to generate the reference stator d- and q-current from the active and reactive power respectively.

The reference rotor d- and q-current are calculated from the reference stator d- and q-current using the equivalent circuit of the DFIG in the dq-frame, Fig. 3.8.

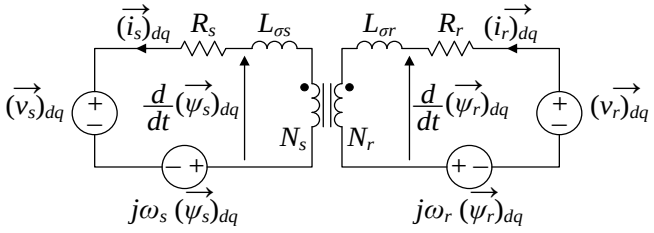

Fig. 3.8: Equivalent circuit of the DFIG in the dq-frame.

The voltage across the stator side is given by (3.20).

$$(\vec{v}_s)_{dq} = -\big(R_s + j\omega_s(L_s + L_{\sigma s})\big)(\vec{\imath}_s)_{dq} + j\omega_s L_m(\vec{\imath}_r)_{dq} - (L_s + L_{\sigma s})\frac{d(\vec{\imath}_s)_{dq}}{dt} + L_m\frac{d(\vec{\imath}_r)_{dq}}{dt} \tag{3.20}$$

In steady-state the derivative terms are zero, and the stator voltage is given by (3.21).

$$(\vec{v}_s)_{dq} = -\big(R_s + j\omega_s(L_s + L_{\sigma s})\big)(\vec{\imath}_s)_{dq} + j\omega_s L_m(\vec{\imath}_r)_{dq} \tag{3.21}$$

Usually, the conventional decoupled control ignores the stator winding resistance compared to the stator impedance and the stator leakage inductance compared with the stator inductance. Then, the rotor d- and q-current can be calculated from the stator d- and q-current using (3.22).

$$(\vec{\imath}_r)_{dq} \approx \frac{N_s}{N_r}(\vec{\imath}_s)_{dq} - j\frac{(\vec{v}_s)_{dq}}{\omega_s L_m} \tag{3.22}$$

Thus, the block diagram of the conventional decoupled P-Q control is depicted in Fig. 3.9.

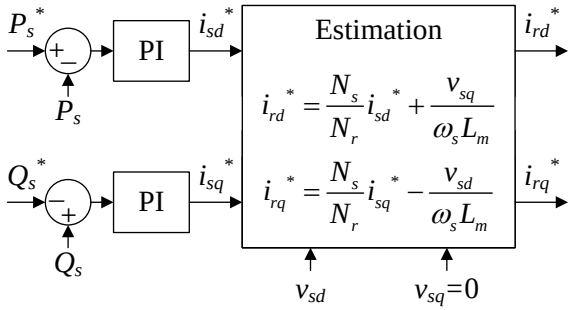

Fig. 3.9: Block diagram of the conventional decoupled P-Q control.

The conventional decoupled control requires knowledge of at least two DFIG parameters, which are the stator-to-rotor turns ratio and the magnetizing inductance. Moreover, the decoupling and consequently the performance is affected by the voltage orientation and the PLL transient response. Moreover, the transfer function of the decoupled control contains the grid voltage amplitude.

To overcome these drawbacks we propose a new decoupled control which

decouples the stator d- and q-current instead of the active and reactive power.

3.2.2 Proposed Decoupled Control

A. Concept

In the proposed method, the reference stator d- and q-currents are calculated from the active and reactive power using (3.23) which does not involve any approximation or require any DFIG parameter.

$$\begin{cases} i_{sd} = \dfrac{v_{gd}P_s + v_{gq}Q_s}{{v_{gd}}^2 + {v_{gq}}^2} \\ i_{sq} = \dfrac{v_{gq}P_s - v_{gd}Q_s}{{v_{gd}}^2 + {v_{gq}}^2} \end{cases} \tag{3.23}$$

The relation between the stator and the rotor currents is linear as was shown in (3.22). In (3.22), the stator d- and q-currents are always decoupled regardless of the grid voltage orientation; this gives the proposed method more flexibility and robustness compared with the conventional decoupled control. The stator d- and q-current can be controlled independently by the rotor d- and q-current respectively. This equation can be further simplified if the stator voltage-related term is regarded constant and is dropped as in (3.24).

$$(\vec{\imath}_r)_{dq} \propto \frac{N_s}{N_r}(\vec{\imath}_s)_{dq} \tag{3.24}$$

The reference rotor d- and q-current can be generated from the stator d- and q-current using PI controllers. Then, the block diagram of the proposed decoupled control is shown in Fig. 3.10.

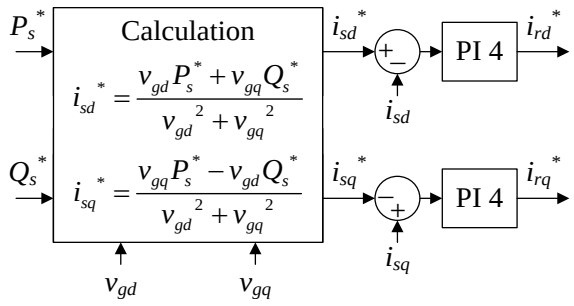

Fig. 3.10: Block diagram of the proposed decoupled P-Q control.

B. Rotor Current Loop (Inner Loop)

Similar to the GSC's control, the RSC's control requires an inner loop to control the rotor d- and q-current by generating the appropriate PWM signals. The RSC's circuit is depicted in Fig. 3.11.

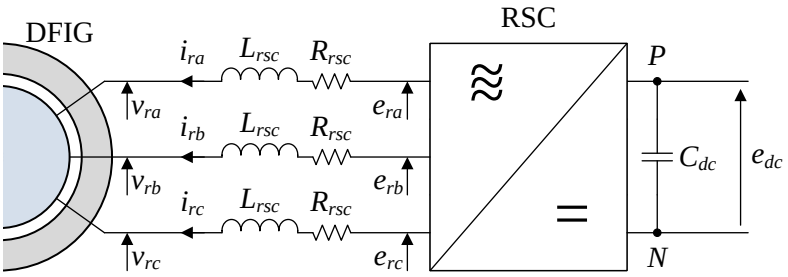

Fig. 3.11: RSC circuit.

The mathematical model of the RSC's circuit is given by (3.25).

$$\begin{pmatrix} v_{rd} \\ v_{rq} \end{pmatrix} = -L_{rsc}\frac{d}{dt}\begin{pmatrix} i_{rd} \\ i_{rq} \end{pmatrix} - R_{rsc}\begin{pmatrix} i_{rd} \\ i_{rq} \end{pmatrix} - \omega_r L_{rsc}\begin{pmatrix} -i_{rq} \\ i_{rd} \end{pmatrix} + \begin{pmatrix} e_{rd} \\ e_{rq} \end{pmatrix} \tag{3.25}$$

To eliminate the need for voltage sensors at the DFIG's rotor, we consider the DFIG acting as an ideal transformer. Then, the DFIG's rotor terminal voltages can be considered constant in the dq-frame, and it can be dropped. Thus, the transfer function can be given by (3.26).

$$\begin{pmatrix} i_{rd} \\ i_{rq} \end{pmatrix} \propto \frac{1}{L_{rsc} \cdot s + R_{rsc}}\begin{pmatrix} e_{rd} + \omega_r L_{rsc} i_{rq} \\ e_{rq} - \omega_r L_{rsc} i_{rd} \end{pmatrix} \tag{3.26}$$

On the right hand side of (3.26), there are rotor current-related terms that should be fed forward to decouple the rotor d- and q-current and to generate the rotor voltage references, which generate the PWM signals using (3.27).

$$\begin{pmatrix} e_{rd} \\ e_{rq} \end{pmatrix} = \frac{e_{dc}}{2}\begin{pmatrix} u_{rd} \\ u_{rd} \end{pmatrix} \tag{3.27}$$

The block diagram of the rotor current loop is depicted in Fig. 3.12.

C. Controller Design

Similar to the GSC's control, the RSC's control has two control loops: The inner

loop, which regulates the rotor currents, and the outer loop (the decoupled control), which regulates the active and reactive power.

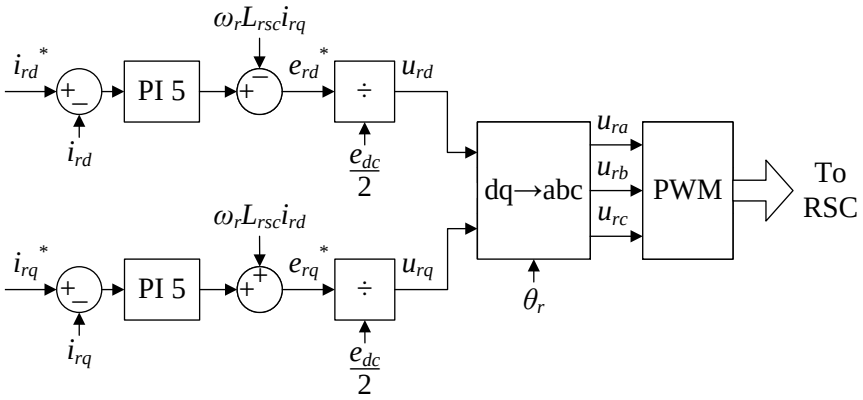

Fig. 3.12: Block diagram of the rotor current loop.

The complete model of the DFIG contains a pair of poorly damped poles near the line frequency [9] [10]. These poles can disturb the performance of the decoupled control and cause poorly damped oscillations. To reduce the effect of these poles, the bandwidth of the proposed decoupled control must be smaller that the line frequency.

Since the bandwidth of the decoupled control is smaller than the DFIG's poorly damped poles, they can be ignored in the controller design. Then, the simplified DFIG model in (3.24) can be used. Thus, the simplified control model of the proposed decoupled control depicted in Fig. 3.13.

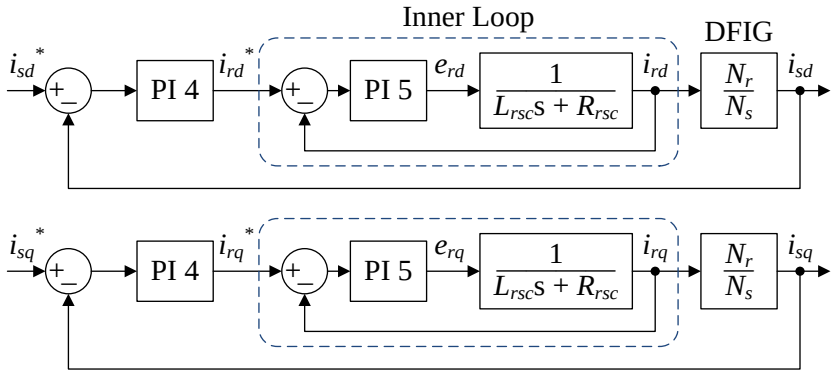

Fig. 3.13: Control model of the proposed decoupled control.

First, the PI controller of the inner loop is designed; this is similar to the design of the GSC's inner loop. Next, the decoupled control is considered, where the inner loop is approximated by a unity gain to simplify the controller design.

The open loop transfer function of the d-component of the decoupled control is given by (3.28), where K_p and K_i are the proportional and integral gains of PI 4 respectively. The transfer function for the q-component is exactly the same.

$$\frac{i_{sd}}{i_{sd}^{*} - i_{sd}} = \frac{\omega_p}{s}\left(\frac{s}{\omega_z} + 1\right) \quad where \quad \begin{cases} \omega_p = \dfrac{N_r}{N_s} K_i \\ \omega_z = \dfrac{K_i}{K_p} \end{cases} \tag{3.28}$$

This transfer function has a pole whose gain is ω_p and a zero at a frequency ω_z. The Bode diagram of the gain of (3.28) is shown in Fig. 3.14.

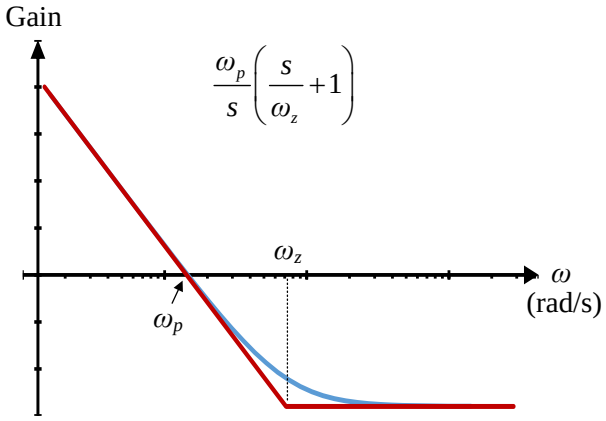

Fig. 3.14: Bode diagram of the open loop transfer function of the decoupled control.

The frequency ω_p, which is equal to the decoupled control bandwidth, should be smaller than the line frequency to reduce the effect of the DFIG's poorly damped poles. The frequency ω_p must be smaller than ω_z to have adequate attenuation at the poorly damped poles. Consequently, the proportional gain K_p must be smaller than the stator-to-rotor turns ratio, $K_p < N_s/N_r$. In this work, the frequency ω_p is selected only five times smaller than the line frequency to achieve fast response at the cost of weaker damping of the DFIG's poorly damped poles. The frequency ω_p is selected around 12 times smaller than the frequency ω_z.

The transfer function of the decoupled control contains the DFIG's stator-to-rotor turns ratio; thus, the transient response is dependent on this parameter. However, the stator-to-rotor turns ratio is slightly affected by saturation and is considered constant up to about 120% of the rated stator flux [11], which is the case in normal operation. Consequently, the proposed decoupled control can be considered independent of variation of the DFIG parameters due to saturation.

Similar to most of the active and reactive power control strategies, the RSC's control requires the slip angle which is the difference between the synchronous angle and the DFIG's rotor angle. The DFIG's rotor angle can be measured using an absolute encoder or estimated using a software estimator.

D. Stability Analysis for Slip Angle Inaccuracy

The measurement or estimation of the slip angle will contain a certain amount of error; mechanical encoders produce a small offset and the calibration of the encoders will contain some inaccuracy, and software estimators can produce significant error due to inaccuracy in its mathematical model. Thus, it is important to investigate the effect of the slip angle inaccuracy.

Denoting the slip angle, which is used by the decoupled control, by $\theta_r{}^e$, which is different from the actual slip angle θ_r by an error $\Delta\theta_r$ as in (3.29).

$$\theta_r{}^e = \theta_r + \Delta\theta_r \tag{3.29}$$

Then, the dq-transformation of the rotor current using this erroneous slip angle, which is denoted by $i_r{}^e$, is related to the correct value by (3.30).

$$\begin{pmatrix} i_{rd}{}^e \\ i_{rq}{}^e \end{pmatrix} = \begin{pmatrix} \cos(\Delta\theta_r) & \sin(\Delta\theta_r) \\ -\sin(\Delta\theta_r) & \cos(\Delta\theta_r) \end{pmatrix} \begin{pmatrix} i_{rd} \\ i_{rq} \end{pmatrix} \tag{3.30}$$

Introducing (3.30) into Fig. 3.13, the decoupled control model with slip angle error is shown in Fig. 3.15.

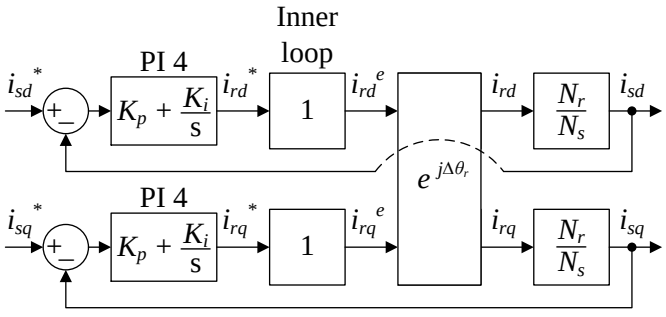

Fig. 3.15: Control model of the proposed decoupled control with slip angle error.

The transfer function of the PI controller, the inner loop, and the DFIG are combined in one transfer function which is denoted by $G = N_r/N_s\ PI4$. Then, the closed loop transfer function of Fig. 3.15 is given by (3.31).

$$\begin{pmatrix} i_{sd} \\ i_{sq} \end{pmatrix} = \frac{\begin{pmatrix} G^2 + G\cos(\Delta\theta_r) & -G\sin(\Delta\theta_r) \\ G\sin(\Delta\theta_r) & G^2 + G\cos(\Delta\theta_r) \end{pmatrix}}{G^2 + 2G\cos(\Delta\theta_r) + 1} \begin{pmatrix} {i_{sd}}^* \\ {i_{sq}}^* \end{pmatrix} \tag{3.31}$$

The stability of (3.31) can be assessed by applying the Routh-Hurwitz stability criterion on the characteristic equation which is given by (3.32).

$$G^2 + 2G\cos(\Delta\theta_r) + 1 = 0 \tag{3.32}$$

Substituting the PI 4 transfer function and the simplified DFIG model into (3.32), the characteristic equation is approximated by (3.33), where "*a*" is the stator-to-rotor turns ratio.

$$\left({K_p}^2 + 2aK_p\cos(\Delta\theta_r) + a^2\right)s^2 + 2K_i\left(K_p + a\cos(\Delta\theta_r)\right)s + {K_i}^2 = 0 \tag{3.33}$$

Applying the Routh-Hurwitz stability criterion on (3.33), provides the following two conditions for stability:

$$\cos(\Delta\theta_r) > \frac{-\left({K_p}^2 + a^2\right)}{2aK_p} \tag{3.34}$$

$$\cos(\Delta\theta_r) > \frac{-K_p}{a} \tag{3.35}$$

Since the proportional gain is smaller than the stator-to-rotor turns ratio, the stability condition in (3.34) is always true.

For the condition in (3.35) to be true, the slip angle error should be within an interval which is given by (3.36).

$$-\cos^{-1}\left(\frac{-K_p}{a}\right) < \Delta\theta_r < \cos^{-1}\left(\frac{-K_p}{a}\right) \tag{3.36}$$

Since the proportional gain is smaller than the stator-to-rotor turns ratio, the stable region is slightly above ±90 degrees. This shows that the proposed decoupled control can tolerate relatively large slip angle error before it become unstable. This makes the proposed decoupled control robust against slip angle inaccuracy, which is ought to the presence of PI controllers.

3.2.3 Negative-Sequence Compensation

During the grid-connected mode, it is important to generate the active and reactive power with minimum ripples. The power ripples, which oscillate at twice the line frequency is caused by the negative-sequence components of the stator voltage and current. These components will generate power ripples whose frequency is double the line's frequency.

Negative-sequence components can be generated due to asymmetrical grid voltages, asymmetrical line impedance, or asymmetrical stator windings of the DFIG. The negative-sequence components cause heating in the DFIG's windings and inflict mechanical stresses on the DFIG shaft. Consequently, it is important to eliminate or reduce the negative-sequence. For this purpose, both the GSC and RSC can be used; however, in this work, only the RSC is used to eliminate the stator negative-sequence current, because the negative-sequence compensation through GSC is well-established in literature.

A. Concept

An asymmetric stator current, in the stationary reference frame, can be written as the sum of the positive- and negative-sequence components which are rotating with the same frequency but in opposite directions as in (3.37) where φ_+ and φ_- are the initial angle of the positive- and negative-sequence currents respectively.

$$\vec{\imath}_s = \vec{\imath}_{s+} + \vec{\imath}_{s-} = \sqrt{\frac{3}{2}}\left(I_{s+}e^{-j(\omega_s t+\varphi_+)} + I_{s-}e^{j(\omega_s t-\varphi_-)}\right) \tag{3.37}$$

Similarly, the stator voltage in the stationary reference frame is given by (3.38).

$$\vec{v}_s = \vec{v}_{s+} + \vec{v}_{s-} = \sqrt{\frac{3}{2}}\left(V_{s+}e^{-j(\omega_s t+\vartheta_+)} + V_{s-}e^{j(\omega_s t-\vartheta_-)}\right) \tag{3.38}$$

Substituting (3.37) and (3.38) into (2.27) and (2.28), the active and reactive power are given by (3.39).

$$P_s + jQ_s = \vec{v}_{s+}{}^* \cdot \vec{\imath}_{s+} + \vec{v}_{s-}{}^* \cdot \vec{\imath}_{s-} + \vec{v}_{s+}{}^* \cdot \vec{\imath}_{s-} + \vec{v}_{s-}{}^* \cdot \vec{\imath}_{s+} \tag{3.39}$$

The active and reactive power are composed of four terms: two constant and two oscillating with opposite frequency at twice the line frequency. Eliminating the stator negative-sequence current reduces the power ripples; it does not completely eliminate them due to the term resulting from the stator negative-sequence voltage.

In the dq-frame, the positive-sequence component will be constant, while the negative-sequence component will be oscillating at twice the line frequency. To effectively isolate the negative-sequence component from the positive-sequence and to simplify the controller design, the stator current is expressed in the negatively-synchronous reference frame. That is, performing the dq-transformation with the opposite angle $T(-\theta_s)$.

In the negatively synchronous reference frame, the negative-sequence component is constant while the positive-sequence component is oscillating at twice the line frequency; thus, it can be filtered out easily using low pass filters. In this work, simple second order low pass filters are adopted.

The mathematical model of the DFIG in the negatively-synchronous reference frame can be obtained from the DFIG's model in the dq-frame by replacing the synchronous frequency with the opposite frequency ($-\omega_s$) and the positive-sequence components of the voltages and currents with the negative-sequence components.

Using the simplified model of the DFIG of (3.24), the simplified model in the negatively-synchronous reference frame, which is denoted by $(\,)_{-dq}$, is given by (3.40).

$$(\vec{\imath}_{r-})_{-dq} \propto \frac{N_s}{N_r}(\vec{\imath}_{s-})_{-dq} \tag{3.40}$$

From (3.40), the stator negative-sequence current can be controlled by the rotor negative-sequence current. Since the relation in (3.40) is linear, simple PI controllers can be used to generate the reference rotor negative-sequence current which needs to be added to the reference rotor positive-sequence current generated by the decoupled control. This requires rotating the reference rotor negative-sequence current back to the dq-frame. Consequently, the block diagram of the negative-sequence compensation is shown in Fig. 3.16.

The total current command is the sum of the rotor current command generated by the decoupled control and by the negative-sequence compensation. This total current

command will be fed to the rotor current loop.

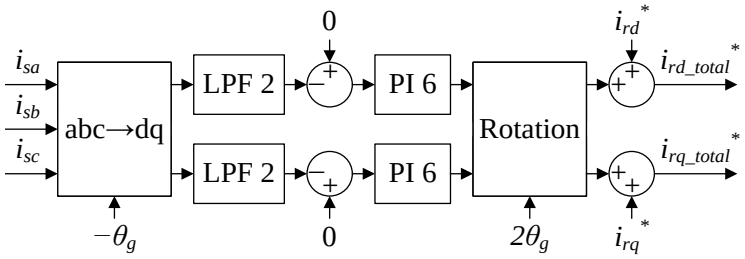

Fig. 3.16: Block diagram of the negative-sequence compensation of the stator current through RSC.

B. Controller Design

In this work, the low pass filter is a simple second order filter, which is given by (3.41).

$$\text{LPF 2} = \left(\frac{1}{T_f s + 1}\right)^2 \tag{3.41}$$

The simplified control model of the negative-sequence compensation is depicted in Fig. 3.17.

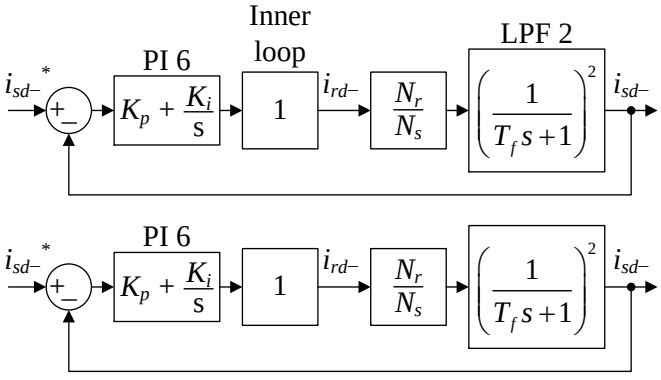

Fig. 3.17: Control model of the negative-sequence compensation of the stator current through RSC

The cutoff frequency of the filter must be small enough to have adequate attenuation at twice the line frequency. However, it should not be very small because it will reduce the response speed. The parameter selection of the PI controllers can be easily accomplished using, for example, Bode diagram to obtain certain gain and phase

margins.

3.3 Simulation and Experiments

3.3.1 Experimental Setup

Both the simulation and the experiments use the same configuration and parameters. They employ a 1.1 kW DFIG whose parameters are listed in Table 3.1.

Table 3.1: DFIG's parameters and rated values.

Parameter	Value	Unit
Power Rating	1.1	kW
Frequency	60	Hz
Number of poles	6	
Synchronous speed	1200	RPM
Stator line-to-line voltage	210	V_{RMS}
Stator current	6.3	A_{RMS}
Rotor current	20.3	A_{RMS}
Stator resistance R_s	0.475	Ω
Rotor resistance R_r	0.04	Ω
Stator leakage inductance $L_{\sigma s}$	7.43	mH
Rotor leakage inductance $L_{\sigma r}$	0.18	mH
Magnetizing inductance L_m	11.2	mH
Stator-to-rotor turns ratio	6.38	

The experimental setup will be explained, and the areas where the simulation and the experimental setup differ will be highlighted.

The photos of the actual experimental setup are shown in Fig. 3.18, and the schematic diagram is depicted in Fig. 3.19. The parameters of this circuit are listed in Table 3.2.

The DFIG is mechanically coupled to an induction machine (IM) which emulates a variable speed prime mover. The speed of the induction machine is controlled by a commercial three-phase inverter which is operating in speed control mode. However, in the simulation, which is carried out using PSCAD software, the DFIG operates in speed control mode where the speed is controlled through the speed input port.

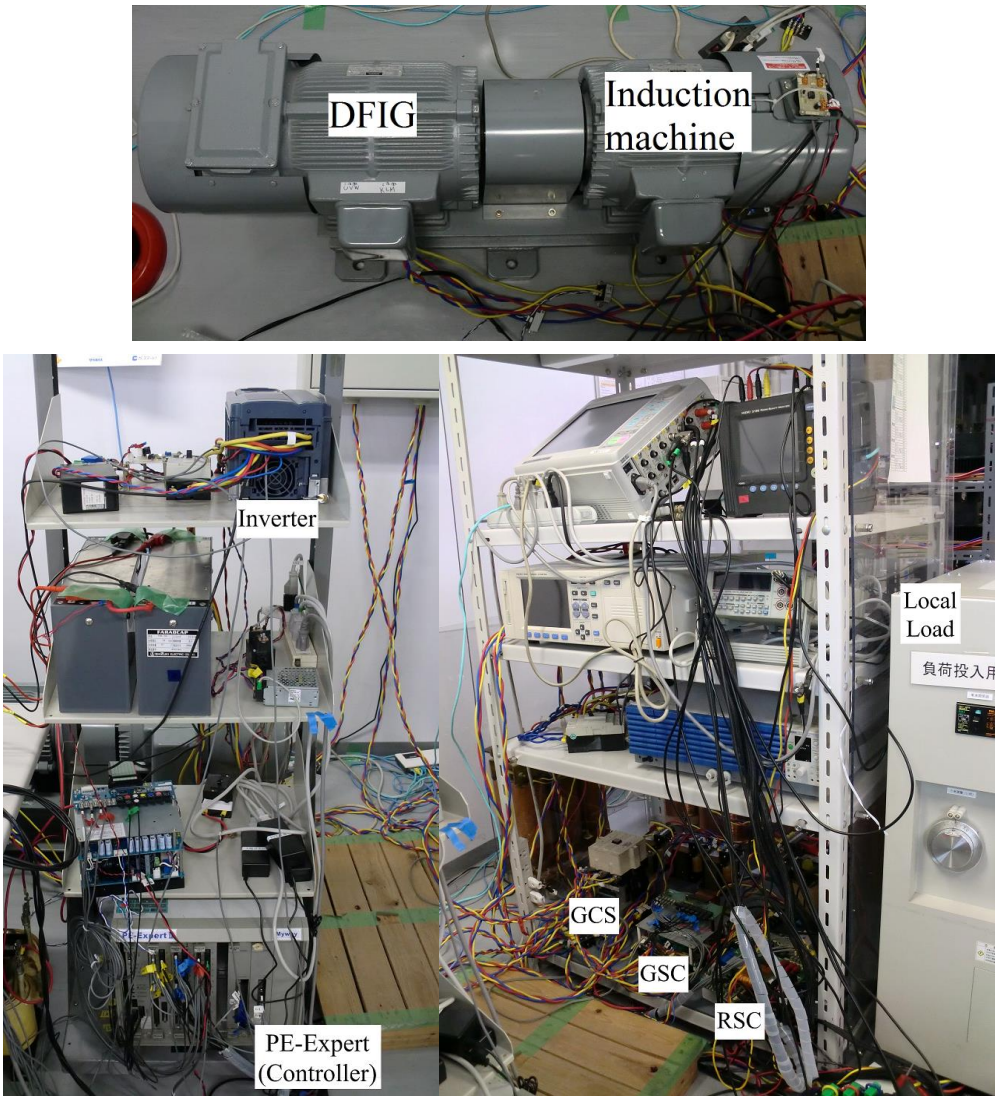

Fig. 3.18: Photos of the experimental setup.

Table 3.2: Parameters of the DFIG's circuit.

Parameter	Value	Unit
Grid line-to-line voltage	200	V_{RMS}
Frequency	60	Hz
L_{rsc}	4	mH
L_{gsc}	6	mH
C_f	30	μF
C_{dc}	2.44	mF
Dc-link voltage	200	V
Transformer turns ratio	0.5	

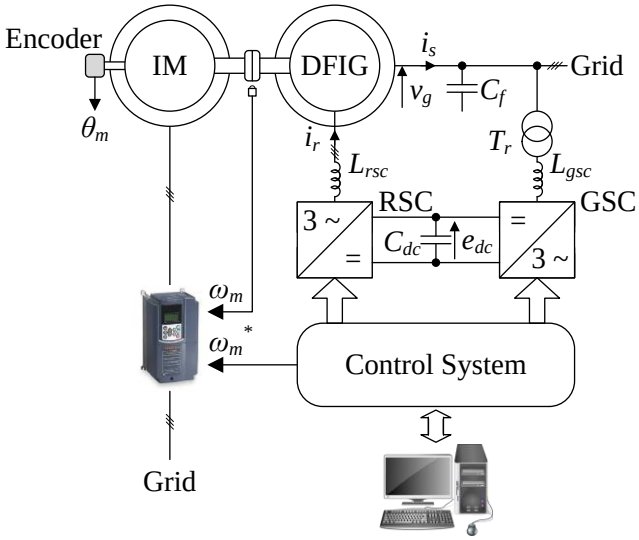

Fig. 3.19: Block diagram of the experimental setup.

The inverter driving the induction machine requires a speed sensor to achieve a closed-loop speed control; for this purpose an optical sensor, which generates 120 pulses per revolution, is used. The DFIG's rotor angle, which is used to calculate the slip angle, is obtained using an absolute encoder mechanically coupled to the shaft.

The grid-connected control system is implemented using a commercial, DSP-based digital control system which is PE-Expert II. The block diagram of the control system is depicted in Fig. 3.20.

The parameters of the PI controllers and the low pass filters in Fig. 3.20 are listed in Table 3.3.

Table 3.3: Parameters of the grid-connected control system.

	K_p	K_i (sec^{-1})	T_f (sec)
LPF 1			0.002
LPF 2			0.08
PI 1	50	200	
PI 2	0.2	0.5	
PI 3	20	200	
PI 4	0.5	500	
PI 5	20	1000	
PI 6	5	20	

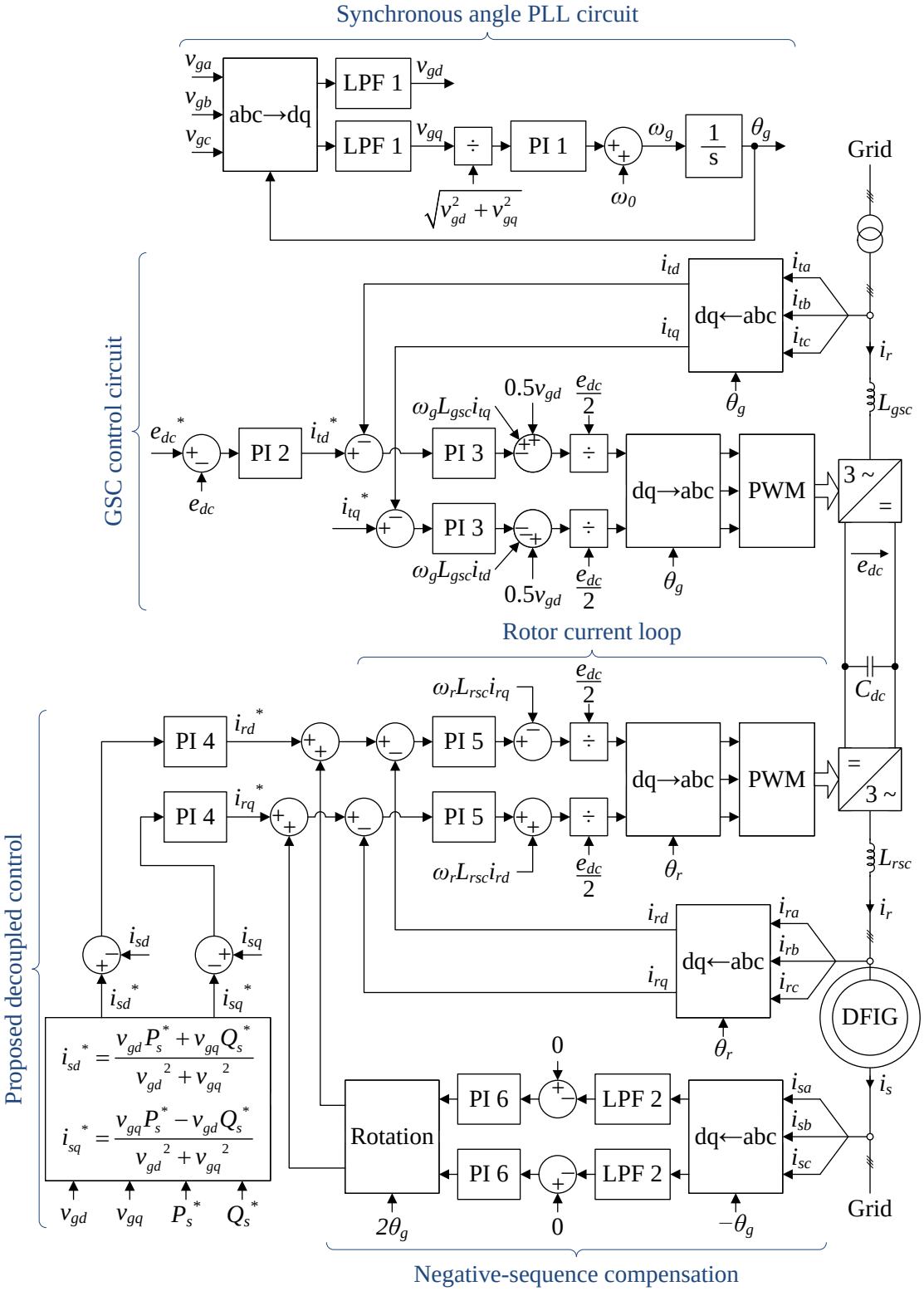

Fig. 3.20: Block diagram of the grid-connected control system.

3.3.2 Simulation Results

First, the step response of the active and reactive power is considered at a constant speed. Two tests are carried out.

In the first test, the speed is fixed at a sub-synchronous speed of 0.8 pu, and the active and reactive power references are stepped at the same time. The results for this test are shown in Fig. 3.21.

In the second test, the speed is fixed at a hyper-synchronous speed of 1.2 pu, and the active and reactive power references are stepped at different moments. The results for this test are shown in Fig. 3.22.

From the results of Fig. 3.21 and Fig. 3.22, the proposed decoupled control has good dynamics with settling time of around 50ms. The responses of the stator active and reactive power are decoupled and independent.

The control system is supposed to operate with variable speed generation systems. Thus, the next test is the variable speed operation. The DFIG speed is varied linearly from a sub-synchronous speed of 0.7 pu to a hyper-synchronous speed of 1.3 pu. When the DFIG reaches the synchronous speed, the active and reactive power references are simultaneously stepped. The results for this test are shown in Fig. 3.23.

From the results of Fig. 3.23, the proposed decoupled control is robust against variation in the DFIG's speed; this makes this control suitable for variable speed generation systems.

Next, the effect of the grid voltage orientation on the proposed decoupled control is investigated. In this test, the DFIG's speed is fixed at the synchronous speed. Initially, the PLL circuit of Fig. 3.2 forces the grid q-voltage to zero; then, it suddenly change to forcing the d-voltage to zero. To avoid disturbing the dc-link controller, a separate PLL circuit is dedicated for the GSC's controller. The results for this test are shown in Fig. 3.24.

The results in Fig. 3.24 show that the stability and the performance of the proposed decoupled control is independent of the grid voltage orientation. However, the active and reactive power responses exhibit a short transition due to the sudden change in the magnetizing current orientation in (3.22), where the magnetizing current is equal to v_s / ($\omega_s L_m$).

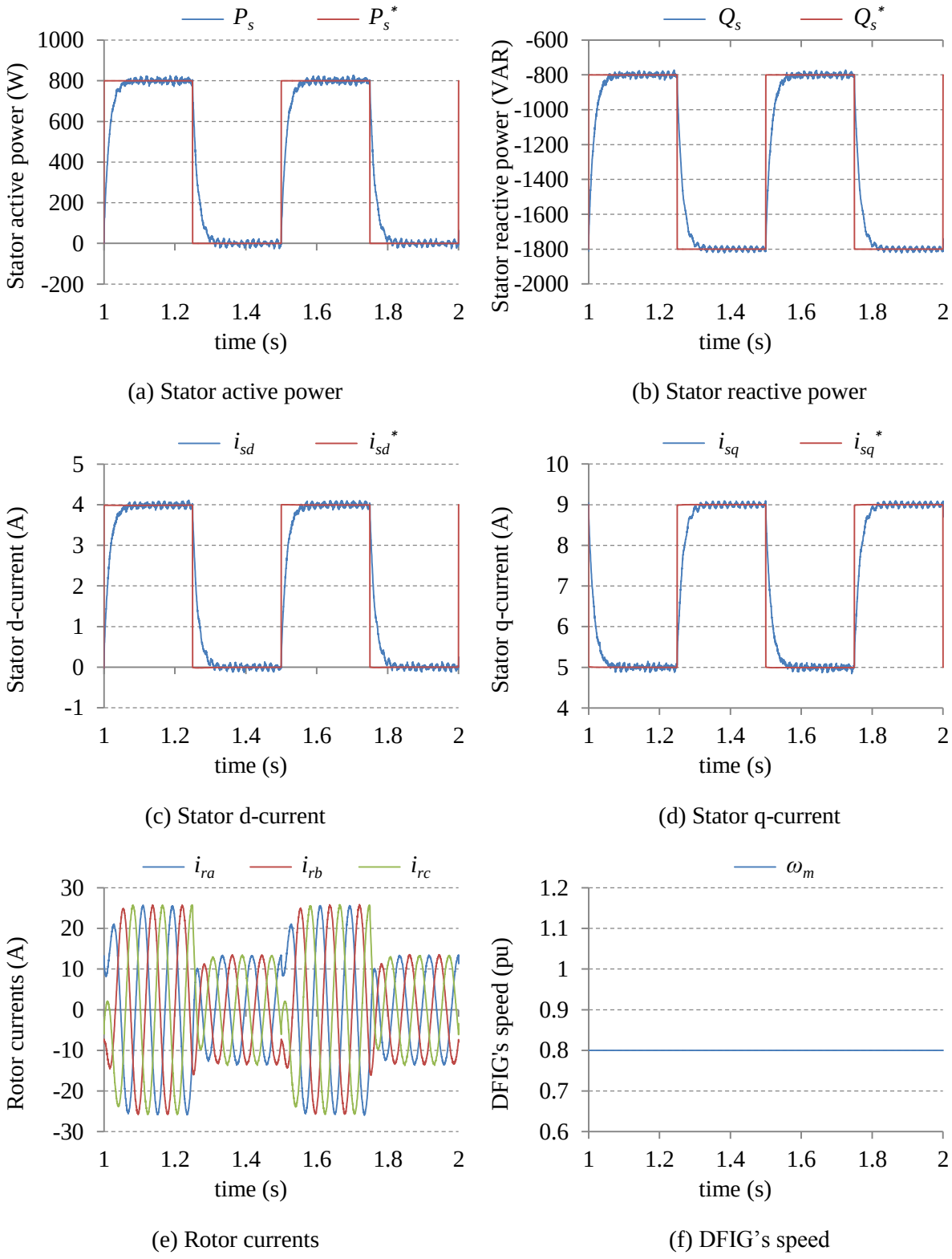

Fig. 3.21: Simulation results for the step response of the active and reactive power with ω_m = 0.8 pu.

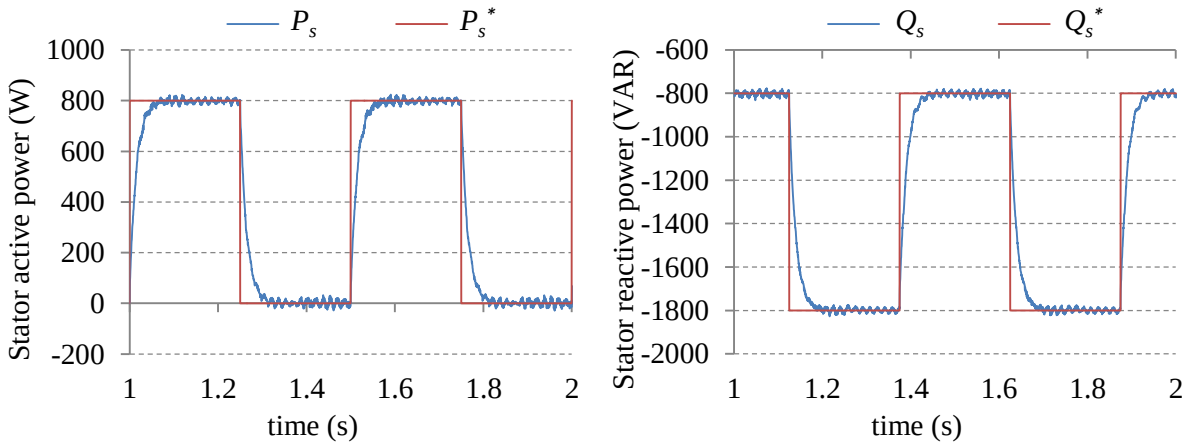

(a) Stator active power

(b) Stator reactive power

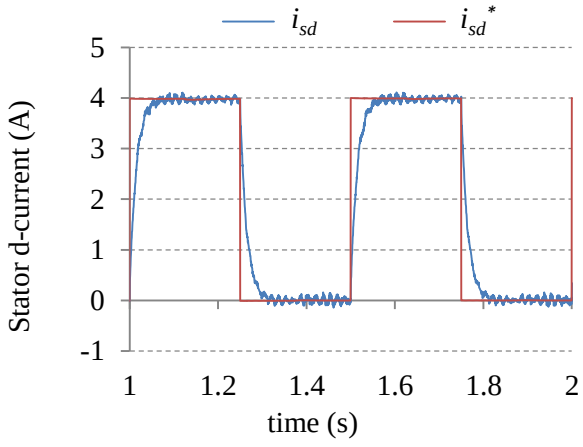

(c) Stator d-current

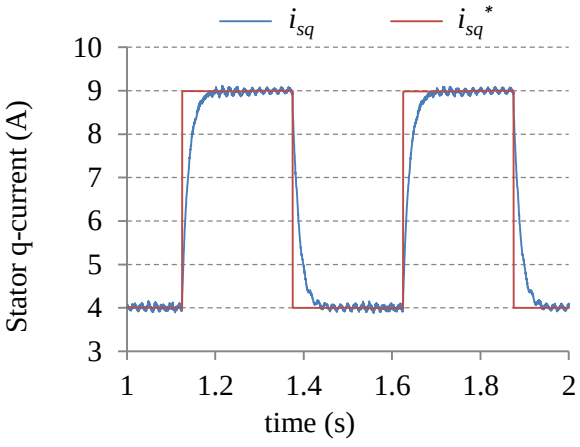

(d) Stator q-current

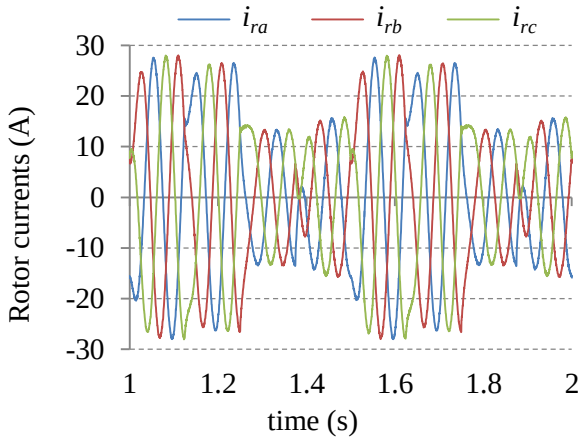

(e) Rotor currents

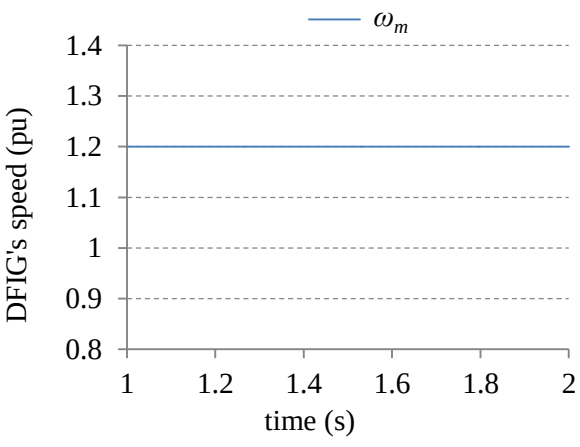

(f) DFIG's speed

Fig. 3.22: Simulation results for the step response of the active and reactive power with ω_m = 1.2 pu.

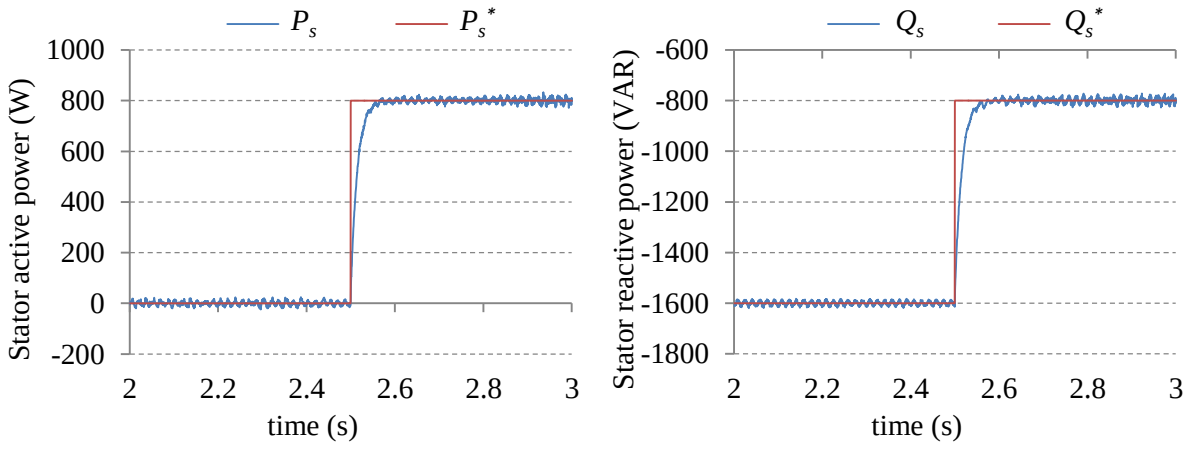

(a) Stator active power

(b) Stator reactive power

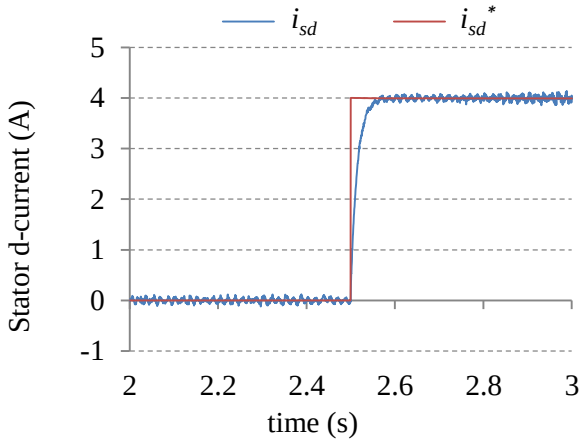

(c) Stator d-current

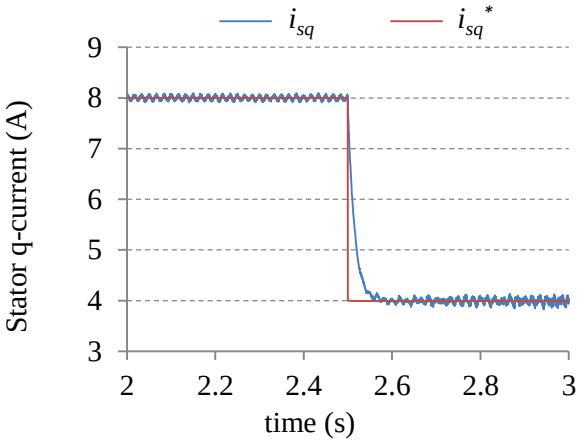

(d) Stator q-current

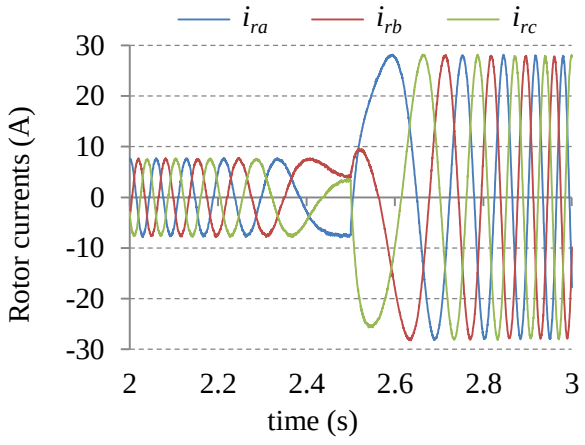

(e) Rotor currents

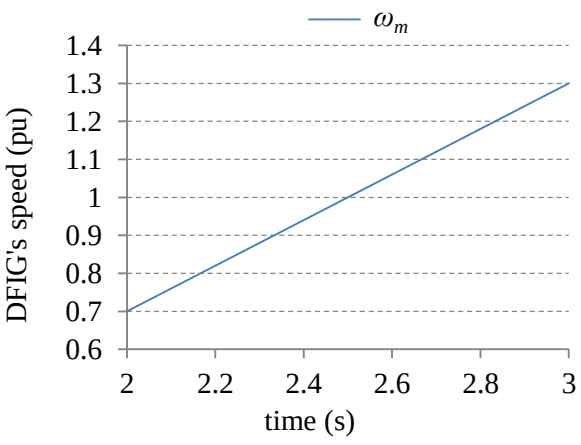

(f) DFIG's speed

Fig. 3.23: Simulation results for variable speed operation.

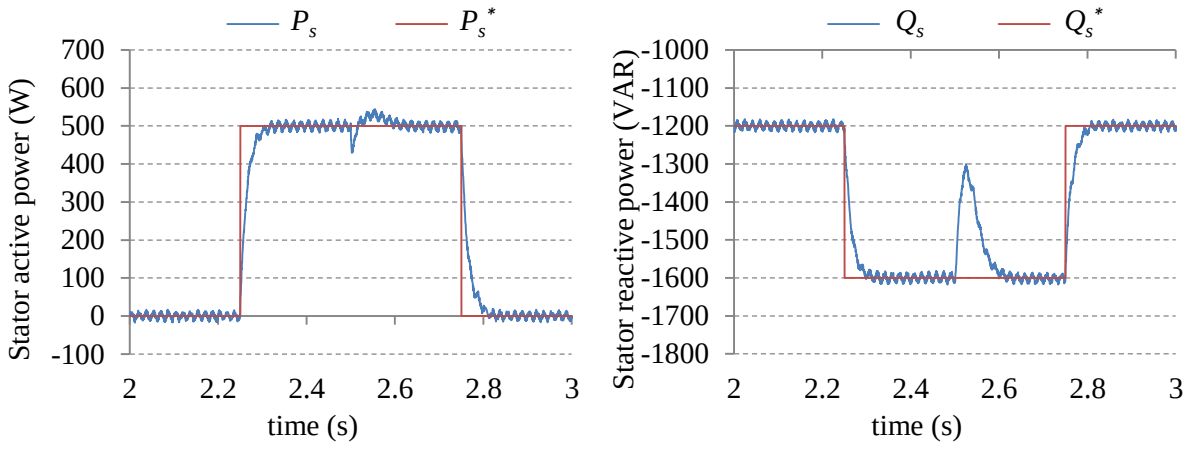

(a) Stator active power

(b) Stator reactive power

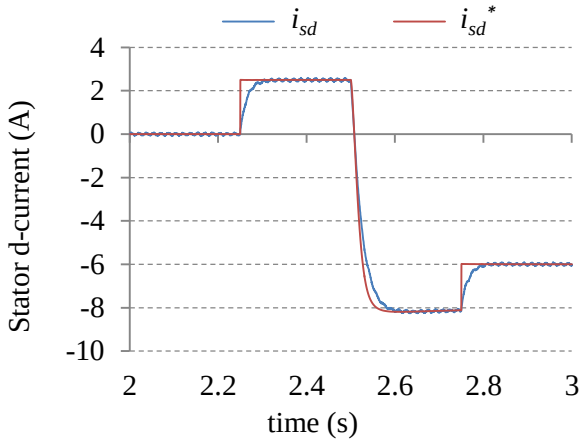

(c) Stator d-current

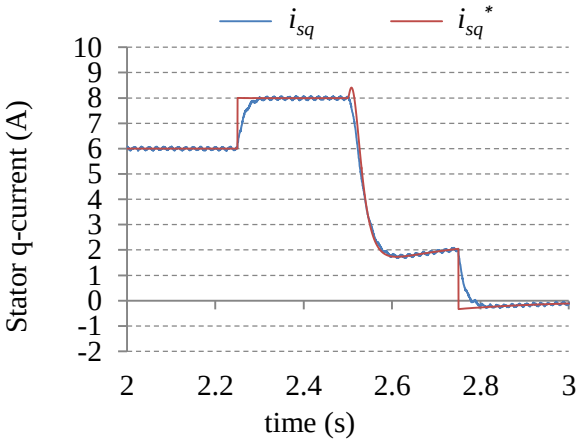

(d) Stator q-current

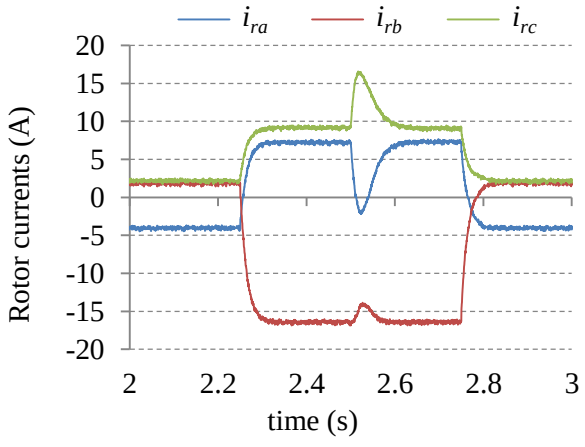

(e) Rotor currents

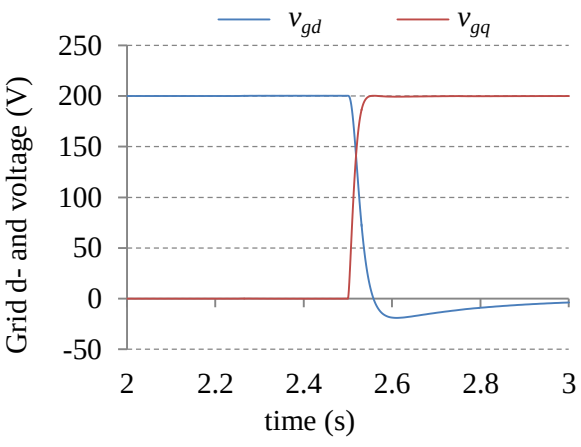

(f) Grid d- and q-voltage

Fig. 3.24: Simulation results for the effect of the grid voltage orientation on the proposed decoupled control with ω_m = 1.0 pu.

Next, the effect of the slip angle inaccuracy is investigated. The stability analysis of the proposed decoupled control against a slip angle error concluded that the proposed decoupled control can tolerate a slip angle error slightly above ±90 degrees. Using (3.38) the proposed decoupled control becomes unstable when the slip angle error is equal to ±94.5 degrees. To verify this analysis, the following two tests are conducted:

First, the slip angle error is fixed at 90 degrees, and the step response of the active and reactive power are investigated. The DFIG speed during this test is fixed at a sub-synchronous speed of 0.8 pu. The results for this test are shown in Fig. 3.25.

Although the responses of the active and reactive power, in Fig. 3.25, have poorly damped oscillations, the proposed decoupled control is still stable with such large slip angle error of 90 degrees.

Next, the slip angle error is increased linearly from zero degree up to 110 degrees. During this test, the active and reactive power references are fixed at 600 W and -1400 VAR respectively. The DFIG speed is fixed at a hyper-synchronous speed of 1.2 pu. The results for this test are shown in Fig. 3.26.

From the results of Fig. 3.26, the proposed decoupled control can tolerate large slip angle error before becoming unstable. The slip angle error at which the system becomes unstable is approximately 92.6 degrees, which is slightly smaller than the expected value in the analysis, which is 94.5 degrees; this difference comes from the simplification involved in the control model of Fig. 3.15.

When the decoupled control becomes unstable, large rotor currents are generated which can exceed the machine rating without the upper limits of the PI controllers.

In the following test, the effect of the grid voltage variation is investigated; first, without saturation of the DFIG core and, then, with saturation. This can be achieved because the PSCAD software allows introducing to the DFIG core a saturation curve.

First, without saturation, the grid voltage amplitude (line-to-line) is increased linearly from around 147 V_{rms} to around 220 V_{rms}. In this test, the DFIG is ideal and does not saturate. The active and reactive power references are fixed at 200 W and −1400 VAR respectively, and the DFIG speed was fixed at a hyper-synchronous speed of 1.1 pu. The results for this test are shown in Fig. 3.27.

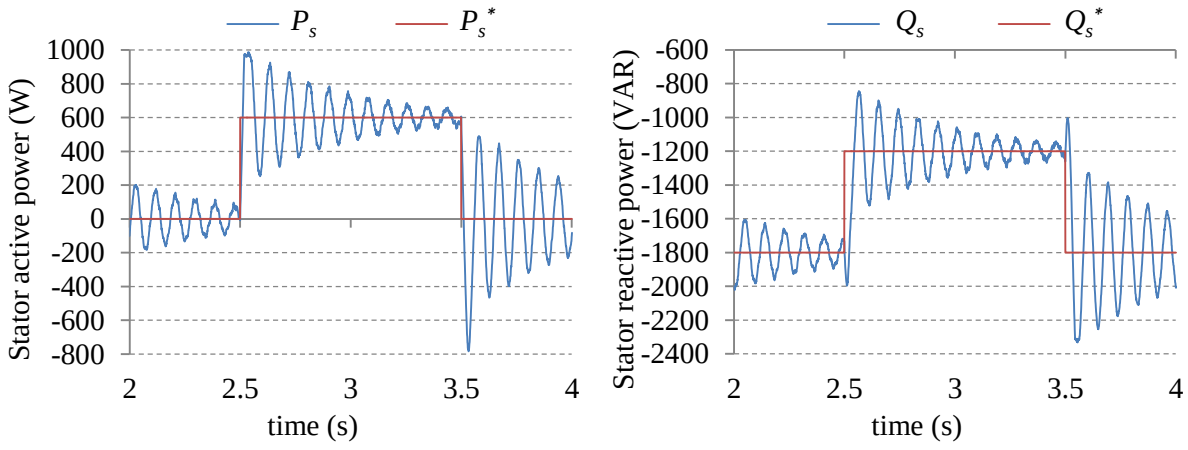

(a) Stator active power

(b) Stator reactive power

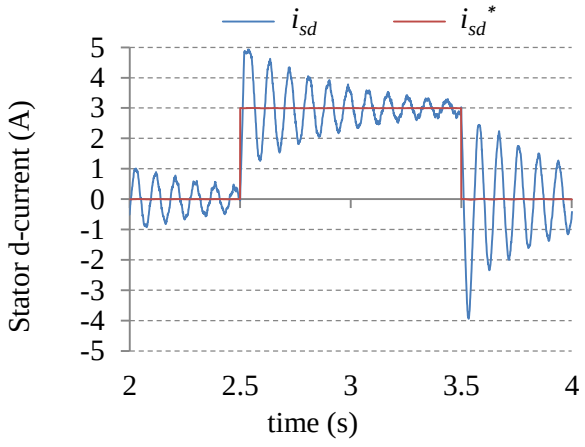

(c) Stator d-current

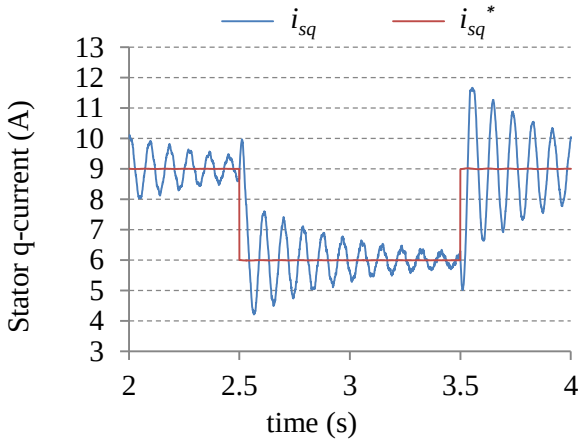

(d) Stator q-current

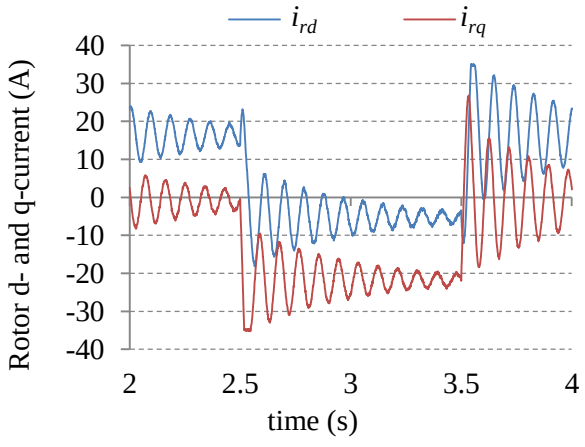

(e) Rotor d- and q-current

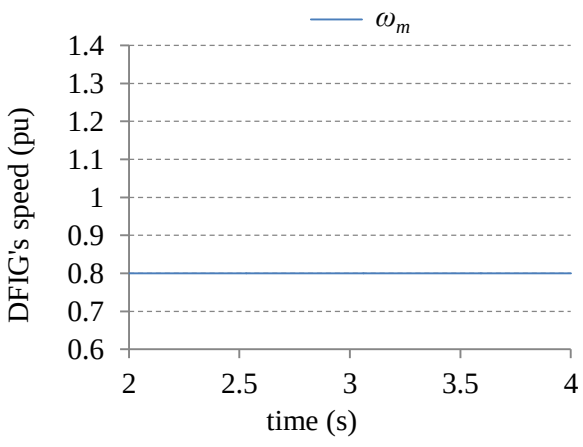

(f) DFIG's speed

Fig. 3.25: Simulation results for the step response with a slip angle error of $\Delta\theta_r$ = 90 degrees and ω_m = 0.8 pu.

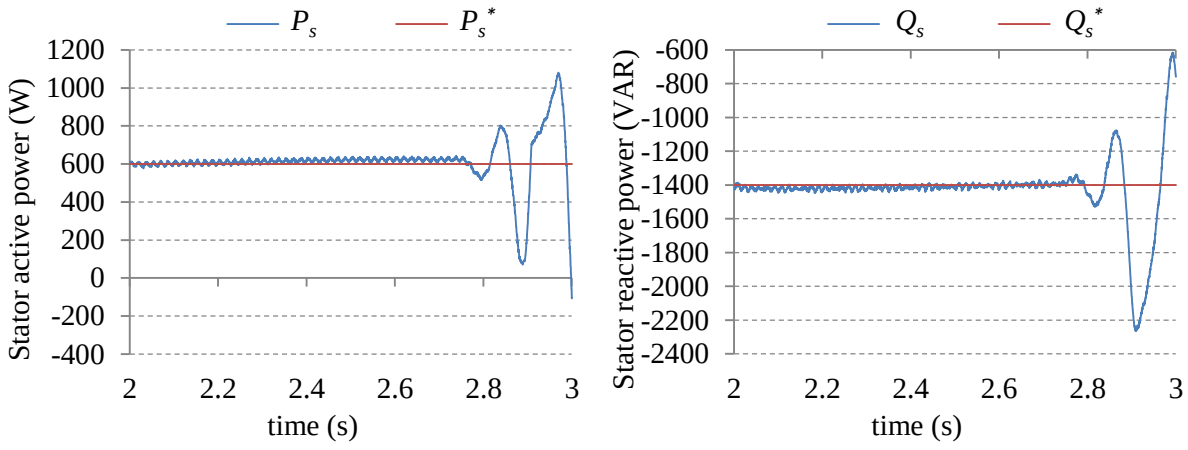

(a) Stator active power

(b) Stator reactive power

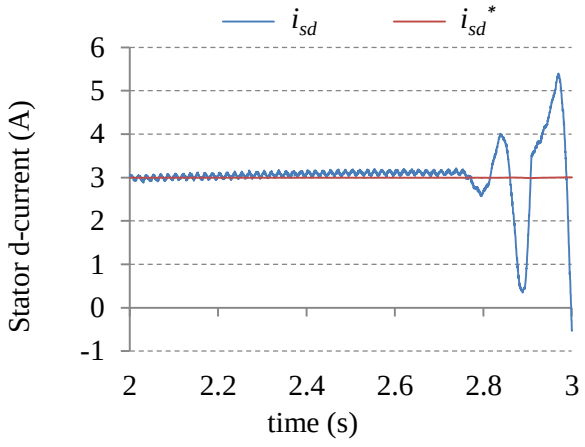

(c) Stator d-current

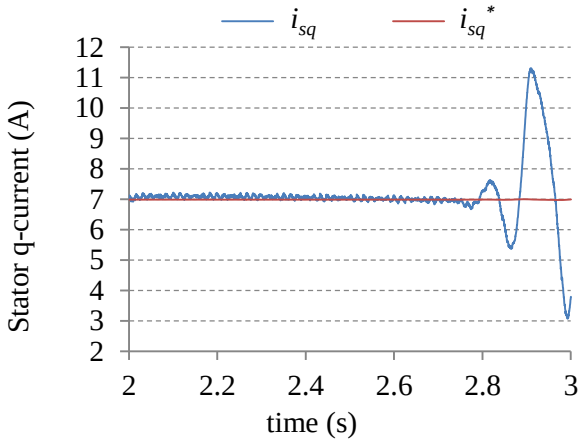

(d) Stator q-current

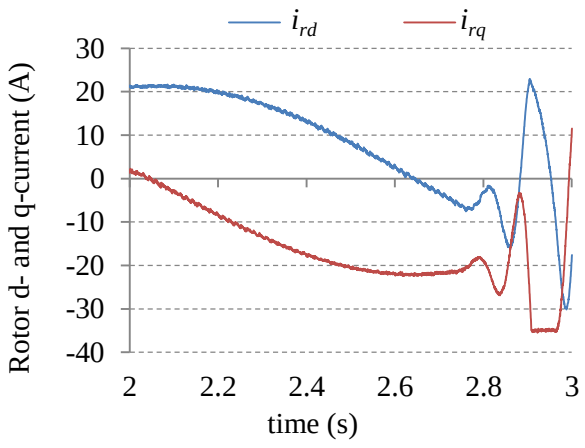

(e) Rotor d- and q-current

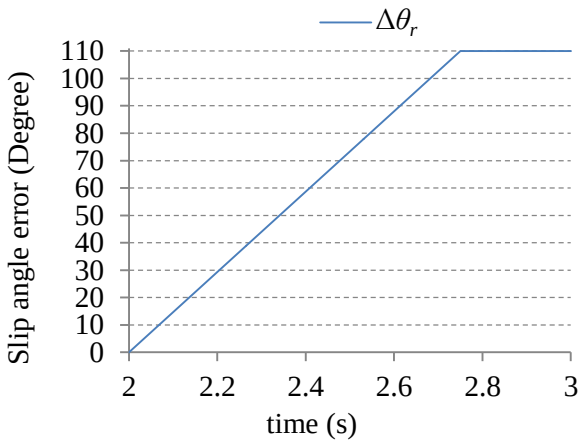

(f) Slip angle error

Fig. 3.26: Simulation results for the effect of increasing the slip angle error on the proposed decoupled control with ω_m = 1.2 pu.

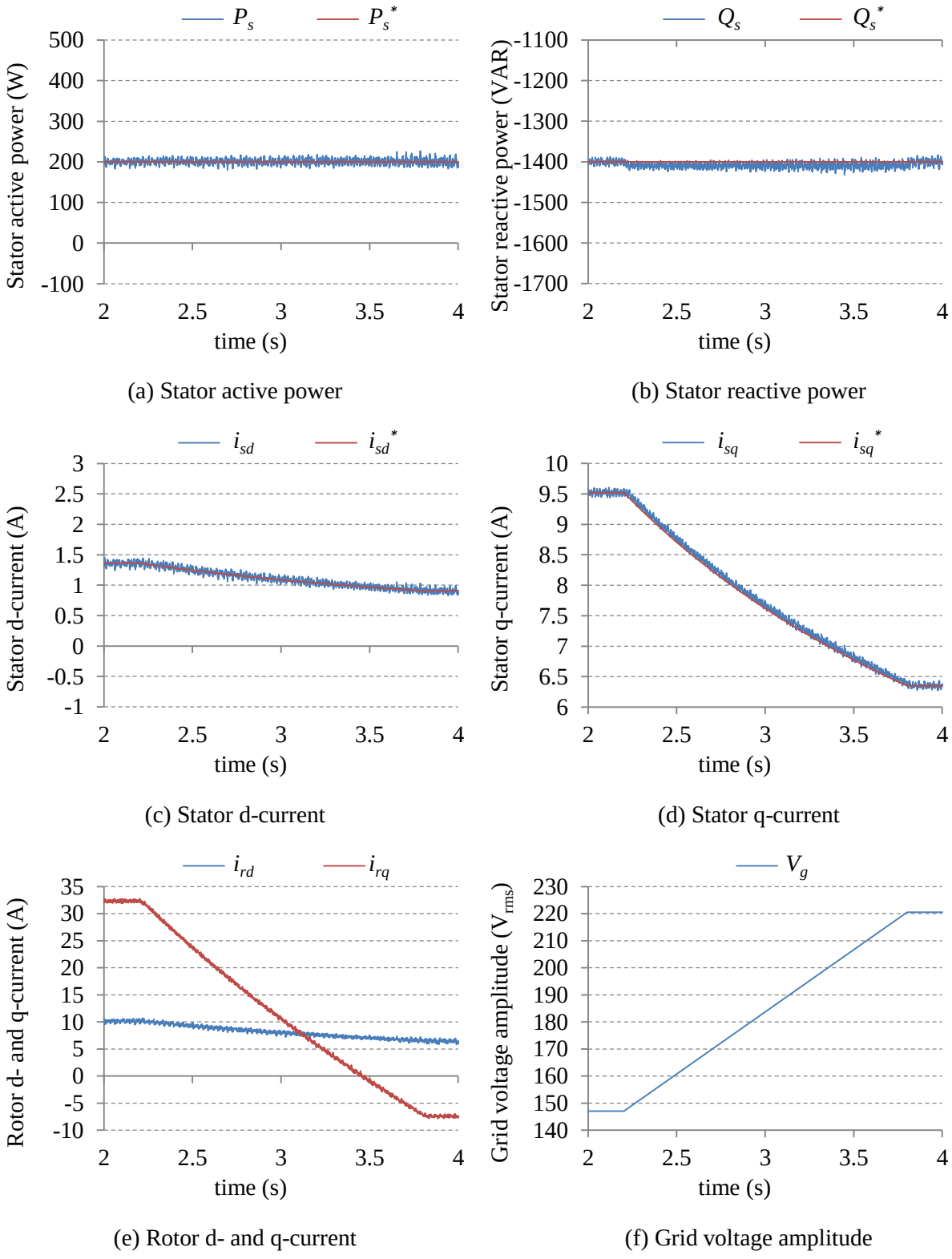

(a) Stator active power

(b) Stator reactive power

(c) Stator d-current

(d) Stator q-current

(e) Rotor d- and q-current

(f) Grid voltage amplitude

Fig. 3.27: Simulation results for the effect of the grid voltage amplitude variation without saturation of the DFIG's core and with ω_m = 1.1 pu.

From the results of Fig. 3.27, the proposed decoupled control is robust against variation in the voltage amplitude. However, it is observed that the stator and rotor q-current undertake larger variation compared to the d-current. The stator d-current has to counteract the voltage variation to regulate the active power. On the other hand, the stator q-current has to counteract both the grid voltage variation and the magnetizing current variation.

Similar to the previous test, the grid voltage amplitude is varied linearly but, this time, the nonlinearity of the DFIG's core is enabled. In this work, the default saturation curve in PSCAD, which is depicted in Fig. 3.28, is adopted.

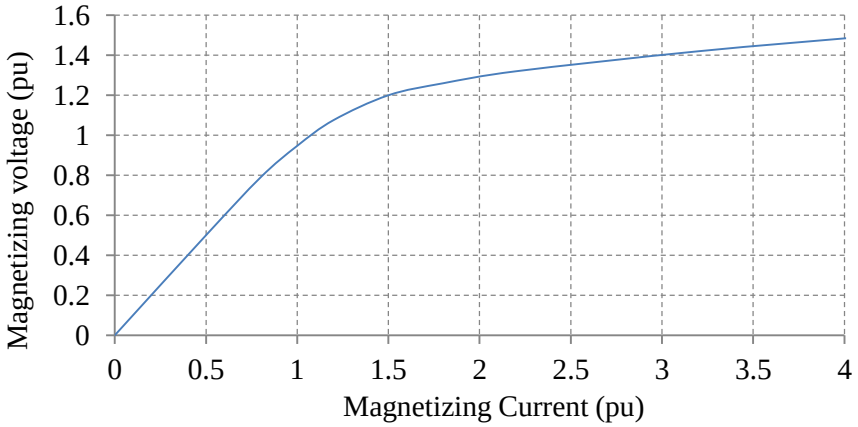

Fig. 3.28: DFIG's saturation curve.

As the grid voltage is increasing and the magnetizing impedance is decreasing, the magnetizing current will become large. Thus, the reactive power is varied to counteract the variation of the magnetizing current; this is done to avoid exceeding the rated rotor current of the DFIG. The DFIG speed, during this test, is fixed at a hyper-synchronous speed of 1.3 pu. The results for this test are shown in Fig. 3.29.

From the results of Fig. 3.29, the performance of the proposed control is not affected by the variation of the grid voltage or the variation of DFIG's parameters due to saturation.

Finally, the negative-sequence compensation performance is investigated. To generate unbalance in the line impedance, a 10 mH inductance is inserted at the phase-b of the DFIG's stator terminal. The performance of the system is investigated without and with negative sequence compensation.

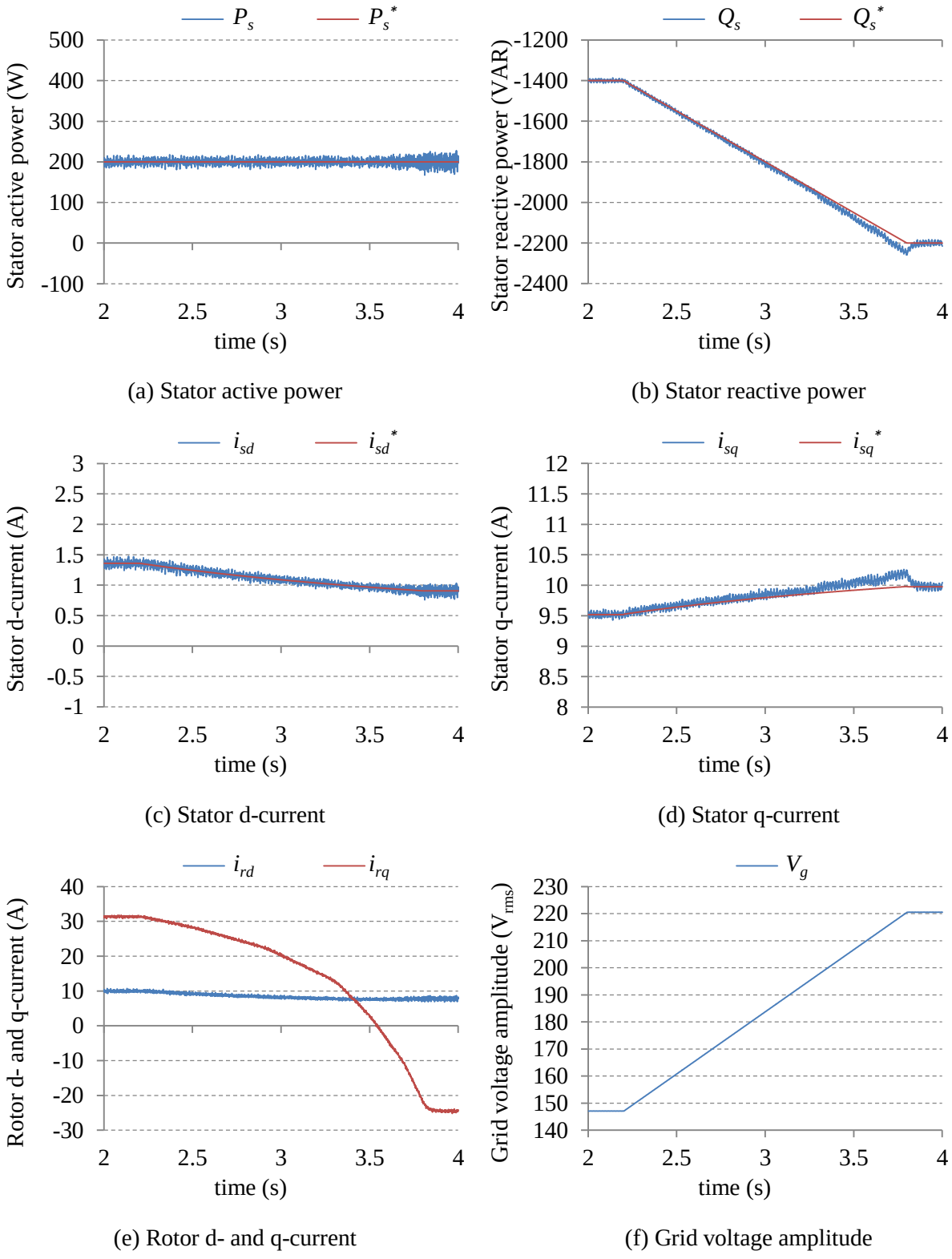

(a) Stator active power

(b) Stator reactive power

(c) Stator d-current

(d) Stator q-current

(e) Rotor d- and q-current

(f) Grid voltage amplitude

Fig. 3.29: Simulation results for the effect of the grid voltage amplitude variation with saturation of the DFIG's core and with ω_m = 1.3 pu.

During this test, the stator active and reactive power references are fixed at 200 W and −1600 VAR respectively. The DFIG speed is fixed at a sub-synchronous speed of 0.9 pu. The results without and with negative-sequence compensation are shown in Fig. 3.30 and Fig. 3.31 respectively.

In Fig. 3.30, due to the unbalanced line impedance, a stator negative-sequence current of 0.3 A amplitude flows into the DFIG's stator. This negative-sequence current produces relatively large oscillations in the active and reactive power responses, whose peak-to-peak amplitudes are 150 W and 150 VAR.

From the results of Fig. 3.31, the negative-sequence compensation control injects into the rotor current a negative-sequence component which generates, at the DFIG's stator, a component that opposes the stator negative-sequence current. This reduces the stator negative-sequence current to a negligible amplitude of around 0.002 A, which reduces the power ripples to around 50 W peak-to-peak, which results from the voltage negative-sequence.

3.3.3 Experimental Results

First, the DFIG speed is varied from a sub-synchronous speed of 0.8 pu to a hyper-synchronous speed of 1.2 pu within 1 sec. At the synchronous speed, the active and reactive power references are stepped from 0 W to 800 W and from −1800 VAR to −1000 VAR respectively. The results for this test are shown in Fig. 3.32.

The proposed decoupled control effectively regulates the stator active and reactive power regardless of the speed variation.

Second, the effect of the voltage grid orientation on the system performance is investigated. Similar to the simulation, the PLL circuit initially forces the q-voltage to zero, then at 0 sec it suddenly changes to forcing the d-voltage to zero. During this test the DFIG speed reference is fixed at a sub-synchronous speed of 0.9 pu. The results for this test are shown in Fig. 3.33.

The results of Fig. 3.33 shows that the stability and performance of the proposed decoupled control is independent of the grid voltage orientation except for a short transition due to the sudden change of the orientation of the magnetizing current. These results demonstrate the flexibility and robustness of the proposed decoupled control against grid voltage orientation.

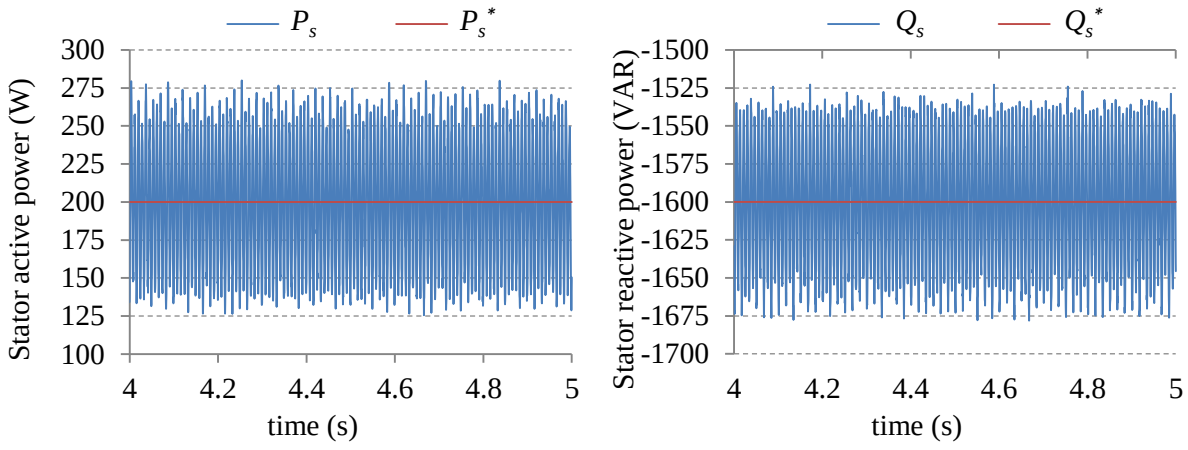

(a) Stator active power

(b) Stator reactive power

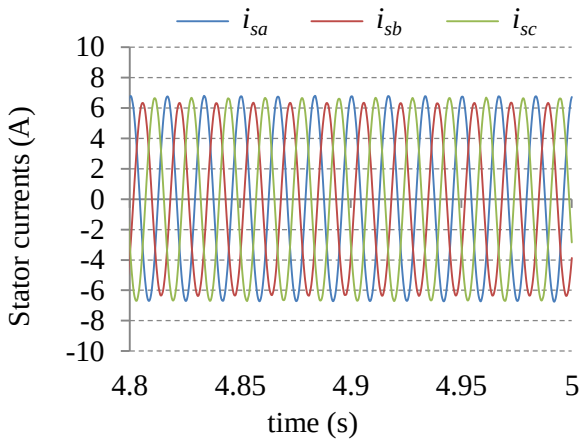

(c) Stator currents

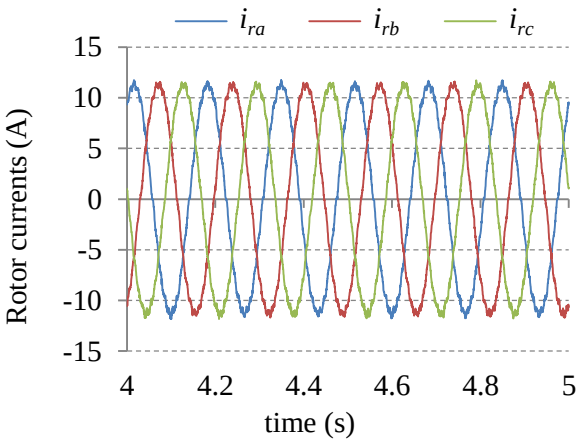

(d) Rotor currents

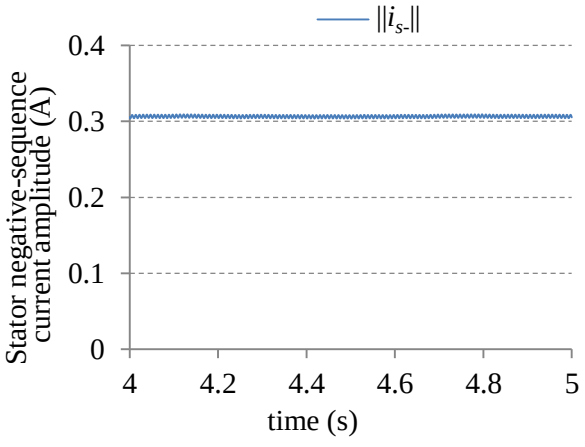

(e) Stator negative-sequence current amplitude

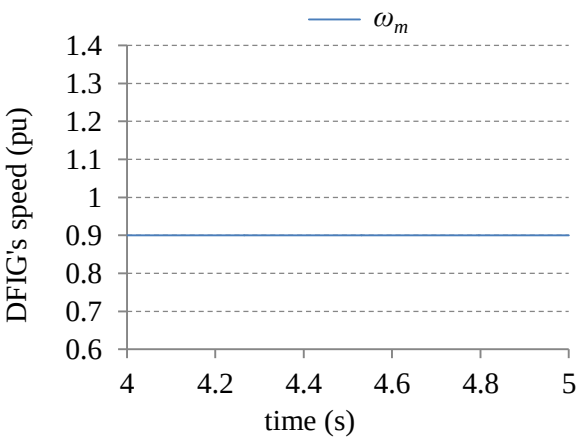

(f) DFIG's speed

Fig. 3.30: Simulation results for the effect of line unbalance without negative-sequence compensation control and with ω_m = 0.9 pu.

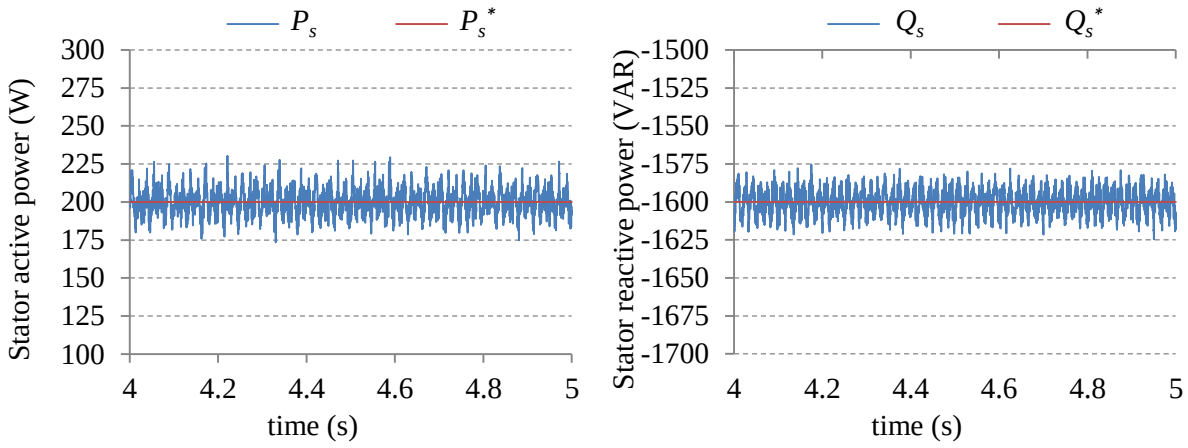

(a) Stator active power

(b) Stator reactive power

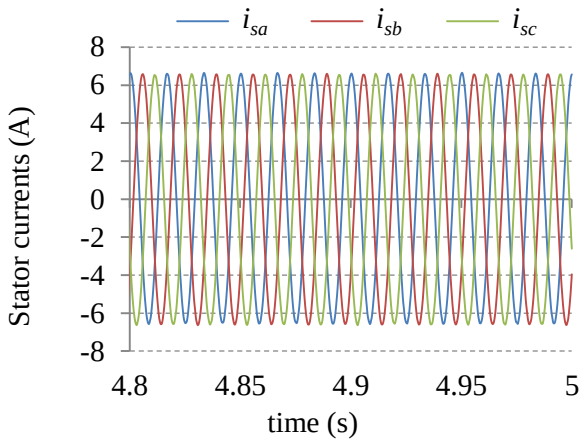

(c) Stator currents

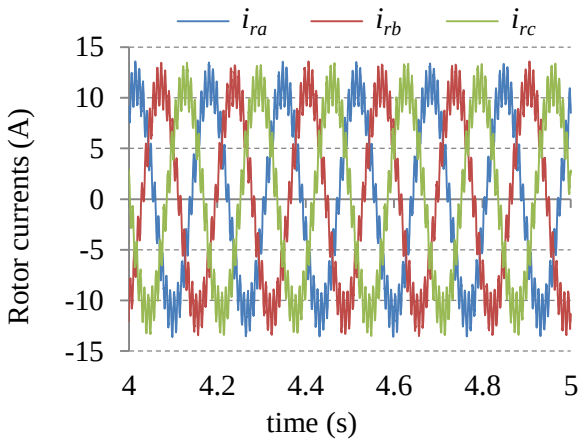

(d) Rotor currents

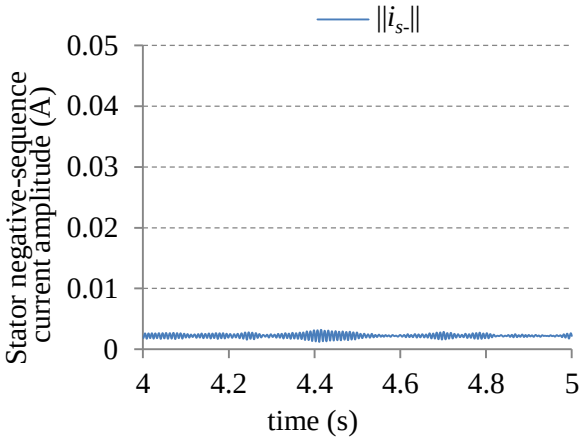

(e) Stator negative-sequence current amplitude

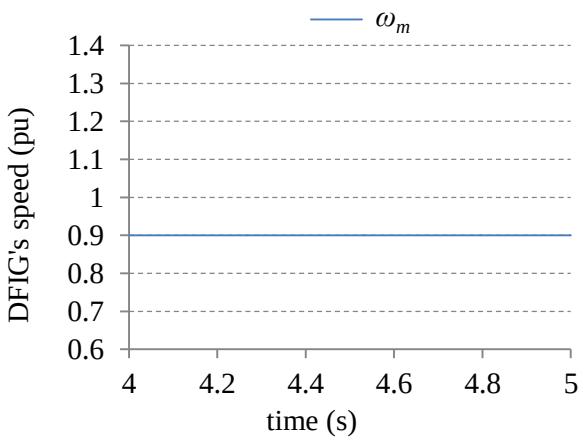

(f) DFIG's speed

Fig. 3.31: Simulation results for the effect of line unbalance with negative-sequence compensation control and with ω_m = 0.9 pu.

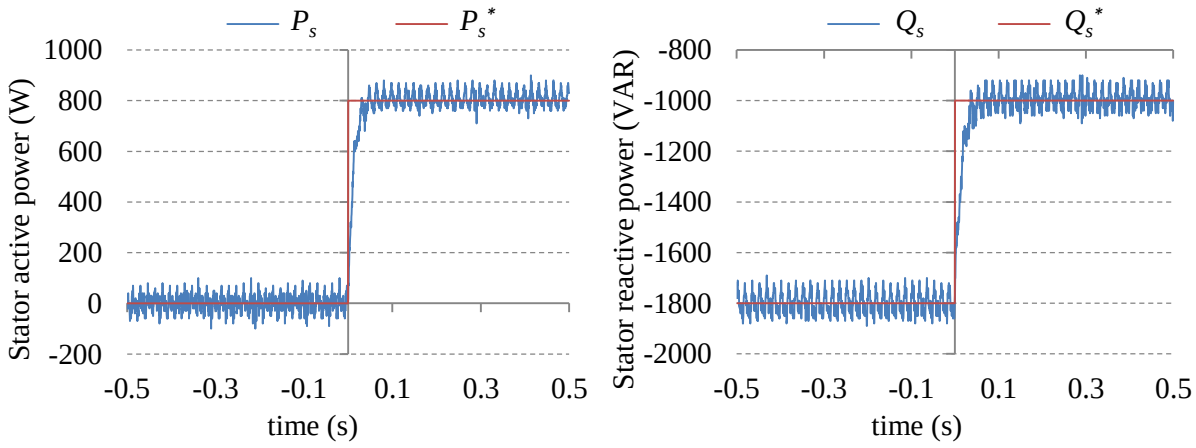

(a) Stator active power

(b) Stator reactive power

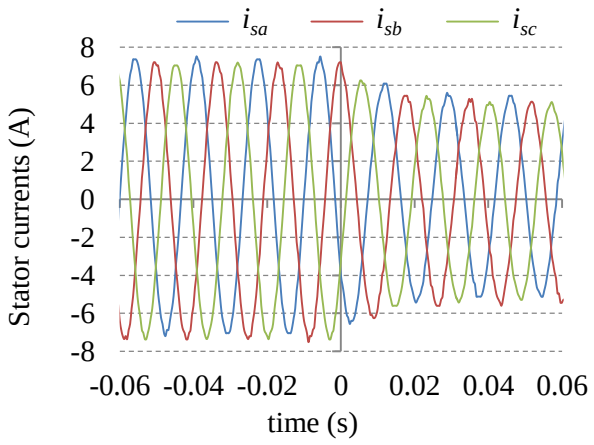

(c) Stator currents

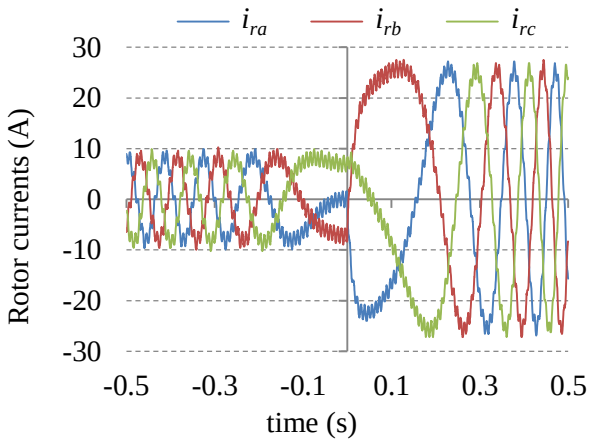

(d) Rotor currents

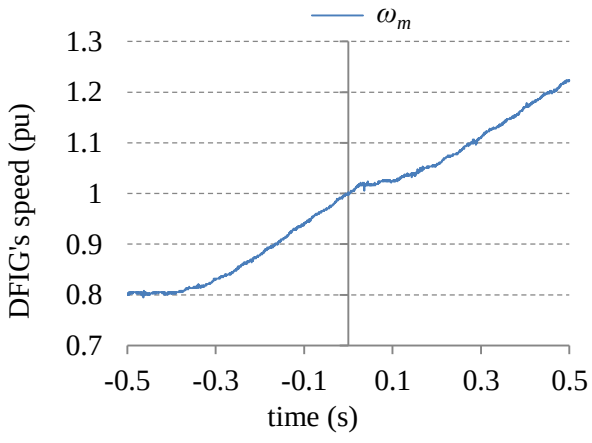

(e) DFIG's speed

Fig. 3.32: Experimental results for variable speed operation where ω_m = 0.8 pu → 1.2 pu.

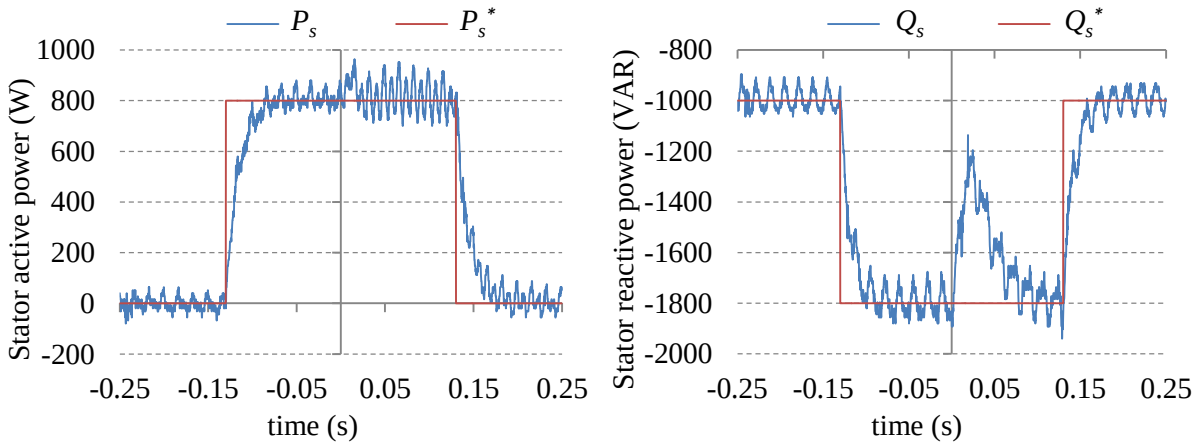

(a) Stator active power

(b) Stator reactive power

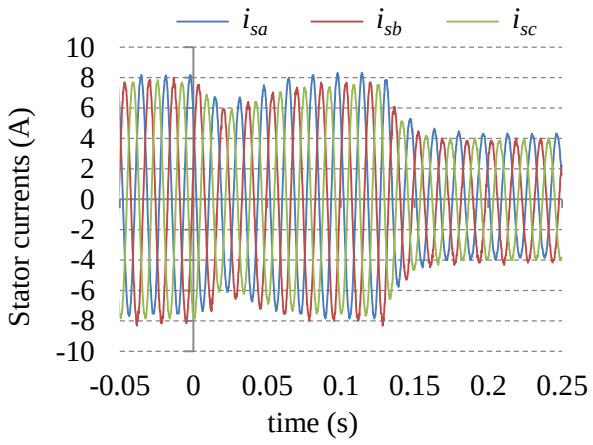

(c) Stator currents

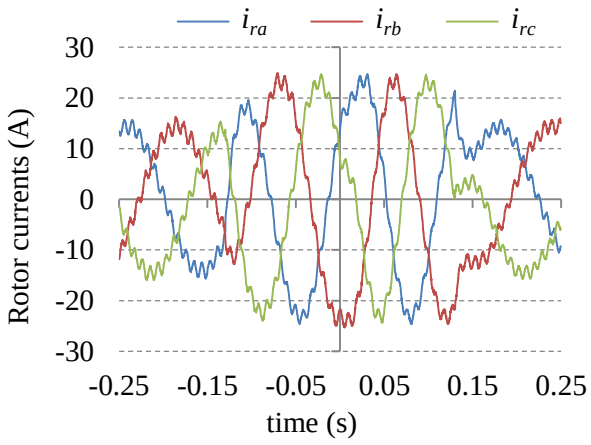

(d) Rotor currents

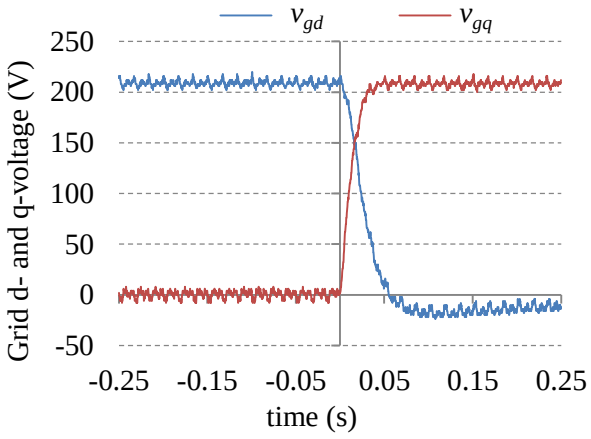

(e) Grid d- and q-voltage

Fig. 3.33: Experimental results for the effect of the grid voltage orientation on the proposed decoupled control with ω_m^* = 0.9 pu.

In Fig. 3.33 (a) and (b), there is a small and slowly-decaying oscillation after the change of orientation; this oscillation is caused by the slow response of the negative-sequence compensation.

Next, the effect of slip angle inaccuracy on the stability of the proposed decoupled control is investigated. The slip angle inaccuracy is increased linearly from zero to around 105 degrees. During this test, the DFIG's reference speed is fixed at a hyper-synchronous speed of 1.1 pu, and the active and reactive power references are fixed at 200 W and −1200 VAR respectively. The results are shown in Fig. 3.34.

From the results of Fig. 3.34, the proposed decoupled control can tolerate large slip inaccuracy, which is slightly above 90 degrees, before becoming unstable. Thus, the proposed decoupled control is robust against slip angle inaccuracy.

In the following experiment, the proposed decoupled control is test under grid voltage variation. Using a programmable three-phase AC source, the grid voltage reference amplitude is linearly decreased from 200 V to 160 V within 0.5 sec. The grid voltage was polluted with a small negative-sequence component of around 1% of the rated voltage, which is caused by an asymmetry in the line impedance. During this test, the DFIG's reference speed is fixed at a hyper-synchronous speed of 1.2 pu. The results for this test are shown in Fig. 3.35.

Similar to the simulation results, the proposed decoupled control is robust against grid voltage variation. Since the grid voltage variation is associated with variation in some of the DFIG's parameters, the proposed decoupled control is also robust against parameter variation due to saturation.

The negative-sequence compensation can eliminate power ripples resulting from the stator negative-sequence current only. Since the grid voltage has a negative-sequence component, it produces additional power ripples as in Fig. 3.35.

Finally, the negative-sequence compensation is investigated. Two test are carried out, without and with negative sequence compensation. The speed in this test is fixed at the synchronous speed, and the active and reactive power references are fixed at 400 W and −1200 VAR respectively. The results for operation without and with negative-sequence compensation are shown in Fig. 3.36 and Fig. 3.37 respectively.

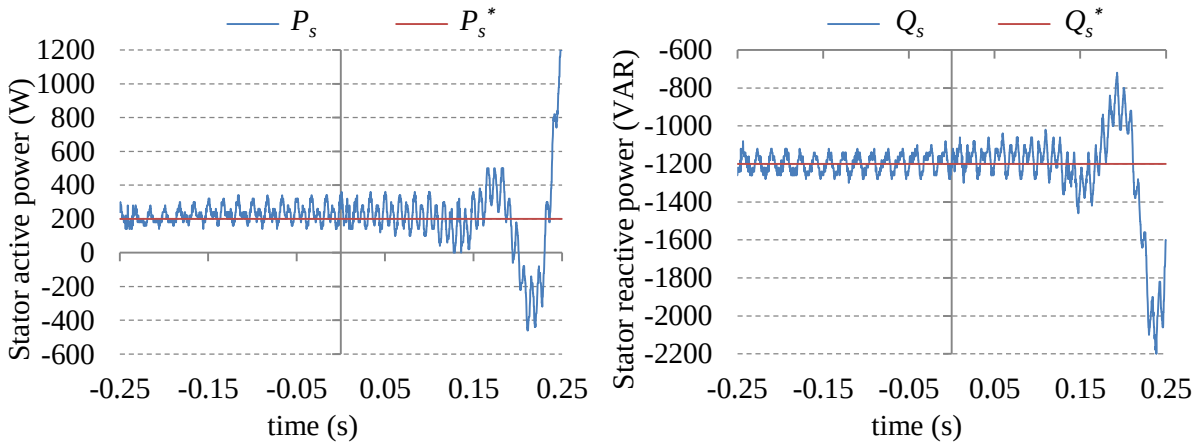

(a) Stator active power

(b) Stator reactive power

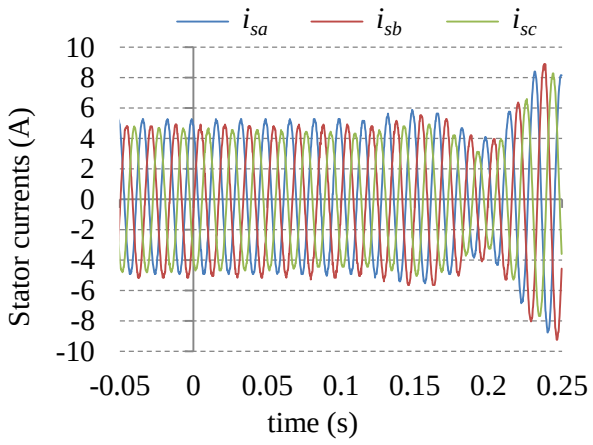

(c) Stator currents

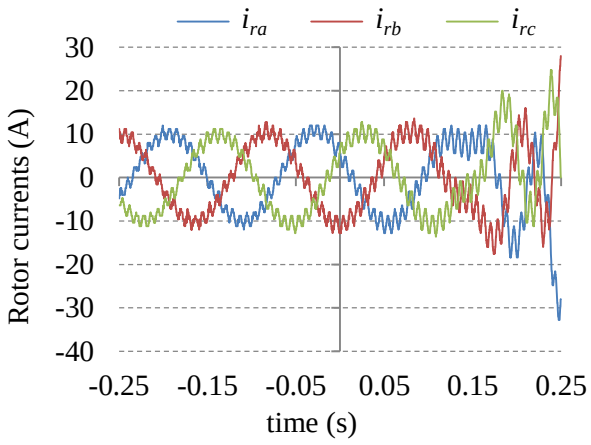

(d) Rotor currents

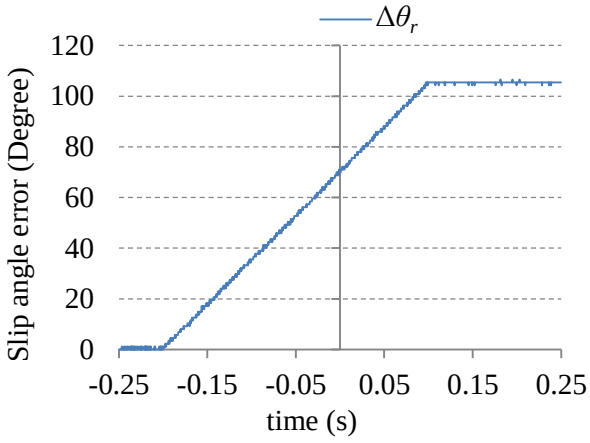

(e) Slip angle error

Fig. 3.34: Experimental results for the effect of increasing the slip angle error on the proposed decoupled control with ω_m^* = 1.1 pu.

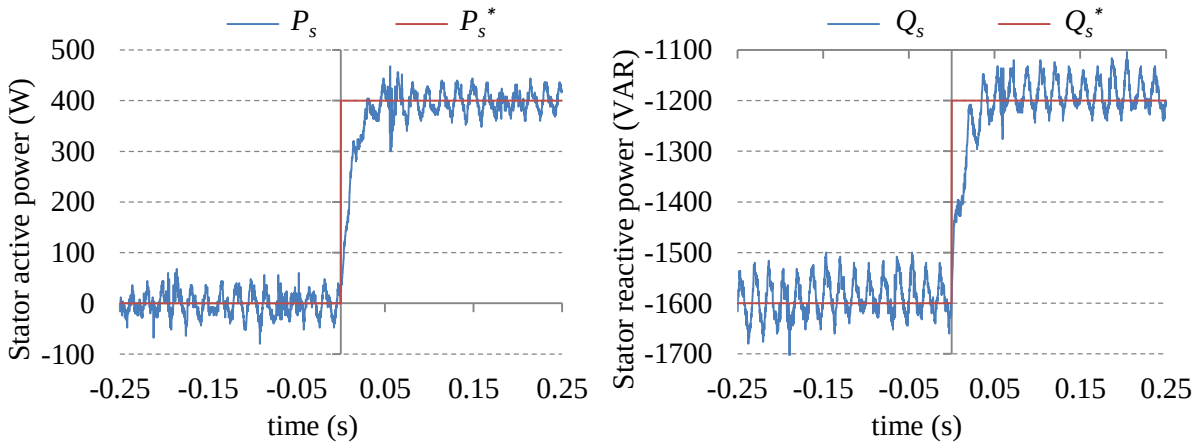

(a) Stator active power

(b) Stator reactive power

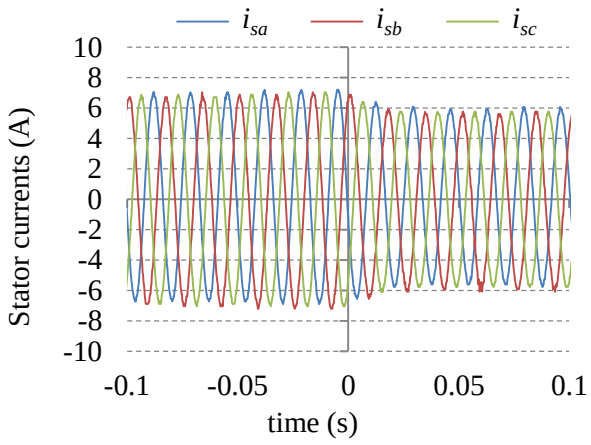

(c) Stator currents

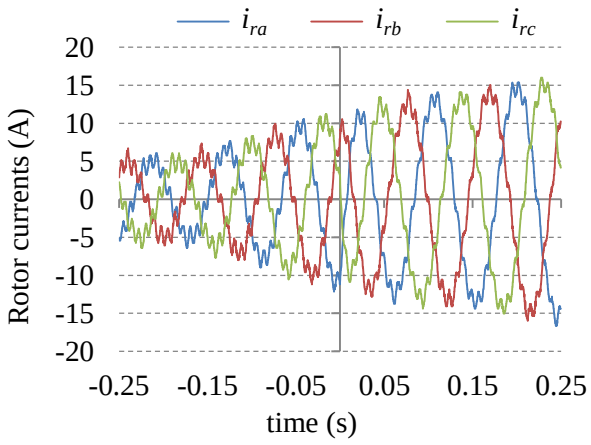

(d) Rotor currents

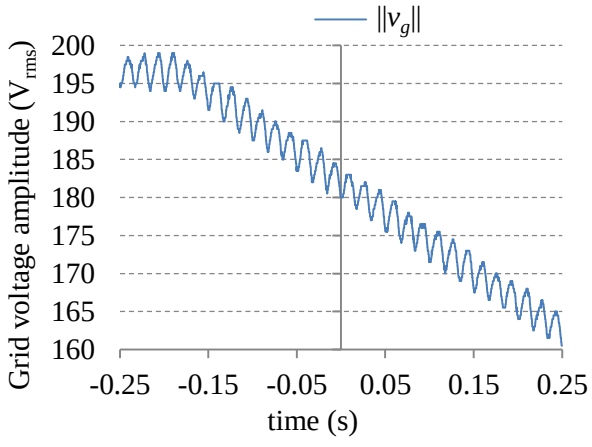

(e) Grid voltage amplitude

Fig. 3.35: Experimental results for the effect of the grid voltage amplitude variation with ω_m^* = 1.1 pu.

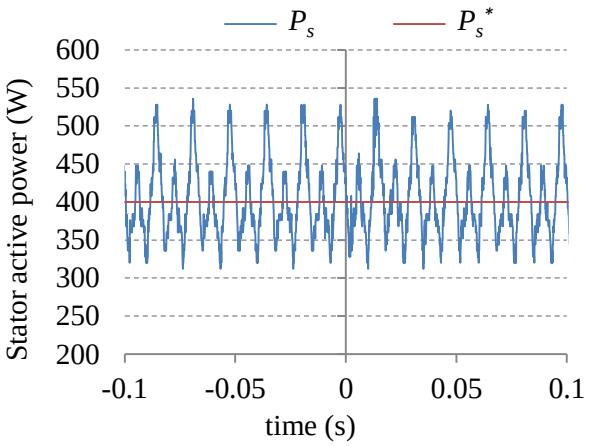

(a) Stator active power

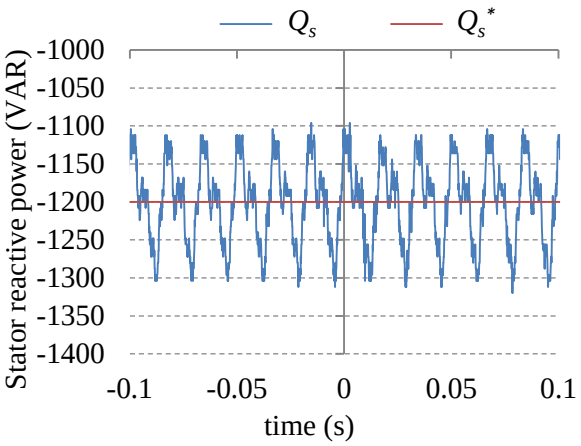

(b) Stator reactive power

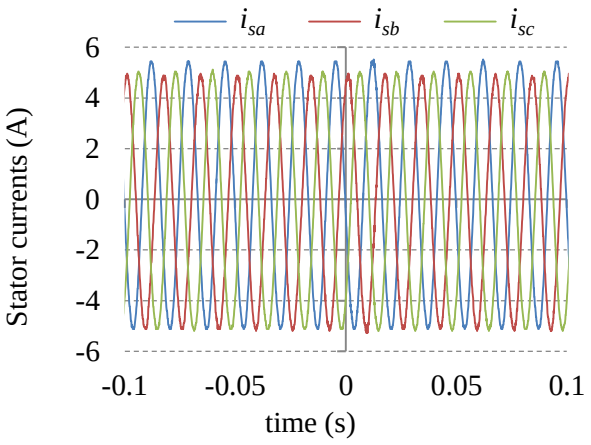

(c) Stator currents

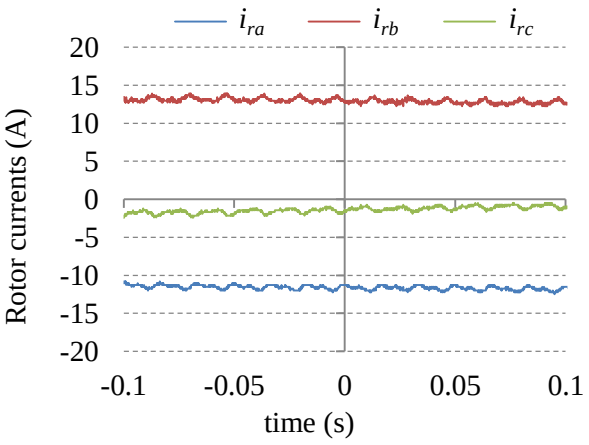

(d) Rotor currents

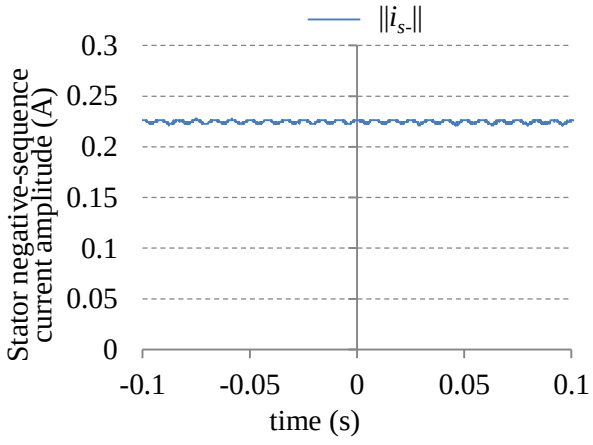

(e) Stator negative-sequence current amplitude

Fig. 3.36: Experimental results without negative-sequence compensation control and with P_s^* = 400 W, Q_s^* = -1200 VAR, and ω_m^* = 1.0 pu.

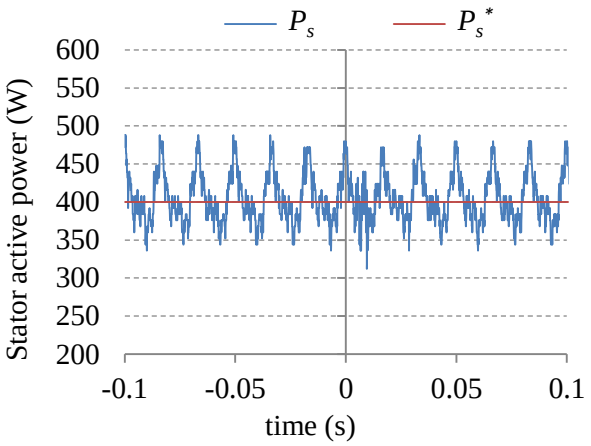

(a) Stator active power

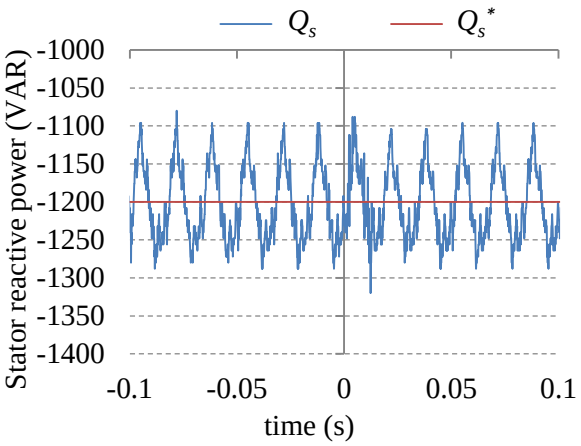

(b) Stator reactive power

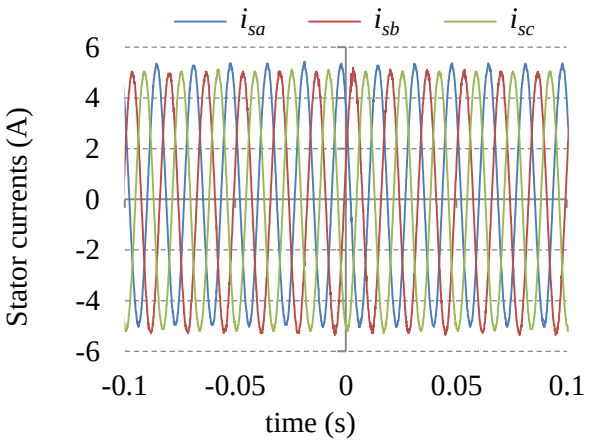

(c) Stator currents

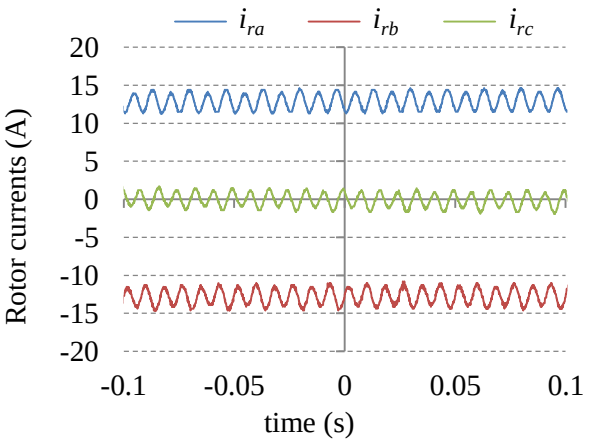

(d) Rotor currents

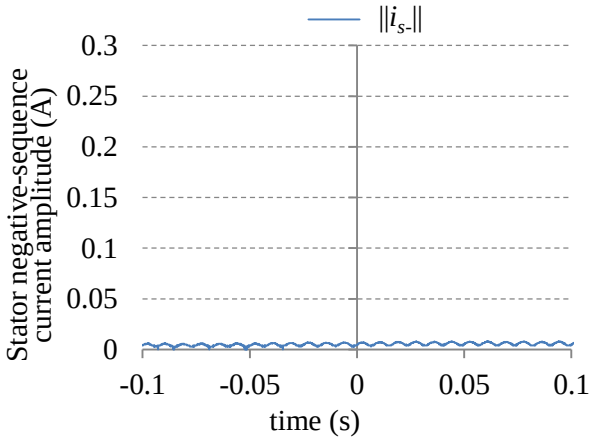

(e) Stator negative-sequence current amplitude

Fig. 3.37: Experimental results without negative-sequence compensation control and with P_s^* = 400 W, Q_s^* = -1200 VAR, and ω_m^* = 1.0 pu.

The results in Fig. 3.36, demonstrate that under normal condition, there is a stator negative-sequence current whose amplitude is around 0.22 A. With the negative-sequence compensation, this negative-sequence current is reduced to around 0.005 A. Therefore, the power ripples resulting from this current are reduce. The power ripples resulting from stator negative-sequence voltage, on the other hand, cannot be reduced with this control. To reduce power ripples resulting from negative-sequence voltages, other negative-sequence compensation schemes can be used such as [12].

3.4 Conclusion

This chapter has introduced the analysis and the design of a control system for the grid-connected DFIG. This control system includes a new decoupled control which has the following advantages:

- The proposed control is robust against speed variation which makes it suitable for variable speed generation systems.
- It achieves decoupled control of the active and reactive power with good dynamical response.
- The online calculation of the proposed decoupled control does not require knowledge of any parameter of the DFIG.
- The decoupling does not require forcing the stator q-voltage to zero and is independent of the grid voltage orientation. Thus, the proposed decoupled control is more flexible and robust.
- The transfer function of the proposed decoupled control is independent of the grid voltage amplitude.
- The proposed control is independent of the parameters variations due to saturation.

The decoupled control was tested successfully with simulation and experiments, and the results were satisfactory.

The proposed decoupled control can replace the conventional decoupled P-Q control which improve the robustness of the DFIG system.

References

[1] R. Pena, J. C. Clare, and G. M. Asher, "Doubly Fed Induction Generator Using Back-to-Back PWM Converters and its Application to Variable-Speed Wind-Energy Generation," in *Proc. IEE Electric Power Applications,* vol. 143, no. 3, pp. 231-241, May 1996.

[2] R. Datta and V. T. Ranganathan, "A Simple Position-Sensorless Algorithm for Rotor-Side Field-Oriented Control of Wound-Rotor Induction Machine," *IEEE Trans. Industrial Electronics*, vol. 48, no. 4, pp. 786-793, Aug. 2001.

[3] S. Arnalite, J. C. Burgos, and J. L. Rodriguez-Amendo, "Direct Torque Control of a Doubly-Fed Induction Generator for Variable Speed Wind Turbines," *Electric Power Components and Systems*, vol. 30, no. 2, pp. 199-216, 2002.

[4] B. B. Pimple, V. Y. Vekhande, and B. G. Fernandes, "A New Direct Torque Control of Doubly-Fed Induction Generator Under Unbalanced Grid Voltage," in *Proc. 26th Annual IEEE APEC Expo., 2011,* pp. 1576-1581.

[5] D. Zhi and L. Xu, "Direct Power Control of DFIG with Constant Switching Frequency and Improved Transient Performance," *IEEE Trans. Energy Conversion,* vol. 22, no. 1, pp. 110-118, Mar. 2007.

[6] B. Singh and N. K. S. Naidu, "Direct Power Control of Single VSC-Based DFIG without Rotor Position Sensor," *IEEE Trans. Ind. Appl.*, vol. 50, no. 6, pp. 4152-4163, Nov./Dec. 2014.

[7] R. Datta and V. T. Ranganathan, "Decoupled Control of Active and Reactive Power for a Grid-Connected Doubly-Fed Wound Rotor Induction Machine without Position Sensors," in *Proc. IEEE/IAS Annual Meeting Conf.*, 1999, Phoenix, pp. 2623-2630.

[8] L. G. B. Rolim, D. R. da Costa, and M. Aredes, "Analysis and Software Implementation of a Robust Synchronizing PLL Circuit Based on the dq Theory," *IEEE Trans. Industrial Electronics*, vol. 53, no. 6, pp. 1919-1926, Dec. 2006.

[9] A. Petersson, L. Harnefors, and T. Thiringer, "Evaluation of Current Control Methods for Wind Turbines Using Doubly-Fed Induction Machines," *IEEE Trans. Power Electronics,* vol. 20, no. 1, pp. 227-235, Jan. 2005.

[10] J. Morren and S. W. H. de Haan, "Ridethrough of Wind Turbines with Doubly-Fed Induction Generator during a Voltage Dip," *IEEE Trans. Energy Conversion,* vol. 20, no. 2, pp. 435-441, Jun. 2005.

[11] N. R. Klaes, "Parameter Identification of an Induction Machine with Regard to Dependencies on Saturation," *IEEE Trans. Industry Applications*, vol. 29, no. 6, pp. 1135-1140, Nov./Dec. 1993.

[12] G. Abad, M. A. Rodriguez, G. Iwanski, and J. Poza, "Direct Power Control of Doubly-Fed-Induction-Generator-Based Wind Turbines under Unbalanced Grid Voltage," *IEEE Trans. Power Electronics*, vol. 25, no. 2, pp. 442-452, Feb. 2010.

Chapter 4

Slip Angle Estimator

Most of the grid-connected control schemes requires knowledge of the slip angle which is calculated using the DFIG's rotor position. The DFIG's rotor position is usually measured using a mechanical encoder. The use of a mechanical encoder has several drawbacks: It increases the system cost and reduces the system robustness and reliability. Moreover, the mounting of the encoder on the DFIG's shaft requires special design of the shaft or special shaft extension; this increases the mechanical design complexity. The interfacing of the encoder increases and complicates the wiring, especially when the control unit must be far from the generator such as in small wind turbines, where the control unit cannot fit inside the nacelle and is located at the base of the turbine's tower. This requires careful wiring design and addition filters to reduce noise.

The drawbacks of mechanical encoders have pushed researchers to investigate software algorithms to obtain the slip angle. In this chapter, a brief review of the software estimators is provided followed by the proposed slip angle estimator which reduces the required number of DFIG parameters compared with other model-based estimators. To understand the effect of parameter inaccuracy on the performance of the proposed estimator, sensitivity analysis is provided.

4.1 Introduction

In literature, considerable research focused on replacing the mechanical encoders with software estimators. There are mainly three types of estimators: The open loop estimators, closed loop estimators, and estimators based on high frequency injection.

The early estimators, such as those in [1]-[4], had an open loop structure. In [1]-[3], the DFIG model is used to obtain an estimation of the rotor current. Then, the estimated and the measured rotor currents are compared to obtain an estimation of the slip angle.

In [4], a slip angle estimator for the torque-reactive power control scheme was proposed; this estimator is based on estimating the rotor flux. Although these estimators are straightforward and easy to realize, they cannot ensure stable convergence under parameter uncertainty or measurement noise [5]. In addition, the rotor flux-based estimator has poor performance when operating around the synchronous speed.

Model reference adaptive system (MRAS) observers are closed loop estimators, and they have better disturbance rejection and better robustness against parameters inaccuracy compared with open loop estimators. The MRAS observers are widely used for speed estimation in cage induction machines due to their simplicity. It was first introduced to cage induction machines in [6] and, later on, it was introduced to the DFIG in [7] and [8]. The general structure of a MRAS observer is depicted in Fig. 4.1.

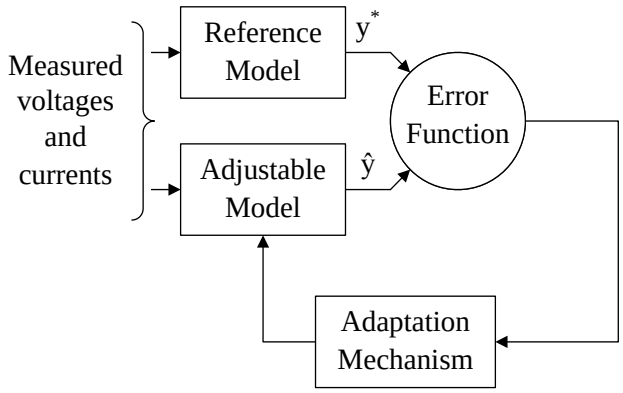

Fig. 4.1: General structure of MRAS observers.

A MRAS observer, which is also referred to as a model-based estimator, uses two different models of the DFIG to estimate the same quantity (y) such as the rotor flux. The two models are the reference model and the adjustable model. The reference model does not involve the slip frequency or angle while the adjustable model does. The estimated slip frequency or angle is used to adjust the adjustable model until its output matches that of the reference model.

The estimated quantity (y) is used to classify the MRAS observers. In literature, several MRAS observers are available for cage induction machines such as the rotor flux MRAS [6] [9], the stator current MRAS [10], the back-emf MRAS [11], and the stator power MRAS [12]. However, the most popular estimator for the induction machine is the rotor flux MRAS.

On the other hand, MRAS observers for DFIG are relatively less reported in

literature. The early observers were the stator flux MRAS [13], the rotor flux MRAS [14], the stator current MRAS [14], and the rotor current MRAS [15]. These four MRAS observers were compared in [14].

In general, the flux MRAS observers are not suitable when no magnetizing current is supplied from the rotor side. Moreover, the rotor flux MRAS has poor performance near the synchronous speed. The stator current MRAS cannot operate stably with small stator current and requires a minimum load to be connected. Among these observers, the rotor current MRAS has the best performance [14] and better robustness against grid voltage dips and stator winding resistance inaccuracy [16].

These observers need an estimation of the stator flux which is implemented by integrating the stator voltage. This implementation suffers from integrator drift and depends on the initial condition. Any small offset in the voltage sensor can drive the integrator into saturation; therefore, additional filters are needed. To overcome this issue, [5] proposed estimating the stator flux using a Luenberger observer. To completely eliminate the need for the stator flux, new MRAS observers were proposed such as the air gap power MRAS in [17] and the torque MRAS in [18].

The sensitivity analysis for parameter inaccuracy of three MRAS observers, which are the rotor current MRAS, the stator flux MRAS and the rotor flux MRAS, was carried out in [19]. In [19], expressions for the estimation error as a function of parameter inaccuracy were provided and used to find the stable region of the vector control. This study, however, completely ignored the effect of the stator winding resistance on the estimators' accuracy.

All MRAS observers require knowledge of several DFIG's parameters such as the stator winding resistance and the mutual inductance. Some attempts to reduce the number of parameters are reported in literature. In [20] and [21], the rotor current MRAS was modified to reduce the number of required parameters from three to two. This estimator was referred to as rotor position PLL. The rotor position PLL ignores the stator winding resistance and the leakage inductance, and it requires the mutual inductance and the DFIG's stator-to-rotor turns ratio. The estimator in [20] requires the magnetizing current which is obtained by integrating the stator voltage, while the estimator in [21] was modified to eliminate the integrator. Since the mutual inductance cannot be measured directly, it has to be estimated. The estimation involves measuring the terminals' quantities and conducting mathematical manipulation; this would increase

the parameter inaccuracy compared with direct measurement.

In Fig. 4.1, the error function is used to obtain the angle difference between the outputs of the two models. Usually, the error function is implemented using the cross product which results in a nonlinear, non-monotonic function. This implementation would produce an oscillatory transient response especially during fast transitions of the speed. To overcome this issue, authors in [5] proposed using the inverse tangent function, the cross product and the dot product to implement the error function. This produces a linear error function which, however, is still non-monotonic. In [22], the inverse tangent function was modified to obtain a monotonic error function by using a latch saturation.

The adaptation mechanism, commonly, uses a PI controller or, more recently, nonlinear controllers such as a hysteresis controller in [23], a sliding mode controller in [9], and a fuzzy logic controller in [9].

The last type of estimators is based on high frequency injection, which is well-known for cage induction machines [24] and is also used for permanent magnet synchronous machines (PMSM) [25]-[27]. This method is suitable when the machine has to operate over wide speed range including low speeds near zero.

The use of signal injection for rotor position estimation of the doubly fed induction machines was first reported in [28]. This method has been revised and improved by several researches such as in [29] and [30]. The operating principle is that the DFIG is regarded as a transformer in which the relative position between the primary and the secondary windings changes as the rotor rotates. Therefore, if a high-frequency signal is injected into the rotor, the phase of the corresponding signal in the stator has a component that is dependent on the rotor position angle. This method is robust against variation in the machine parameters. However, injection of high frequency signals in the DFIG's rotor is not simple to achieve in relatively large machines such as those used in wind power generation.

4.2 New Rotor Current-Based Slip Angle Estimator

The proposed slip angle estimator is similar to the rotor current MRAS observer because they are based on estimating the rotor current; however, the propose estimator has an improved implementation which produces improvements such as reduced

number of DFIG parameters, and eliminating the need for the stator flux.

To appreciate the proposed estimator, the rotor current MRAS is introduced first. Then, the proposed slip angle estimator is presented.

4.2.1 Rotor Current MRAS Observer

The equivalent circuit of the DFIG is shown in Fig. 4.2, where generator notation for the stator current is employed.

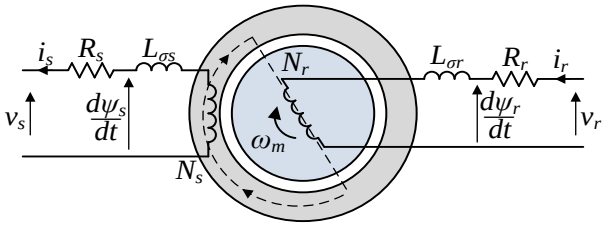

Fig. 4.2: Single-phase equivalent circuit of a DFIG.

The stator side of the DFIG is modeled in the stator reference frame using (2.15) which is repeated in (4.1).

$$\vec{v}_s = -R_s\vec{\imath}_s + \frac{d\vec{\psi}_s}{dt} \tag{4.1}$$

Rewriting (4.1), the stator flux linkage can be estimated using (4.2).

$$\hat{\vec{\psi}}_s = \int \left(\vec{v}_s + \hat{R}_s\vec{\imath}_s\right)dt \tag{4.2}$$

On the other hand, the stator flux linkage in the stator reference frame is given by (2.18) which is repeated in (4.3).

$$\vec{\psi}_s = -(L_s + L_{\sigma s})\vec{\imath}_s + L_m e^{-j\theta_m}\vec{\imath}_r \tag{4.3}$$

Rewriting (4.3), the rotor current can be estimated in the rotor reference frame using (4.4).

$$\hat{\vec{\imath}}_r = e^{j\hat{\theta}_m}\frac{\hat{\vec{\psi}}_s + \left(\hat{L}_s + \hat{L}_{\sigma s}\right)\vec{\imath}_s}{\hat{L}_m} \tag{4.4}$$

The adjustable model of the rotor current MRAS is defined by (4.4), while the reference model is simply the measured rotor current.

The error function for the rotor current MRAS is defined by (4.5).

$$\varepsilon_r = \frac{\hat{\vec{\imath}}_r \times \vec{\imath}_r}{\|\vec{\imath}_r\|^2} \tag{4.5}$$

Based on the previous study, the block diagram of the rotor current MRAS is depicted in Fig. 4.3.

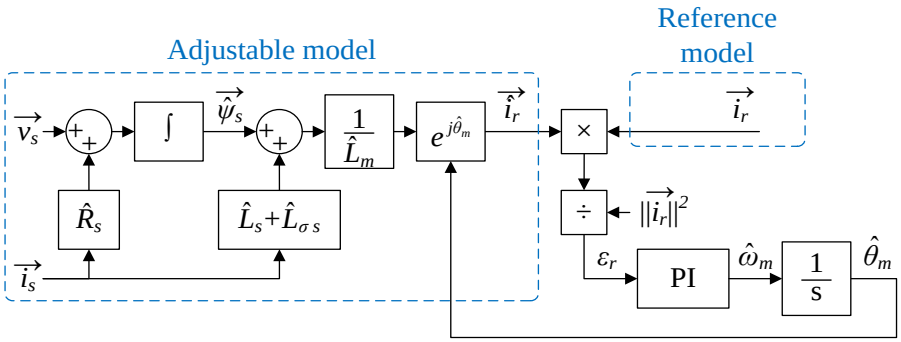

Fig. 4.3: Block diagram of the rotor current MRAS observer.

The rotor current MRAS observer requires three parameters which are the stator winding resistance, the mutual inductance, and the stator inductance. In addition, it requires estimating an intermediate quantity which is the stator flux linkage.

The stator flux linkage is estimated by integrating the stator voltage. The integrator is sensitive to any offset in the voltage or the current sensor which can drive the integrator into saturation. To solve this problem additional filters are needed. Moreover, the integrator output depends on the initial condition.

To reduce the number of DFIG parameters and eliminate the need for an intermediate quantity, we have proposed a new slip angle estimator.

4.2.2 Proposed Slip Angle Estimator

A. Concept

In designing most estimators, the T-equivalent circuit of the DFIG is used, where all variables are referred to the stator side. In this case, the DFIG's turns ratio is

implicitly multiplied by the rotor voltage, current and flux. Thus, the turns ratio is implicitly needed. In order to explicitly show the turns ratio, we will adopt the transformer-equivalent circuit.

The proposed estimator is based on estimating the rotor current in the synchronous reference frame (dq-frame). The transformer-equivalent circuit of the DFIG in this reference frame is shown in Fig. 4.4.

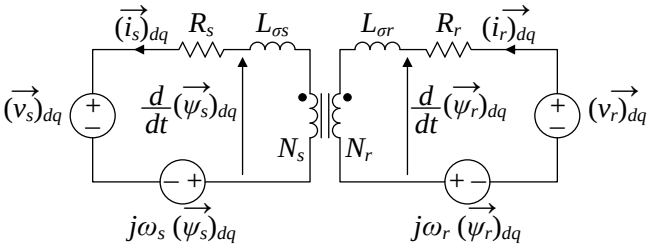

Fig. 4.4: Equivalent circuit of the DFIG in the dq-frame.

The voltage equation across the stator side is given by (4.6). During steady-state the derivative term is zero, which simplifies the model as shown in (4.7).

$$(\vec{v}_s)_{dq} = -R_s(\vec{\imath}_s)_{dq} + j\omega_s\left(\vec{\psi}_s\right)_{dq} + \frac{d\left(\vec{\psi}_s\right)_{dq}}{dt} \tag{4.6}$$

$$(\vec{v}_s)_{dq} = -R_s(\vec{\imath}_s)_{dq} + j\omega_s\left(\vec{\psi}_s\right)_{dq} \tag{4.7}$$

The stator flux linkage in the dq-frame is given by (4.8).

$$\left(\vec{\psi}_s\right)_{dq} = -(L_s + L_{\sigma s})(\vec{\imath}_s)_{dq} + L_m(\vec{\imath}_r)_{dq} \tag{4.8}$$

Substituting (4.8) into (4.7), we get (4.9) which can be used to estimate the rotor current in the dq-frame. This estimation does not require any knowledge of the DFIG's rotor current or the DFIG's rotor position.

$$(\vec{\imath}_r)_{dq} = \frac{(\vec{v}_s)_{dq} + \left(R_s + j\omega_s(L_s + L_{\sigma s})\right)(\vec{\imath}_s)_{dq}}{j\omega_s L_m} \tag{4.9}$$

Although (4.9) does not require the stator flux linkage, it still requires three DFIG parameters. To reduce the number of parameters, we introduce a new vector, X, which is

parallel to the rotor current in the dq-frame as shown in (4.10). This vector is estimated instead of estimating the rotor current. This does not affect the estimator's performance because both vectors are parallel and have the same angle.

$$\vec{X} = k \cdot (\vec{\imath}_r)_{dq} \tag{4.10}$$

To reduce the number of parameters, the scaling factor *k*, in (4.10), is chosen equal to the mutual impedance as in (4.11).

$$k = \omega_s L_m \tag{4.11}$$

Substituting (4.11) and (4.10) into (4.9), the vector X is estimated using (4.12), which requires two parameters.

$$\vec{X} = \left(-j\hat{R}_s + \omega_s\left(\hat{L}_s + \hat{L}_{\sigma s}\right)\right)(\vec{\imath}_s)_{dq} - j(\vec{v}_s)_{dq} \tag{4.12}$$

For medium and large DFIGs, the stator winding resistance is very small compared with the stator impedance, and it is always ignored. In this case, the number of DFIG parameters is reduced to only one parameter which is the stator inductance as shown in (4.13).

$$\vec{X} = \omega_s\left(\hat{L}_s + \hat{L}_{\sigma s}\right)(\vec{\imath}_s)_{dq} - j(\vec{v}_s)_{dq} \tag{4.13}$$

The stator inductance is the inductance seen from the stator side, and it is the sum of the stator leakage and self-inductance. This inductance can be measured directly at the stator side under nominal operating condition, which enable the estimator to use real machine parameters.

In the proposed slip angle estimator, the reference model is the estimated vector X, where the reference angle is the slip angle corresponding to the vector X. The adjustable model is the measured rotor current when, using the estimated slip angle, it is expressed in the dq-frame, which is denoted by an *e* superscript.

The cross product between the output of the reference model and of the adjustable model is given by (4.14), where δ_r is the slip angle error or, in other words, the difference between the reference slip angle and the estimated slip angle.

$$\vec{X} \times \left(\vec{\imath}_r{}^{e}\right)_{dq} = \left\|\vec{X}\right\| \cdot \left\|\left(\vec{\imath}_r{}^{e}\right)_{dq}\right\| \sin(\delta_r) \tag{4.14}$$

The error function is defined as the normalized cross product as in (4.15).

$$\varepsilon_r = \frac{\vec{X} \times \left(\vec{\imath}_r{}^{e}\right)_{dq}}{\left\|\vec{X}\right\| \cdot \left\|\left(\vec{\imath}_r{}^{e}\right)_{dq}\right\|} = \sin(\delta_r) \tag{4.15}$$

When the error ε_r is fed to a properly tuned PI controller, it will generate an estimation of the slip angular frequency $\hat{\omega}_r$ which will generate an estimation of the slip angle $\hat{\theta}_r$ when fed to an integrator. The block diagram of the proposed slip angle estimator is shown in Fig. 4.5.

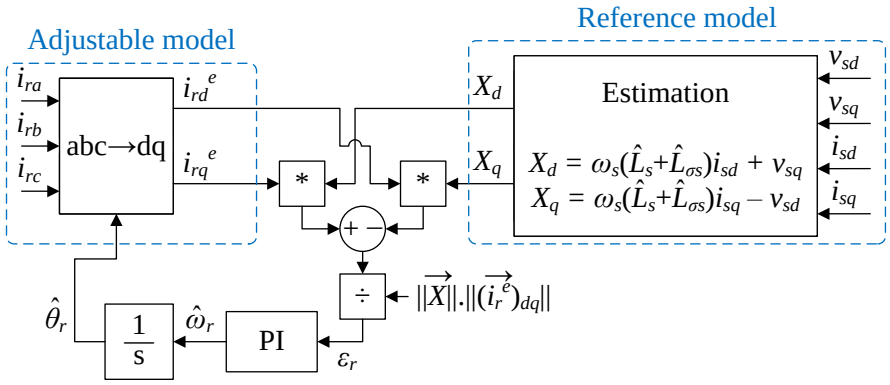

Fig. 4.5: Block diagram of the proposed slip angle estimator.

B. Controller Design

The simplified nonlinear control model of the proposed slip angle estimator is depicted in Fig. 4.6. In this model, the effect of the sampling delay, distortion of the stator voltages and currents, and the effect of the DFIG's poorly damped poles located near the line frequency are neglected.

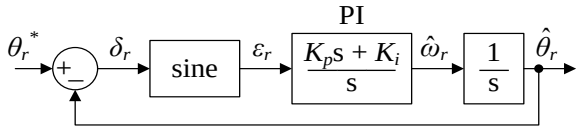

Fig. 4.6: Control model of the proposed estimator.

For small variation around the reference angle, the sine function can be approximated by a unity gain as in (4.16).

$$\varepsilon_r = \sin(\delta_r) \approx \delta_r \tag{4.16}$$

Then, the PI parameters selection procedure is similar to that of the stator voltage

PLL circuit in section 3.1.1, and it is briefly presented.

The transfer function of the small signal model is given by (4.17).

$$\frac{\hat{\theta}_r}{\delta_r} = \frac{K_p s + K_i}{s^2} \tag{4.17}$$

To simplify the previous transfer function, new parameters are introduced as in (4.18), and the transfer function using these parameters is given by (4.19)

$$\begin{cases} K_i = {\omega_k}^2 \\ K_p = \alpha \cdot \omega_k \end{cases} \tag{4.18}$$

$$\frac{\hat{\theta}_r}{\delta_r} = \frac{{\omega_k}^2}{s^2}\left(\alpha \frac{s}{\omega_k} + 1\right) \tag{4.19}$$

The frequency in (4.19) is normalized to ω_k, and the different performance criteria, such as the rise time, becomes function of α only. The variation of the normalized bandwidth and the overshoot are depicted in Fig. 4.7 as functions of α.

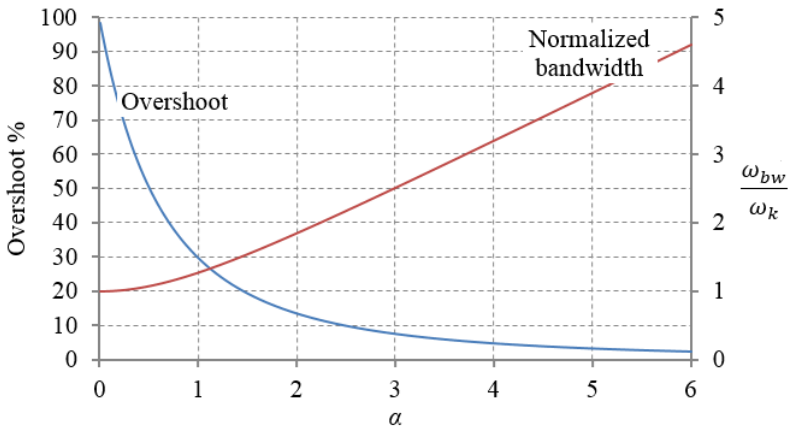

Fig. 4.7: The overshoot and the normalized bandwidth of the proposed estimator.

Using the desired overshoot, the value of α and the normalized bandwidth are determined from Fig. 4.7. Then, using the desired bandwidth, the value of ω_k is obtained. Using the values of α and ω_k, the PI's parameters are selected.

The error function implemented using the cross product is nonlinear and non-monotonic, which can result in an oscillatory transient response of the estimated slip frequency especially during fast transition of the DFIG's speed.

To achieve fast, non-oscillatory transient response without using the inverse tangent function of [22], the proposed estimator is designed with a relatively wide bandwidth. The bandwidth, however, must be smaller than the line frequency to reduce the effect of the DFIG's poorly damped poles.

In this work, the overshoot was selected around 12% which corresponds to α equals 2.2, and the normalized bandwidth is equal to 2. The open-loop bandwidth is selected around eight times smaller than the line angular frequency, 45 rad/s; consequently ω_k is 22.5 rad/s. Then, the PI parameters are $K_p \approx 50$ and $K_i \approx 500$.

Since the bandwidth is relatively large, the estimator attenuation at the DFIG's poorly damped poles is relatively low, and we would expect some ripples in the steady-state response of the estimated slip frequency and angle.

4.3 Sensitivity Analysis

The proposed estimator ignores the stator winding resistance, and it uses the stator inductance for estimating the slip angle. The stator inductance is affected by the grid voltage amplitude due to saturation. Consequently, the estimator will operate with mismatched value of the DFIG parameters. Thus, it is important to investigate the effect of parameter mismatch on the accuracy of the proposed estimator.

4.3.1 Mathematical Analysis

The stator inductance inaccuracy ΔL_s, which is defined by (4.20), is the difference between the correct value of the stator inductance and the value used by the proposed estimator. The stator impedance inaccuracy is defined by (4.21)

$$\Delta L_s = (L_s + L_{\sigma s}) - \left(\hat{L}_s + \hat{L}_{\sigma s}\right) \tag{4.20}$$

$$\Delta Z_s = \omega_s \Delta L_s \tag{4.21}$$

Substituting (4.21) and (4.9) into (4.13), the vector X is given by (4.22), where Z_m is the mutual impedance $Z_m = \omega_s L_m$.

$$\vec{X} = Z_m(\vec{\imath}_r)_{dq} + jR_s(\vec{\imath}_s)_{dq} - \Delta Z_s(\vec{\imath}_s)_{dq} \tag{4.22}$$

The ignored stator winding resistance and the stator inductance inaccuracy produce an estimation error $\Delta\theta_r$ which is defined by (4.23).

$$\Delta\theta_r = \theta_r - \hat{\theta}_r \tag{4.23}$$

The output of the adjustable model, which is the dq-transformation of the measured rotor current using the erroneously estimated slip angle, is related to the correct value of the rotor current in the dq-frame by (4.24).

$$\left(\vec{\imath}_r{}^{e}\right)_{dq} = e^{j\Delta\theta_r}(\vec{\imath}_r)_{dq} \tag{4.24}$$

Substituting (4.24) into (4.22), the vector X is given by (4.25).

$$\vec{X} = Z_m e^{-j\Delta\theta_r}\left(\vec{\imath}_r{}^{e}\right)_{dq} + jR_s(\vec{\imath}_s)_{dq} - \Delta Z_s(\vec{\imath}_s)_{dq} \tag{4.25}$$

Since the PI control in Fig. 4.5 forces the error function to zero, the cross product in (4.14) is equal to zero in the steady-state. Then, an expression for the estimation error can be obtained by substituting (4.25) into (4.14), and it is given by (4.26), where the θ_{is} is the angle of the stator current in the dq-frame and $\theta_{ir}{}^{e}$ is the angle of the output of the adjustable model.

$$\begin{aligned} &Z_m\|\vec{\imath}_r\|^2\sin(\Delta\theta_r) - R_s\|\vec{\imath}_r\|\|\vec{\imath}_s\|\cos(\theta_{ir}{}^{e} - \theta_{is}) \\ &- \Delta Z_s\|\vec{\imath}_r\|\|\vec{\imath}_s\|\sin(\theta_{ir}{}^{e} - \theta_{is}) = 0 \end{aligned} \tag{4.26}$$

Equation (4.26) can be written as in (4.27).

$$\sin(\Delta\theta_r) = \frac{R_s}{Z_m}\frac{\|\vec{\imath}_s\|}{\|\vec{\imath}_r\|}\cos(\theta_{ir}{}^{e} - \theta_{is}) + \frac{\Delta Z_s}{Z_m}\frac{\|\vec{\imath}_s\|}{\|\vec{\imath}_r\|}\sin(\theta_{ir}{}^{e} - \theta_{is}) \tag{4.27}$$

In (4.27), the estimation error is independent of the stator inductance inaccuracy, if the angle of the rotor current $\theta_{ir}{}^{e}$ is equal to the angle of the stator current θ_{is} or have a difference equal to ±180 degrees.

Equation (4.27) is difficult to analyze because the estimation error is present in both sides of the equation. The angle $\theta_{ir}{}^{e}$ implicitly contains the estimation error as can be seen when referring to (4.24). Equation (4.27) can be written as in (4.28).

$$\sin(\Delta\theta_r) - \frac{R_s}{Z_m}\frac{\|\vec{\imath}_s\|}{\|\vec{\imath}_r\|}\cos(\theta_{ir} - \theta_{is} + \Delta\theta_r) - \frac{\Delta Z_s}{Z_m}\frac{\|\vec{\imath}_s\|}{\|\vec{\imath}_r\|}\sin(\theta_{ir} - \theta_{is} + \Delta\theta_r) = 0 \tag{4.28}$$

Solving (4.28), the estimation error can be calculated as in (4.29), where the variable n is zero or one depending on the sign of the denominator being positive or negative respectively as in (4.30).

$$\Delta\theta_r = \tan^{-1}\left[\frac{\frac{R_s}{Z_m}\frac{\|\vec{\imath}_s\|}{\|\vec{\imath}_r\|}\cos(\theta_{ir}-\theta_{is}) + \frac{\Delta Z_s}{Z_m}\frac{\|\vec{\imath}_s\|}{\|\vec{\imath}_r\|}\sin(\theta_{ir}-\theta_{is})}{1+\frac{R_s}{Z_m}\frac{\|\vec{\imath}_s\|}{\|\vec{\imath}_r\|}\sin(\theta_{ir}-\theta_{is}) - \frac{\Delta Z_s}{Z_m}\frac{\|\vec{\imath}_s\|}{\|\vec{\imath}_r\|}\cos(\theta_{ir}-\theta_{is})}\right] + n\pi \qquad (4.29)$$

$$n = \begin{cases} 0 \; if \; \text{sign}\left(1+\frac{R_s}{Z_m}\frac{\|\vec{\imath}_s\|}{\|\vec{\imath}_r\|}\sin(\theta_{ir}-\theta_{is}) - \frac{\Delta Z_s}{Z_m}\frac{\|\vec{\imath}_s\|}{\|\vec{\imath}_r\|}\cos(\theta_{ir}-\theta_{is})\right) \geq 0 \\ 1 \quad otherwise \end{cases} \qquad (4.30)$$

4.3.2 Effect of the Stator Winding Resistance R_s

For medium and large DFIGs, the stator winding resistance is very small compared to the stator impedance and is always ignored. For small DFIGs, the stator winding resistance is not negligible compared to the stator impedance. In either case, ignoring the stator winding resistance would produce an estimation error that need to be determined.

To simplify the analysis, the stator inductance is assumed to be accurate, that is ΔL_s is zero. The effect of stator winding resistance on the estimation error is investigated for different rotor d- and q-currents using (4.29) and (4.30). The main parameters of the experimental DFIG are listed in Table 4.1

Table 4.1: DFIG's parameters and rated values.

Parameter	Value	Unit
Power Rating	1.1	kW
Stator line-to-line voltage	210	V_{RMS}
Frequency	60	Hz
Number of poles	6	
Stator resistance R_s	0.475	Ω
Rotor resistance R_r	0.04	Ω
Stator leakage inductance $L_{\sigma s}$	7.43	mH
Rotor leakage inductance $L_{\sigma r}$	0.18	mH
Magnetizing inductance L_m	11.2	mH
Stator-to-rotor turns ratio	6.38	

The estimation error for different rotor d- and q-currents are shown in Fig. 4.8.

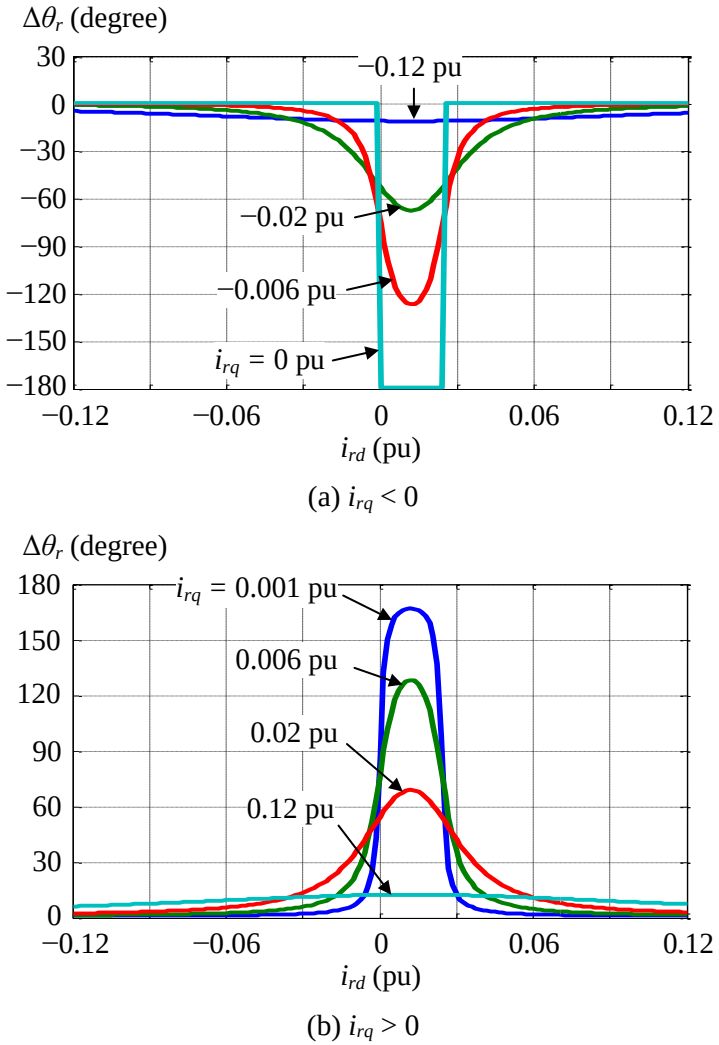

Fig. 4.8: The estimation error for different rotor currents with $\Delta L_s = 0$ and $R_s = 0.5\ \Omega$.

In Fig. 4.8, the rotor current is displayed in per unit (pu), where the base value is 19.3 A_{RMS} and, in the dq-frame, it is 33.4 A.

From Fig. 4.8, ignoring the stator winding resistance produces an estimation error which varies with the rotor d- and q-current. When the rotor currents are small, this estimation error is very large (above ±90 degrees) and can cause the decoupled control to become unstable as was concluded in Chapter 3. However, when the rotor currents are not small, the estimation error is negligible.

The parameters in Table 3.1 are for a small DFIG of only 1.1 kW. For medium and large DFIGs, the stator winding resistance is much smaller. Thus, the estimation error is calculated for a stator resistance of 0.2 Ω, and the results are shown in Fig. 4.9.

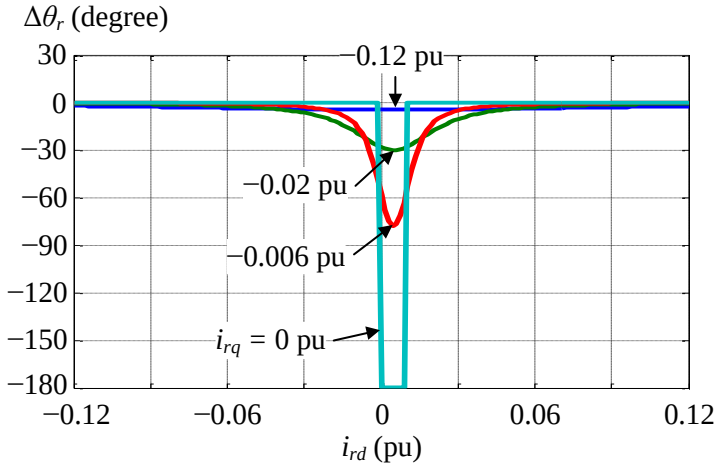

(a) $i_{rq} \leq 0$

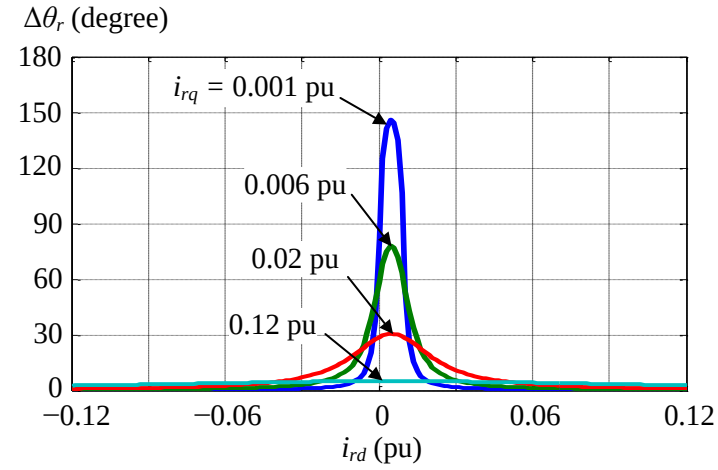

(b) $i_{rq} > 0$

Fig. 4.9: The estimation error for different rotor currents with $\Delta L_s = 0$ and $R_s = 0.2\ \Omega$.

From Fig. 4.9, for medium and large DFIGs, the estimation error resulting from the stator winding resistance and the unstable region become smaller.

4.3.3 Effect of the Stator Inductance Inaccuracy ΔL_s

Assuming the value of the stator winding resistance to be fixed, the estimation error in (4.29) is a function of three variable which are the stator inductance inaccuracy and the rotor d- and q-current. Consequently, in the following analysis, one variable is fixed and the other two variables are varied.

First, the stator inductance inaccuracy is fixed, and the effect of the rotor d- and q-current on the estimation error is investigated. The stator inductance inaccuracy is fixed to 0.2 of the inductance value, $\Delta L_s = 0.2\ L_s$. In this case, the estimation error as a

function of the rotor d- and q-current is shown in Fig. 4.10.

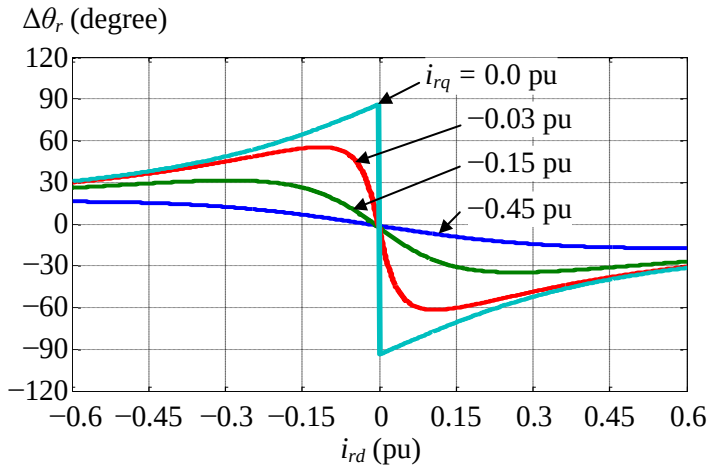

(a) $i_{rq} \leq 0$

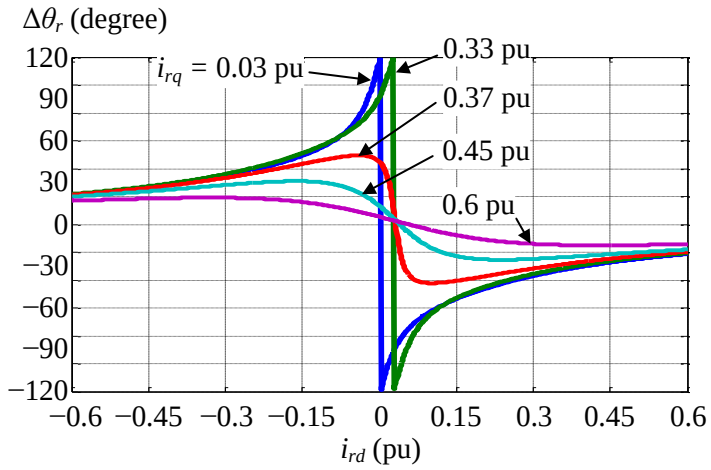

(b) $i_{rq} > 0$

Fig. 4.10: The estimation error for different rotor currents with $\Delta L_s / L_s = 0.2$.

We observer that, when the rotor q-current is negative, but not zero, the estimation error is within the stable region of the decoupled control, which is slightly above ±90 degrees. Generally speaking, the estimation error decreases as the rotor d-and q-current increase; however, around zero this is not true.

The estimation error initially increases as the rotor d-current increases before it starts to decrease. The estimation error increases as the rotor q-current increases from zero. Then, it is almost unaffected by the increase of the rotor q-current between 0.03 pu to 0.33 pu; beyond this interval, the estimation error decreases as the rotor q-current increases.

Next, the stator inductance inaccuracy is fixed to −0.2 of the inductance value, $\Delta L_s = -0.2\ L_s$, and the estimation error, in this case, is shown in Fig. 4.11.

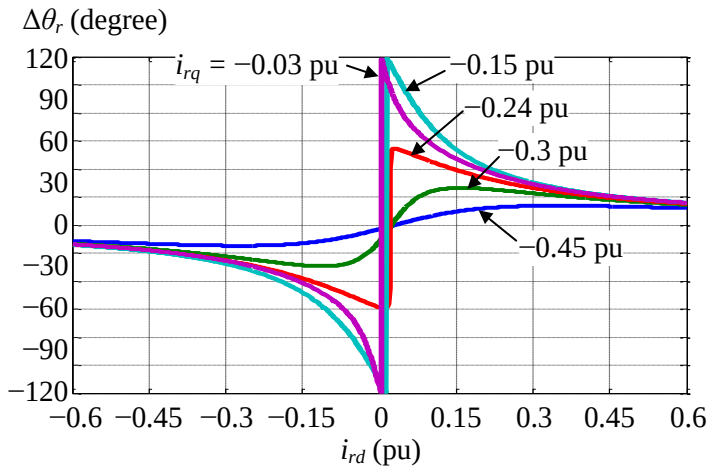

(a) $i_{rq} < 0$

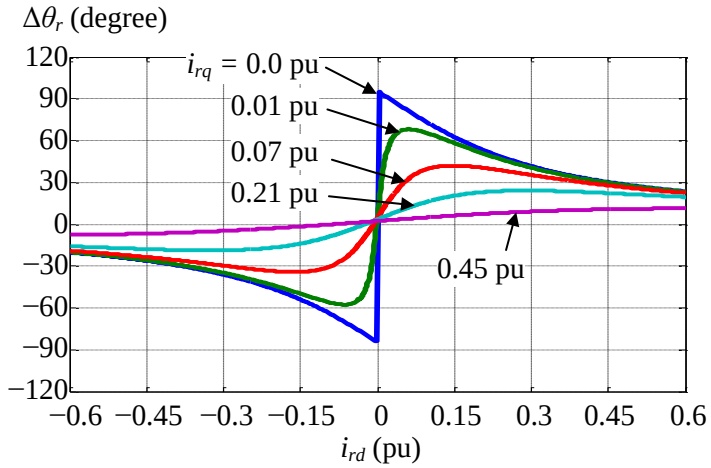

(b) $i_{rq} \geq 0$

Fig. 4.11: The estimation error for different rotor currents with $\Delta L_s / L_s = -0.2$.

Similar results to that of Fig. 4.10 are obtained in Fig. 4.11, but the sign of the estimation error and of the rotor q-current are reversed. In this case, the estimation error is within the stable region of the decoupled control when the rotor q-current is positive, but not zero.

The effect of a larger stator inductance inaccuracy, $\Delta L_s = 0.4\ L_s$, is investigated, and the estimation error is shown in Fig. 4.12.

In principle, the results in Fig. 4.12 are similar to Fig. 4.10. However, the estimation error is larger for the same rotor d- and q-current. The estimation error is still

within the stable region of the decoupled control when the rotor q-current is negative.

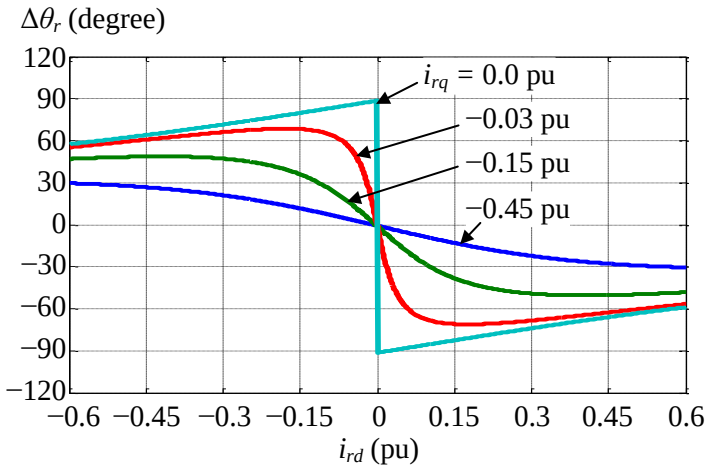

(a) $i_{rq} \leq 0$

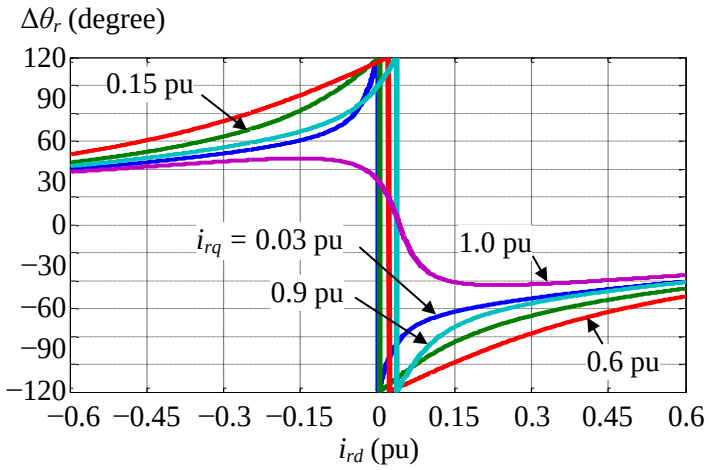

(b) $i_{rq} > 0$

Fig. 4.12: The estimation error for different rotor currents with $\Delta L_s / L_s = 0.4$.

For positive rotor q-current, with larger stator inductance inaccuracy, the region where the estimation error is almost unaffected by the increasing rotor q-current is wider.

Next, the rotor d-current is fixed to zero, and the estimation error is considered as a function of the stator inductance inaccuracy. In this case, the estimation error is shown in Fig. 4.13 for several rotor q-currents.

The results in Fig. 4.13, demonstrate that when the stator inductance inaccuracy is in opposite sign with the rotor q-current, the estimation error is within the stable region of the decoupled control regardless of the stator inductance inaccuracy. This makes the

proposed estimator very robust under such condition. In addition, the estimation error decreases as the rotor q-current increases.

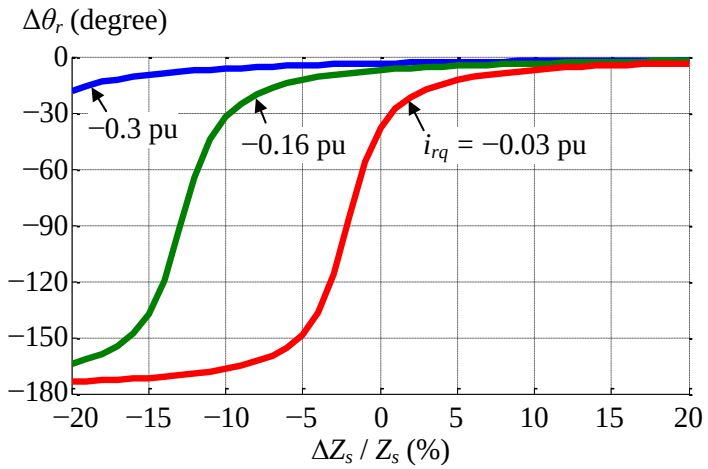

(a) $i_{rq} < 0$

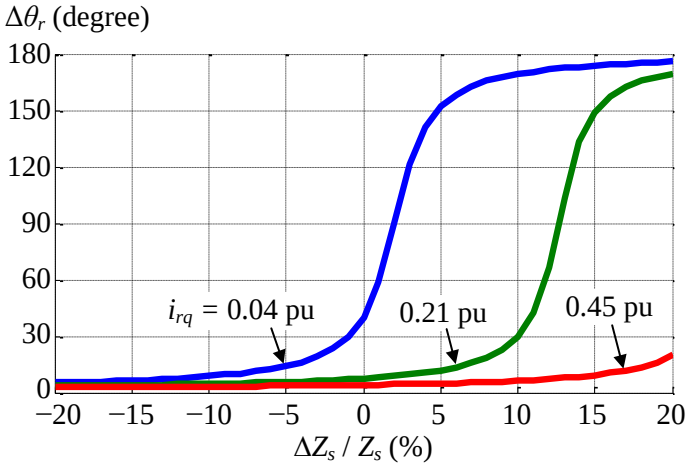

(b) $i_{rq} > 0$

Fig. 4.13: The estimation error as a function of the stator inductance inaccuracy with $i_{rd} = 0$.

Finally, the rotor q-current is fixed to zero, and the estimation error is considered as a function of the stator inductance inaccuracy. The estimation error in this case is shown in Fig. 4.14 for several values of the rotor d-current.

Fig. 4.14 shows that the estimation error decreases as the rotor d-current increases. In addition, the estimation error is within the stable region of the decoupled control regardless of the stator inductance inaccuracy; this, however, is true as long as the estimation error is below 100%.

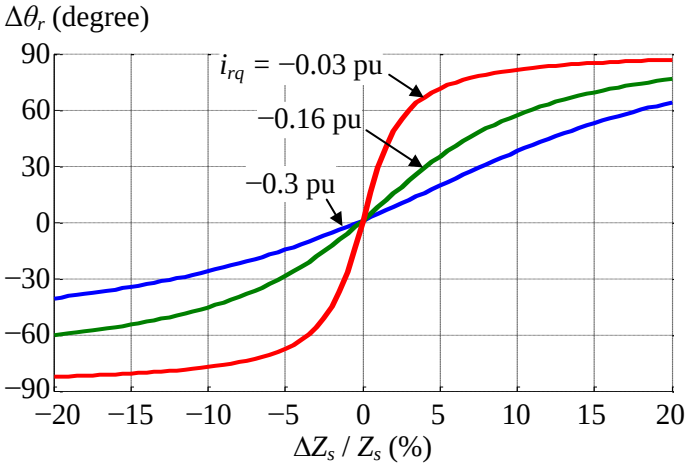

(a) $i_{rd} < 0$

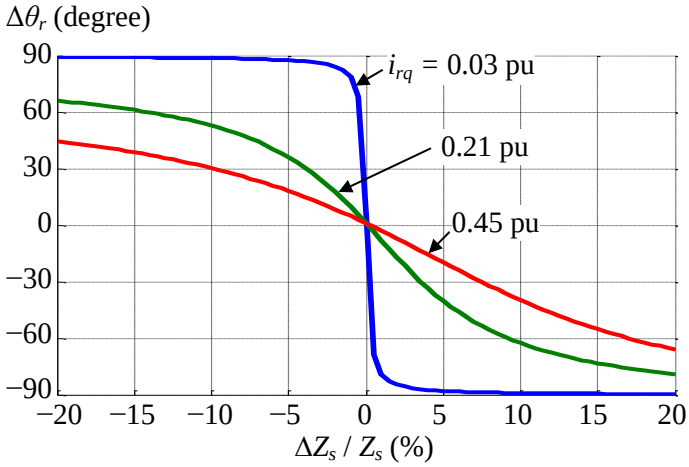

(b) $i_{rd} > 0$

Fig. 4.14: The estimation error as a function of the stator inductance inaccuracy with $i_{rq} = 0$.

4.4 Simulation and Experiments

4.4.1 Experimental Setup

The parameters of the DFIG were listed in Table 3.1 and in Table 4.1. The schematic diagram of the experimental setup is depicted in Fig. 4.15. The parameters of this circuit were listed in Table 3.2. The grid-connected control system of chapter 3, which was depicted in Fig. 3.20 is equipped with the proposed slip angle estimator to obtain the slip angle. The parameters of the grid-connected control system were given in Table 3.2. The PI parameters of the proposed slip angle estimator are $K_p = 50$ and $K_i = 500$.

Several tests are carried out under different conditions to investigate the performance of the proposed estimator and to evaluate its accuracy by comparing it with the measured slip angle.

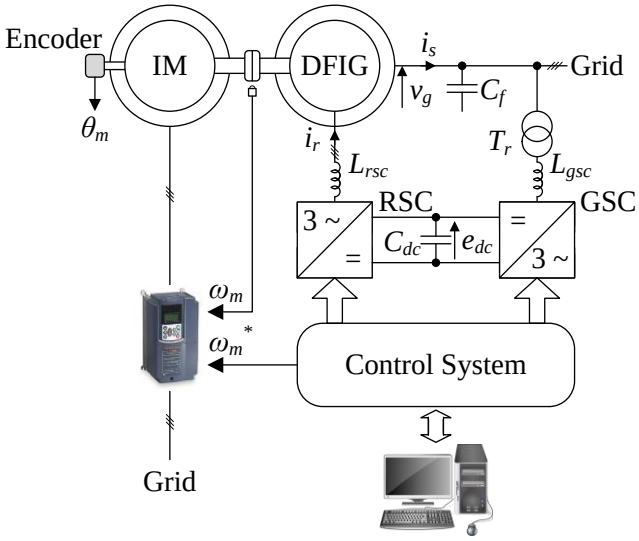

Fig. 4.15: Block diagram of the experimental setup.

4.4.2 Simulation Results

First, the starting on the fly of the system with the proposed estimator is investigated. In this test, the DFIG is rotating while it is connected to the grid. Initially, the back-to-back converter and the grid-connected control, except for the PLL circuit of Fig. 3.2, are disabled. Then, at 1.1 sec they are suddenly enabled. This test is similar to a step response of the slip frequency and the slip angle. Several starting on the fly tests are carried out for different rotor d- and q-currents.

In the first test, the DFIG's speed is fixed at a sub-synchronous speed of 0.9 pu. The active and reactive power references are fixed at 0 W and −1300 VAR respectively; this produces small rotor d- and q-current of $i_{rd}^e = 0$ A and $i_{rq}^e = -1.6$ A respectively. The results for this test are shown in Fig. 4.16.

Referring to Fig. 4.16, the proposed estimator can start on the fly even with such small rotor current which produces an estimation error of around −27 degrees. This estimation error is caused by the ignored stator winding resistance. This can be proved by noticing that the angle $\theta_{ir}^e - \theta_{is}$ is equal to −180 degrees and, according to (4.27), the estimation error in this case is negative and is caused by the ignored stator winding resistance.

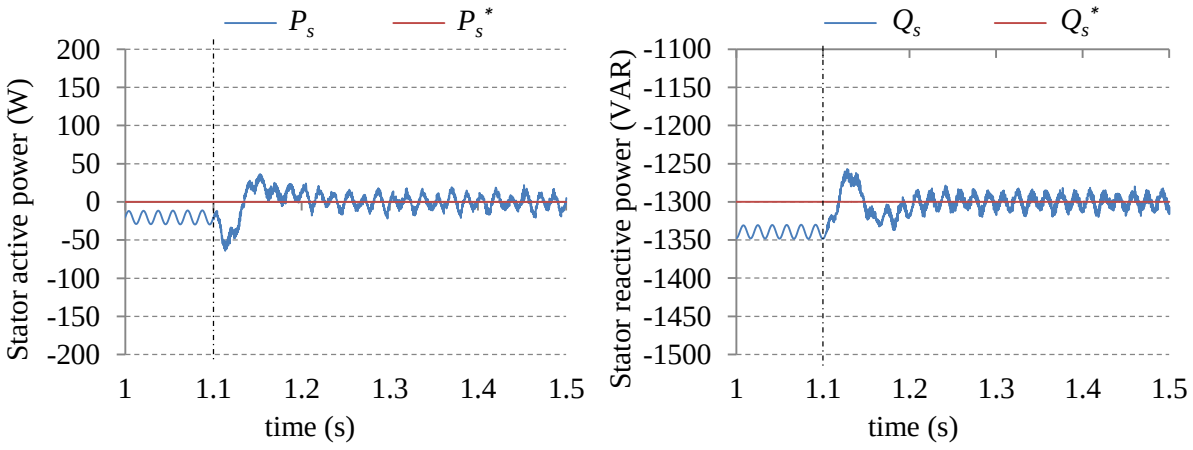

(a) Stator active power

(b) Stator reactive power

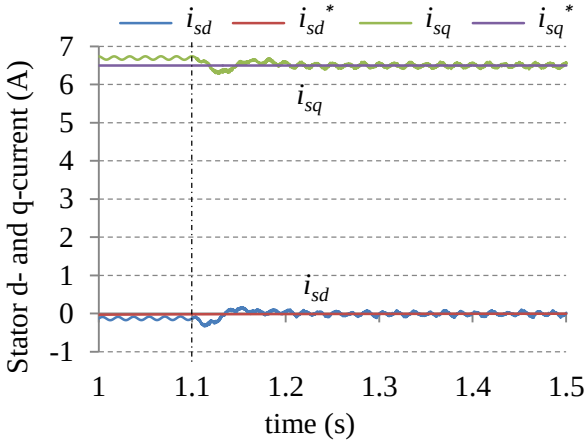

(c) Stator d- and q-current

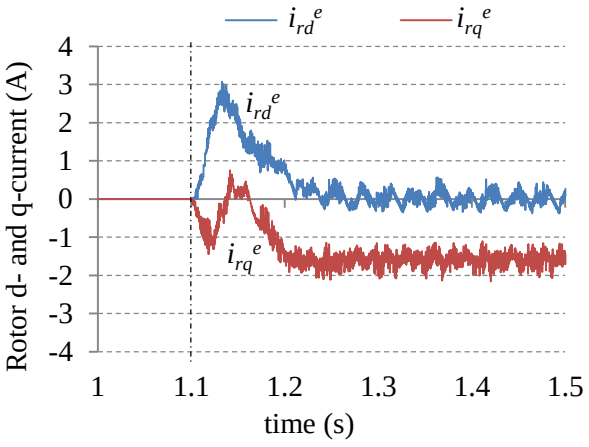

(d) Rotor d- and q-current

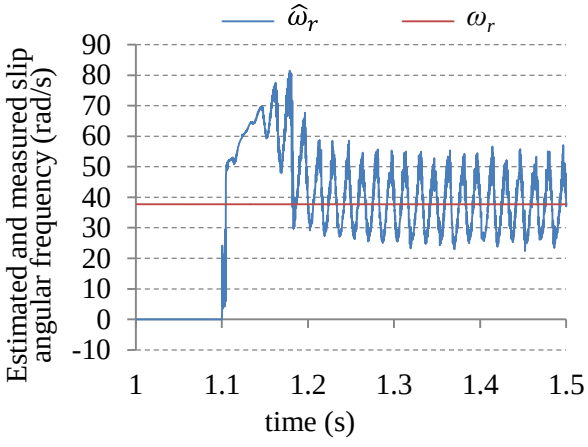

(e) Estimated and measured slip angular frequency

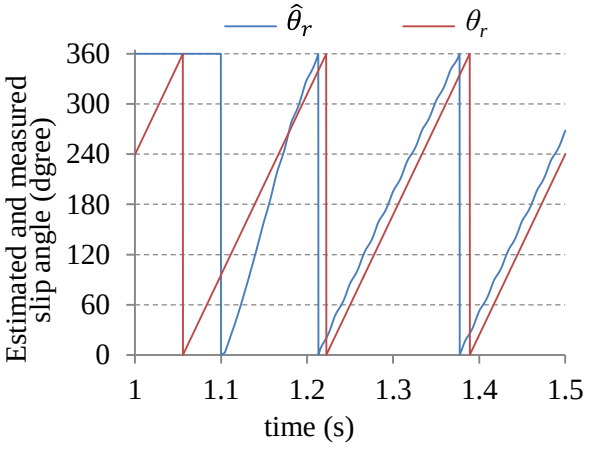

(f) Estimated and measured slip angle

Fig. 4.16: Simulation results for starting on the fly with P_s^* = 0 W, Q_s^* = −1300 VAR, and ω_m = 0.9 pu.

In addition, there are relatively large ripples on the estimated slip angular frequency which results from the wide bandwidth of the proposed estimator.

The second test is similar to the first one but this time the reactive power reference is fixed at −1300 VAR. This produces rotor d- and q-current of i_{rd}^{e} = 0 A and i_{rq}^{e} = 6 A respectively. The results for this test are shown in Fig. 4.17.

Referring to Fig. 4.17, the estimation error, which is 8.4 degrees, is smaller because the rotor current is larger. Since the angle $\theta_{ir}^{e} - \theta_{is}$ is now equal to 180 degrees the estimation error, which is caused by the stator winding resistance, is positive. We also notice that the ripples of the estimated slip angular frequency are smaller in this test.

In the third test, the DFIG speed is fixed at a hyper-synchronous speed of 1.1 pu. The active and reactive power references are chosen equal to 100 W and −1340 VAR respectively. These references produces rotor d- and q-current of i_{rd}^{e} = 4 A and i_{rq}^{e} = 0 A respectively. The results of this test are shown in Fig. 4.18.

In this case, the angle $\theta_{ir}^{e} - \theta_{is}$ is very close to –90 degrees and, according to (4.27), the estimation error is caused by the stator inductance inaccuracy only. Since the proposed estimator is using the correct value of the stator inductance, the estimation error is very close to zero.

Considering the amplitude of the ripples in the estimated slip angular frequency, they seem to depend on the amplitude of the rotor current. As the rotor current increases, these ripples decreases and vice versa.

In the final starting on the fly test, the DFIG speed is fixed at a sub-synchronous speed of 0.8 pu. The active and reactive power references are fixed to 600 W and −1000 VAR respectively, which produces large rotor d- and q-current of i_{rd}^{e} = 22 A and i_{rq}^{e} = −12 A respectively. The results for this test are shown in Fig. 4.19.

Since the rotor d- and q-currents are relatively large, the effect of the stator winding resistance is negligible and the estimation error is almost zero. In addition, the ripples of the estimated slip angular frequency is very small.

The previous starting on the fly tests support the results of the sensitivity analysis, and demonstrate the ability of the proposed estimator to start on the fly within shot time. It should be mentioned that if the initial slip angle error is larger, the transient response could become oscillatory due to the nonlinear, non-monotonic error function.

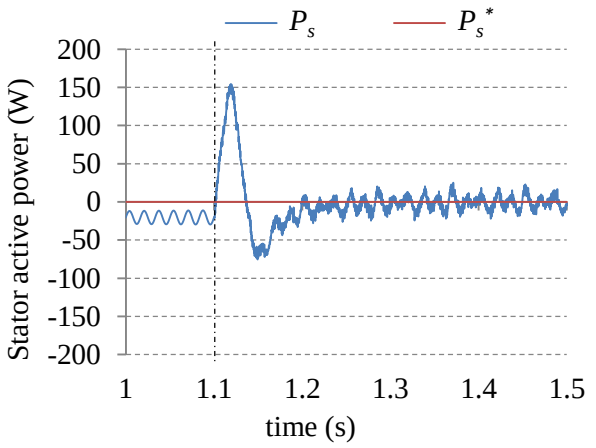

(a) Stator active power

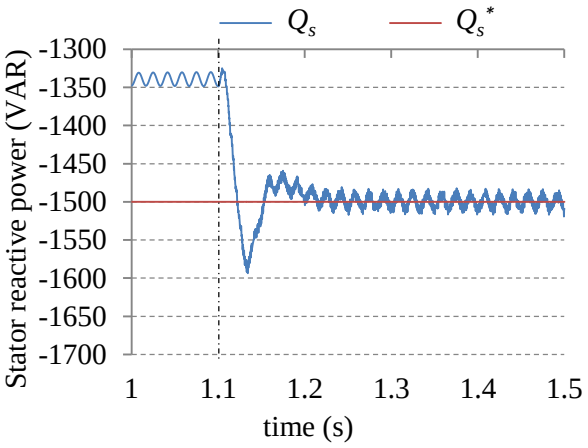

(b) Stator reactive power

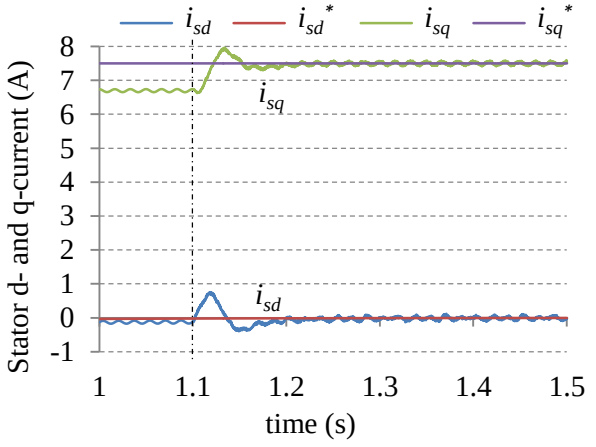

(c) Stator d- and q-current

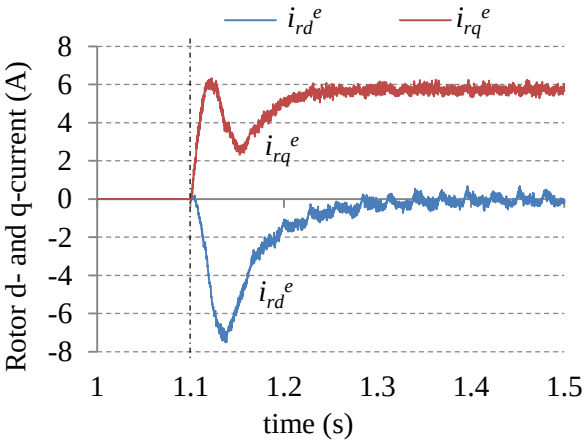

(d) Rotor d- and q-current

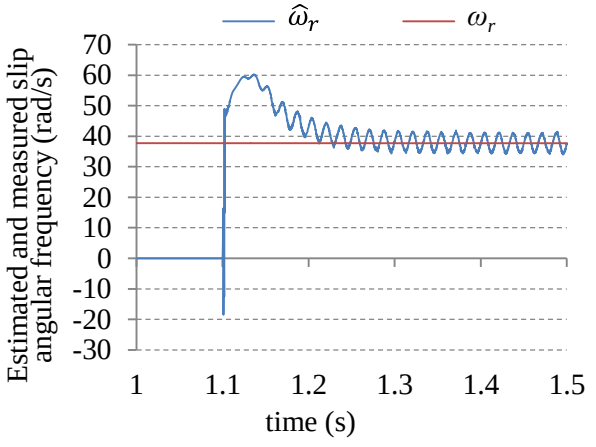

(e) Estimated and measured slip angular frequency

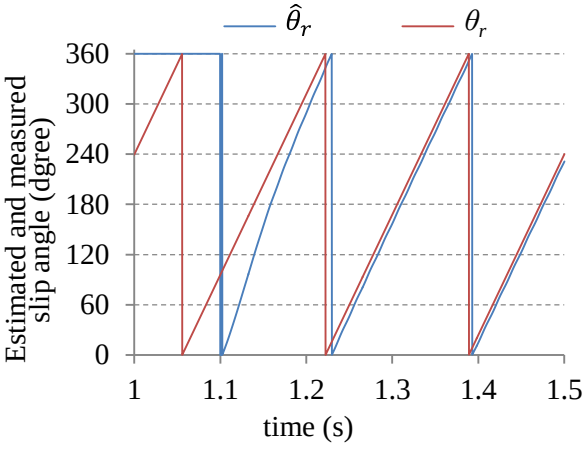

(f) Estimated and measured slip angle

Fig. 4.17: Simulation results for starting on the fly with P_s^* = 0 W, Q_s^* = −1500 VAR, and ω_m = 0.9 pu.

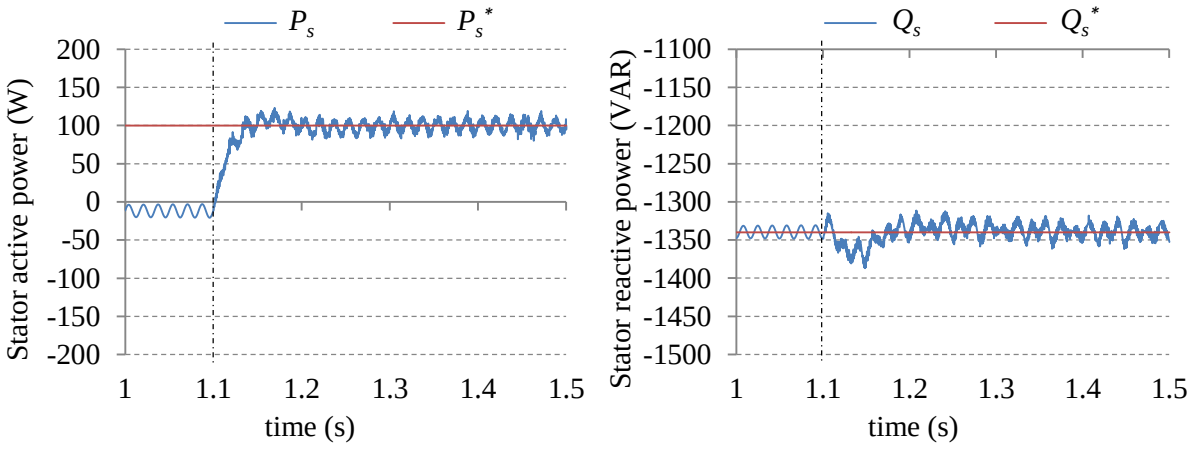

(a) Stator active power

(b) Stator reactive power

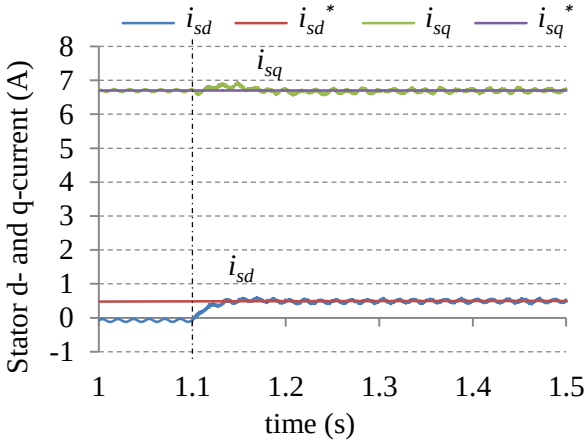

(c) Stator d- and q-current

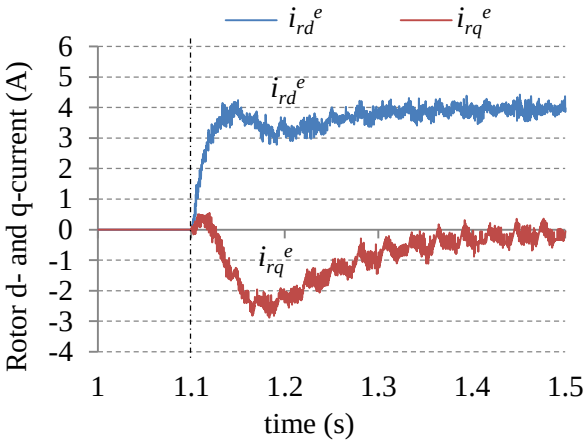

(d) Rotor d- and q-current

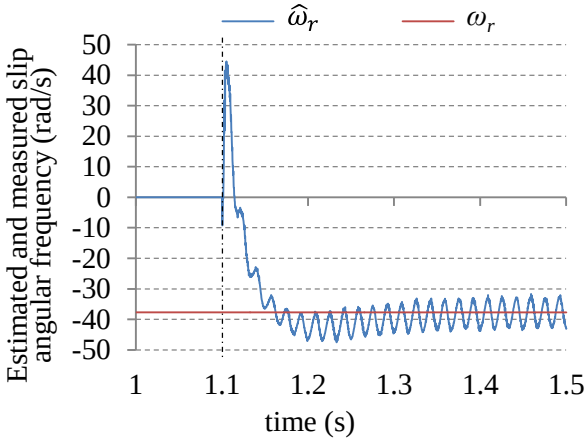

(e) Estimated and measured slip angular frequency

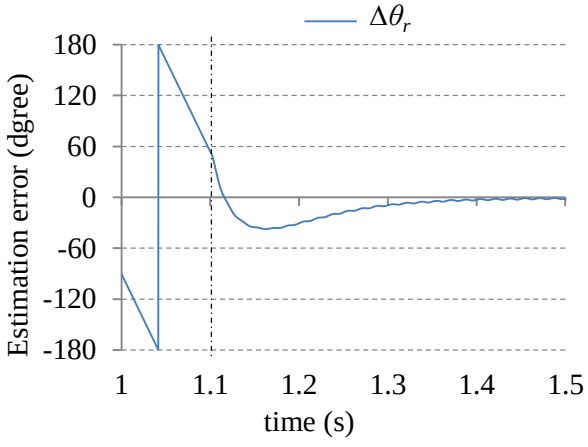

(f) Estimation error

Fig. 4.18: Simulation results for starting on the fly with P_s^* = 100 W, Q_s^* = −1340 VAR, and ω_m = 1.1 pu.

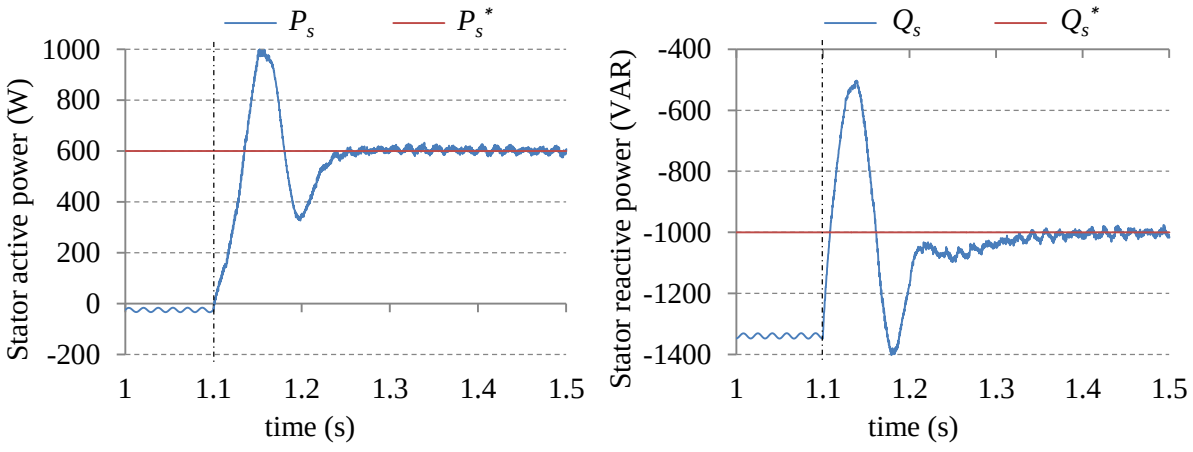

(a) Stator active power

(b) Stator reactive power

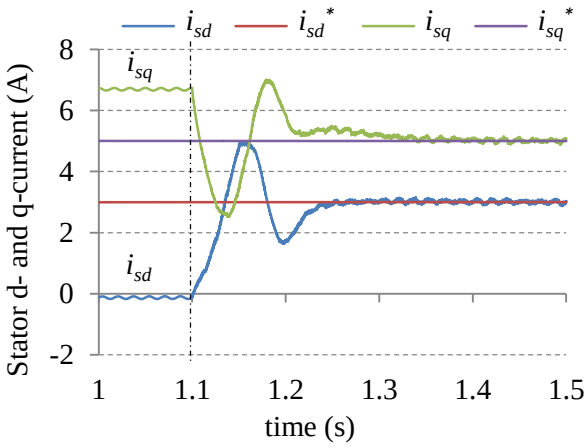

(c) Stator d- and q-current

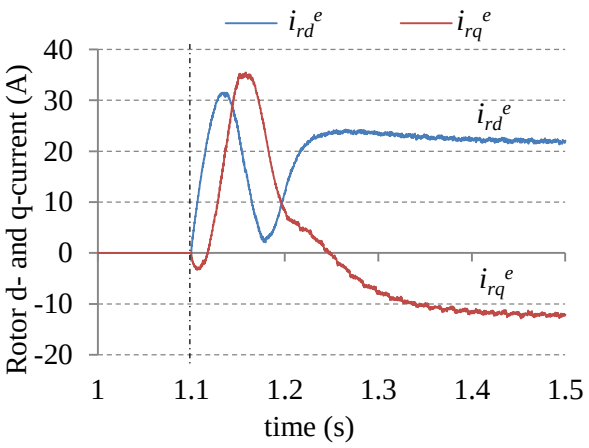

(d) Rotor d- and q-current

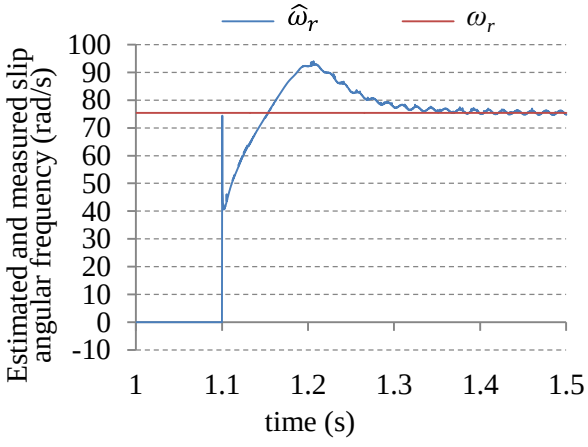

(e) Estimated and measured slip angular frequency

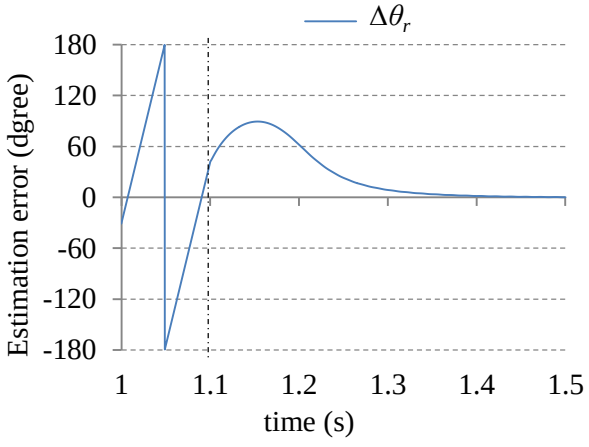

(f) Estimation error

Fig. 4.19: Simulation results for starting on the fly with P_s^* = 600 W, Q_s^* = −1000 VAR, and ω_m = 0.8 pu.

Next, the variable speed operation is considered. The DFIG speed is varied from a sub-synchronous speed of 0.75 pu to a hyper-synchronous speed of 1.25 pu within 0.8 sec. During this test, the active and reactive power references are fixed at 800 W and −1800 VAR respectively. The results for this test are shown in Fig. 4.20.

From the results in Fig. 4.20, the proposed estimator effectively tracks the slip frequency and slip angle. This enables the decoupled control to regulate the active and reactive power despite the fast speed variation. During the variable speed test, the estimation error increases because of the slip angle varies as a second order polynomial while the estimator's controller is designed to track a first order polynomial. This is a very well-known issue in control engineering.

The proposed estimator is designed using the steady-state model of the DFIG. Thus, it is important to investigate the effect of active and reactive power steps on the performance of the proposed estimator.

During this test, the active power reference is stepped between 0 W and 800 W, and the reactive power reference is stepped between −1200 VAR and −2000 VAR. The DFIG speed is fixed at a sub-synchronous speed of 0.8 pu. The results for this test are shown in Fig. 4.21.

From the results of Fig. 4.21, as the active and reactive power vary, the stator and the rotor d- and q-currents vary. Since the estimation error is affected by the stator and the rotor d- and q-currents, the estimation error also varies. Moreover, at 1.4 sec, the rotor d- and q-current become zero, this produces a relatively large transition in the estimated slip frequency and a relatively large estimation error. This, however, does not have a serious effect on the performance of the system, because the estimation error is well inside the stable region of the decoupled control.

Finally, the effect of the stator inductance inaccuracy on the performance of the proposed estimator is investigated. Two tests are carried out for this purpose.

First, the stator inductance inaccuracy is linearly increased from −50% to 50%, and the stator active and reactive power references are fixed at 0 W and −1800 VAR respectively; this produces a rotor d-current equal to zero (i_{rd} = 0 A), while the rotor q-current is positive, which corresponds to Fig. 4.13 (b). During this test, the DFIG speed is fixed at a sub-synchronous speed of 0.8 pu. The results for this test are shown in Fig. 4.22.

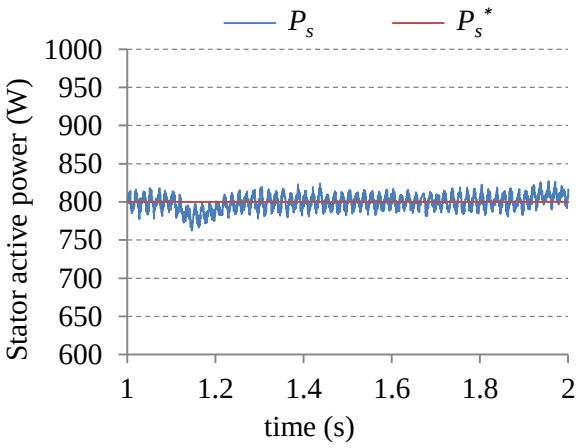

(a) Stator active power

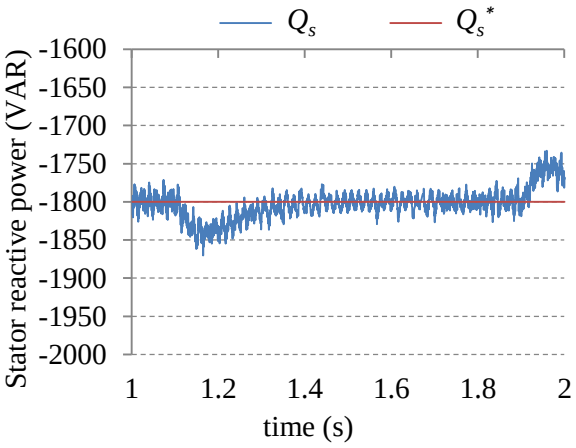

(b) Stator reactive power

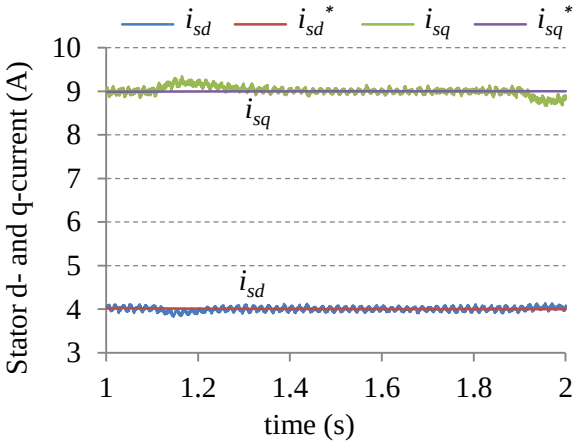

(c) Stator d- and q-current

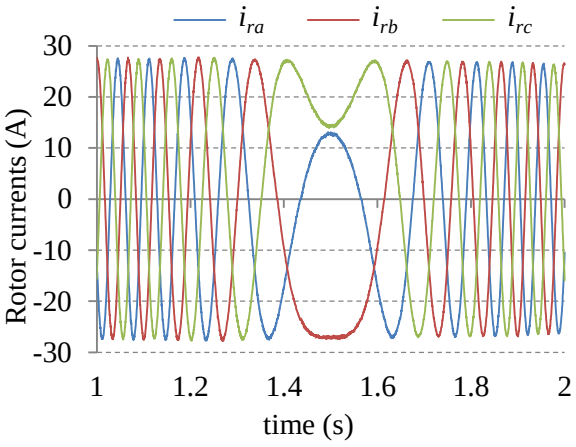

(d) Rotor currents

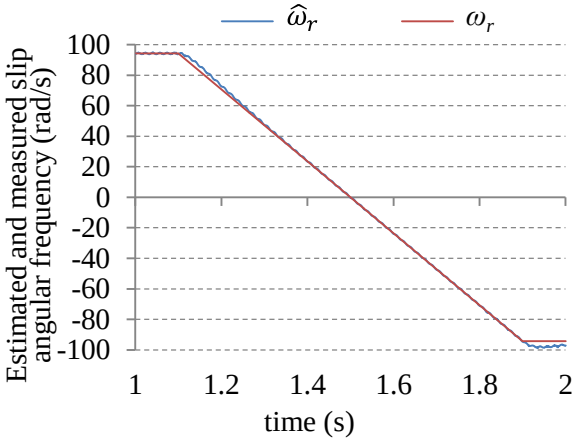

(e) Estimated and measured slip angular frequency

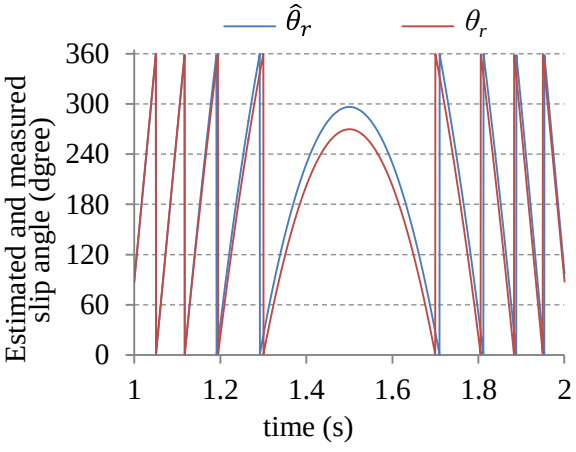

(f) Estimated and measured slip angle

Fig. 4.20: Simulation results for variable speed operation with P_s^* = 0 W and Q_s^* = −1500 VAR.

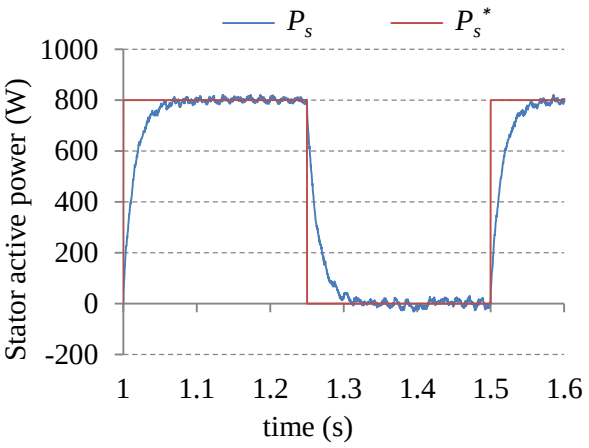

(a) Stator active power

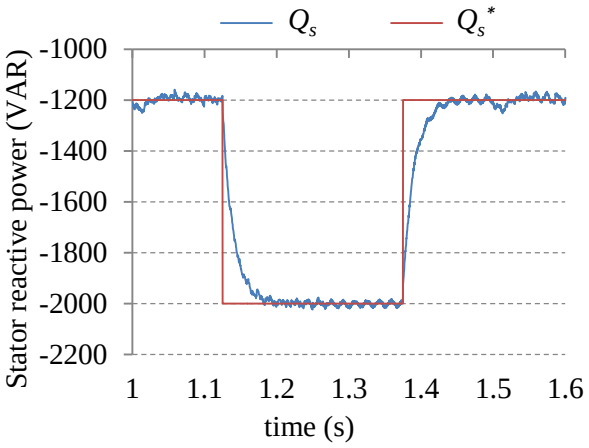

(b) Stator reactive power

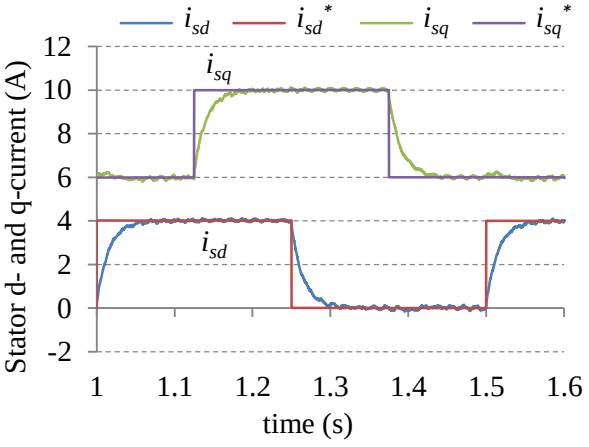

(c) Stator d- and q-current

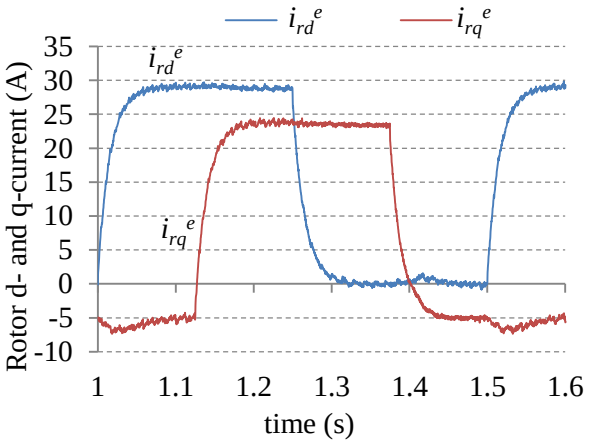

(d) Rotor d- and q-current

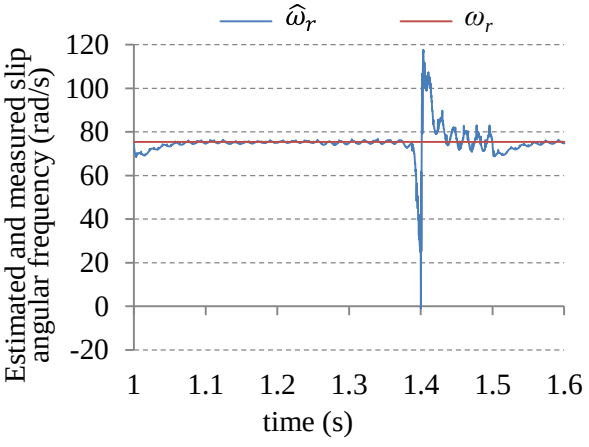

(e) Estimated and measured slip angular frequency

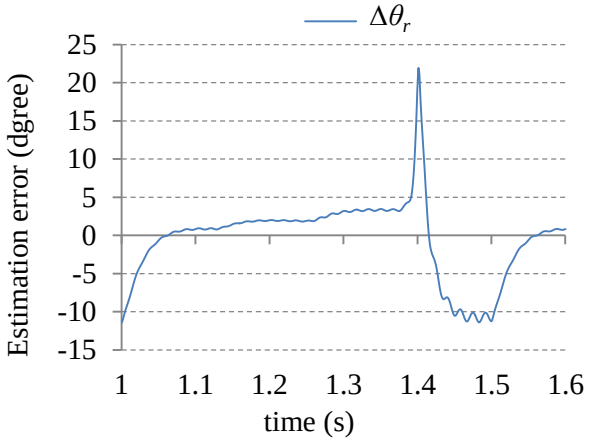

(f) Estimation error

Fig. 4.21: Simulation results for the effect of the power step response with ω_m = 0.8 pu.

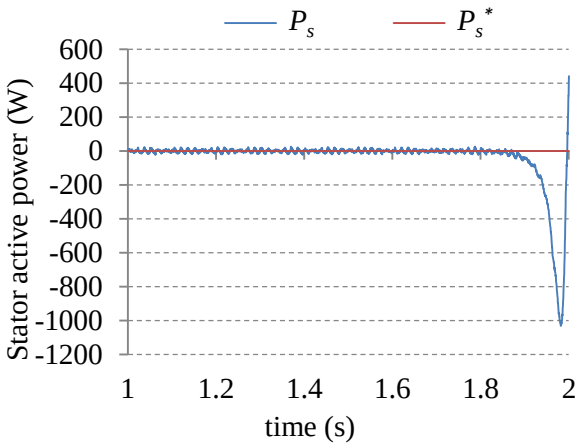

(a) Stator active power

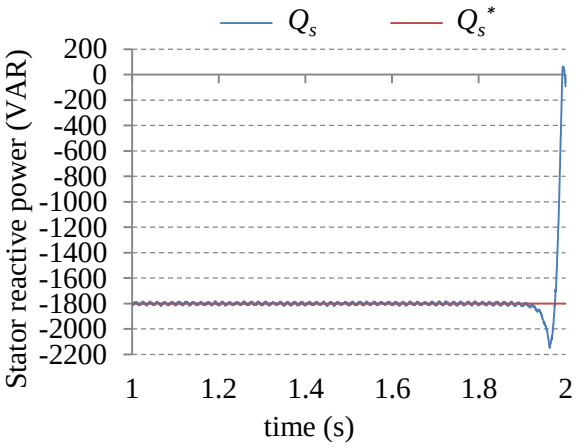

(b) Stator reactive power

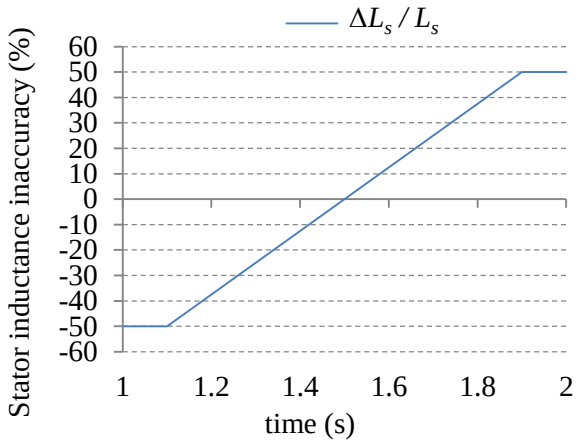

(c) Stator inductance inaccuracy

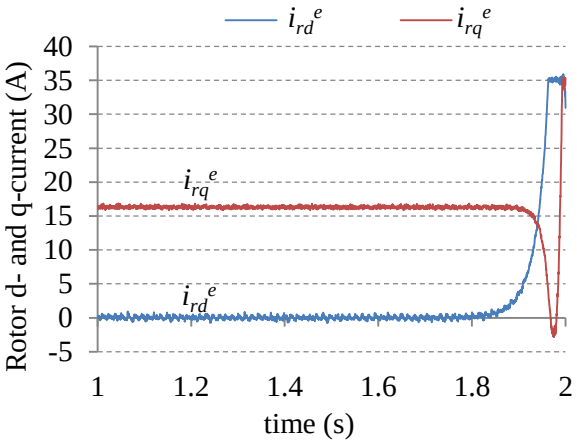

(d) Rotor d- and q-current

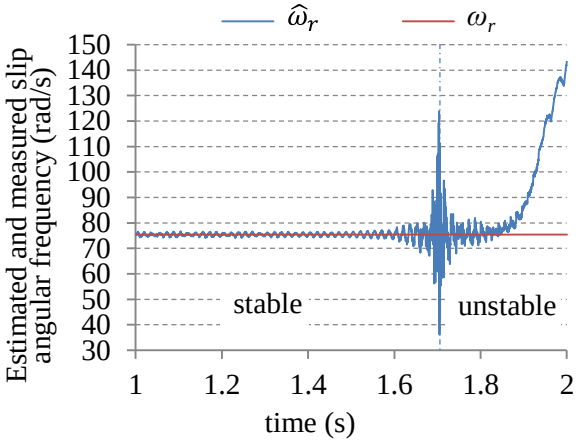

(e) Estimated and measured slip angular frequency

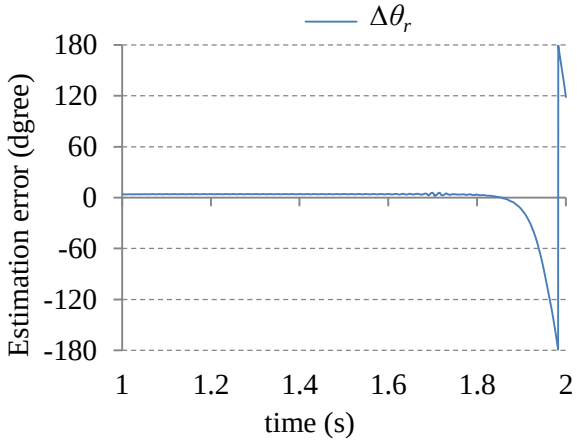

(f) Estimation error

Fig. 4.22: Simulation results for the effect of stator inductance inaccuracy with P_s^* = 0 W, Q_s^* = −1800 VAR (i_{rd} = 0 A), and ω_m = 0.8 pu.

The results of Fig. 4.22 comply with the results of the sensitivity analysis, Fig. 4.13 (b). The estimation error is very small and positive when the inaccuracy is negative. The estimation error is not affected by the stator inductance inaccuracy as long as it is under a certain threshold. Once the stator inductance inaccuracy reaches that threshold, the estimated slip frequency becomes extremely oscillatory while the slip angle is at the boundary of stability region of the decoupled control. Any further increase in the inductance inaccuracy will cause the decoupled control system becomes unstable.

Since the proposed estimator compares the angle between two vectors, it is stable as long as the rotor and the stator currents are stable. Once the decoupled control becomes unstable, the proposed estimator becomes unstable and the sensitivity analysis becomes invalid, because it is derived in steady-state.

Second, the stator inductance inaccuracy is linearly increased from −50% to 50%, while the stator active and reactive power references are fixed at 800 W and −1340 VAR respectively; this produces a rotor q-current equal to zero (i_{rq} = 0 A), while the rotor d-current is positive, which corresponds to Fig. 4.14 (b). During this test, the DFIG speed is fixed at a sub-synchronous speed of 0.8 pu. The results for this test are shown in Fig. 4.23. The results comply with the results in Fig. 4.14 (b). The system remains stable because the estimation error is within the stable region.

4.4.3 Experimental Results

Since the PLL circuit of Fig. 3.2 forces the stator q-voltage to zero, the active and reactive power are proportional to the stator d- and q-current respectively as in (3.19). Thus, instead of the stator active and reactive power, the stator d- and q-currents are shown in all following experiments.

First, the starting on the fly experiment is carried out. Similar to the simulation, during this test, the DFIG is connected to the grid and is rotating with a sub-synchronous speed of 0.9 pu, while the back-to-back converter and the control system, except for the PLL circuit, are disabled. At 0 sec, the back-to-back converter and the control system is suddenly enabled.

Two test for the starting on the fly are carried out: With small and relatively large rotor currents. In the first experiment, the stator d- and q-current references are fixed at 0 A and 7 A respectively. This produces rotor d- and q-current of i_{rd}^{e} = 0 A and i_{rq}^{e} = −4 A respectively. The results for this test are shown in Fig. 4.24.

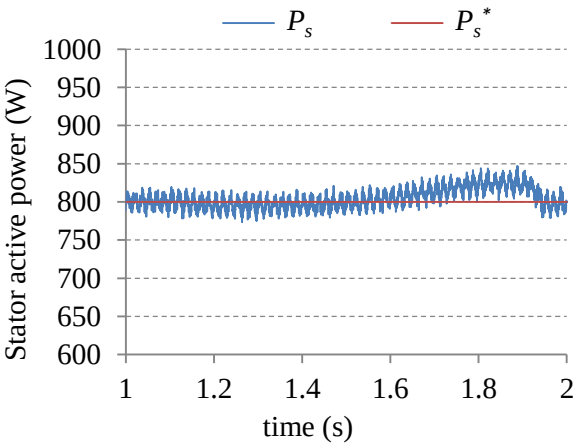

(a) Stator active power

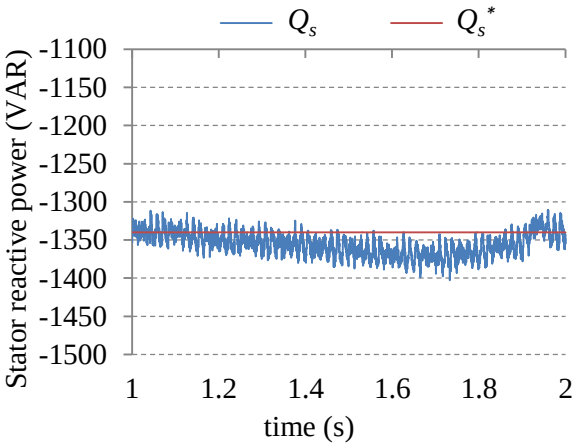

(b) Stator reactive power

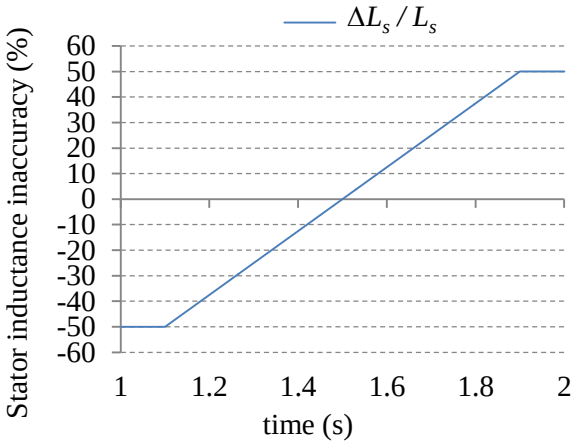

(c) Stator inductance inaccuracy

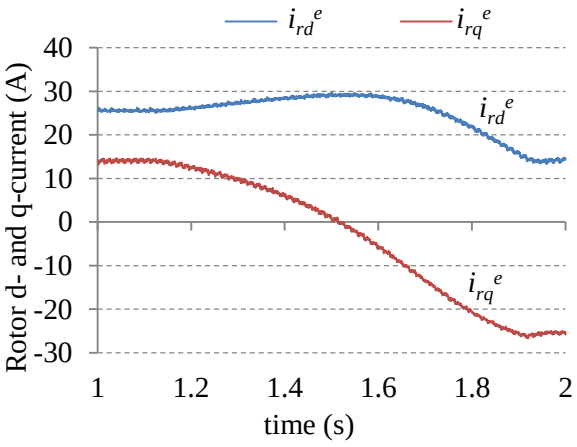

(d) Rotor d- and q-current

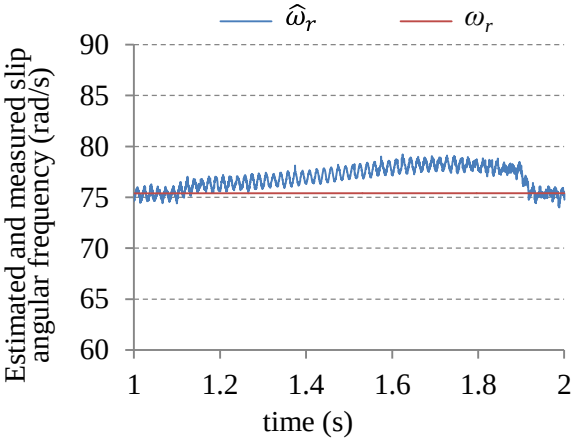

(e) Estimated and measured slip angular frequency

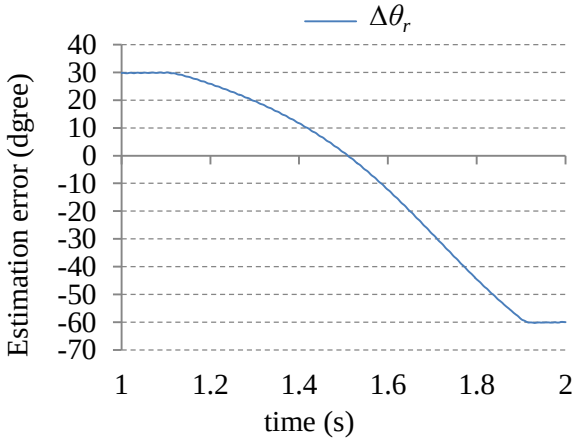

(f) Estimation error

Fig. 4.23: Simulation results for the effect of stator inductance inaccuracy with P_s^* = 800 W, Q_s^* = −1340 VAR (i_{rq} = 0 A), and ω_m = 0.8 pu.

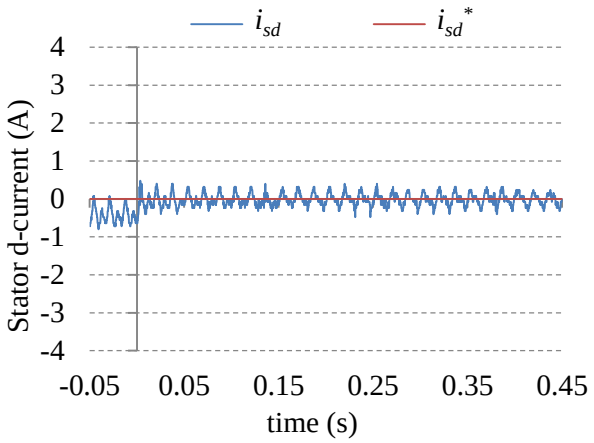

(a) Stator d-current

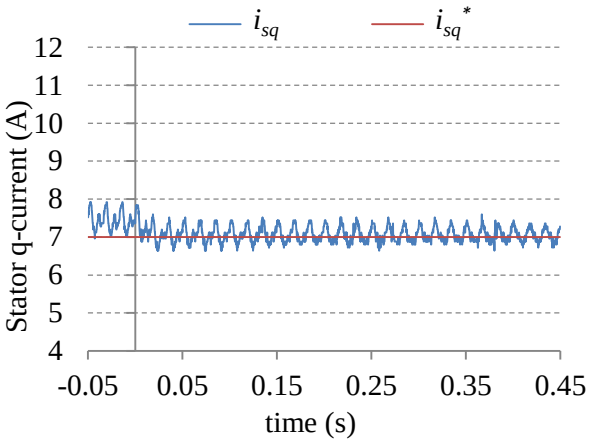

(b) Stator q-current

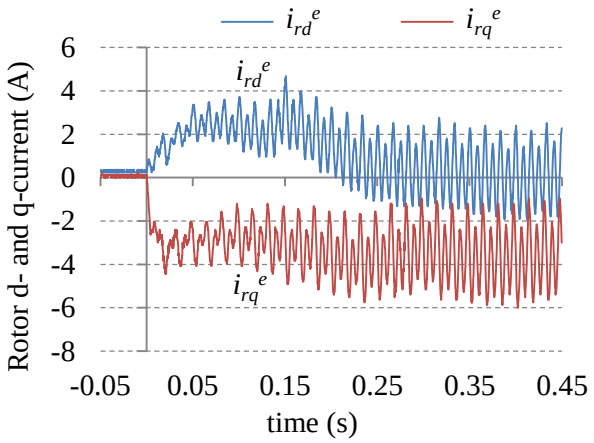

(c) Rotor d- and q-current

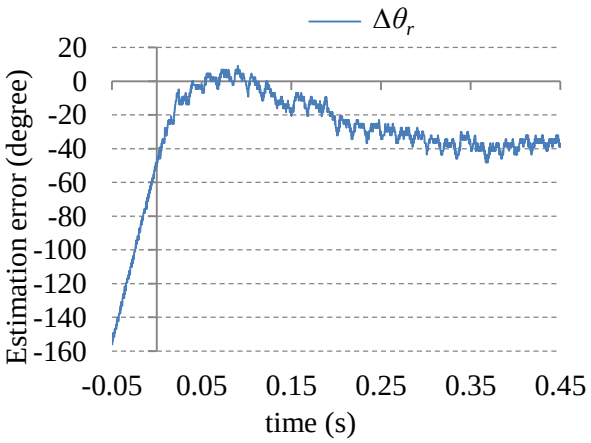

(d) Estimation error

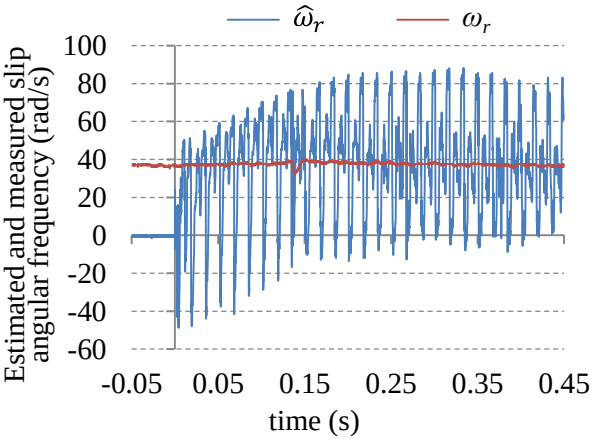

(e) Estimated and measured slip angular frequency

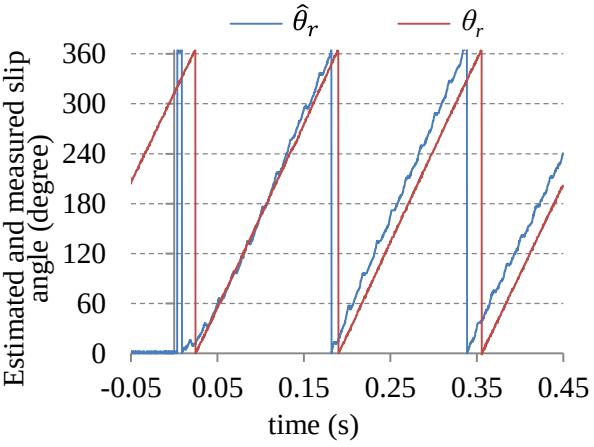

(f) Estimated and measured slip angle

Fig. 4.24: Experimental results for starting on the fly with i_{sd}^* = 0 A, i_{sq}^* = 7 A, and ω_m = 0.9 pu.

Referring to Fig. 4.24, the proposed estimator can start on the fly even with small rotor current. Compared with the simulation, the results are similar except for the estimation error which is larger at around −40 degrees.

Since this estimation error is caused by the stator winding resistance, we expect that the actual value of the stator winding resistance to be larger than its standard value. When measured, it was found three times larger than its value in Table 4.1.

In the second starting on the fly test, the stator d- and q-current references are fixed to 3 A and 6 A respectively. This produces relatively large rotor d- and q-current of i_{rd}^{e} = 22 A and i_{rq}^{e} = −12 A respectively. The results for this test are shown in Fig. 4.25.

Referring to Fig. 4.25, with large rotor currents, the estimation error is very small, and the ripples of the estimated slip angular frequency are smaller.

There is a transient decrease of the DFIG speed when the system starts on the fly in Fig. 4.24; this is caused by the sudden increase of the electrical torque and the transient response of the prime mover's torque which is normal in practical systems.

Second, the variable speed operation is investigated. The DFIG speed is varied from a sub-synchronous speed of 0.8 pu to a hyper-synchronous speed of 1.2 pu within 1 sec. During this test the stator d- and q-current references are fixed at 2 A and 7 A respectively. The results for this test are shown in Fig. 4.26.

The results of the variable speed operation in Fig. 4.26 are similar to the simulation results. The proposed estimator effectively tracks the slip frequency and angle, which enables the decoupled control to regulate the stator d- and q-current and consequently the active and reactive power.

Next, the effect of the step response of the active and reactive power on the estimator is investigated. During this test, the reference speed is fixed at a hyper-synchronous speed of 1.1 pu. The stator d-current reference is stepped between 0 A and 4 A, while the rotor q-current reference is stepped between 4 A and 8 A. The results for this test are shown in Fig. 4.27.

The estimation error and the amplitude of ripples of the estimated slip angular frequency varies as the stator and rotor d- and q-currents vary. Since the estimation error is well inside the stable region, the performance of the system is not affected.

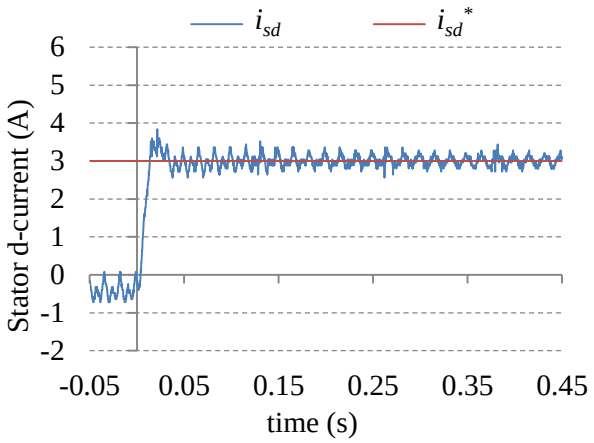

(a) Stator d-current

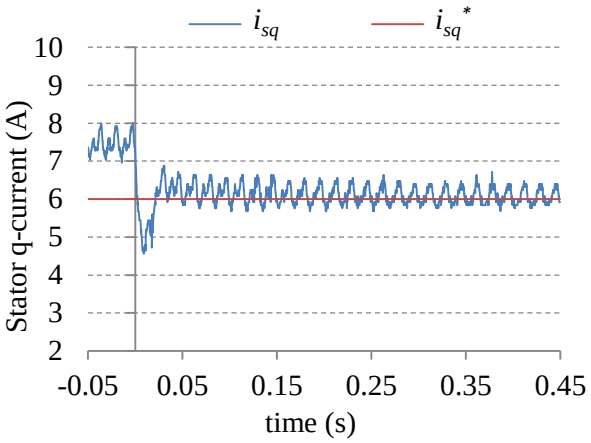

(b) Stator q-current

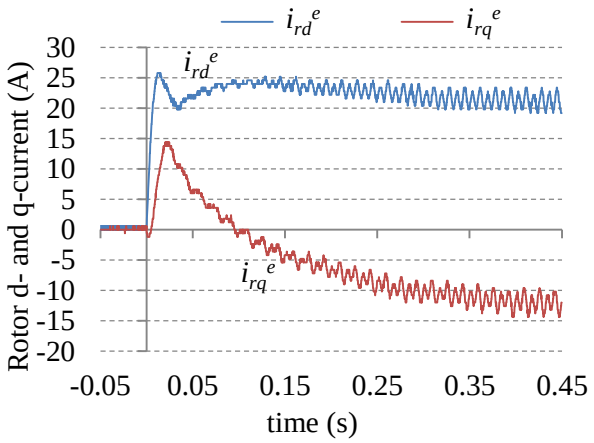

(c) Rotor d- and q-current

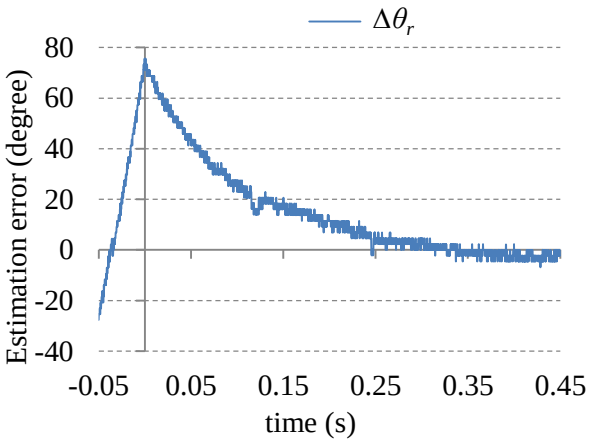

(d) Estimation error

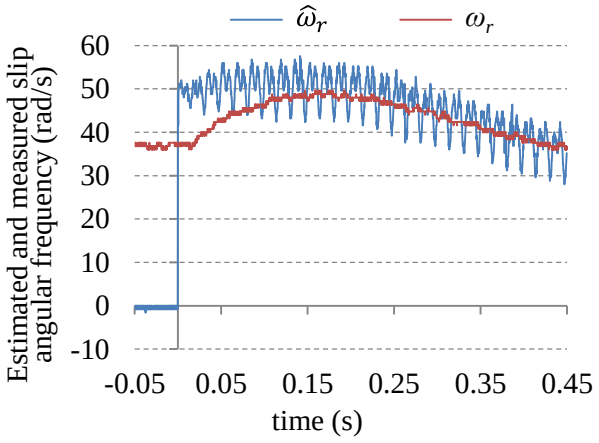

(e) Estimated and measured slip angular frequency

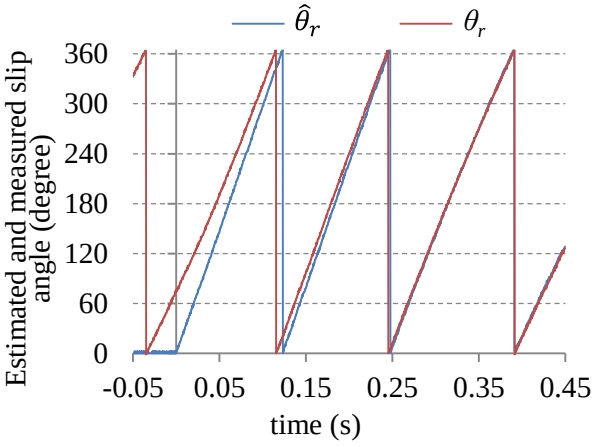

(f) Estimated and measured slip angle

Fig. 4.25: Experimental results for starting on the fly with i_{sd}^* = 3 A, i_{sq}^* = 6 A, and ω_m = 0.9 pu.

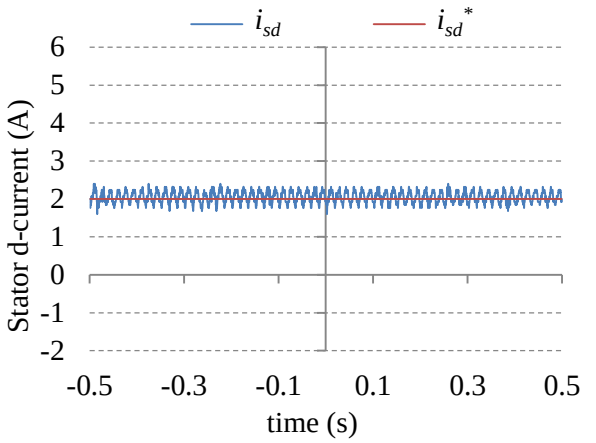

(a) Stator d-current

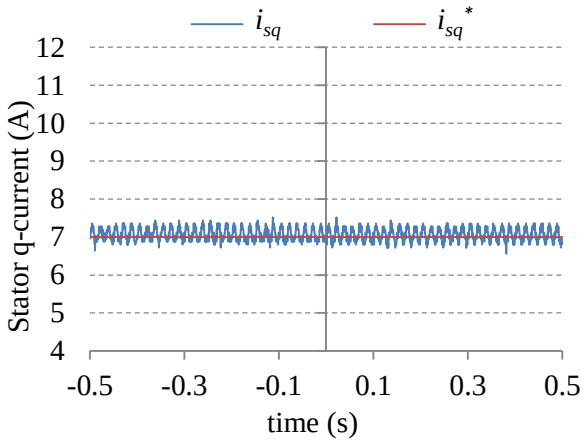

(b) Stator q-current

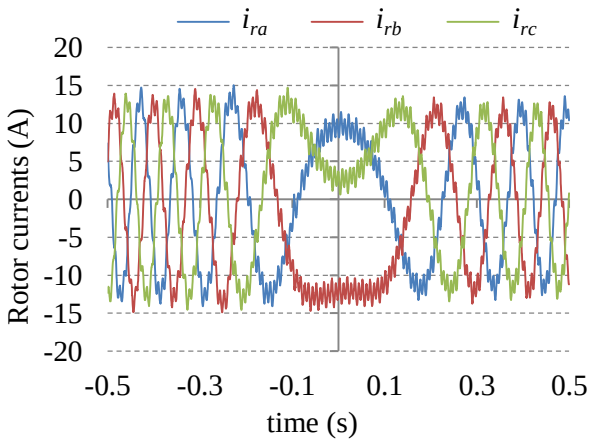

(c) Rotor currents

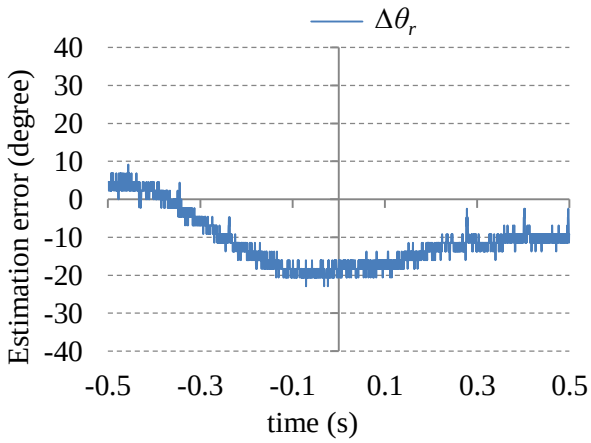

(d) Estimation error

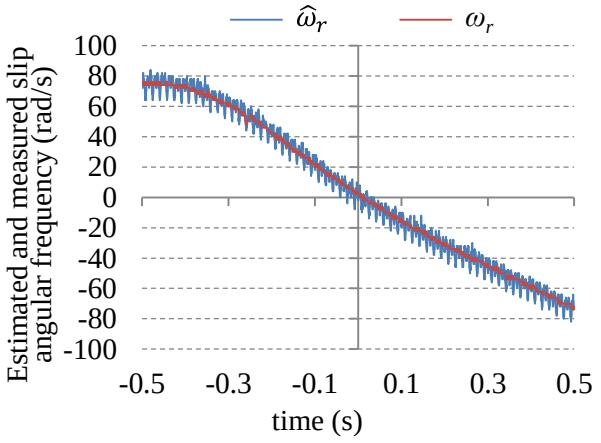

(e) Estimated and measured slip angular frequency

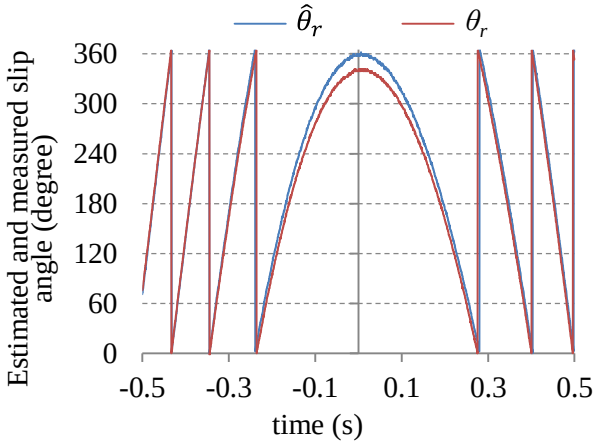

(f) Estimated and measured slip angle

Fig. 4.26: Experimental results for variable speed operation with i_{sd}^* = 2 A and i_{sq}^* = 7 A.

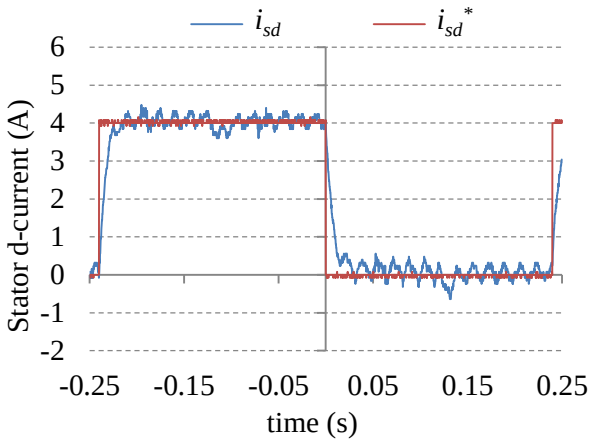

(a) Stator d-current

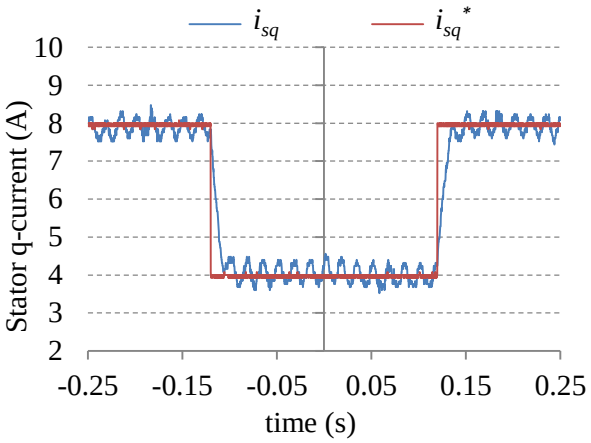

(b) Stator q-current

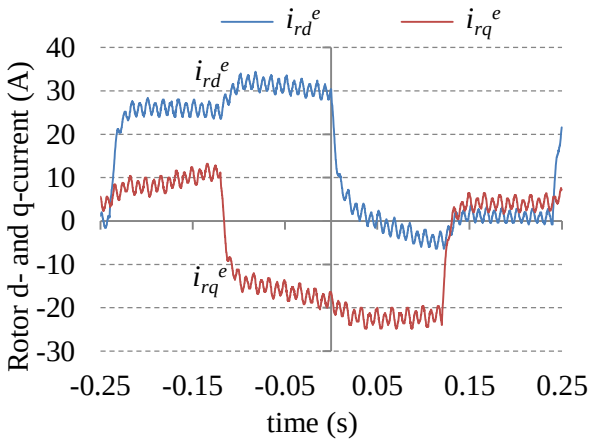

(c) Rotor d- and q-current

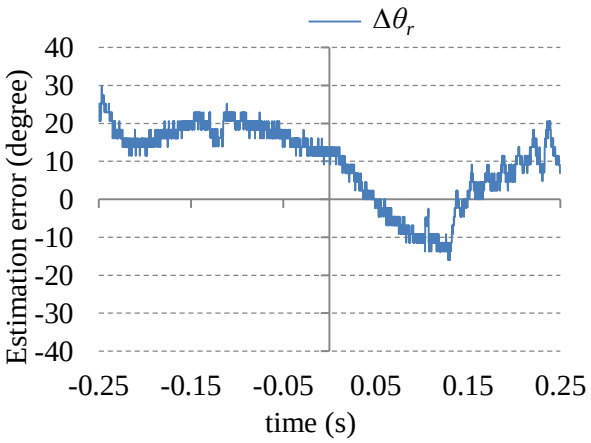

(d) Estimation error

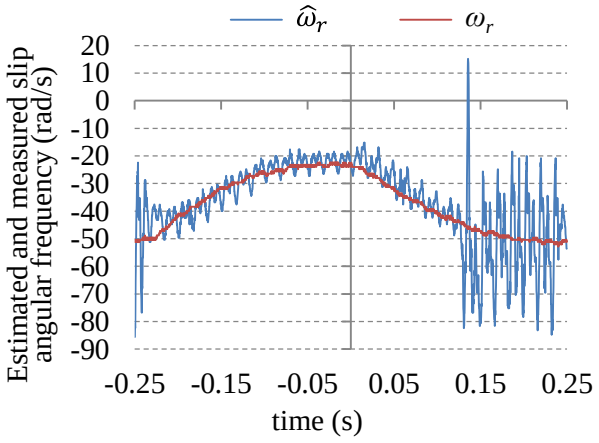

(e) Estimated and measured slip angular frequency

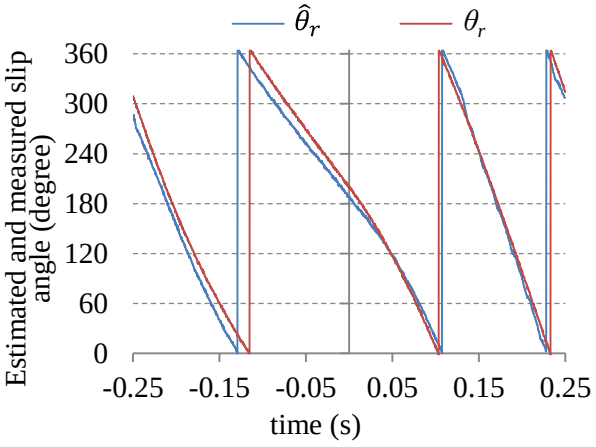

(f) Estimated and measured slip angle

Fig. 4.27: Experimental results for the effect of the power step response with ω_m = 1.1 pu.

Next, the effect of stator inductance inaccuracy on the proposed estimator is investigated. Initially, the proposed estimator uses the correct value of the stator inductance; then, suddenly, a very large inaccuracy, ΔL_s / L_s = −311%, is suddenly introduced to the reference model of the proposed estimator at 0 sec. The DFIG speed is fixed at the synchronous speed, and stator q-current reference is fixed at 8 A.

Two tests are conducted for two different rotor d-current. In the first test, the stator d-current reference is fixed to 0 A, which produces rotor d- and q-current of i_{rd}^e = 0 A and i_{rq}^e = 4.2 A respectively. The results of this test are shown in Fig. 4.28.

Referring to Fig. 4.28, the performance of the proposed estimator is not affected by this large inductance inaccuracy. Since the angle $\theta_{ir}^e - \theta_{is}$ is equal to 0 degree and, according to (4.26), the estimation error in this case is caused only by the ignored stator winding resistance and is not affected by the stator inductance inaccuracy. These results supports the sensitivity analysis.

In the second test, the stator d-current reference is fixed at 1 A; this produces rotor d- and q-current of i_{rd}^e = 8 A and i_{rq}^e = 5.2 A respectively. Since the angle $\theta_{ir}^e - \theta_{is}$ is not equal to 0 or ±180 degrees, we expect the estimation error to be affected by the stator inductance inaccuracy. The results for this test are shown in Fig. 4.29.

From the results of Fig. 4.29, the sudden increase of stator inductance inaccuracy causes the estimation error to increase to around 60 degrees. However, the estimated slip frequency is not affected except for a small transition. Since the estimation error is still within the stable region of the decoupled control, the system remains stable.

Finally, the DFIG speed is fixed at the synchronous speed and the stator d- and q-current references are fixed at 0 A and 8 A respectively. In this case, the estimation error is caused by the stator winding resistance. The steady-state response is investigated under different condition. First, the steady-state response under normal operation without any additional condition is shown in Fig. 4.30.

In the results of Fig. 4.30, there is an estimation error of around 30 degrees which, according to the sensitivity analysis, is caused by the stator winding resistance. In the following experiment this point will be proved experimentally. In addition, there is large ripples on the rotor d- and q-currents that need to be explained.

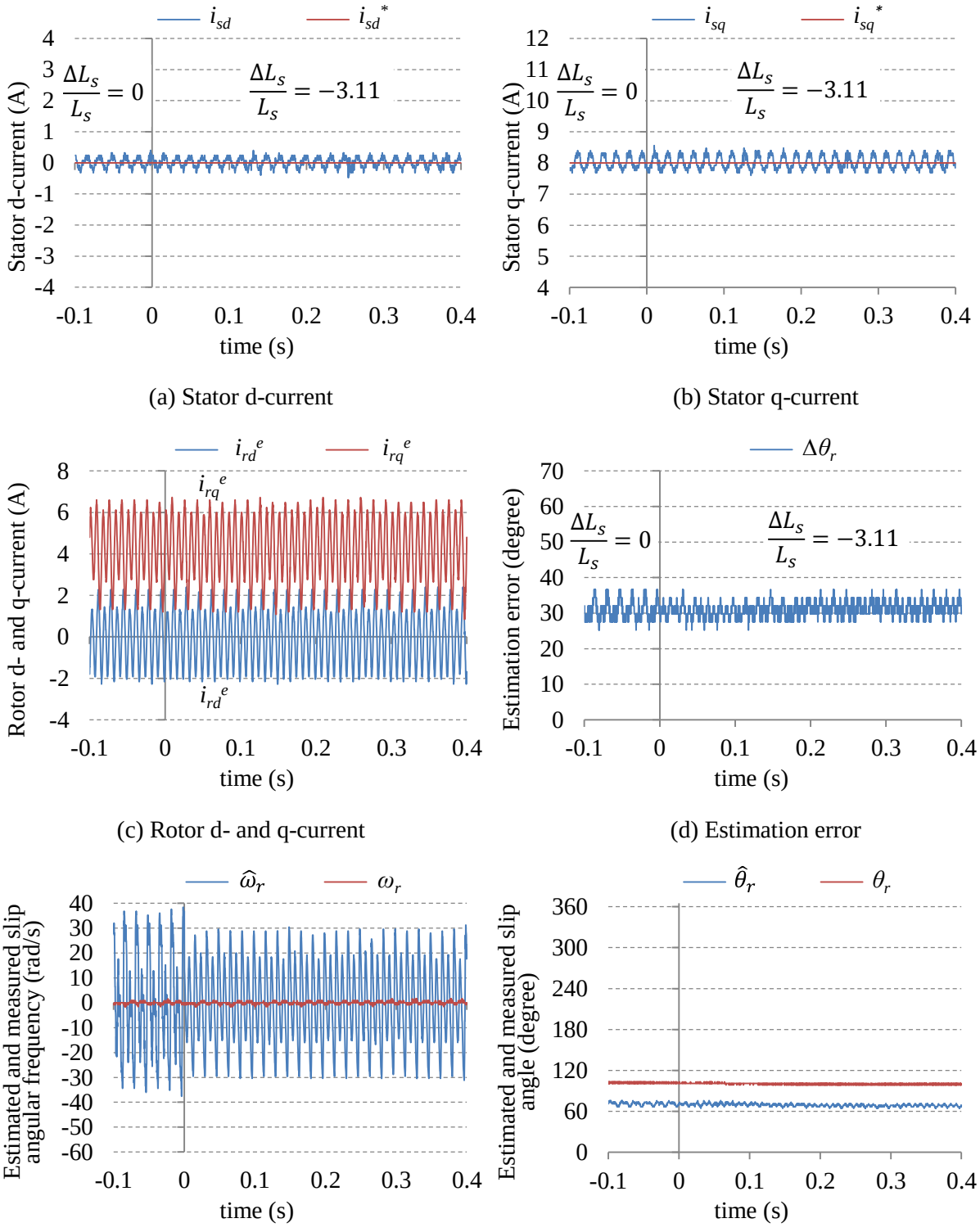

(a) Stator d-current

(b) Stator q-current

(c) Rotor d- and q-current

(d) Estimation error

(e) Estimated and measured slip angular frequency

(f) Estimated and measured slip angle

Fig. 4.28: Experimental results for the effect of sudden change of stator inductance inaccuracy with i_{sd}^* = 0 A, i_{sq}^* = 8 A. and ω_m = 1.0 pu.

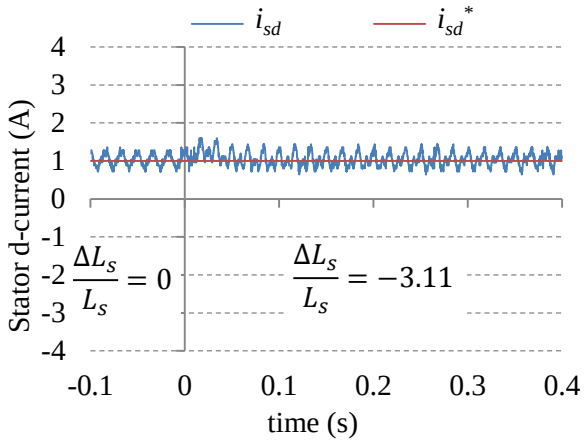

(a) Stator d-current

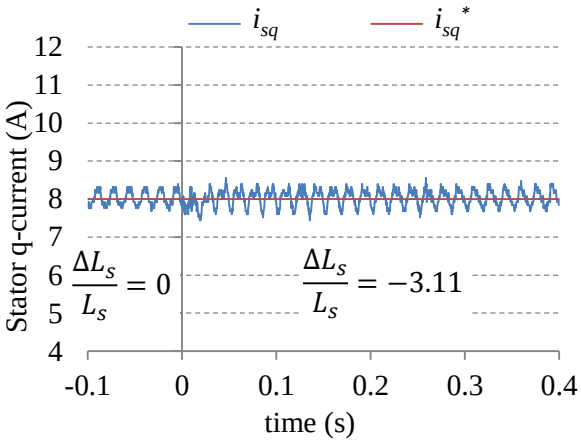

(b) Stator q-current

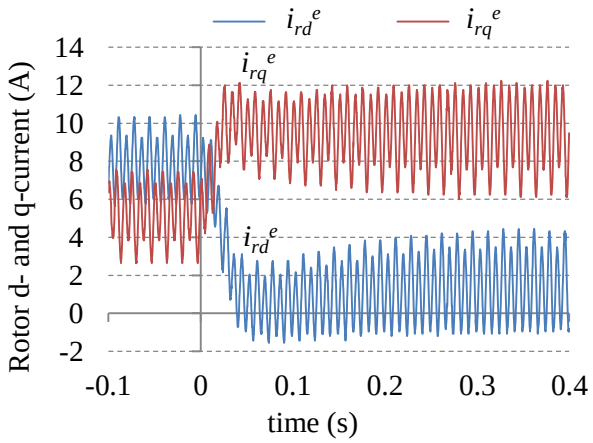

(c) Rotor d- and q-current

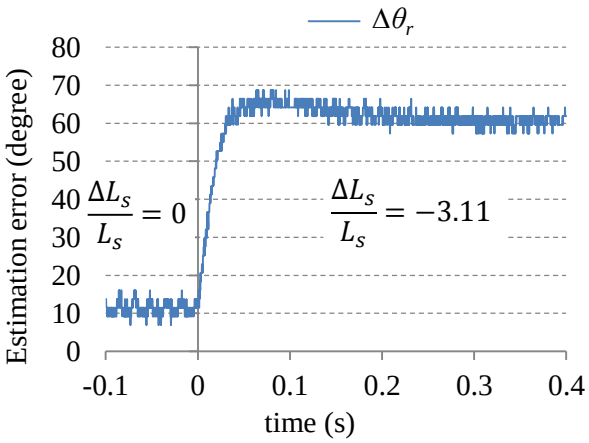

(d) Estimation error

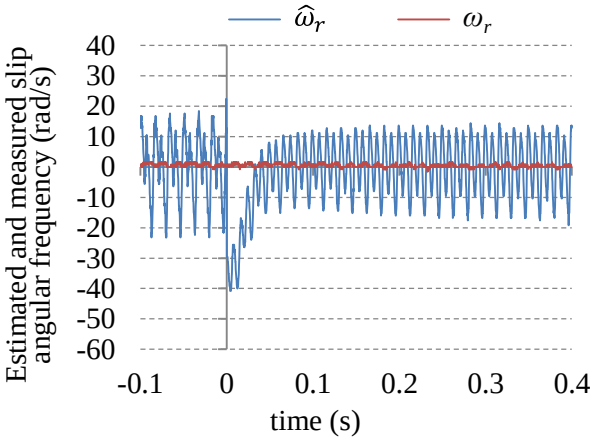

(e) Estimated and measured slip angular frequency

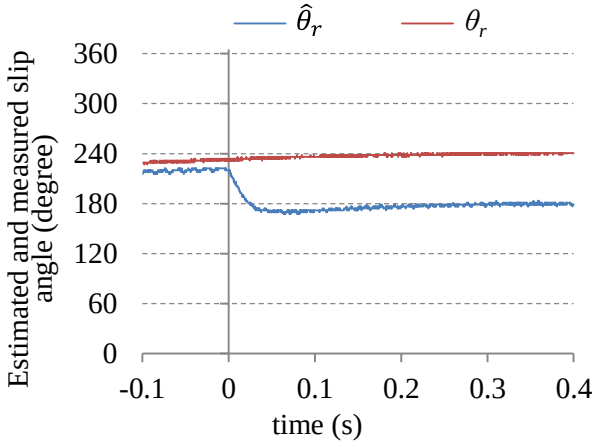

(f) Estimated and measured slip angle

Fig. 4.29: Experimental results for the effect of sudden change of stator inductance inaccuracy with i_{sd}^* = 1 A, i_{sq}^* = 8 A. and ω_m = 1.0 pu.

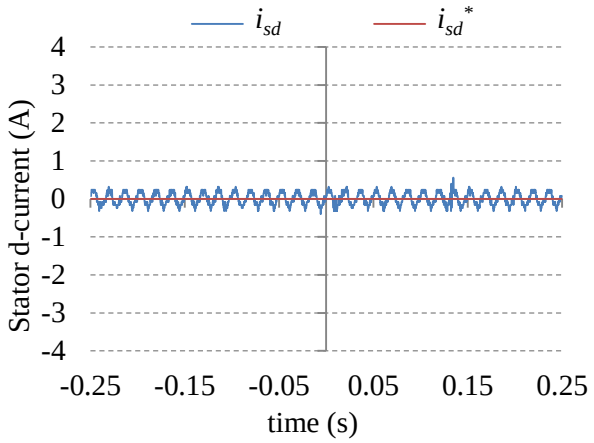

(a) Stator d-current

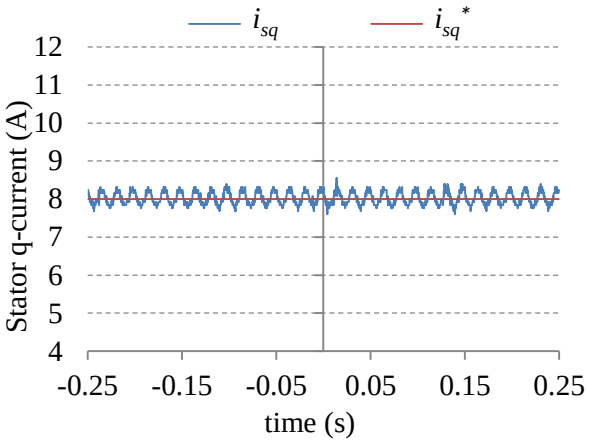

(b) Stator q-current

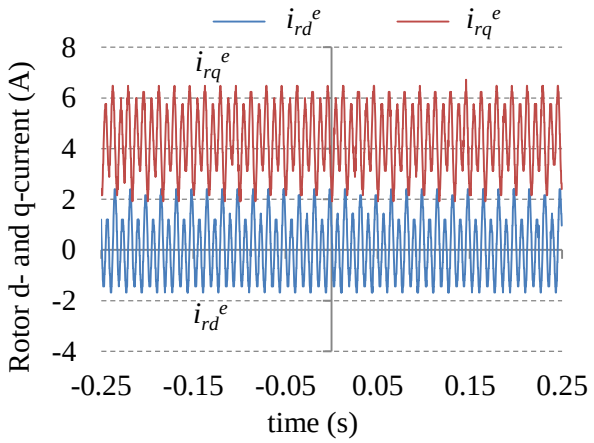

(c) Rotor d- and q-current

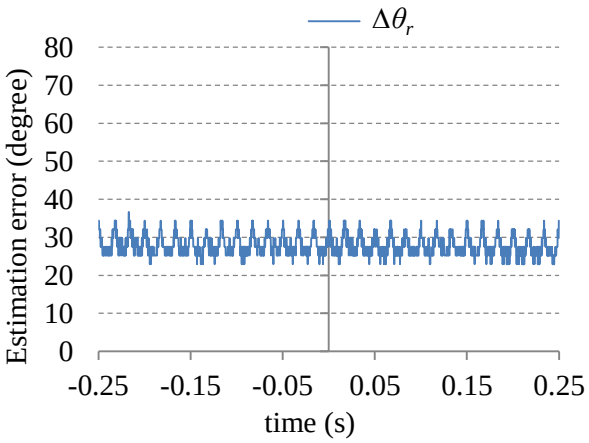

(d) Estimation error

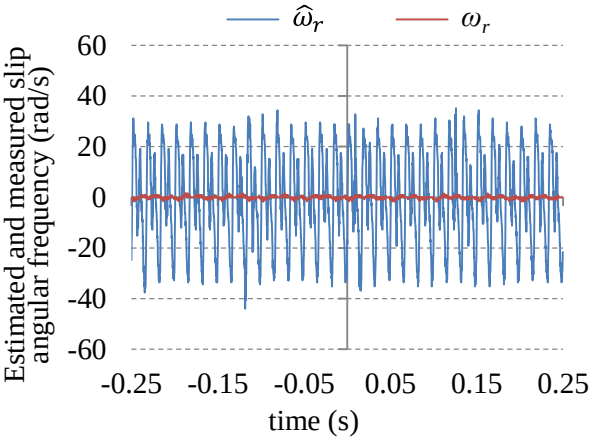

(e) Estimated and measured slip angular frequency

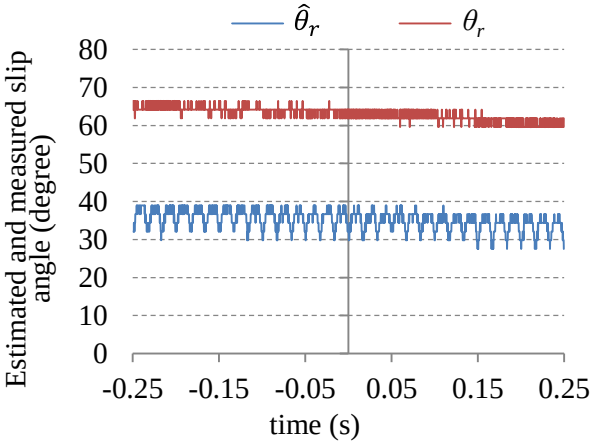

(f) Estimated and measured slip angle

Fig. 4.30: Experimental results for steady-state response

with i_{sd}^* = 1 A, i_{sq}^* = 8 A. and ω_m = 1.0 pu.

To prove that the estimation error in Fig. 4.30 is caused by the stator winding resistance, the experiment is repeated without ignoring the stator winding resistance. The proposed estimator is modified to include the stator winding resistance using (4.12), and the results for this test are shown in Fig. 4.31.

When the stator winding resistance is included in the proposed estimator, the estimation error becomes very small. This proves that the estimation error in Fig. 4.30 is caused by the ignored stator winding resistance.

The large ripples of the rotor d- and q-current are generated by the negative-sequence compensation control, Fig. 3.16. To prove this point, the experiment of Fig. 4.30 is repeated without negative-sequence compensation control, and the results are shown in Fig. 4.32.

From Fig. 4.32, the rotor current ripples are significantly reduced when the negative-sequence compensation control is disabled. However, the ripples of the stator d- and q-current are slightly increased. Due to the DFIG's turns ratio of 6.38, large rotor negative-sequence currents are needed to eliminate the small stator current ripples.

Finally, the ripples of the estimated slip angular frequency is considered. It was mentioned earlier that, because the estimator is designed with a wide bandwidth, ripples will appear in the estimated slip frequency and angle.

To support this statement experimentally, the proposed slip angle estimator is redesigned to have the same overshot but a 4.5 times smaller bandwidth. In this case, the PI parameters of the proposed slip angle estimator are K_p = 11.2 and K_i = 25. The results for this test are shown in Fig. 4.33.

From the results of Fig. 4.33, we conclude that the ripples of the estimated slip angular frequency is caused by the wide bandwidth of the proposed estimator. As the bandwidth is decreased the ripples also decrease. However, this causes the response of the estimator to become slow. Thus, a compromise in needed based on the design requirements. Additional filter can help in reducing the ripples.

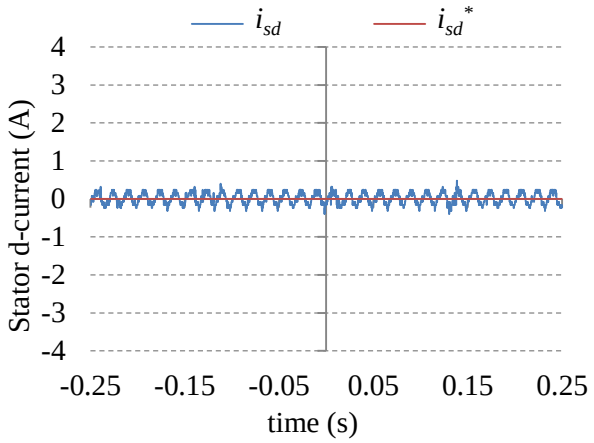

(a) Stator d-current

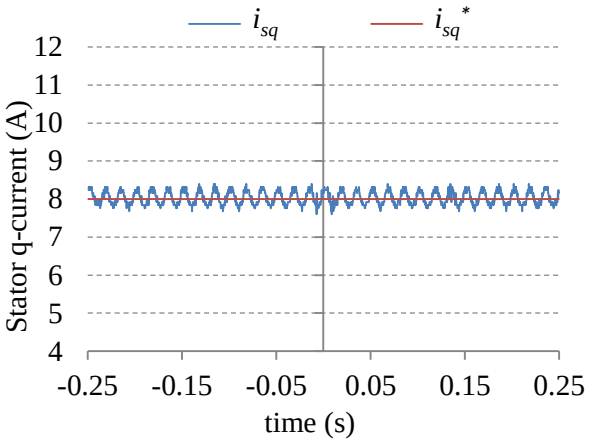

(b) Stator q-current

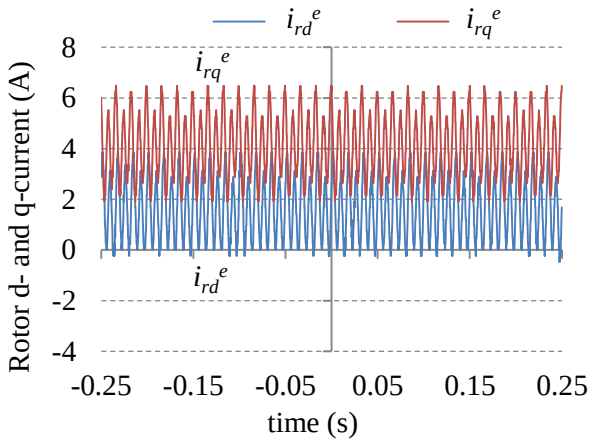

(c) Rotor d- and q-current

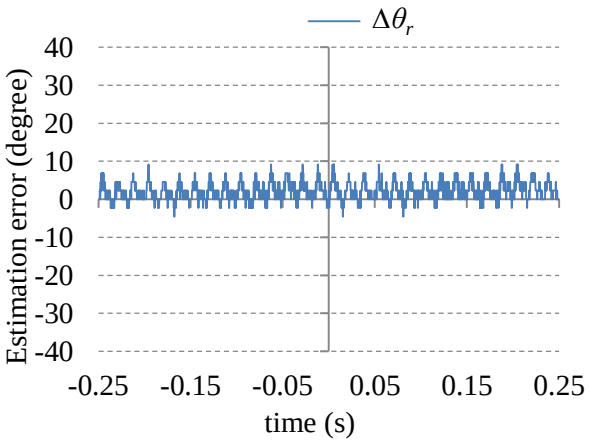

(d) Estimation error

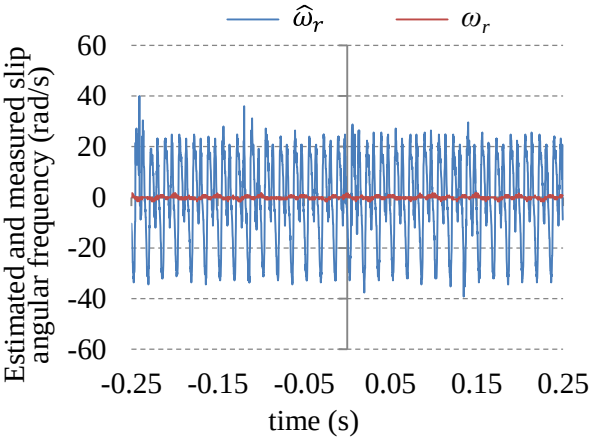

(e) Estimated and measured slip angular frequency

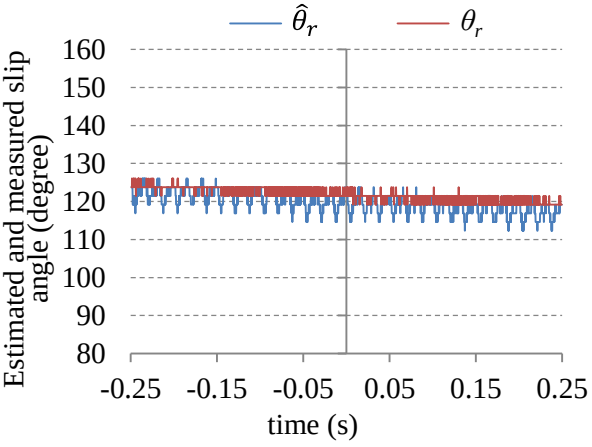

(f) Estimated and measured slip angle

Fig. 4.31: Experimental results for steady-state response without ignoring the stator winding resistance and with i_{sd}^* = 1 A, i_{sq}^* = 8 A. and ω_m = 1.0 pu.

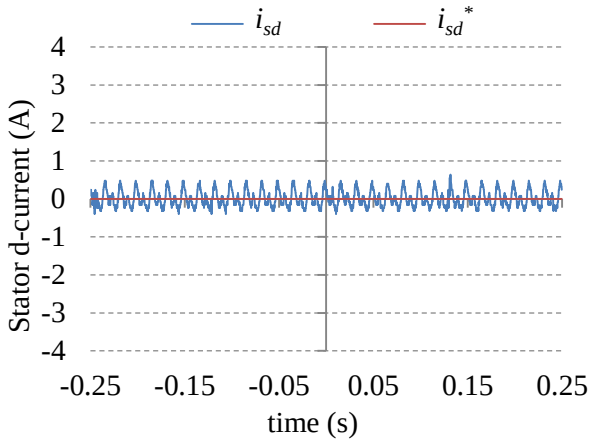

(a) Stator d-current

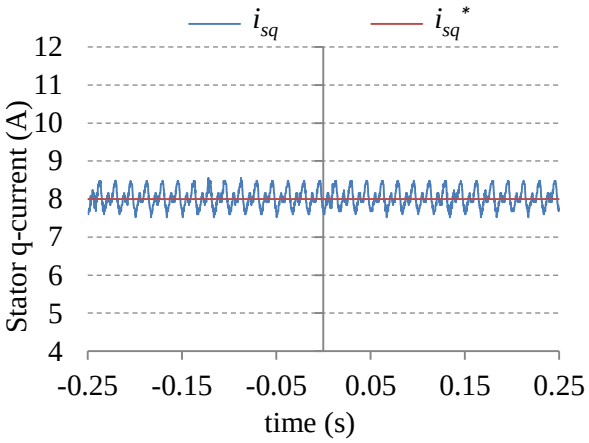

(b) Stator q-current

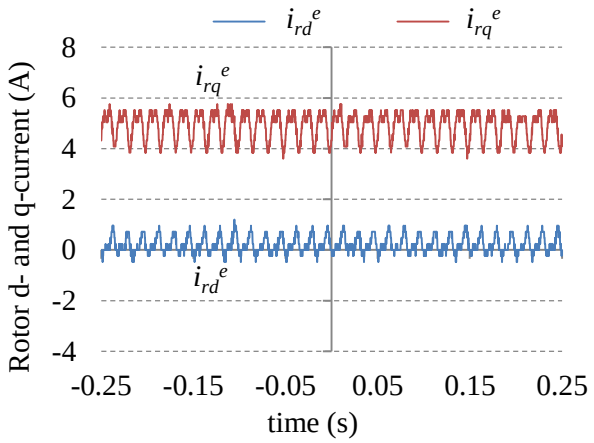

(c) Rotor d- and q-current

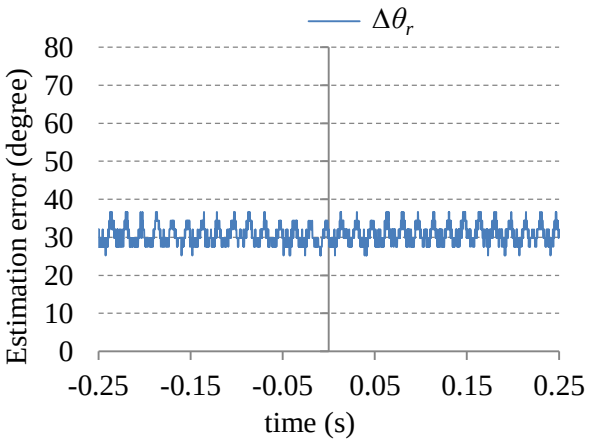

(d) Estimation error

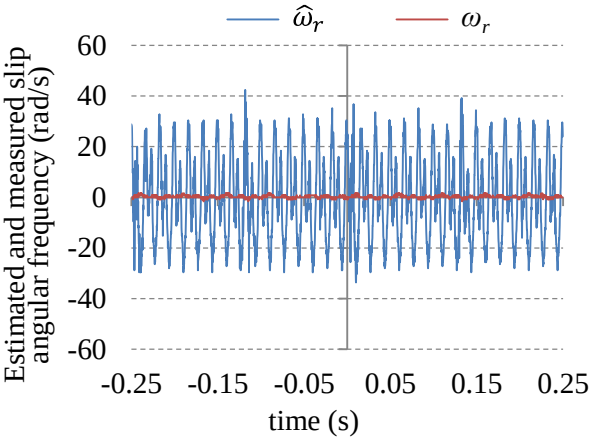

(e) Estimated and measured slip angular frequency

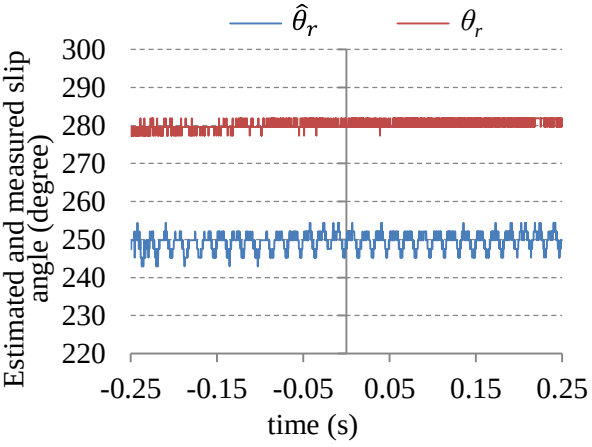

(f) Estimated and measured slip angle

Fig. 4.32: Experimental results for steady-state response without negative-sequence compensation with i_{sd}^* = 1 A, i_{sq}^* = 8 A. and ω_m = 1.0 pu.

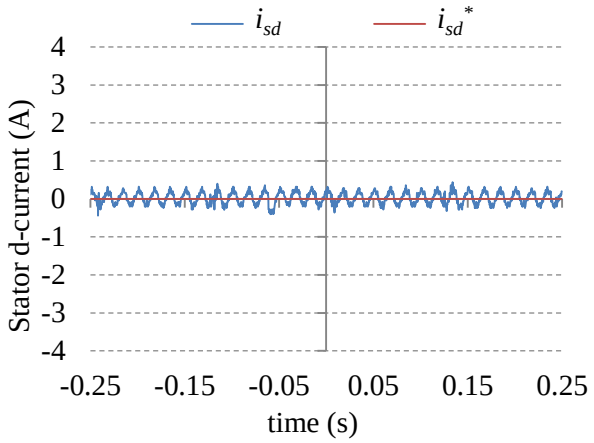

(a) Stator d-current

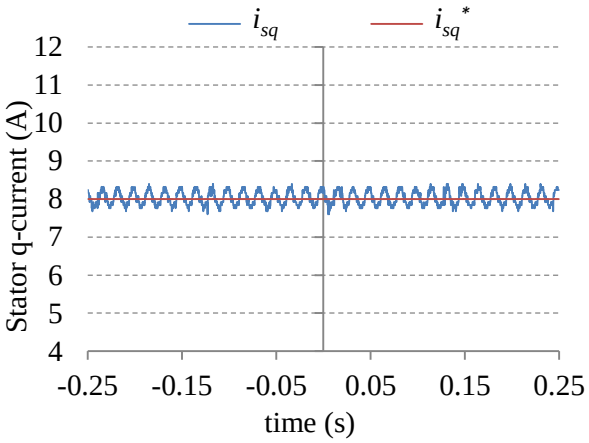

(b) Stator q-current

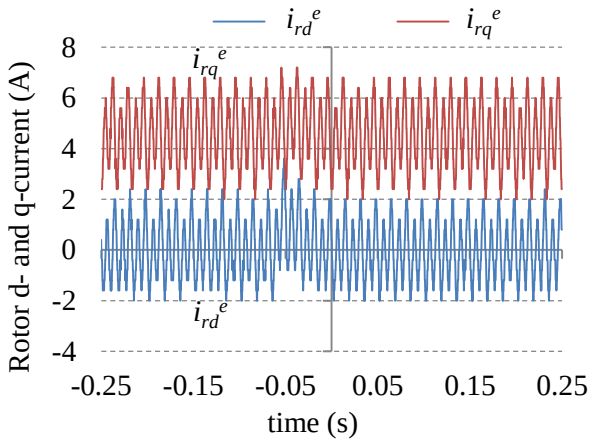

(c) Rotor d- and q-current

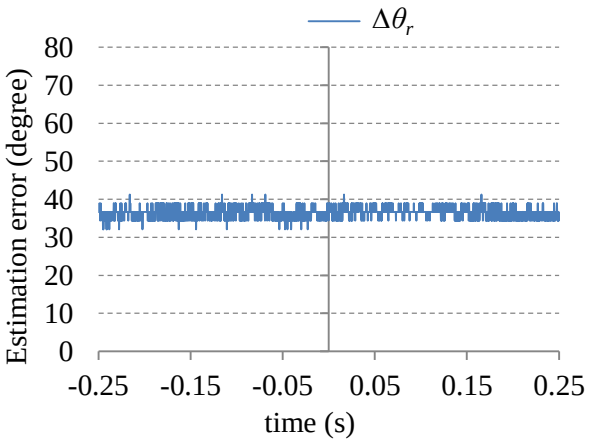

(d) Estimation error

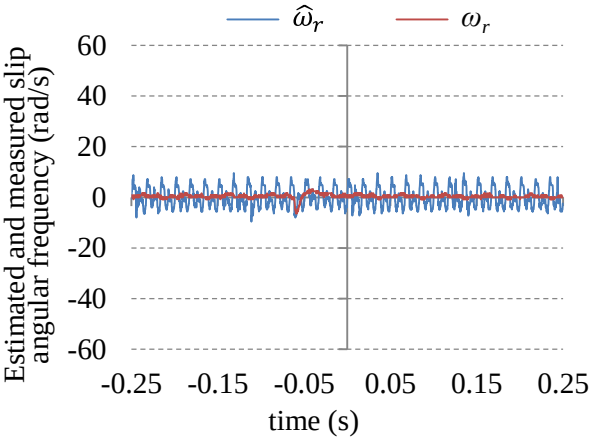

(e) Estimated and measured slip angular frequency

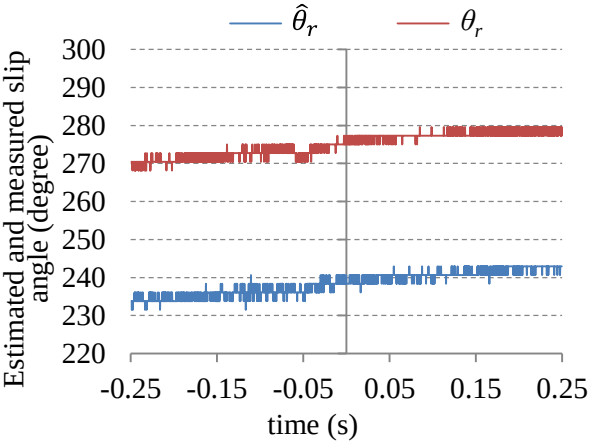

(f) Estimated and measured slip angle

Fig. 4.33: Experimental results for steady-state response with smaller bandwidth of the slip angle estimator with i_{sd}^* = 1 A, i_{sq}^* = 8 A. and ω_m = 1.0 pu.

4.5 Conclusion

This chapter has proposed a new slip angle estimator for the grid-connected DFIG to eliminate the need for speed and position encoders. The proposed estimator is based on rotor current estimation, and it has the following advantages:

- The proposed estimator requires the least number of parameters which is the stator inductance only.
- The proposed estimator, unlike some other estimators, does not ignore the stator leakage inductance. This improves the model accuracy.
- The stator inductance is the inductance seen from the stator side, and it can be measured directly. Thus, the proposed estimator uses measured parameters which improves the model accuracy.
- The proposed estimator does not require knowledge of the stator flux, which eliminate the voltage integration problems such as integrator drift and dependency on initial conditions.

Sensitivity analysis of the proposed estimator for parameters inaccuracy was provide in details. The stator winding resistance can be ignored especially for medium and large DFIG, and its effect is insignificant as long as the rotor current is not near zero. The accuracy is mainly affected by the stator inductance inaccuracy.

The proposed estimator was tested extensively with simulation and experiments. The results supported the theoretical study and the sensitivity analysis. In general, the proposed estimator is robust as long as the rotor currents are not almost zero.

References

[1] M. T. Abolhassani, P. Niazi, H. A. Toliyat, and P. Enjeti, “A Sensorless Integrated Doubly-Fed Electric Alternator/Active Filter (IDEA) for Variable Speed Wind Energy System,” in *Proc. 38th IAS Annual meeting*, Oct. 2003, Vol. 1, pp. 507-514.

[2] L. Morel, H. Godfroid, A. Mirzaian, J. M. Kauffmann, “Double-Fed Induction Machine: Converter Optimisation and Field Oriented Control without Position Sensor,” in *Proc. IEE Electic Power Applications*, vol. 145, no. 4, Jul. 1998, pp. 360-368.

[3] B. Hopfensperger, D. J. Atkinson, and R. A. Lakin, “Stator-Flux-Oriented Control of a Doubly-Fed Induction Machine with and without Position Encoder,” in *Proc. IEE Electic Power Applications*, vol. 147, no. 4, Jul. 2000, pp. 241-250.

[4] L. Xu and W. Cheng, “Torque and Reactive Power Control of a Doubly Fed Induction Machine by Position Sensorless Scheme,” *IEEE Trans. Industry Applications*, vol. 31, no. 3, pp. 636-642, May/Jun. 1995.

[5] D. G. Forchetti, G. O. Garcia, and M. I. Valla, “Adaptive Observer for Sensorless Control of Stand-Alone Doubly-Fed Induction Generator,” *IEEE Trans. Industrial Electronics*, vol. 56, no. 10, pp. 4174-4180, Oct. 2009.

[6] C. Schauder, “Adaptive Speed Identification for Vector Control of Induction Motors without Rotational Transducers,” *IEEE Trans. Industry Applications*, vol. 28, no. 5, pp. 1054-1061, Sep./Oct. 1992.

[7] R. Ghosn, C. Asmar, M. Pietrzak-David and B. De Fornel, "A MRAS-sensorless speed control of doubly fed induction machine", *Proc. Int. Conf. Elect. Mach.*, pp.26 -28 2002.

[8] R. Ghosn, C. Asmar, M. Pietrzak-David and B. De Fornel, "A MRAS Luenberger sensorless speed control of doubly fed induction machine", *Proc. Eur. Power Electron. Conf.*, 2003.

[9] S. M. Gadoue, D. Giaouris, and J. W. Finch, “MRAS Sensorless Vector Control of an Induction Motor Using New Sliding-Mode and Fuzzy-Logic Adaptation Mechanisms,” *IEEE Trans. Energy Conversion*, vol. 25, no. 2, pp. 394-402, Jun. 2010.

[10] T. O. Kowalska and M. Dybkowski, “Stator-Current-Based MRAS Estimator for a Wide Range Speed-Sensorless Induction-Motor Drive,” *IEEE Trans. Industrial Electronics*, vol. 57, no. 4, pp. 1296-1308, Apr. 2010.

[11] M. Rashed and A. F. Stronach, “A Stable Back-EMF MRAS-Based Sensorless Low-Speed Induction Motor Drive Insensitive to Stator Resistance Variation,” in *Proc. IEE Electic Power Applications*, vol. 151, no. 6, Nov. 2004, pp. 685-693.

[12] A. V. Ravi Teja, C. Chakraborty, S. Maiti, and Y. Hori, “A New Model Refernce Adaptive Controller for Four Quadrant Vector Controlled Induction Motor Drives,” *IEEE Trans. Industrial Electronics*, vol. 59, no. 10, pp. 3757-3767, Oct. 2012.

[13] R. Cardenas, R. Pena, J. Proboste, G. Asher, and J. Clare, “MRAS Observer for Sensorless Control of Standalone Doubly Fed Induction Generators,” *IEEE Trans. Energy Conversion*, vol. 20, no. 4, pp. 710-718, Dec. 2005.

[14] R. Cardenas, R. Pena, J. Clare, G. Asher, and J. Proboste, “MRAS Observers for Sensorless Control of Doubly-Fed Induction Generators,” *IEEE Trans. Power Electronics*, vol. 23, no. 3, pp. 1075-1084, May 2008.

[15] R. Pena, R. Cardenas, J. Proboste, G. Asher, and J. Clare, “Sensorless Control of Doubly-Fed Induction Generators Using a Rotor-Current Based MRAS Observer,” *IEEE Trans. Industrial Electronics*, vol. 55, no. 1, pp. 330-339, Jan. 2008.

[16] V. Verma, M. J. Hossain, T. Saha, and C. Chakraborty, “Performance of MRAS Based Speed Estimators for Grid Connected Doubly Fed Induction Machines During Voltage Dips,” in *Proc. IEEE Power and Energy Society General Meeting*, pp. 1-8, Jul. 2012.

[17] G. D. Marques and D. M. Sousa, “Air-Gap-Power-Vector-Based Sensorless Method for DFIG Control without Flux Estimator,” *IEEE Trans. Industrial Electronics*, vol. 58, no. 10, pp. 4717-4726, Oct. 2011.

[18] G. D. Marques and D. M. Sousa, “New Sensorless Rotor Position Estimator of a DFIG Based on Torque Calculations-Stability Study,” *IEEE Trans. Energy Conversion*, vol. 27, no. 1, pp. 196-203, March 2012.

[19] M. S. Carmeli, F. Castelli-Dezza, M. Iacchetti, and R. Perini, “Effects of Mismatched Parameters in MRAS Sensorless Doubly Fed Induction Machine Drives,” *IEEE Trans. Power Electronics*, vol. 25, no. 11, pp. 2842-2851, Nov. 2010.

[20] B. Shen, B. Mwinyiwiwa, Y. Zhang, and B. T. Ooi, “Sensorless Maximum Power Point Tracking of Wind by DFIG Using Rotor Position Phase Locked Loop (PLL),” *IEEE Trans. Power Electronics*, vol. 24, no. 4, pp. 942-951, April 2009.

[21] B. Mwinyiwiwa, Y. Zhang, B. Shen, and B. T. Ooi, “Rotor Position Phase-Locked Loop for Decoupled P-Q Control of DFIG for Wind Power Generation,” *IEEE Trans. Energy Conversion*, vol. 24, no. 3, pp. 758-765, Sep. 2009.

[22] G. Iwanski, M. Szypulski, T. Luszczyk, and P. Pura, “Cross and Dot Product Based MRAS Observer of the Rotor Position of Doubly Fed Induction Machine,” in *Proc. 9th International Conf. EVRE*, Mar. 2014, pp. 1-5.

[23] G. D. Marques, F. Pires, S. Sousa, and D. M. Sousa, “A DFIG Sensorless Rotor-Position Detector Based on a Hysteresis Controller,” *IEEE Trans. Energy Conversion*, vol. 26, no. 1, pp. 9-17, March 2011.

[24] J. Holtz, "Sensorless control of induction machines - With or without signal injection?" *IEEE Trans. Ind. Electron.*, vol. 53, no. 1, pp.7 -30, 2005.

[25] D. Reigosa, P. Gracia, F. Briz, D. Raca, and R. D. Lorenz, "Modeling and adaptive decoupling of

transient resistance and temperature effects in carrier-based sensorless control of PM synchronous machines," *IEEE Trans. Ind. Appl.*, vol. 46, no. 1, pp.139 -149, 2010.

[26] D. Raca, P. Garcia, D. Reigosa, F. Briz, and R. D. Lorenz, "Carrier Signal Selection for Sensorless Control of PM Synchronous Machines at Very Low and Zero Speeds," *IEEE Trans. Ind. Appl.*, vol. 46, no. 1, pp.167-178, Jan./Feb. 2010.

[27] Y. Yoon, S. Sul, S. Morimoto, and K. Ide, "High bandwidth sensorless algorithm for ac machines based on square-wave type voltage injection," *IEEE Trans. Ind. Appl.*, vol. 47, no. 3, pp. 1361–1379, May/Jun. 2011.

[28] S. Georges, G. Ragi, P.-D. Maria, and D. F. Bernard, "A comparison of sensorless speed estimation for a doubly fed induction machine," in *Proc. Eur. Conf. Power Electron. Appl*., 2005, p. 9.

[29] L. Xu, E. Inoa, Y. Liu, and B. Guan, "A New High-Frequency Injection Method for Sensorless Control of Doubly Fed Induction Machines," *IEEE Trans. Ind. Appl.*, vol. 48, no. 5, pp. 1556–1564, Sep./Oct. 2012.

[30] D. D. Reigosa, F. Briz, C. Blanco, and J. M. Guerrero, "Sensorless Control of Doubly Fed Induction Generators Based on Stator High-Frequency Signal Injection," *IEEE Trans. Ind. Appl.*, vol. 50, no. 5, pp. 1361–1379, Sep./Oct. 2014.

Chapter 5

Stand-Alone Mode of Operation

Due to the increased interest in a stable and reliable power supply, the distributed generation systems have emerged. In these systems the generator must be prepared to disconnect from the grid, in case of grid failure, and to maintain power supply to a local load as shown in Fig. 5.1. This mode is not suitable for wind turbine because the output power depends on the unpredicted nature. Diesel and natural gas engines are widely used for this mode of operation.

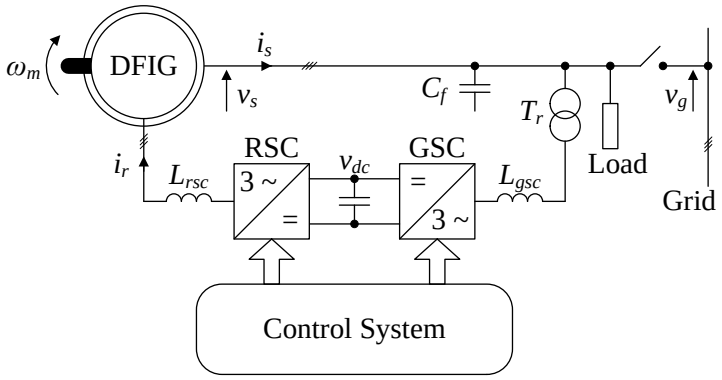

Fig. 5.1: Schematic diagram of the stand-alone DFIG.

During the grid-connected mode, the amplitude and the frequency of the generated voltage are maintained by the grid. During the stand-alone mode, the grid-connected control cannot maintain the voltage amplitude and frequency. Thus, a different control is needed for stand-alone. In this work, the sensorless direct voltage control is adopted.

The direct voltage control was first introduced in [1] and [2]. This control does not require any DFIG parameter, and it achieves sensorless control. The use of direct voltage control during the synchronization mode for smooth connection to the grid was discussed in [3].

The direct voltage control defines a new synchronous reference frame for the rotor quantities, which causes the direct voltage control to lose track of the slip angle. The

absence of slip angle information causes inrush currents when the DFIG is connected to the grid even after synchronization, and reduces the voltage quality for some loads due to large stator negative-sequence voltages.

In this chapter, the direct voltage control is introduced, and its limitations are explained. To overcome these limitations, a new estimator of the rotor current angle is proposed and integrated into the direct voltage control. Finally, the method for synchronization and connection to the grid are introduced.

5.1 Control of the RSC

The control of the RSC must regulate the voltage amplitude and frequency and, in this work, it is based on the direct voltage control. First the conventional direct voltage and its limitations are introduced. Then, the proposed method to overcome these limitations is explained.

5.1.1 Conventional Direct Voltage Control

A. Concept

The equivalent circuit of the DFIG during the stand-alone operation is shown in Fig. 5.2. The load Z_L includes the local load, the filtering capacitor, and the GSC. The GSC can be included in the load Z_L because it is drawing sinusoidal currents, and it can be regarded as a linear load in parallel with the local load.

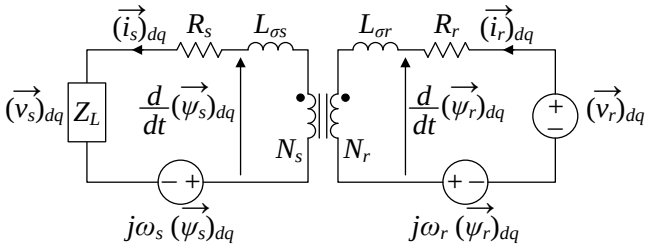

Fig. 5.2: Equivalent circuit of the DFIG in the dq-frame during stand-alone operation.

The voltage across the DFIG's stator, during steady-state, is given by (5.1).

$$(\vec{v}_s)_{dq} = -\big(R_s + j\omega_s(L_s + L_{\sigma s})\big)(\vec{\imath}_s)_{dq} + j\omega_s L_m(\vec{\imath}_r)_{dq} \tag{5.1}$$

On the other hand, the stator voltage and current are related by the load as shown

in (5.2).

$$(\vec{v}_s)_{dq} = Z_L(\vec{i}_s)_{dq} \tag{5.2}$$

The mathematical model of the stand-alone operation is obtained by substituting (5.2) into (5.1), and it is given (5.3).

$$(\vec{v}_s)_{dq} = \frac{j\omega_s L_m \cdot Z_L}{R_s + j\omega_s(L_s + L_{\sigma s}) + Z_L}(\vec{i}_r)_{dq} \tag{5.3}$$

By introducing an equivalent load Z_L as in (5.4), the model is given by (5.5).

$$Z_{eq} = \frac{j\omega_s L_m \cdot Z_L}{R_s + j\omega_s(L_s + L_{\sigma s}) + Z_L} \tag{5.4}$$

$$(\vec{v}_s)_{dq} = Z_{eq} \cdot (\vec{i}_r)_{dq} \tag{5.5}$$

Since the equivalent load Z_{eq} is dependent on the local load and on the DFIG's parameters, it is normally unknown and variable. This complicates the control of the individual stator d- and q-voltage.

On the other hand, if the polar coordinates are used, we get (5.6).

$$\begin{cases} \left\|(\vec{v}_s)_{dq}\right\| = \left\|Z_{eq}\right\| \cdot \left\|(\vec{i}_r)_{dq}\right\| \\ \angle(\vec{v}_s)_{dq} = \angle Z_{eq} + \angle(\vec{i}_r)_{dq} \end{cases} \tag{5.6}$$

Since the relation between the amplitude of the stator voltage and that of the rotor current is linear, a PI controller can be used to generate the rotor current amplitude command required to regulate the stator voltage amplitude.

The direct voltage control generates the reference amplitude of the rotor current, but it cannot generate the individual rotor d- and q-current references. To solve this issue, a new synchronous reference frame, xy-frame, is defined for the rotor quantities; this frame is aligned with the rotor current command as shown in Fig. 5.3.

Consequently, the rotor current references in the xy-frame are given by (5.7).

$$\begin{cases} {i_{rx}}^* = \left\|(\vec{i}_r)_{dq}\right\|^* \\ {i_{ry}}^* = 0 \end{cases} \tag{5.7}$$

In addition, the relation between the angle of the stator voltage and that of the rotor

current is also linear. Thus, a PI controller can be used to generate the rotor angle, which is denoted by θ_r^e. The reference angle for the stator voltage is generated by integrating the reference frequency, in our case 60 Hz. The input of the PI controller, which is the angle error, is obtained using the dq-transformation in a similar manner to the PLL circuit of Fig. 3.2

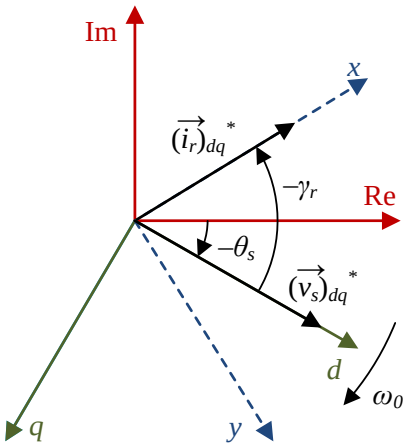

Fig. 5.3: Vector diagram for the direct voltage control.

Thus, the direct voltage control, which is shown in Fig. 5.4, is composed of two components: The amplitude control and the angle control.

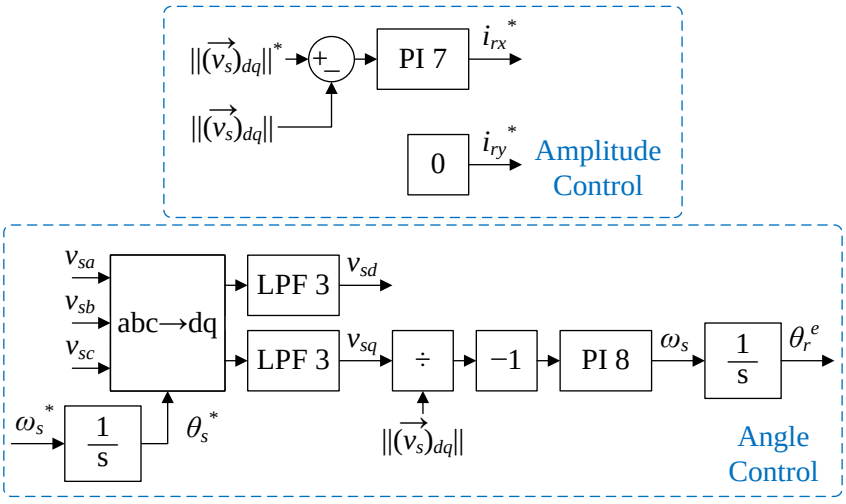

Fig. 5.4: Schematic diagram of the direct voltage control.

B. Limitations

The main limitation of the direct voltage control is that it cannot obtain the slip angle, because of the definition of the new xy-frame.

The rotor current in the dq-frame and in the xy-frame are related by a rotation as in (5.8).

$$(\vec{\imath}_r)_{dq} = e^{j\gamma_r}(\vec{\imath}_r)_{xy} \tag{5.8}$$

The angle control block of the direct voltage control generates an angle which is different from the slip angle as in (5.9).

$$\theta_r{}^e = \theta_r + \gamma_r \tag{5.9}$$

The angle γ_r, which is referred to as the rotor current angle, represents the angle between the dq-frame and the xy-frame, and it depends on the DFIG parameters and the load as shown in (5.10).

$$\gamma_r = -\angle Z_{eq} = -\angle\left(\frac{j\omega_s L_m \cdot Z_L}{R_s + j\omega_s(L_s + L_{\sigma s}) + Z_L}\right) \tag{5.10}$$

Using the parameters of the DFIG which are listed in Table 5.1, the variations of the angle γ_r is are plotted in Fig. 5.5, where the local load is a series-resistive-reactive load; the R_L is the resistive component and X_L is the reactive component.

Table 5.1: DFIG's parameters and rated values.

Parameter	Value	Unit
Power Rating	1.1	kW
Stator line-to-line voltage	210	V_{RMS}
Frequency	60	Hz
Number of poles	6	
Stator resistance R_s	0.475	Ω
Rotor resistance R_r	0.04	Ω
Stator leakage inductance $L_{\sigma s}$	7.43	mH
Rotor leakage inductance $L_{\sigma r}$	0.18	mH
Magnetizing inductance L_m	11.2	mH
Stator-to-rotor turns ratio	6.38	

From Fig. 5.5, the rotor current angle is unknown and varies largely with the load. Thus, the direct voltage control cannot obtain the slip angle. The absence of the slip angle gives rise to other limitations:

One limitation of the direct voltage control is that it cannot achieve smooth connection to the grid even after synchronization with the grid voltage.

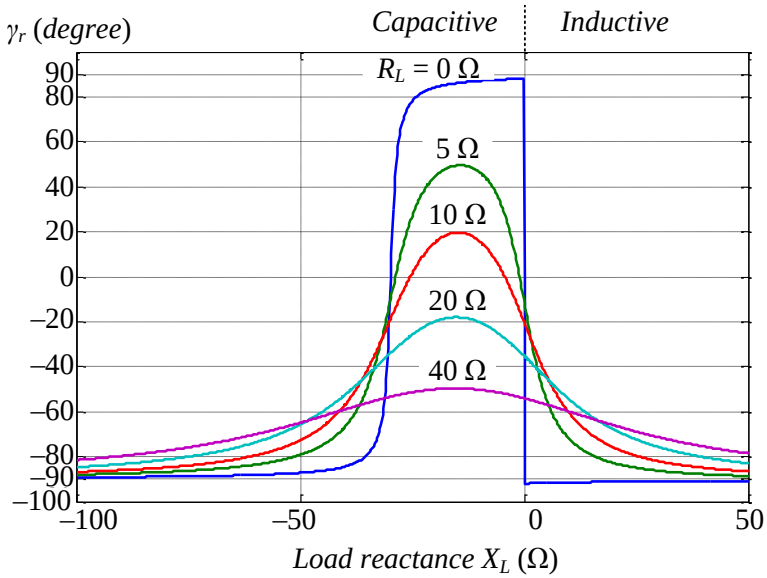

Fig. 5.5: Variation of the angle γ_r with load.

The grid-connected control uses the slip angle while the direct voltage control uses a different angle which is θ_r^e. As a result, at the moment of connection, there is a sudden change in the rotor current angle which causes an inrush current at the DFIG stator terminal.

Another limitation is related to the negative-sequence compensation which becomes unstable for some loads.

The negative-sequence compensation is carried out in the negatively-synchronous reference frame. The DFIG model in this frame is given by (5.11).

$$(\vec{v}_{s-})_{-dq} = -\big(R_s - j\omega_s(L_s + L_{\sigma s})\big)(\vec{\imath}_{s-})_{-dq} - j\omega_s L_m(\vec{\imath}_{r-})_{-dq} \tag{5.11}$$

The mathematical model of (5.11) can be simplified if the term related to the stator current is considered constant and is dropped. Then, the model is simply given by (5.12).

$$(\vec{v}_{s-})_{-dq} \propto -j\omega_s L_m(\vec{\imath}_{r-})_{-dq} \tag{5.12}$$

During the stand-alone mode, the negative-sequence compensation reduces the stator negative-sequence voltage by generating appropriate rotor negative-sequence currents. However, with the direct voltage control, the rotor current are expressed in the

xy-frame, and the model of (5.12) cannot be used.

The rotor current in the negatively synchronous dq-frame and the negatively synchronous xy-frame are related as in (5.13).

$$(\vec{\imath}_{r-})_{-dq} = e^{j\gamma_r}(\vec{\imath}_{r-})_{-xy} \tag{5.13}$$

Substituting (5.13) into (5.12), the negative-sequence model with the conventional direct voltage control is given by (5.14); this model depends on an unknown angle γ_r which varies with the load.

$$(\vec{v}_{s-})_{-dq} \propto -j\omega_s L_m e^{j\gamma_r}(\vec{\imath}_{r-})_{-xy} \tag{5.14}$$

To solve this issue, the angle γ_r was assumed constant at 0 degree in [4]; this corresponds to a limited range of load. Later on, the angle γ_r was assumed constant at -90 degrees in [5], which corresponds to a wider range of loads. When the angle γ_r is largely different from -90 degrees, in the case of some capacitive loads, the negative-sequence compensation will become unstable producing large rotor negative-sequence currents which increase the stator negative-sequence voltage instead of reducing it.

Since the limitations of the direct voltage control results from the absence of the slip angle, the solution is to obtain the slip angle. For this purpose, an estimator of the rotor current angle, which is referred to as rotor current angle estimator, is proposed and integrated into the direct voltage control; this configuration is referred to as modified direct voltage control.

5.1.2 Modified Direct Voltage Control

A. Rotor Current Angle Estimator

The idea for estimator the angle γ_r is derived from the concept of the slip angle estimator introduced in chapter 4.

Using (5.1), the rotor current in the dq-frame can be estimated without knowledge of the actual rotor current or the DFIG's rotor position; this, however, requires knowledge of several DFIG's parameters.

To reduce the number of parameters, a vector X, which is parallel to the rotor current in the dq-frame, is introduced and is estimated instead of directly estimating the rotor current. The vector X is defined as in (5.15).

$$\vec{X} = \omega_s L_m (\vec{\imath}_r)_{dq} \tag{5.15}$$

For medium and large DFIGs, the stator winding resistance is very small compared with the stator impedance, and it is always neglected. Therefore, the vector X is estimated using (5.16), which requires one parameter only, $L_s + L_{\sigma s}$.

$$\vec{X} = \omega_s (L_s + L_{\sigma s})(\vec{\imath}_s)_{dq} - j(\vec{v}_s)_{dq} \tag{5.16}$$

The angle of the vector X, which is referred to as γ_r^*, is the reference value for the angle of the measured rotor current when expressed in the xy-frame which, from now on, is not necessarily aligned with the rotor current. The target is to rotate the xy-frame to become identical to the dq-frame.

The cross product is used to obtain the angle difference between the two vectors, (5.17).

$$(\vec{\imath}_r)_{xy} \times \vec{X} = \left\|(\vec{\imath}_r)_{xy}\right\| \cdot \left\|\vec{X}\right\| \sin(\gamma_r{}^* - \hat{\gamma}_r) \tag{5.17}$$

Similar to the error function of the slip angle estimator, the error function is defined as the normalized cross product, (5.18).

$$\xi_r = \frac{(\vec{\imath}_r)_{xy} \times \vec{X}}{\left\|(\vec{\imath}_r)_{xy}\right\| \cdot \left\|\vec{X}\right\|} = \sin(\gamma_r{}^* - \hat{\gamma}_r) \tag{5.18}$$

The error in (5.18) is fed to a PI controller to obtain an estimation of the rotor current angle. The block diagram of the proposed rotor current angle estimator is depicted in Fig. 5.6.

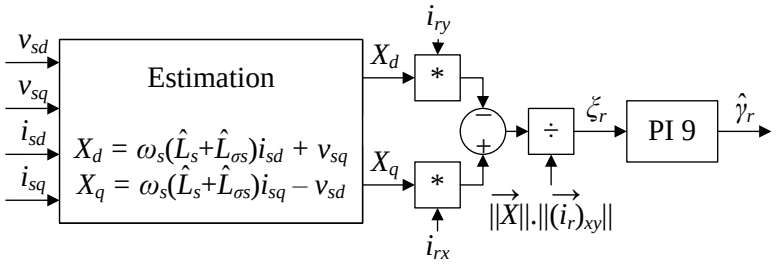

Fig. 5.6: Schematic diagram of the proposed rotor current angle estimator.

B. The Modified Direct Voltage Control

The xy-frame was introduced and aligned with the rotor current reference to avoid

calculating the d- and q-components. However, since the proposed rotor current angle estimator obtains an estimation of the angle γ_r, it can be used to calculate the rotor d- and q-current references.

The concept of the modified direct voltage control can be grasped from the vector diagram of the modified direct voltage control which is shown in Fig. 5.7.

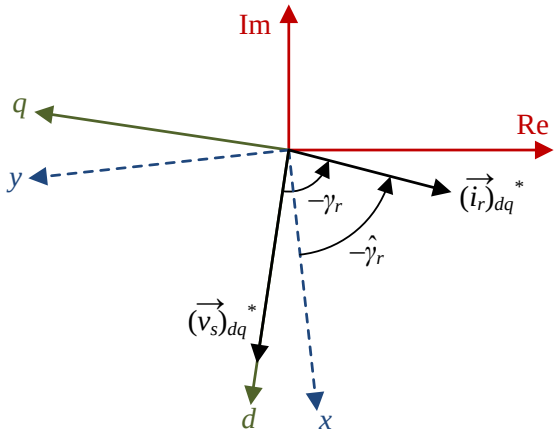

Fig. 5.7: Vector diagram for the modified direct voltage control.

In the modified direct voltage control, the xy-frame is rotated by the estimated rotor current angle, which is accomplished using new rotor current references as in (5.19).

$$\begin{cases} {i_{rx}}^* = \left\|(\vec{\imath}_r)_{dq}\right\|^* \cos(\hat{\gamma}_r) \\ {i_{ry}}^* = \left\|(\vec{\imath}_r)_{dq}\right\|^* \sin(\hat{\gamma}_r) \end{cases} \tag{5.19}$$

The angle control block of the direct voltage control in Fig. 5.4 generates the angle of the xy-frame, and since the xy-frame is rotated by the estimated angle, as in Fig. 5.7, the modified direct voltage control generates an angle which is given by (5.20).

$${\theta_r}^e = \theta_r + \gamma_r - \hat{\gamma}_r \tag{5.20}$$

If the estimation of the rotor current angle is accurate, then the modified direct voltage control will obtain the slip angle. The block diagram of the modified direct voltage control is shown in Fig. 5.8.

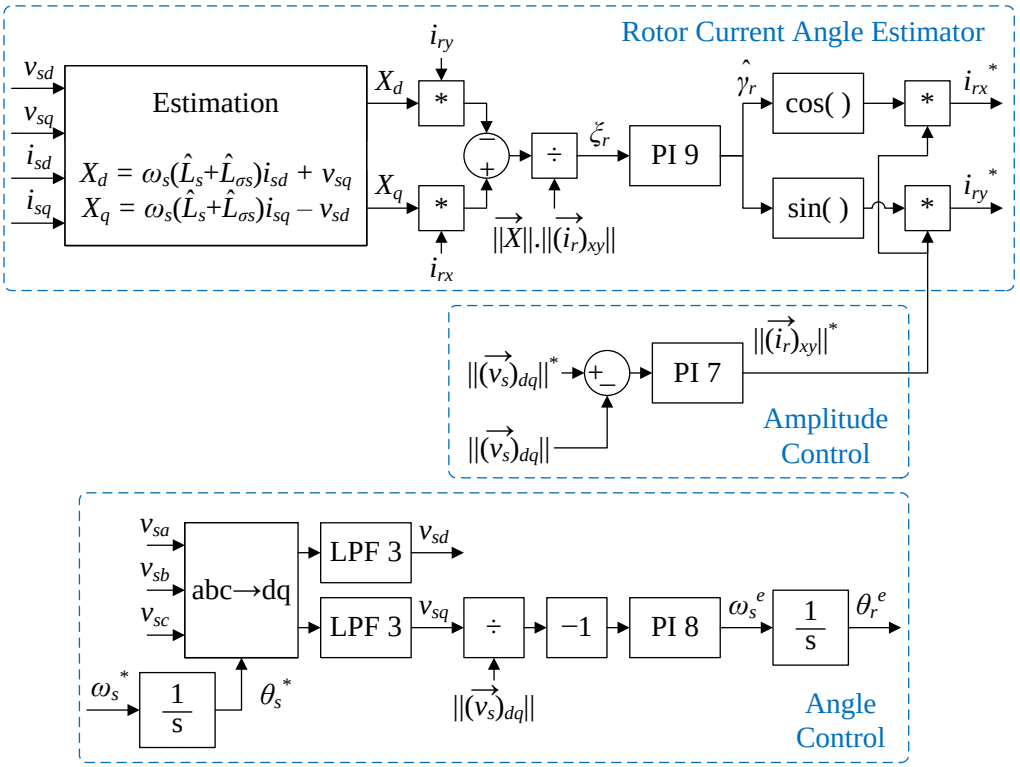

Fig. 5.8: Schematic diagram of the modified direct voltage control.

C. Controller Design

The model of the angle control block is similar to the model of the PLL circuit of Fig. 3.2. Therefore, the PI controller design procedure is exactly the same.

The model of the amplitude control block is derived as follows: The PI 7 controller generates the reference amplitude of the rotor current, which is effected by the rotor current loop. The rotor current loop is much faster than the amplitude control block and, consequently, it can be approximated by a unity gain.

The DFIG model of (5.5) will generate the amplitude of the stator voltage, which is fed-back to the control after being filtered by the low pass filter LPF 3. The control model of the amplitude control is depicted in Fig. 5.9

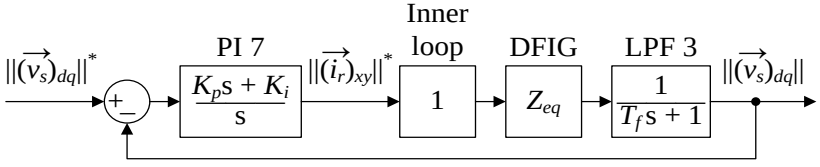

Fig. 5.9: Control model of the amplitude control block.

The damping of this system is affected by the local load. The less loaded the DFIG, the less damped the voltage response becomes. This is why the PI parameters should be designed for the worst case scenario which is under no load condition [6]. The design can be carried out using, for example, Bode diagram.

Finally, the control model for the proposed rotor current angle estimator is derived. The estimated angle is used to rotate and to decompose the rotor current amplitude reference to its x- and y-components. Since the response of the rotor current loop is very fast, the rotor current is also rotated by the same angle almost instantly.

Ignoring the effect of sampling delay, distortion of the voltages and currents, and the poorly damped poles of the DFIG, the control model is simply shown in Fig. 5.10.

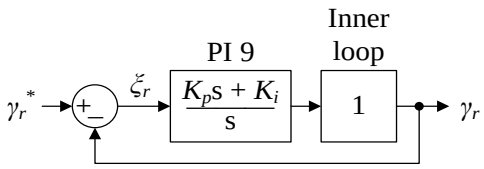

Fig. 5.10: Control model of the rotor current angle estimator.

The angle control block of Fig. 5.8 is continuously subtracting the estimated rotor current angle from its output as in (5.20). Thus, the bandwidth of the proposed rotor current angle estimator, which is equal to K_i, should be at least ten times smaller than the bandwidth of the angle control block of Fig. 5.8 to avoid disturbing its performance. In this work, it is selected exactly ten times smaller.

To reduce the effect of the DFIG's poorly damped poles located near the line frequency, the PI 9 controller should be designed to achieve adequate attenuation at the line frequency. This requires the proportional gain to be much smaller than one, $K_p << 1$.

5.1.3 Negative-Sequence Compensation

A. With the Conventional Direct Voltage Control

Similar to the grid-connected case, the negative-sequence compensation is designed in the negatively-synchronous reference frame. In this frame, the stator positive-sequence voltage is rotating at twice the line frequency. Therefore, low pass filters should be used to filter out the positive-sequence and to isolate the negative-sequence.

For the conventional direct voltage control, the DFIG model depends on the rotor current angle γ_r as in (5.14). In [5], the angle γ_r was assumed constant at −90 degrees. In this case, the DFIG model is given by (5.21) or, in matrix form, by (5.22).

$$(\vec{v}_{s-})_{-dq} \propto -\omega_s L_m (\vec{\imath}_{r-})_{-xy} \tag{5.21}$$

$$\begin{pmatrix} v_{sd-} \\ v_{sq-} \end{pmatrix} \propto -\omega_s L_m \begin{pmatrix} i_{rx-} \\ i_{ry-} \end{pmatrix} \tag{5.22}$$

From (5.22), the stator negative-sequence d-voltage can be controlled by the rotor negative-sequence x-current, and the q-voltage can be controlled by the y-current.

The rotor negative-sequence current references are rotated back to the positively-synchronous reference frame and, then, they are added to the rotor current references generated by the conventional direct voltage control.

The block diagram of the negative-sequence compensation with the conventional direct voltage control is shown in Fig. 5.11.

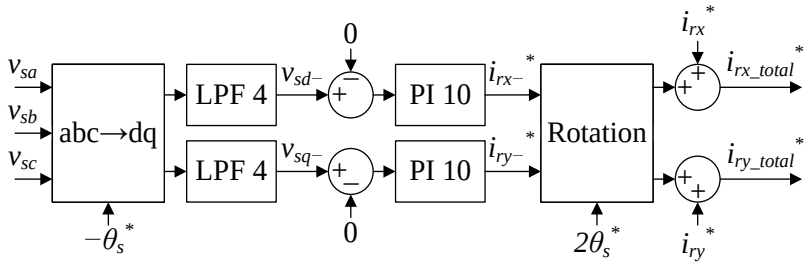

Fig. 5.11: Block diagram of the negative-sequence compensation with the conventional direct voltage control.

The simplified control model of the negative-sequence compensation is obtained by approximating the rotor current loop by a unity gain, and by ignoring the DFIG's poorly damped poles located near the line frequency; the DFIG model is approximated by (5.14). Then, the control model is shown in Fig. 5.12.

The negative-sequence compensation with the conventional direct voltage control depends on the angle γ_r, and will become unstable for some loads. The angle γ_r at which the negative-sequence compensation becomes unstable can be found by applying the Routh-Hurwitz stability criterion to the characteristic equation of the control model of Fig. 5.12, which can be obtained as follows:

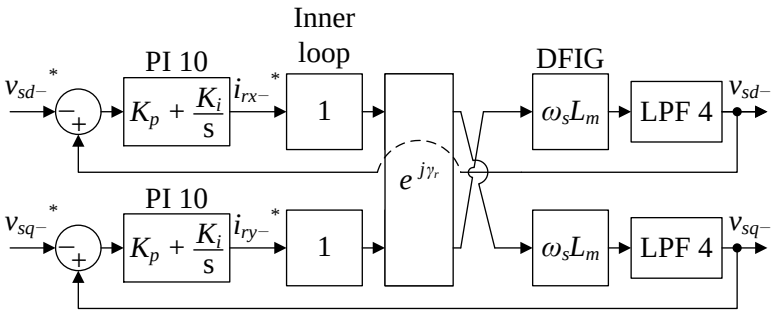

Fig. 5.12: Control model of the negative-sequence compensation with the conventional direct voltage control.

The transfer function of the PI controller, the rotor current loop, the DFIG, and the low pass filter are combined in one transfer function which is denoted by G; then, the closed-loop transfer function is given by (5.23).

$$\begin{pmatrix} v_{sd-} \\ v_{sq-} \end{pmatrix} = \frac{\begin{pmatrix} G^2 - G\sin(\gamma_r) & -G\cos(\gamma_r) \\ G\cos(\gamma_r) & G^2 - G\sin(\gamma_r) \end{pmatrix}}{G^2 - 2G\sin(\gamma_r) + 1} \begin{pmatrix} v_{sd-}^* \\ v_{sq-}^* \end{pmatrix} \tag{5.23}$$

From (5.23), the characteristic equation is given by (5.24).

$$G^2 - 2G\sin(\gamma_r) + 1 = 0 \tag{5.24}$$

B. With the Modified Direct Voltage Control

The DFIG model in the negatively-synchronous reference frame with the modified direct voltage control can be obtained by combining (5.14) and (5.20), and it is given by (5.25).

$$(\vec{v}_{s-})_{-dq} \propto -j\omega_s L_m e^{j(\gamma_r - \hat{\gamma}_r)} (\vec{i}_{r-})_{-xy} \tag{5.25}$$

The estimation accuracy is similar to the accuracy of the slip angle estimator introduced in chapter 4. If the correct value of the stator inductance is used, the estimation error will be caused by the stator winding resistance and will be very small especially for medium and large DFIGs. Assuming the estimation of the rotor current angle to be accurate, the model in (5.25) becomes as given by (5.26).

$$(\vec{v}_{s-})_{-dq} \propto -j\omega_s L_m (\vec{i}_{r-})_{-xy} \tag{5.26}$$

The model in (5.26) is given, in matrix form, by (5.27).

$$\begin{pmatrix} v_{sd-} \\ v_{sq-} \end{pmatrix} \propto \omega_s L_m \begin{pmatrix} i_{ry-} \\ -i_{rx-} \end{pmatrix} \approx \omega_s L_m \begin{pmatrix} i_{rq-} \\ -i_{rd-} \end{pmatrix} \tag{5.27}$$

From (5.27), the stator negative-sequence d-voltage can be controlled by the rotor negative-sequence q-current, and the q-voltage can be controlled by the d-current.

The rotor negative-sequence current references are rotated back to the positively synchronous reference frame and are added to the rotor current references generated by the modified direct voltage control.

The block diagram of the negative-sequence compensation with the modified direct voltage control is shown in Fig. 5.13.

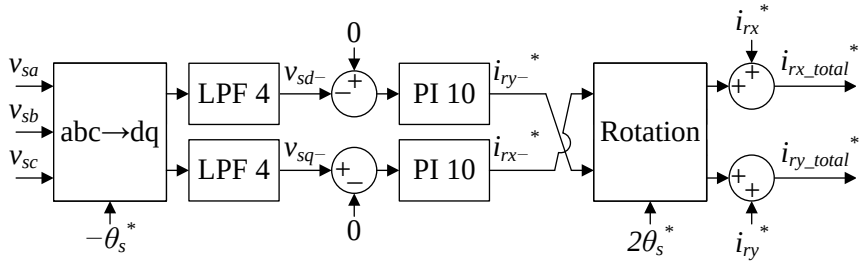

Fig. 5.13: Block diagram of the negative-sequence compensation with the modified direct voltage control.

Similarly, the control model is obtained by approximating the rotor current loop by a unity gain, and by ignoring the DFIG's poorly damped poles.

Assuming the proposed rotor current angle estimator to be accurate, the DFIG model is given by (5.27). Thus, the control model of the negative-sequence compensation with the modified direct voltage control is shown in Fig. 5.14.

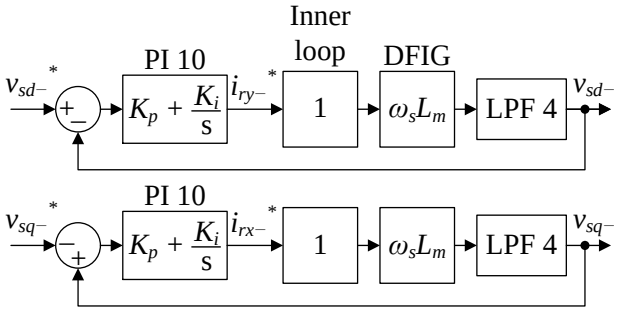

Fig. 5.14: Control model of the negative-sequence compensation with the modified direct voltage control.

C. Controller Design

The design of the negative-sequence compensation is the same with the conventional and with the modified direct voltage control.

The low pass filter is selected a simple second order filter as in (5.28).

$$LPF\ 4 = \frac{1}{\left(T_f s + 1\right)^2} \tag{5.28}$$

The time constant T_f is selected to effectively reduce the nominal voltage, whose frequency in the negatively-synchronous reference frame is twice the line frequency.

Using Bode diagram method, the parameters of the PI 10 controller are selected to achieve enough phase and gain margins.

The bandwidth of the negative-sequence compensation must be smaller than the line frequency to reduce the effect of the DFIG's poorly damped poles. In addition, the bandwidth must be smaller than the amplitude control block in Fig. 5.8 to avoid disturbing its performance.

The total rotor current references are the sum of the references generated by the direct voltage control and by the negative-sequence compensation. These references are effected using the same rotor current loop as during the grid-connected mode.

5.2 Synchronization Mode of Operation

5.2.1 Introduction

Normally, the generation system is connected to the grid and operates in grid-connected mode. However, the stand-alone mode is needed in case of grid failure to maintain power supply to the local load. Once the grid is recovered, the generation system must be reconnected to the grid.

The sudden change of the control system from the stand-alone mode to the grid-connected mode and the sudden connection of the DFIG to the grid will cause inrush currents unless special countermeasures are taken. The inrush currents will inflect mechanical stresses on the DFIG's shaft, decrease the lifetime of the grid-connecting-switch, and it might cause tripping of electrical equipment.

One of the main reasons for the inrush current is the sudden change of the voltage angle. Thus, a temporary mode of operation which is referred to as the synchronization mode is employed prior to the connection to the grid.

For the synchronization mode, the target is to align the generated voltage with that of the grid while the DFIG is still disconnected from the grid. Therefore, the synchronization mode is essentially a stand-alone mode. The synchronization mode should guarantee a zero voltage switching of the grid-connecting-switch.

In this work, the synchronization control will synchronize both the amplitude and the angle of the DFIG's voltage with that of the grid.

5.2.2 Synchronization Control

The control system during the synchronization mode is the same as during the stand-alone mode, which is the direct voltage control. The only differences are the references for the amplitude and for the angle of the stator voltage. These references should guarantee a smooth and gradual synchronization with the grid.

A. Amplitude Synchronization

At the beginning of the synchronization mode, the reference amplitude for the amplitude control block of Fig. 5.8 is the stand-alone amplitude reference. At the end of the synchronization mode, the reference amplitude is equal to the amplitude of the grid voltage.

To achieve smooth transition between the two amplitudes, we adopt the mathematical formula which gives a point (P) that lies on the line between two points, A and B. This formula is given by (5.29), where $0 \leq u \leq 1$.

$$P = (1 - u) \cdot A + u \cdot B \tag{5.29}$$

If the variable (u) in (5.29) is varies from 0 to 1, the point P will move from point A till point B. This idea can be used to gradually change the amplitude reference to become the grid voltage amplitude; this process is referred to as amplitude synchronization.

The amplitude reference during the synchronization mode, which is referred to as $||v_s||^{syn}$, is defined by (5.30), where the variable u is defined by (5.31), where the

synchronization mode starts at t_1 and finishes at t_2.

$$\|v_s\|^{syn} = (1-u)\cdot\left\|(\vec{v}_s)_{dq}\right\|^{*} + u\cdot\left\|\left(\vec{v}_g\right)_{dq}\right\| \tag{5.30}$$

$$u = \begin{cases} 0 & if \quad t < t_1 \\ \dfrac{t-t_1}{t_2-t_1} & if \quad t_1 \le t \le t_2 \\ 1 & if \quad t > t_2 \end{cases} \tag{5.31}$$

The amplitude synchronization process is displayed in Fig. 5.14. Normally, the value of the voltage amplitude during stand-alone is very close to the grid voltage amplitude; however, it is exaggerated in Fig. 5.15.

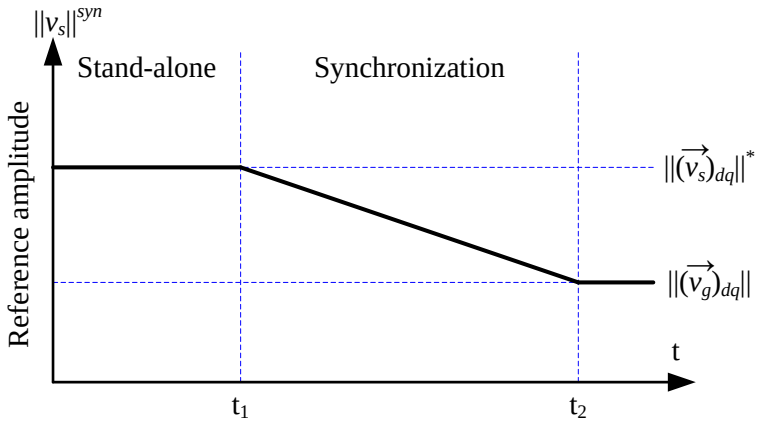

Fig. 5.15: Amplitude synchronization process.

Based on the previous study, the block diagram of the amplitude control during the synchronization mode is shown in Fig. 5.16.

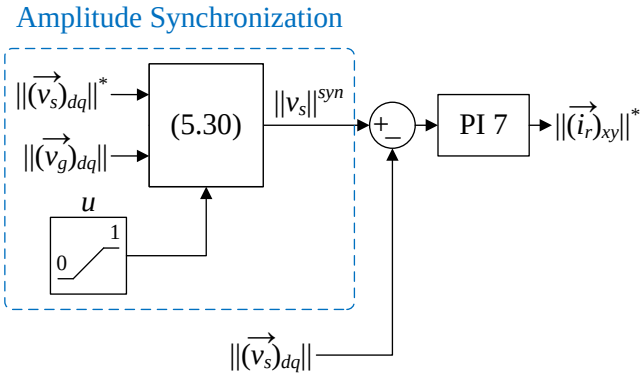

Fig. 5.16: Block diagram of the amplitude control during the synchronization mode.

B. Angle Synchronization

At the beginning of the synchronization mode, the reference angle for the angle control block of Fig. 5.8 is $\theta_s^* = \omega_s^* t$; this angle is generated by integrating the reference angular frequency. At the end of the synchronization mode, the reference angle for the angle control block should be equal to the angle of the grid voltage. The angle of the grid voltage is obtained using the PLL circuit of Fig. 3.2.

During the synchronization mode, the reference angle is gradually varied from θ_s^*, until it becomes equal to the grid angle. This process is referred to as angle synchronization, ant it implies that the frequency of the stator voltage is increased or decreased beyond its nominal value. The frequency variation, during the synchronization mode, should remain within the tolerances defined by the grid code.

Similar to the amplitude synchronization, the formula in (5.29) is used for the angle synchronization. To reduce the frequency variation during the synchronization, we make use of the periodic nature of the angle. If the initial angle difference is bigger than π, the grid angle is modified by subtracting or adding 2π.

Thus, the reference angle during the synchronization mode, which is referred to as θ_s^{syn}, is given by (5.32), where the variable u is given by (5.31).

$$\theta_s{}^{syn} = \begin{cases} (1-u)\cdot\theta_s{}^* + u\cdot\theta_g & if \quad \left|\theta_g - \theta_s{}^*\right| \le \pi \\ (1-u)\cdot\theta_s{}^* + u\cdot\left(\theta_g \pm 2\pi\right) & if \quad \pi < \left|\theta_g - \theta_s{}^*\right| \le 2\pi \end{cases} \tag{5.32}$$

The angle synchronization process is displayed in Fig. 5.17 for the two cases in (5.32).

Referring to Fig. 5.17, the slope of the angle θ_s^{syn} during the synchronization mode increases or decreases which results in an increase or decrease in the frequency of the stator voltage. The frequency variation is determined by the duration of the synchronization mode, $t_2 - t_1$, and it must be within the acceptable tolerances.

The frequency during synchronization mode can be obtained by taking the derivative of (5.32), and it is given by (5.33).

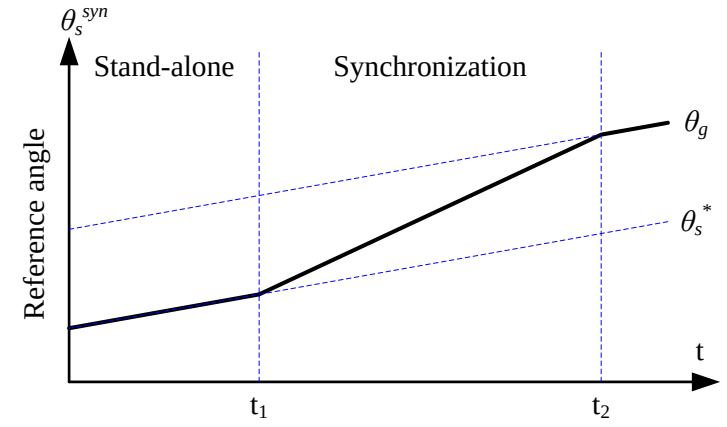

(a) $0 \le \theta_g - \theta_s^* < \pi$

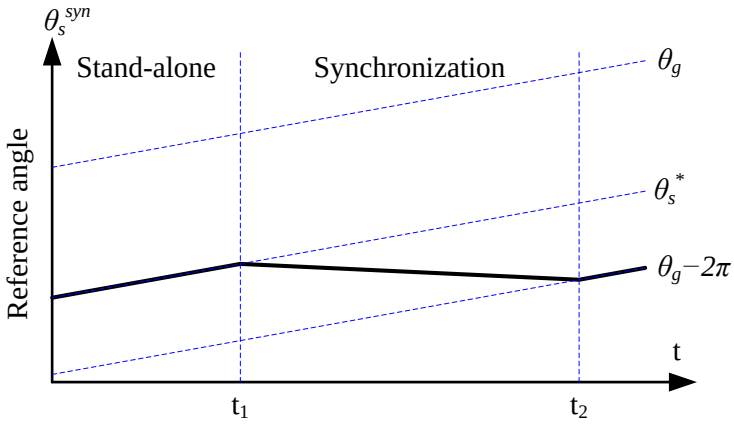

(b) $\pi < \theta_g - \theta_s^* \le 2\pi$

Fig. 5.17: Angle synchronization process.

$$\omega_s{}^{syn} = \frac{d}{dt}\theta_s{}^{syn}$$

$$= \begin{cases} \omega_s{}^* + u\dfrac{d(\theta_g - \theta_s{}^*)}{dt} + (\theta_g - \theta_s{}^*)\cdot\dfrac{du}{dt} & if \quad |\theta_g - \theta_s{}^*| \le \pi \\ \omega_s{}^* + u\dfrac{d(\theta_g - \theta_s{}^*)}{dt} + (\theta_g - \theta_s{}^* \pm 2\pi)\cdot\dfrac{du}{dt} & if \quad \pi < |\theta_g - \theta_s{}^*| \le 2\pi \end{cases} \tag{5.33}$$

Assuming that the angle θ_s^* and the angle of the grid voltage have the same frequency and substituting (5.31) into (5.33), we get (5.34).

$$\omega_s{}^{syn} - \omega_s{}^* = \begin{cases} \dfrac{(\theta_g - \theta_s{}^*)}{t_2 - t_1} & if \quad |\theta_g - \theta_s{}^*| \le \pi \\ \dfrac{(\theta_g - \theta_s{}^* \pm 2\pi)}{t_2 - t_1} & if \quad \pi < |\theta_g - \theta_s{}^*| \le 2\pi \end{cases} \tag{5.34}$$

During the synchronization mode, the variation of the angular frequency and of the frequency are given by (5.35) and (5.36) respectively.

$$|{\omega_s}^{syn} - {\omega_s}^*| \leq \frac{\pi}{t_2 - t_1} \tag{5.35}$$

$$|\Delta f_s| \leq \frac{0.5}{t_2 - t_1} \tag{5.36}$$

Equation (5.36) is used to determine the duration of the synchronization mode to ensure that the frequency will remain within the grid tolerance. In this work the tolerance is assume equal to 0.2 Hz and, consequently, the duration should be at least 2.5 sec.

The block diagram of the angle control block during the synchronization mode is shown in Fig. 5.18.

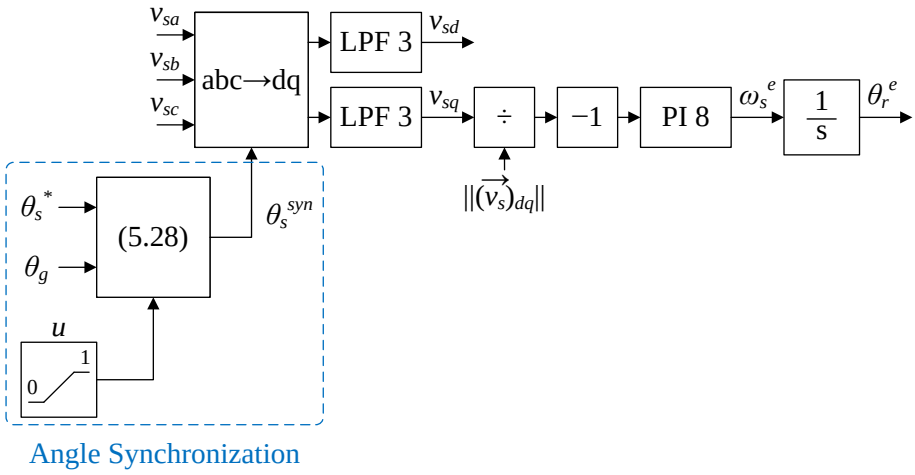

Fig. 5.18: Block diagram of the angle control block during synchronization mode.

5.2.3 Grid Connection Procedure

At the end of the synchronization mode, the stator and the grid voltages are synchronized in terms of the angle and the amplitude; that is they both have the same angle and amplitude. Then, the DFIG can be connected to the grid, and the control system should simultaneously be changed to the grid-connected control.

To ensure smooth connection, the grid-connected control system's initial active and reactive power references and the initial rotor current references are set equal to their instantaneous value at the instant of connection. In addition, the initial slip frequency

and angle of the slip angle estimator of Fig. 4.5 is set equal to their instantaneous value at the instant of connection.

5.3 Simulation and Experiments

5.3.1 Experimental Setup

In the simulation and the experiments, a 1.1 kW DFIG, whose parameters were listed in Table 5.1, is employed. The parameters of the experimental setup, which is shown in Fig. 5.19, were listed in Table 3.2. However, the filtering capacitor C_f in the simulation was different from the experiment and was equal to 10 μF. The GSC consumes a capacitive, reactive power of −600 VAR.

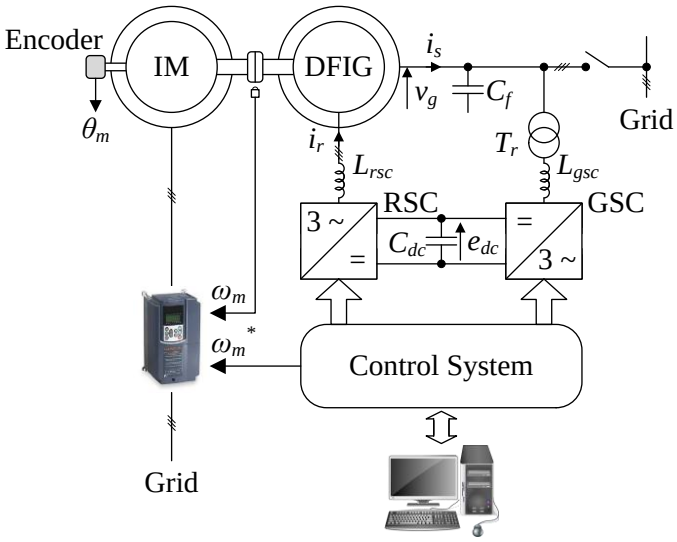

Fig.5.19: Schematic diagram of the experimental setup.

The block diagram of the complete control system during the stand-alone mode is shown in Fig. 5.20, and its parameters are listed in Table 5.2. The PLL circuit of Fig. 3.2 is used to measure the stator voltage frequency.

For the synchronization mode, the control is same as in Fig. 5.20 except for the reference amplitude and angle which are generated using (5.30) and (5.32) respectively.

For grid connection tests, the DFIG is connected to the grid directly after the synchronization is completed. The block diagram of the grid-connected control, whose parameters were listed in Table 3.3, was shown in Fig. 3.20.

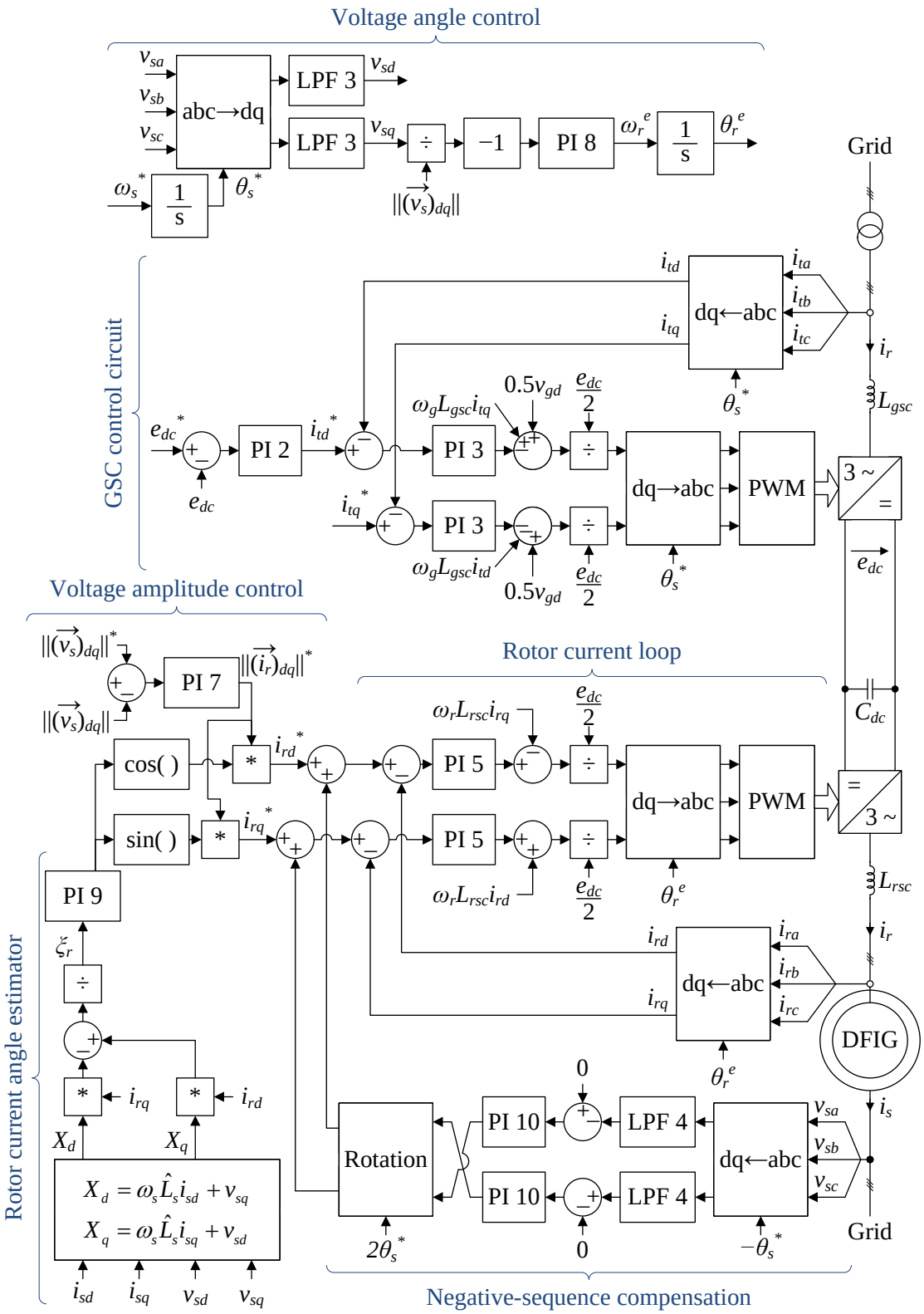

Fig.5.20: Block diagram of the stand-alone control system.

Table 5.2: Parameters of the stand-alone control system.

	K_p	K_i (sec^{-1})	T_f (sec)
LPF 3			0.002
LPF 4			0.08
PI 2	0.2	0.5	
PI 3	20	200	
PI 5	20	1000	
PI 7	0.02	5	
PI 8	80	500	
PI 9	0.085	8.5	
PI 10	0.24	0.5	

5.3.2 Simulation Results

A. Stand-Alone Mode

First, the variable speed operation is investigated. The DFIG speed is varied from a sub-synchronous speed of 0.8 pu to a hyper-synchronous speed of 1.2 pu within 0.6 sec. When the DFIG's speed reaches the synchronous speed, a balanced resistive load of 100 Ω is suddenly connected. The results with the conventional and the modified direct voltage control are shown in Fig. 5.21 and Fig. 5.22 respectively.

The results in Fig. 5.21 and Fig. 5.22 demonstrates the robustness of the direct control method against variation in the speed; thus, it is suitable for variable speed generation systems. In addition, these results support the mathematical analysis: The stator voltage response of both the conventional and the modified method is similar; however, for the conventional method, a new reference frame for the rotor current is defined in which the rotor q-current is zero. This causes the control to lose track of the slip angle. On the other hand, the modified method accurately tracks the slip angle.

As the responses of the conventional and the modified method in the previous test are similar, the importance of obtaining the slip angle is questioned. To demonstrate one advantage of the modified method, a series-resistive-capacitive load, which produces an angle γ_r largely different from −90 degrees, is suddenly connected. During this test, the speed of the DFIG is fixed at a hyper-synchronous speed of 1.2 pu. The load of choice is R = 30 Ω and C = 120 μF, which produces an angle γ_r approximately equal to zero. The results for this test with the conventional method are shown in Fig. 5.23.

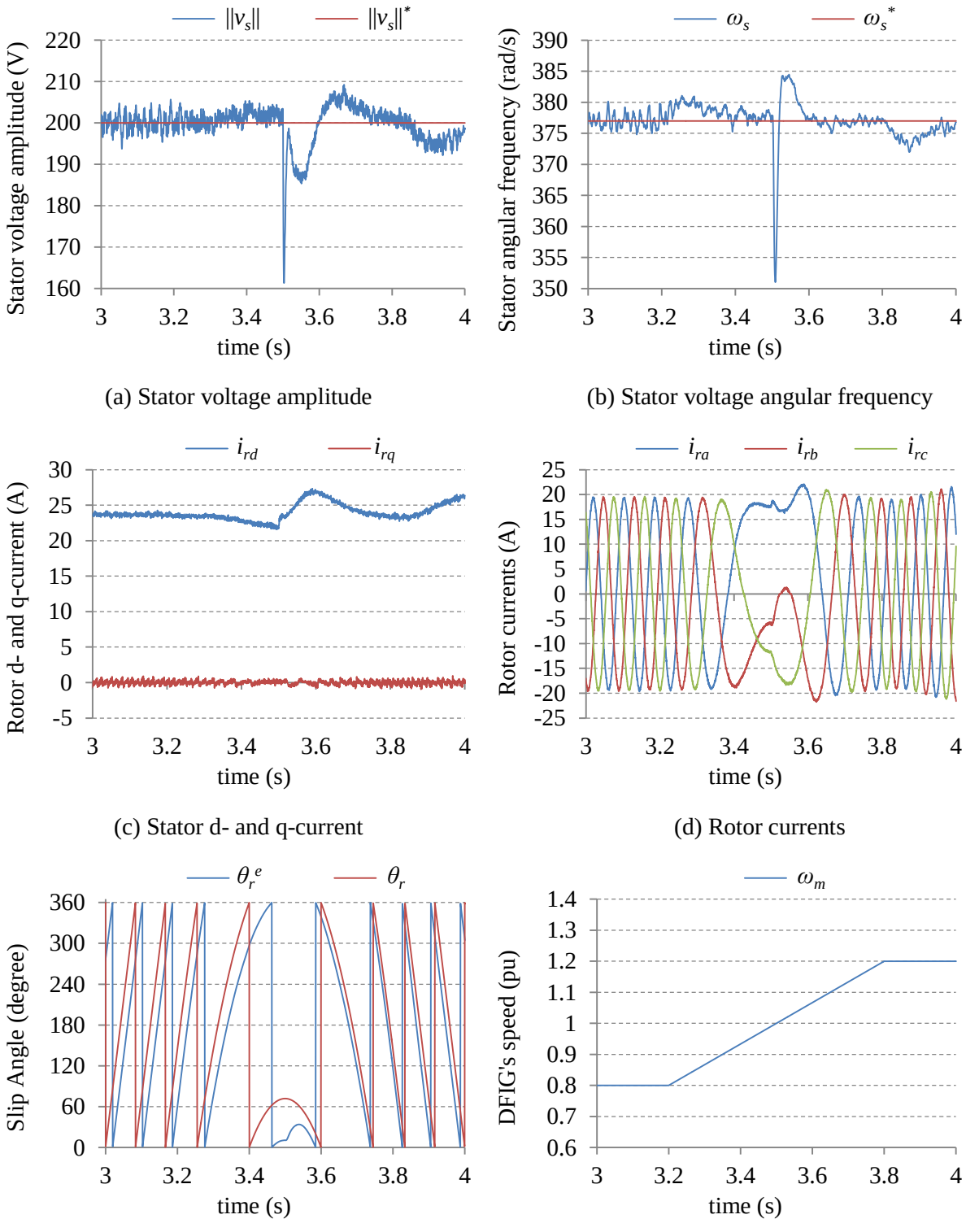

(a) Stator voltage amplitude

(b) Stator voltage angular frequency

(c) Stator d- and q-current

(d) Rotor currents

(e) Estimated and measured slip angle

(f) DFIG's speed

Fig. 5.21: Simulation results for variable speed operation with the conventional direct voltage control, where a resistive load of 100 Ω is connected at 3.5 sec.

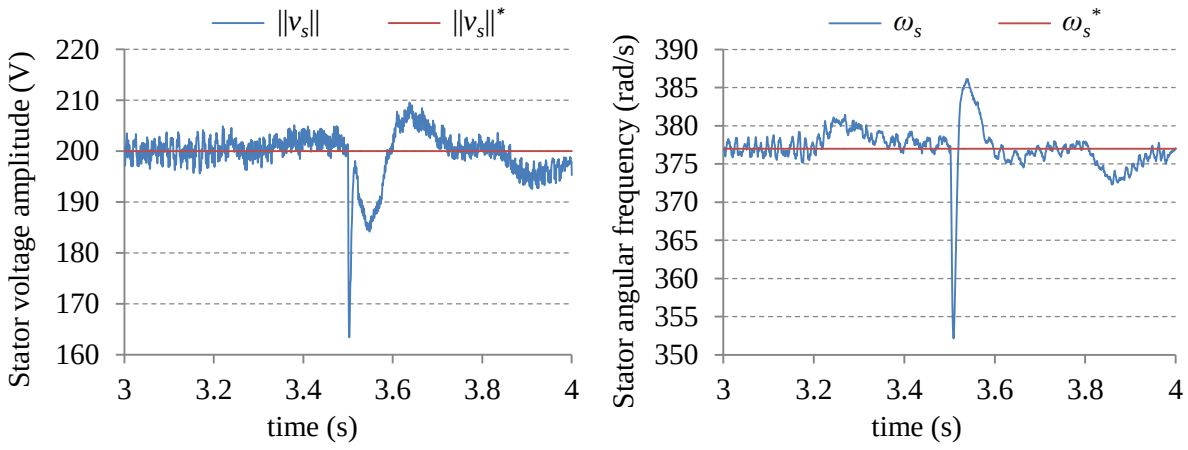

(a) Stator voltage amplitude

(b) Stator voltage angular frequency

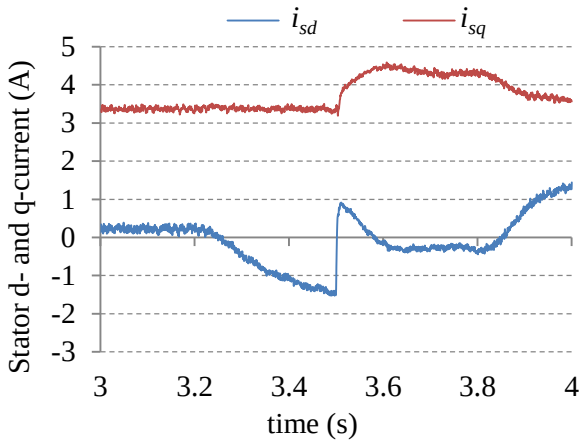

(c) Stator d- and q-current

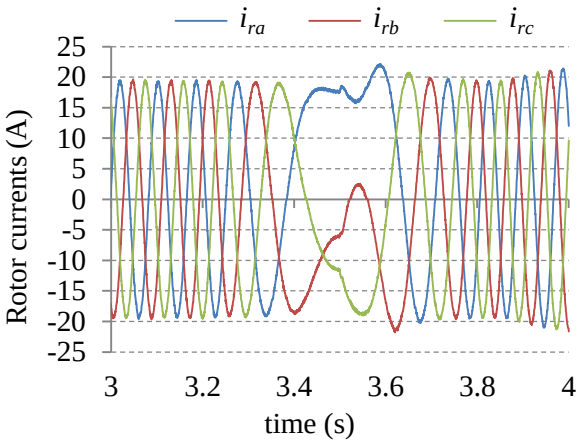

(d) Rotor currents

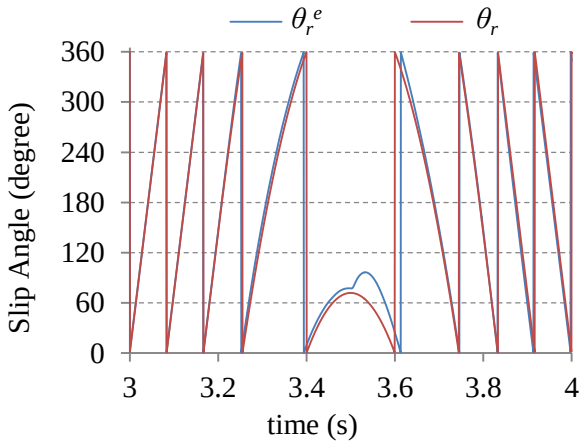

(e) Estimated and measured slip angle

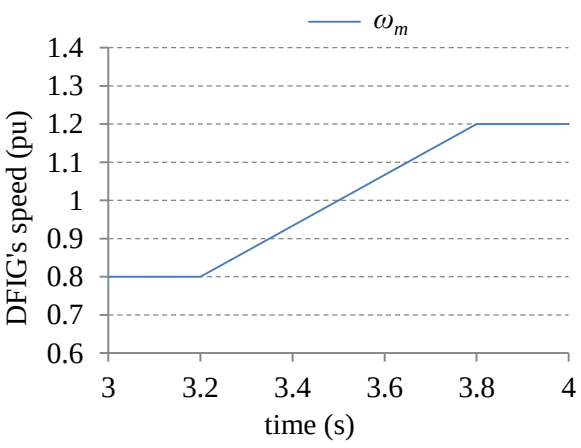

(f) DFIG's speed

Fig. 5.22: Simulation results for variable speed operation with the modified direct voltage control, where a resistive load of 100 Ω is connected at 3.5 sec.

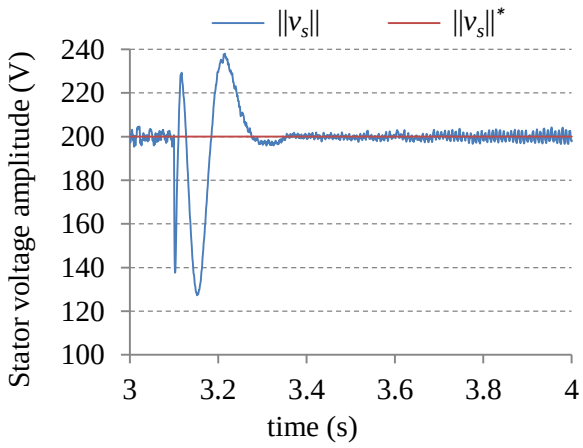

(a) Stator voltage amplitude

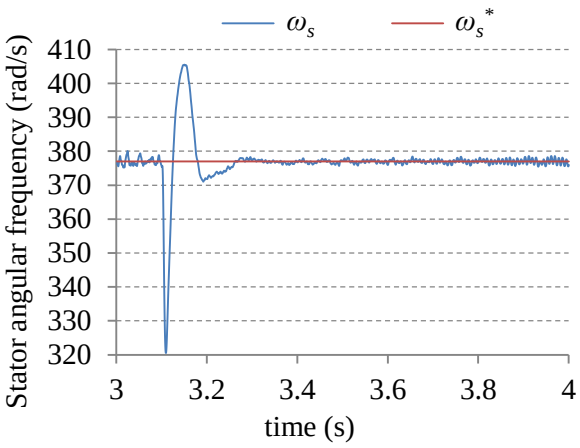

(b) Stator voltage angular frequency

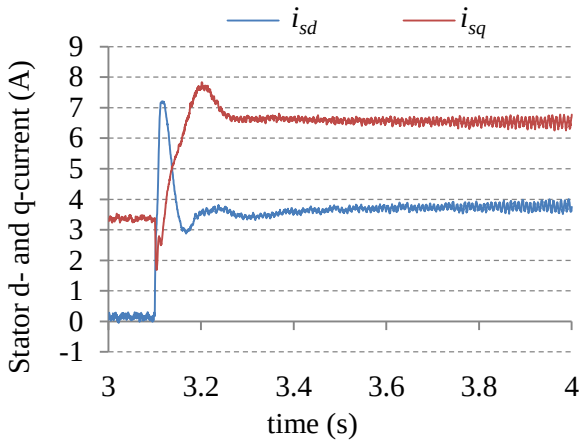

(c) Stator d- and q-current

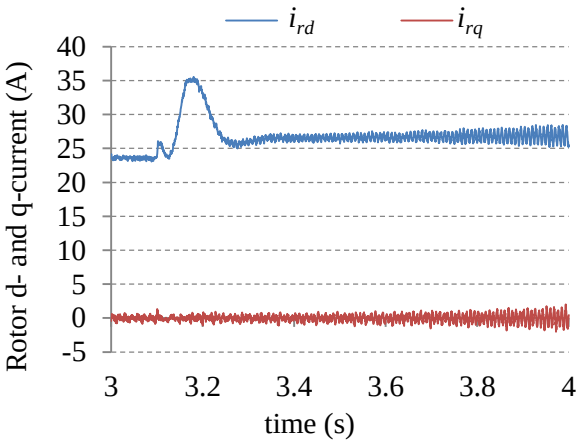

(d) Rotor d- and q-current

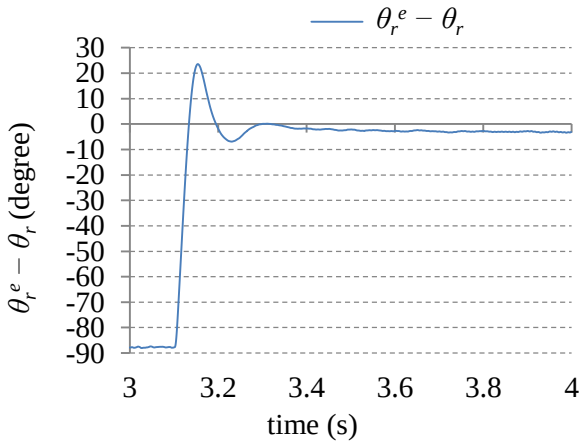

(e) Estimation error of the slip angle

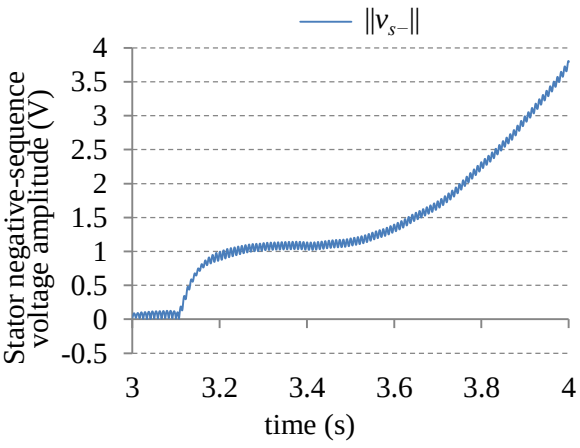

(f) Stator negative-sequence voltage amplitude

Fig. 5.23: Simulation results of the conventional direct voltage control for sudden connection of series-resistive-capacitive load of R = 30 Ω and C = 120 μF, with ω_m = 1.2 pu.

From Fig. 5.23, this capacitive load causes a large variation in the angle γ_r, from around −90 degrees to around zero degree. Although the amplitude and the angle control are stable, the negative-sequence compensation becomes unstable even though the load is balanced. The results of this test at steady-state are shown in Fig. 5.24.

The negative-sequence compensation produces rotor negative-sequence currents which increase the stator negative-sequence voltage. These rotor negative-sequence currents keep increasing until, at steady-state, the PI controllers of the negative-sequence compensation are saturated. Such stator negative-sequence voltage would cause malfunctioning or even tripping of electrical equipment.

The same capacitive load is considered with the modified direct voltage control. The results at the instant of load connection and at steady-state are shown in Fig. 5.25 and Fig. 5.26 respectively. Since the modified direct voltage control extracts the slip angle, the negative-sequence compensation control stability is independent of the load, and the whole control system is stable.

Next, the performance under unbalanced load is investigated. First, an unbalanced resistive-capacitive load, which is given in Table 5.3, is used. The results at steady-state for the conventional and the modified direct voltage control are shown in Fig. 5.27 and Fig. 5.28 respectively.

Table 5.3: Parameters of the simulation's capacitive load

	R (Ω)	C (μF)
Phase-a	20	120
Phase-b	30	120
Phase-c	30	120

Similar to the balanced capacitive load case, the unbalanced capacitive load causes the negative-sequence compensation with the conventional method to become unstable, because of the absence of the slip angle. On the other hand, the modified method obtains the slip angle and, consequently, the negative sequence compensation is stable regardless of the load.

The unstable region of the negative-sequence compensation corresponds to a limited range of capacitive loads which produces an angle γ_r largely different from −90 degrees. For inductive loads, the negative-sequence compensation is always stable, and the conventional and the modified method will have similar responses.

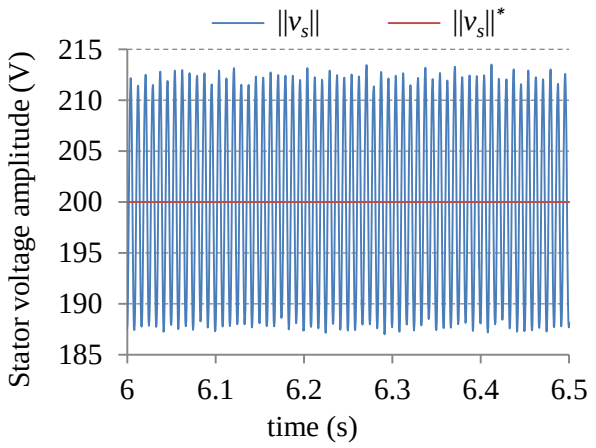

(a) Stator voltage amplitude

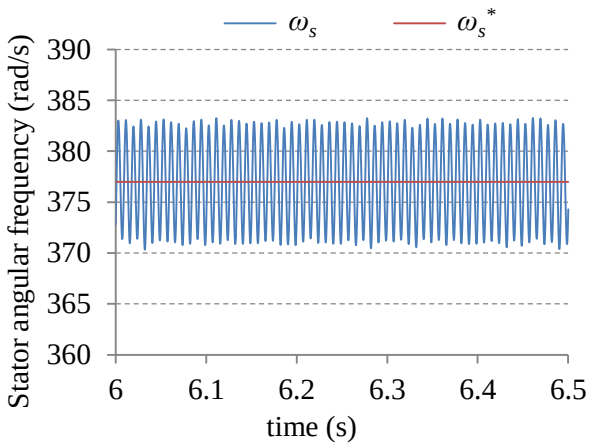

(b) Stator voltage angular frequency

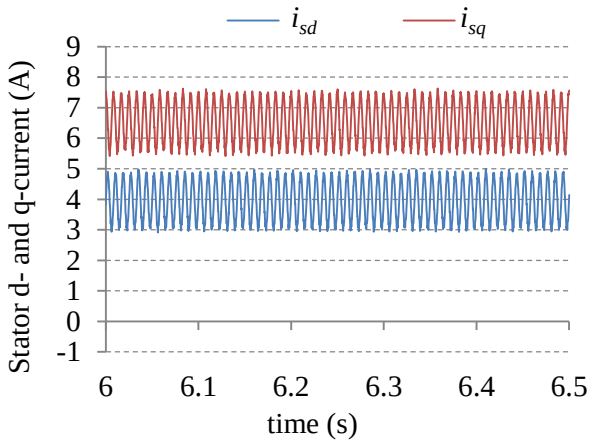

(c) Stator d- and q-current

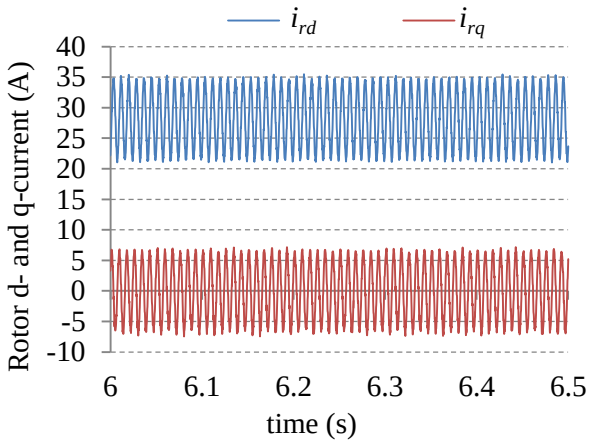

(d) Rotor d- and q-current

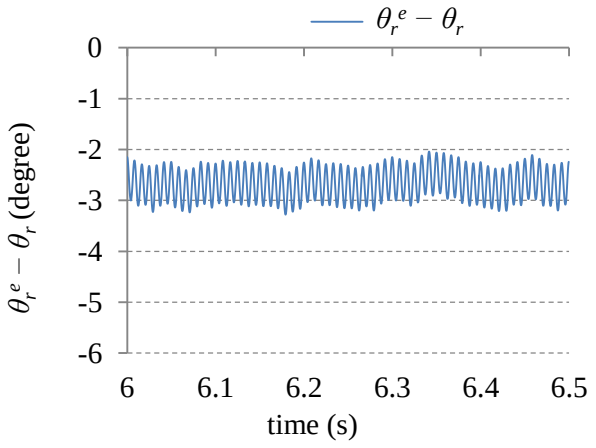

(e) Estimation error of the slip angle

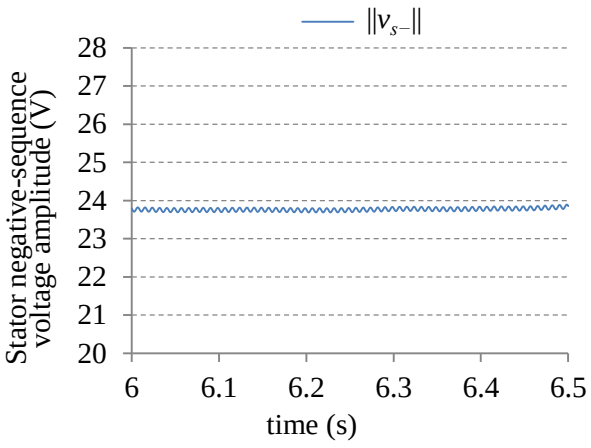

(f) Stator negative-sequence voltage amplitude

Fig. 5.24: Simulation results of the conventional direct voltage control at steady-state with a series-resistive-capacitive load of R = 30 Ω and C = 120 μF, and ω_m = 1.2 pu.

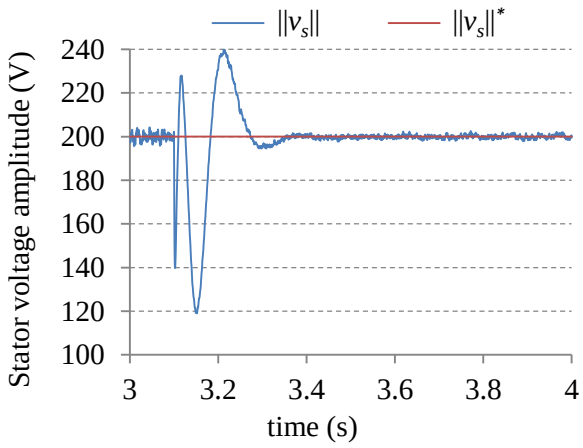

(a) Stator voltage amplitude

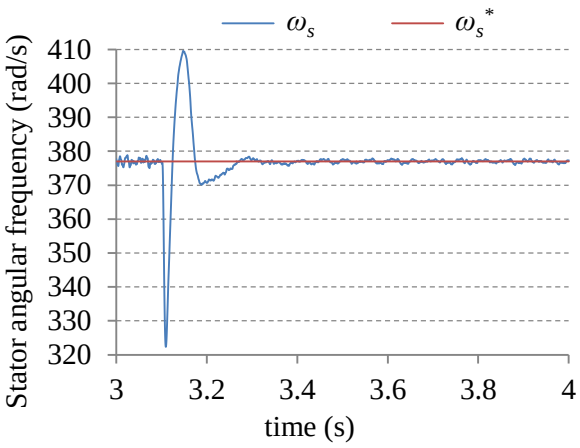

(b) Stator voltage angular frequency

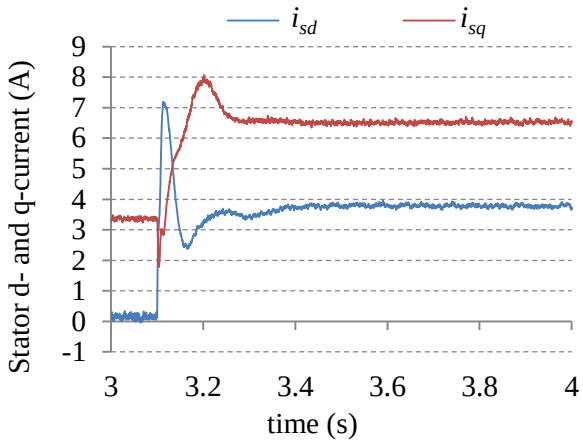

(c) Stator d- and q-current

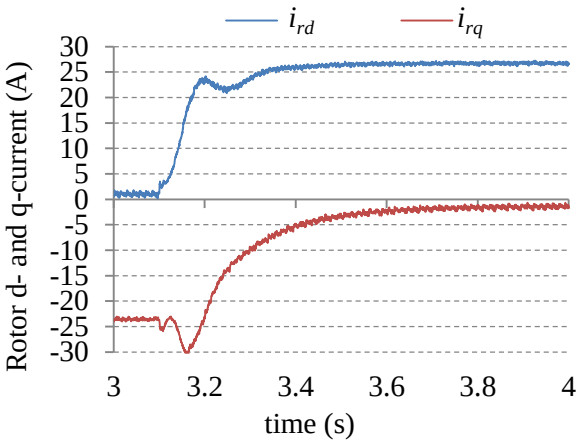

(d) Rotor d- and q-currents

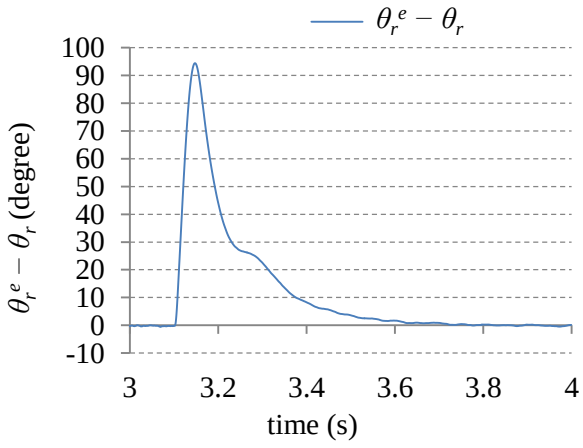

(e) Estimation error of the slip angle

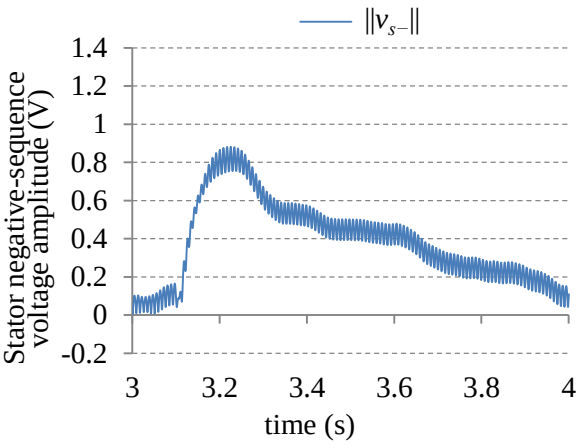

(f) Stator negative-sequence voltage amplitude

Fig. 5.25: Simulation results of the modified direct voltage control for sudden connection of series-resistive-capacitive load of R = 30 Ω and C = 120 μF, with ω_m = 1.2 pu.

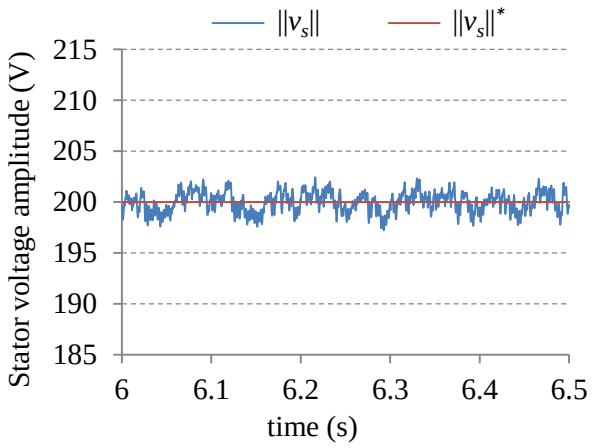

(a) Stator voltage amplitude

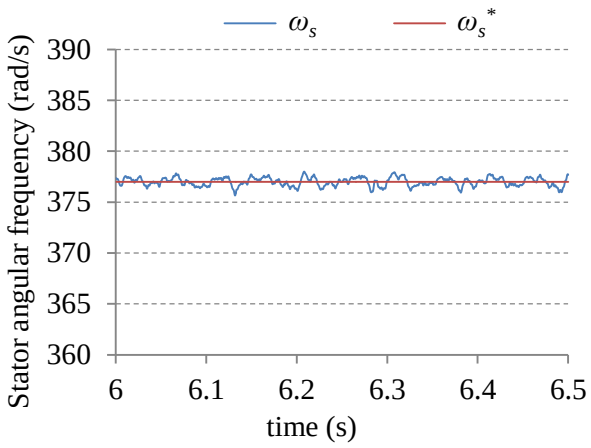

(b) Stator voltage angular frequency

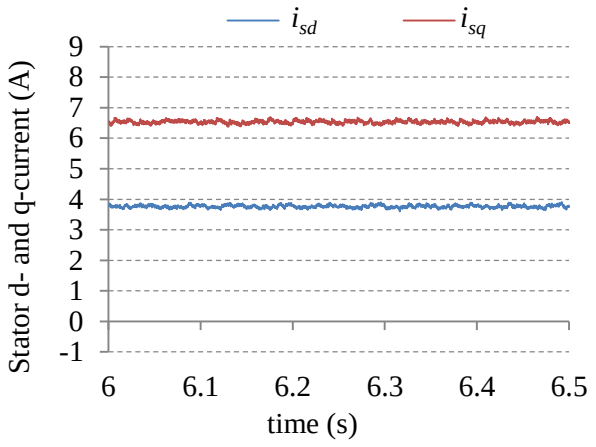

(c) Stator d- and q-current

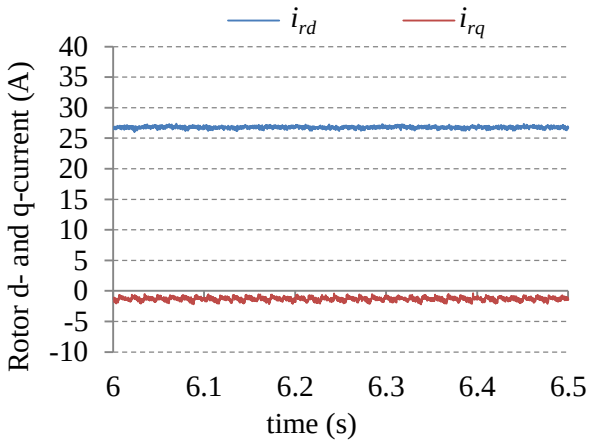

(d) Rotor d- and q-currents

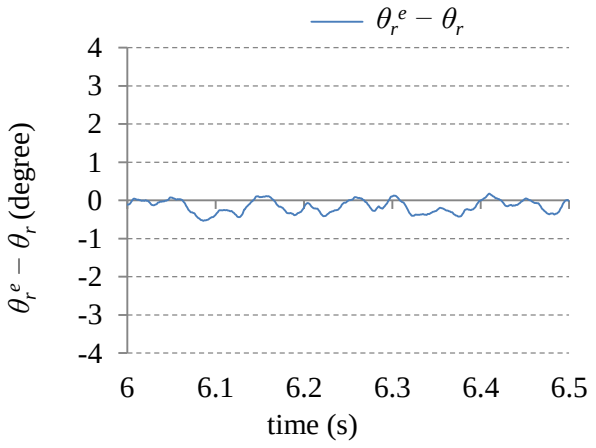

(e) Estimation error of the slip angle

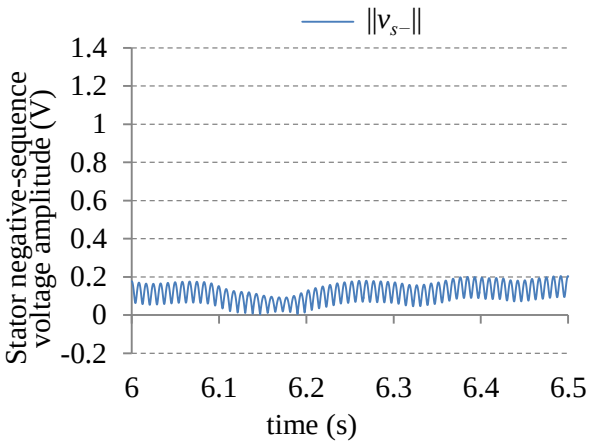

(f) Stator negative-sequence voltage amplitude

Fig. 5.26: Simulation results of the modified direct voltage control at steady-state with a series-resistive-capacitive load of R = 30 Ω and C = 120 μF, and ω_m = 1.2 pu.

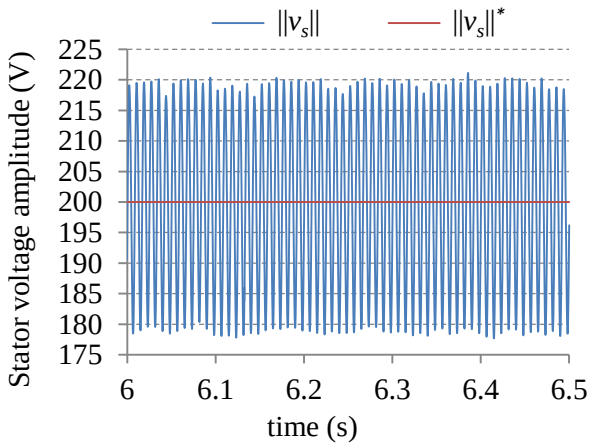

(a) Stator voltage amplitude

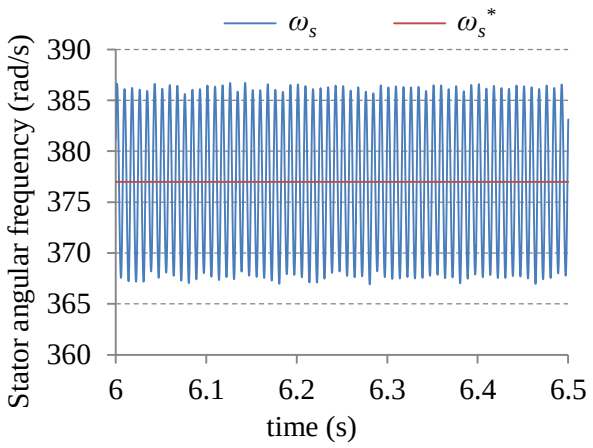

(b) Stator voltage angular frequency

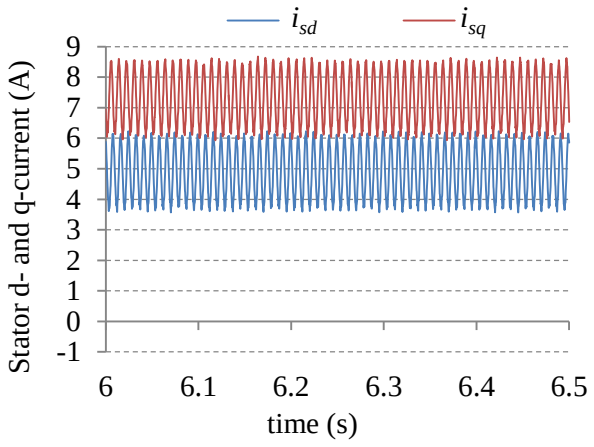

(c) Stator d- and q-current

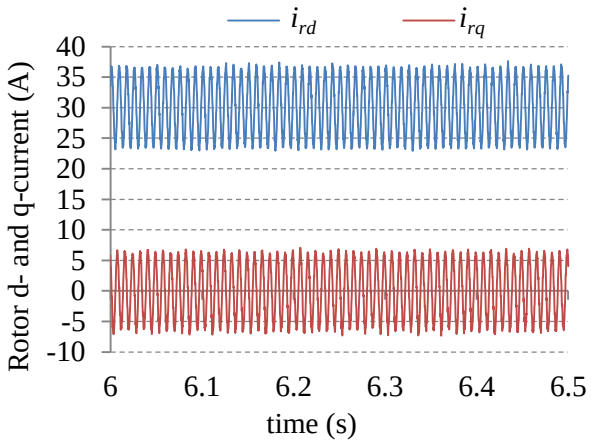

(d) Rotor d- and q-current

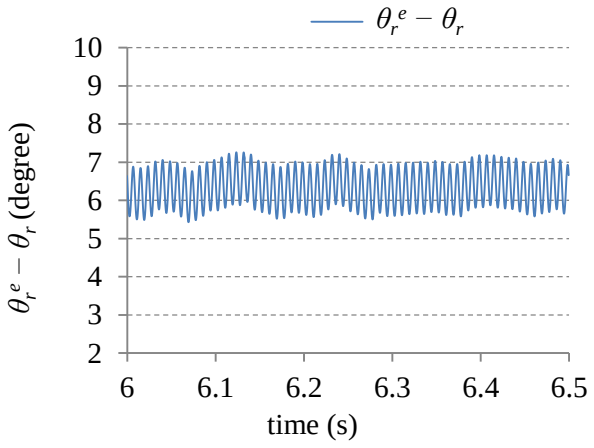

(e) Estimation error of the slip angle

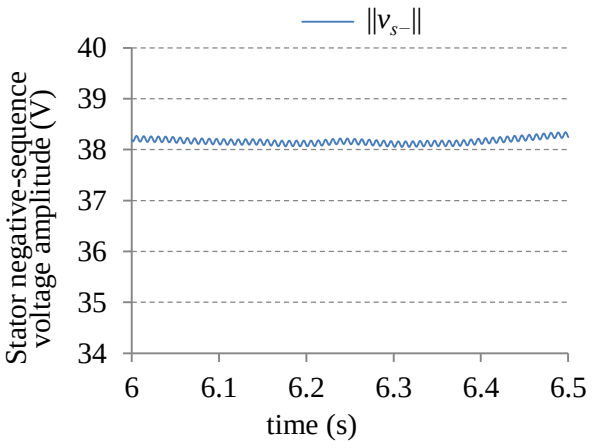

(f) Stator negative-sequence voltage amplitude

Fig. 5.27: Simulation results of the conventional direct voltage control at steady-state with the unbalanced series-resistive-capacitive load of Table 5.3, and ω_m = 1.2 pu.

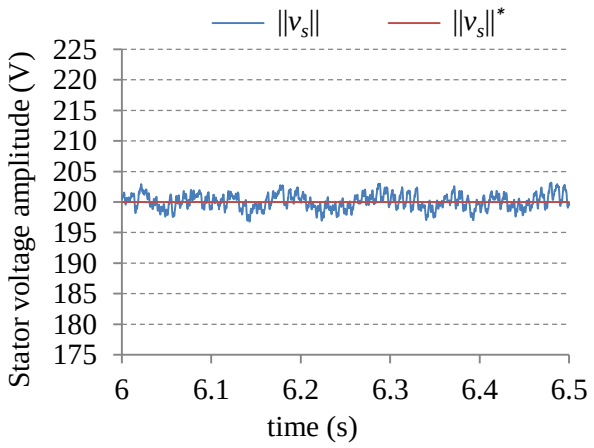

(a) Stator voltage amplitude

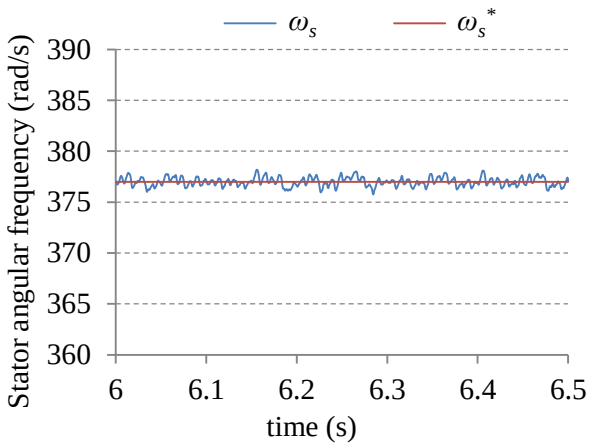

(b) Stator voltage angular frequency

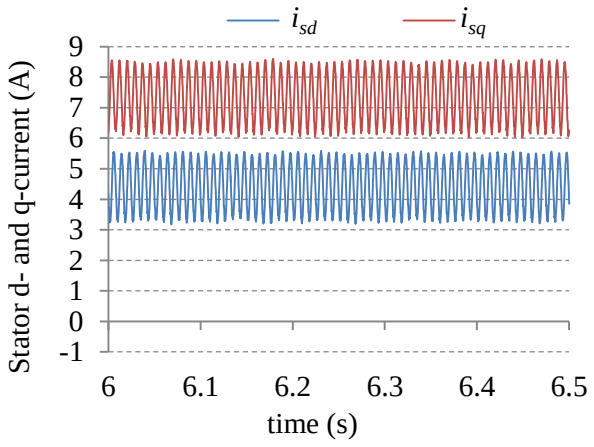

(c) Stator d- and q-current

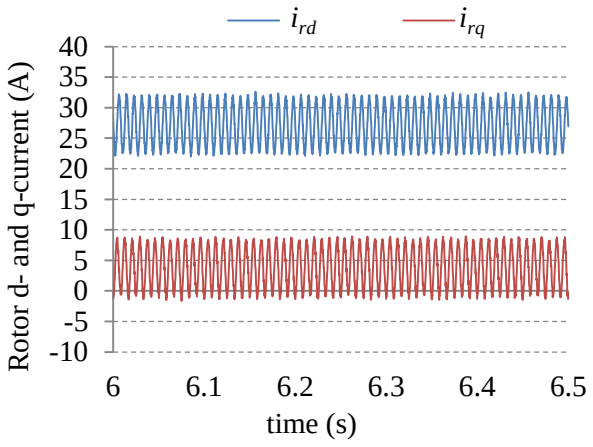

(d) Rotor d- and q-current

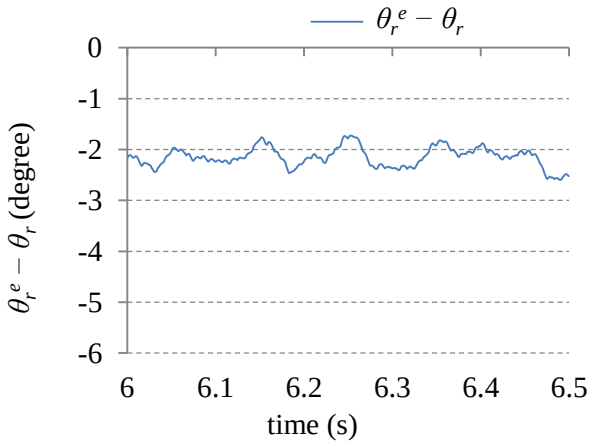

(e) Estimation error of the slip angle

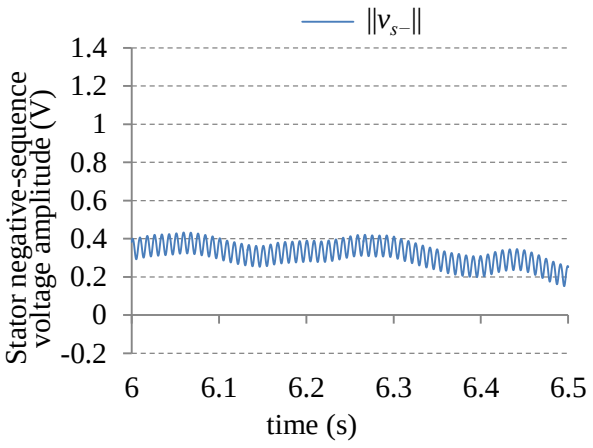

(f) Stator negative-sequence voltage amplitude

Fig. 5.28: Simulation results of the modified direct voltage control at steady-state with the unbalanced series-resistive-capacitive load of Table 5.3, and ω_m = 1.2 pu.

Second, an unbalanced resistive-inductive load, which is given in Table 5.4, is used. During this test the DFIG speed is fixed at a sub-synchronous speed of 0.9 pu. The results, for the conventional method, at the instant of connection and during steady-state are shown in Fig. 5.29 and Fig. 5.30 respectively, while the results, for the modified method, at the instant of connection and during steady-state are shown in Fig. 5.31 and Fig. 5.32 respectively.

Table 5.4: Parameters of the simulation's inductive load

	R (Ω)	L (H)
Phase-a	200	0.05
Phase-b	100	0.15
Phase-c	100	0.15

From the previous results, the performance of the conventional and the modified method is similar for inductive loads, and the negative-sequence compensation is stable. The main difference is the slip angle: The conventional method cannot obtain the slip angle, while the modified method successfully tracks the slip angle. There is, however, a small estimation error which results from the ignored stator winding resistance.

B. Synchronization Mode

In the following tests, the duration of the synchronization mode is 2.5 sec; it starts at 2.1 sec and finishes at 4.6 sec. The DFIG remains in the stand-alone mode after the synchronization is completed. The DFIG speed is fixed at the synchronous speed.

First, the synchronization mode with no load condition is considered. The initial difference between the angle of the stator voltage and the angle of the grid voltage is equal to –180 degrees, which produces the maximum frequency variation. The results with the conventional and the modified direct voltage control are shown in Fig. 5.33 and Fig. 5.34 respectively.

Finally, the synchronization mode with a balanced series-resistive-inductive load, which is R = 200 Ω and L = 0.1 H, is considered. The initial difference between the angle of the stator voltage and the angle of the grid voltage is equal to 150 degrees. The results with the conventional and the modified direct voltage control are shown in Fig. 5.35 and Fig. 5.36 respectively.

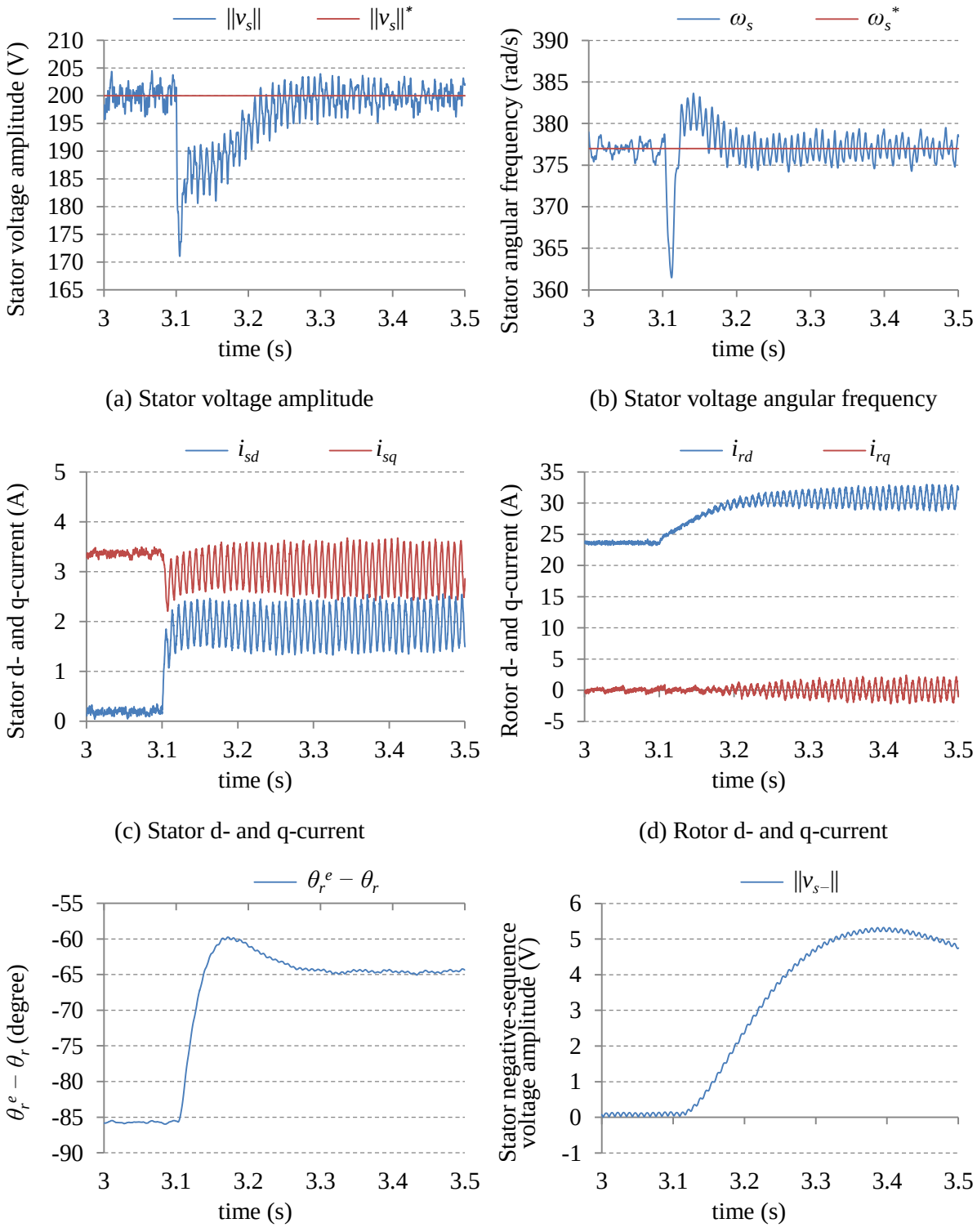

(a) Stator voltage amplitude

(b) Stator voltage angular frequency

(c) Stator d- and q-current

(d) Rotor d- and q-current

(e) Estimation error of the slip angle

(f) Stator negative-sequence voltage amplitude

Fig. 5.29: Simulation results of the conventional direct voltage control for sudden connection of an unbalanced series-resistive-inductive load, and ω_m = 0.9 pu.

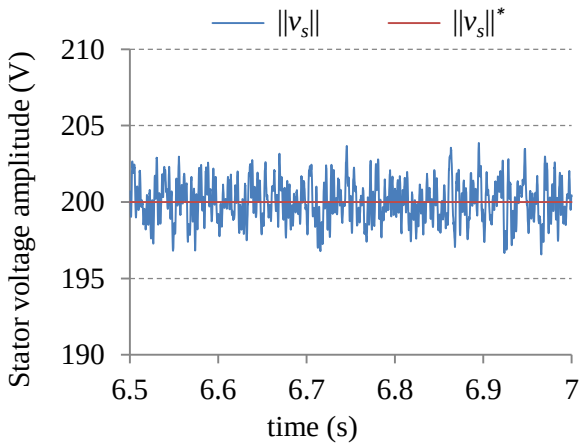

(a) Stator voltage amplitude

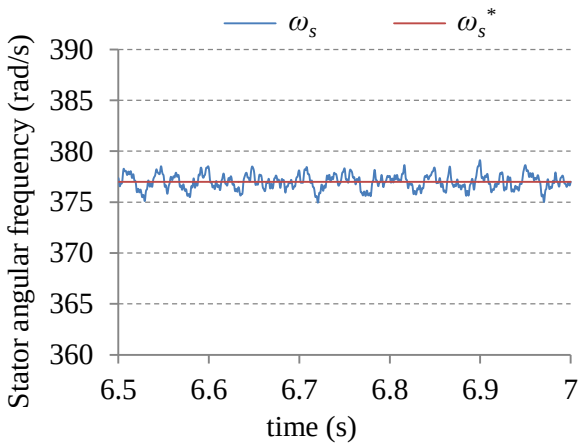

(b) Stator voltage angular frequency

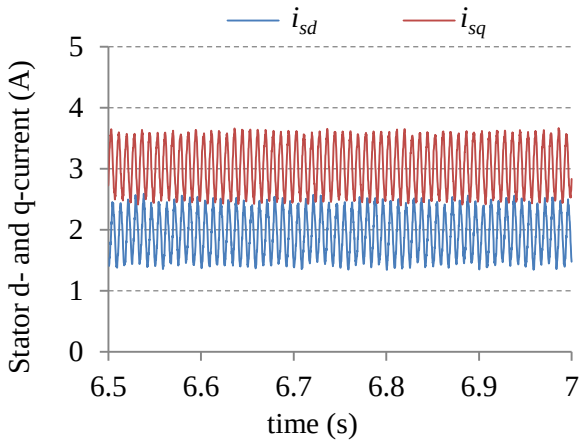

(c) Stator d- and q-current

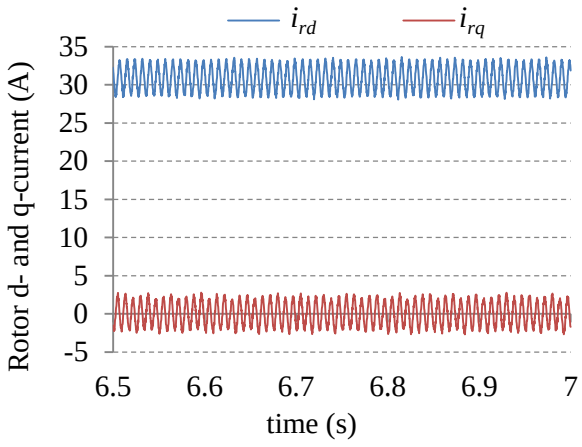

(d) Rotor d- and q-current

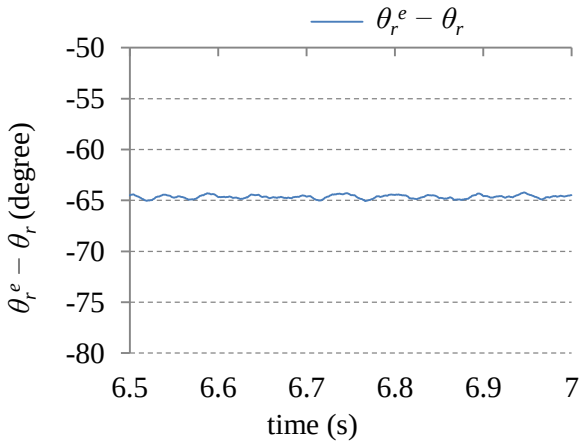

(e) Estimation error of the slip angle

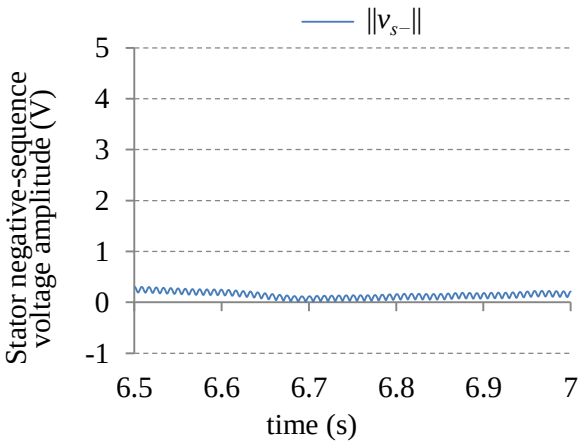

(f) Stator negative-sequence voltage amplitude

Fig. 5.30: Simulation results of the conventional direct voltage control at steady-state with an unbalanced series-resistive-inductive load, and ω_m = 0.9 pu.

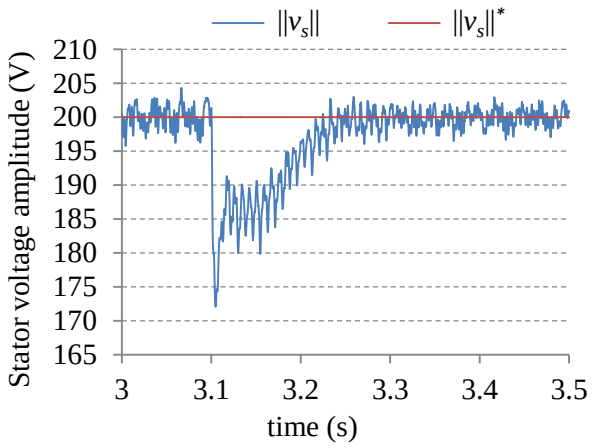

(a) Stator voltage amplitude

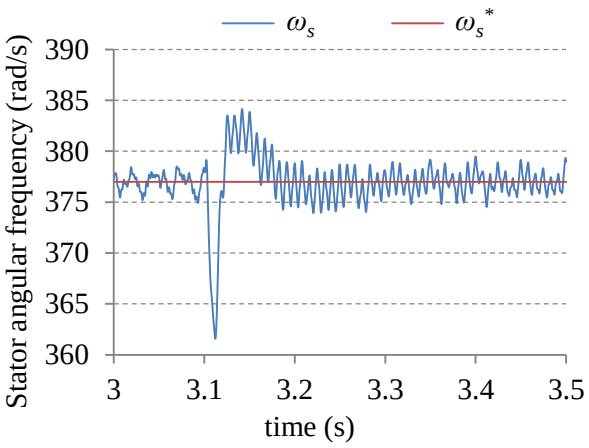

(b) Stator voltage angular frequency

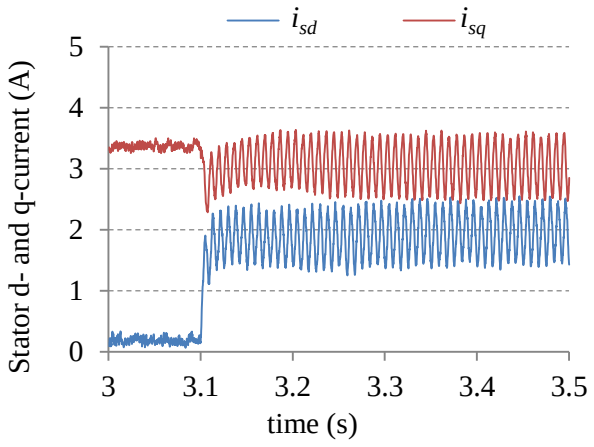

(c) Stator d- and q-current

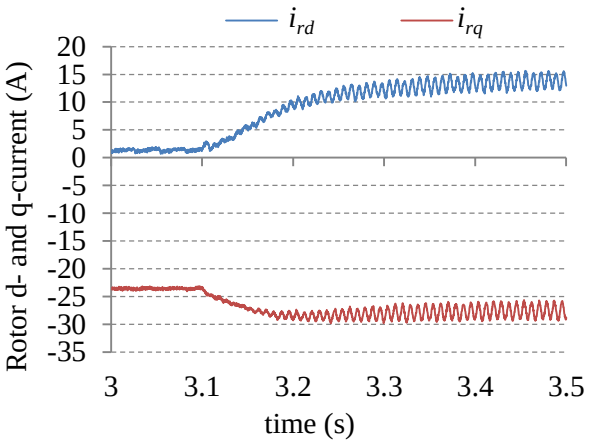

(d) Rotor d- and q-current

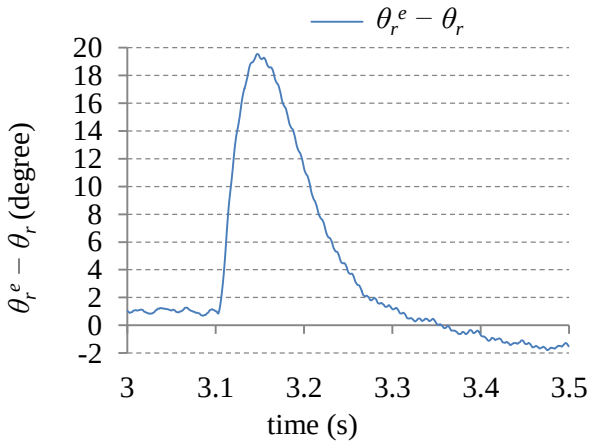

(e) Estimation error of the slip angle

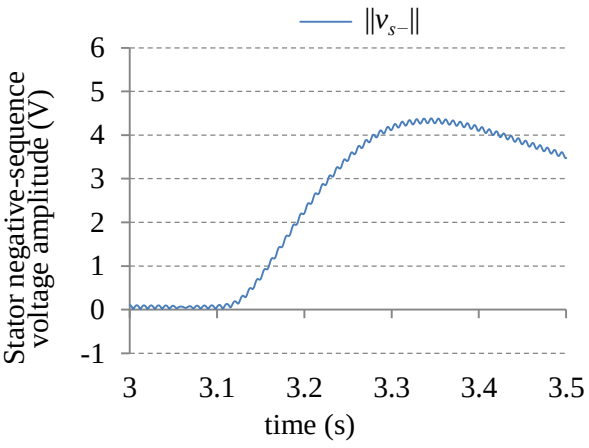

(f) Stator negative-sequence voltage amplitude

Fig. 5.31: Simulation results of the modified direct voltage control for sudden connection of an unbalanced series-resistive-inductive load, and ω_m = 0.9 pu.

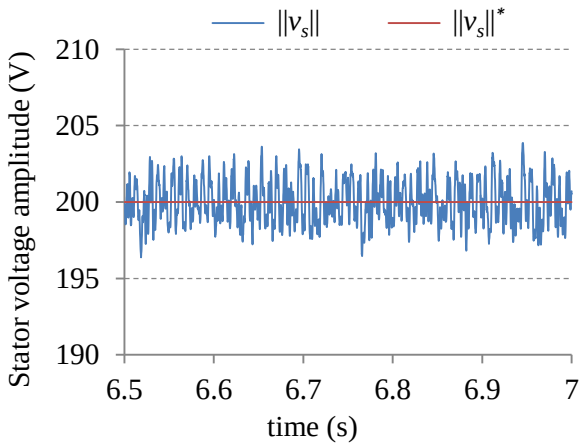

(a) Stator voltage amplitude

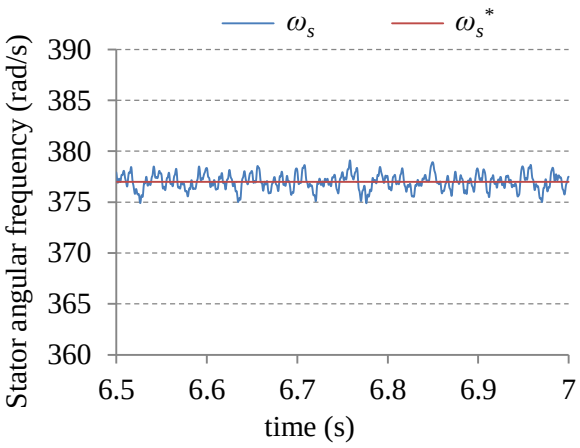

(b) Stator voltage angular frequency

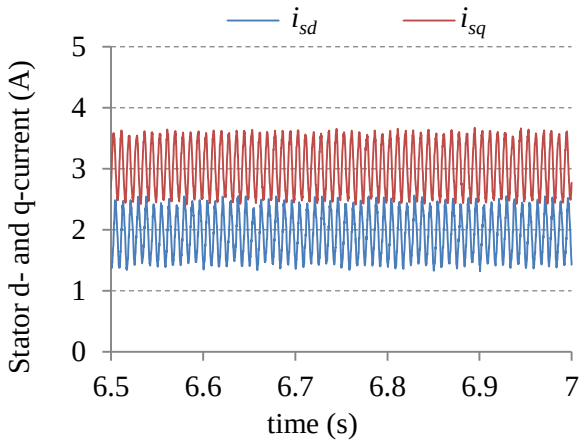

(c) Stator d- and q-current

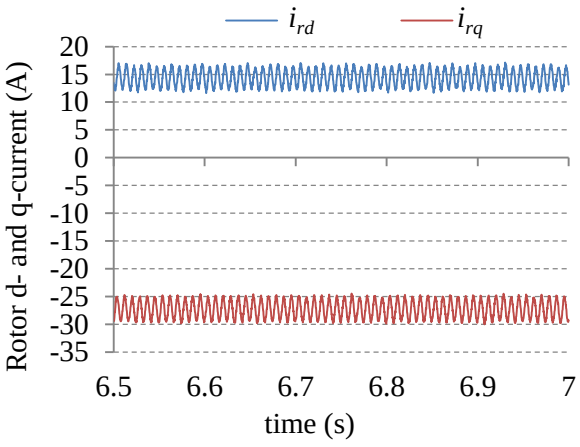

(d) Rotor d- and q-current

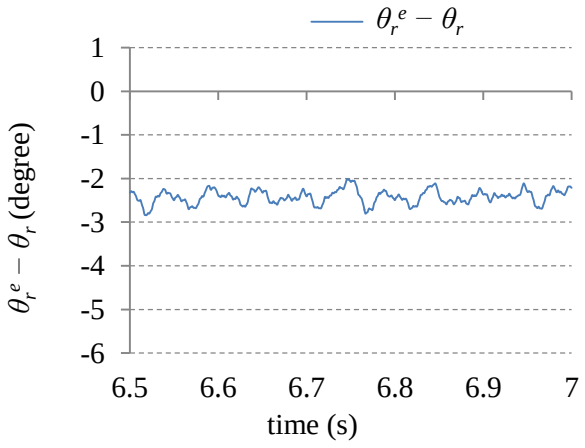

(e) Estimation error of the slip angle

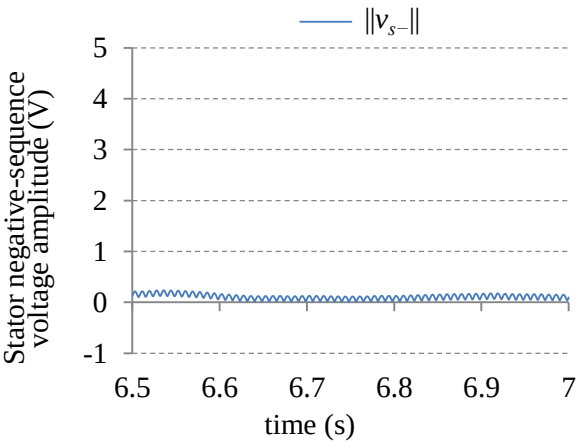

(f) Stator negative-sequence voltage amplitude

Fig. 5.32: Simulation results of the modified direct voltage control at steady-state with an unbalanced series-resistive-inductive load, and ω_m = 0.9 pu.

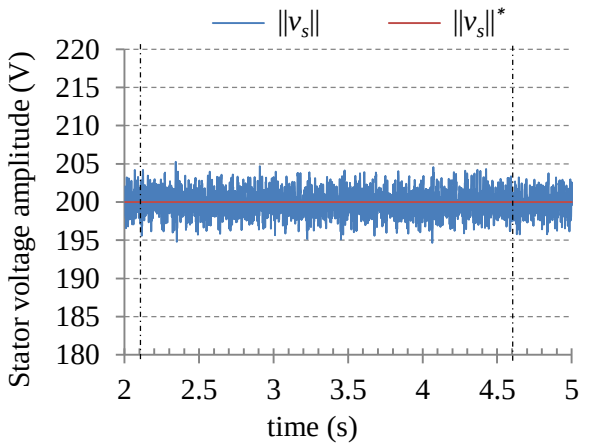

(a) Stator voltage amplitude

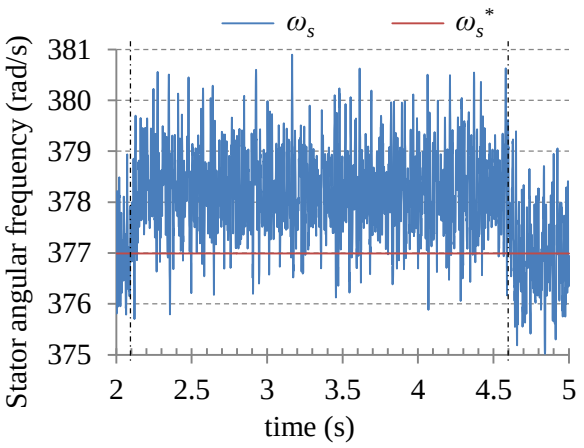

(b) Stator voltage angular frequency

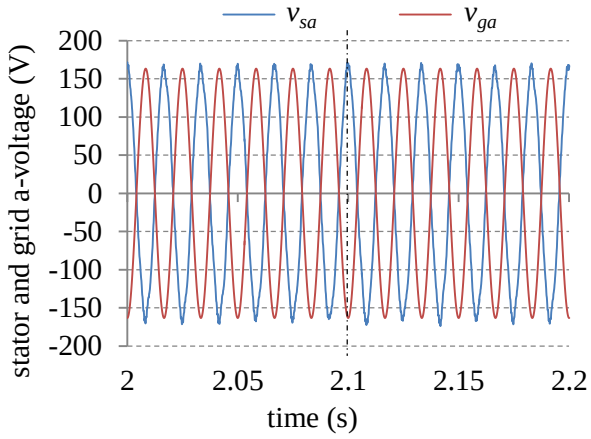

(c) Stator and grid a-voltage at the beginning of synchronization

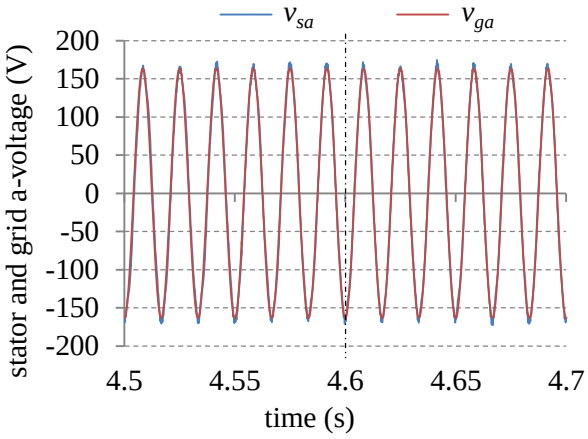

(d) Stator and grid a-voltage at the end of synchronization

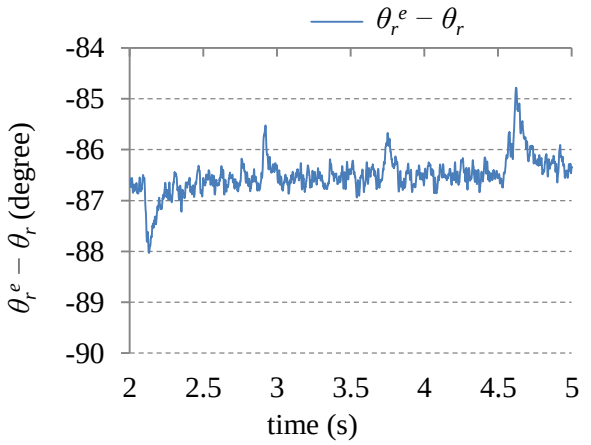

(e) Estimation error of the slip angle

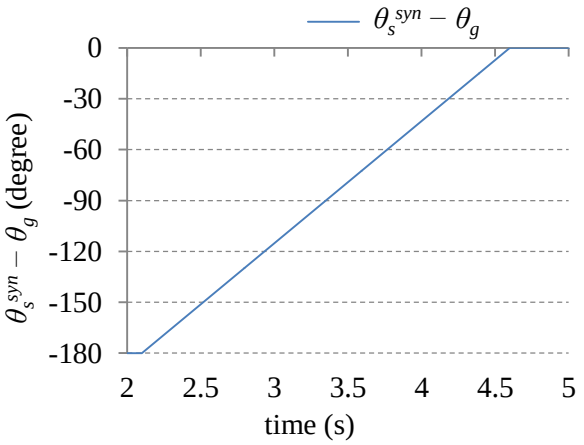

(f) Synchronization and grid angle difference

Fig. 5.33: Simulation results of the conventional direct voltage control for the synchronization with no load condition and ω_m = 1.0 pu.

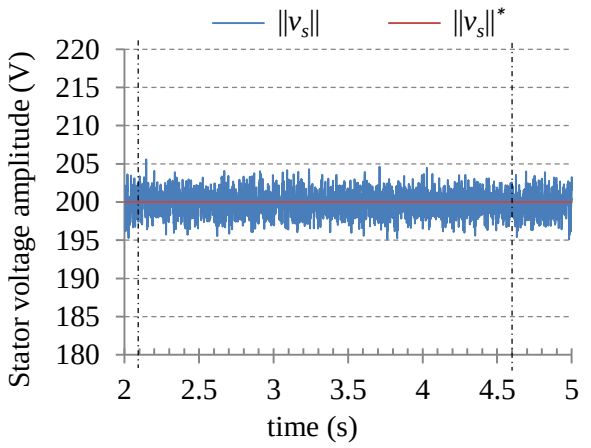

(a) Stator voltage amplitude

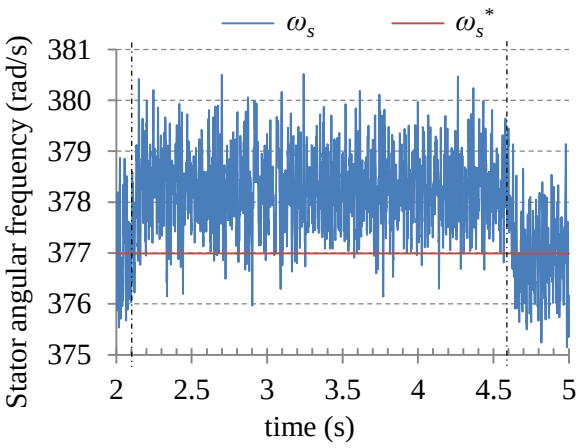

(b) Stator voltage angular frequency

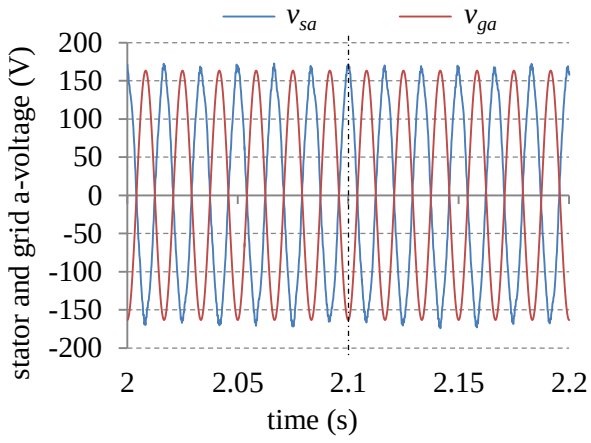

(c) Stator and grid a-voltage at the beginning of synchronization

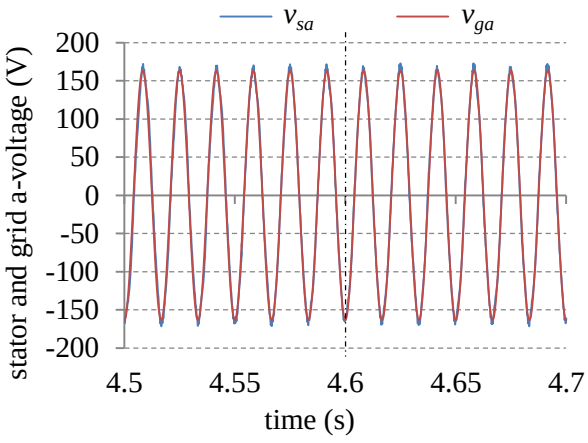

(d) Stator and grid a-voltage at the end of synchronization

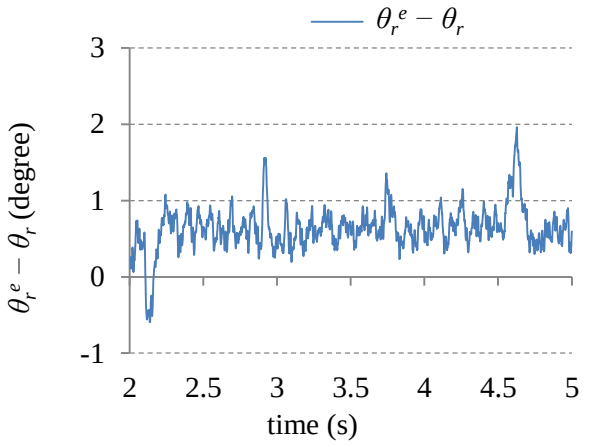

(e) Estimation error of the slip angle

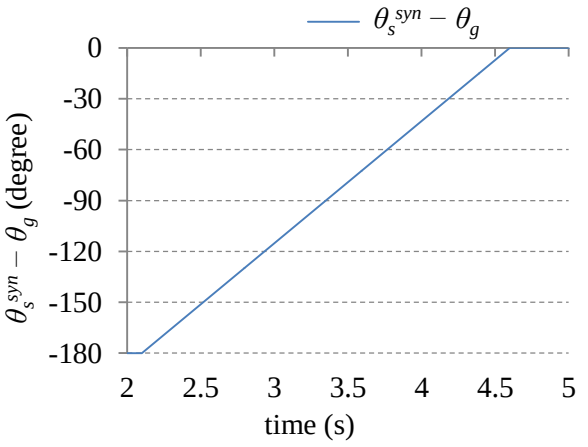

(f) Synchronization and grid angle difference

Fig. 5.34: Simulation results of the modified direct voltage control for the synchronization with no load condition and ω_m = 1.0 pu.

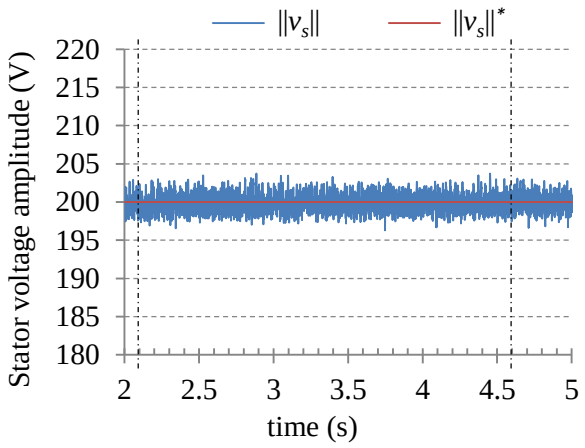

(a) Stator voltage amplitude

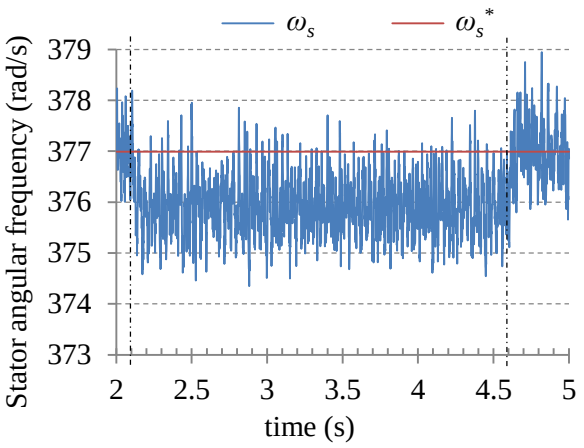

(b) Stator voltage angular frequency

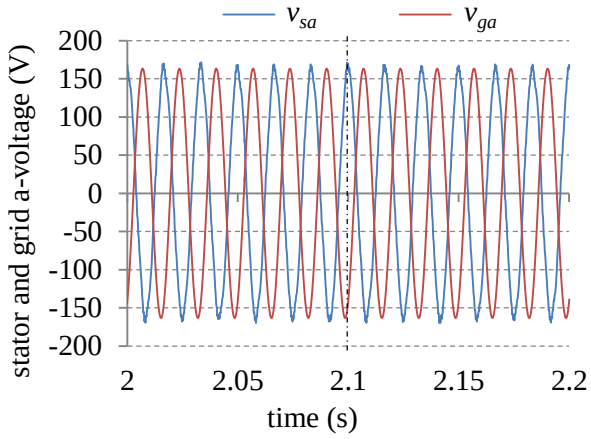

(c) Stator and grid a-voltage at the beginning of synchronization

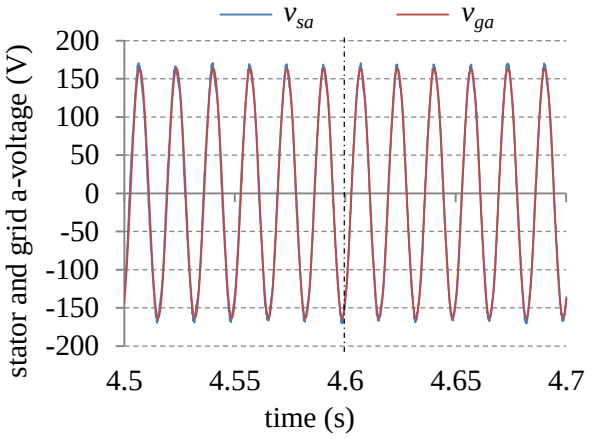

(d) Stator and grid a-voltage at the end of synchronization

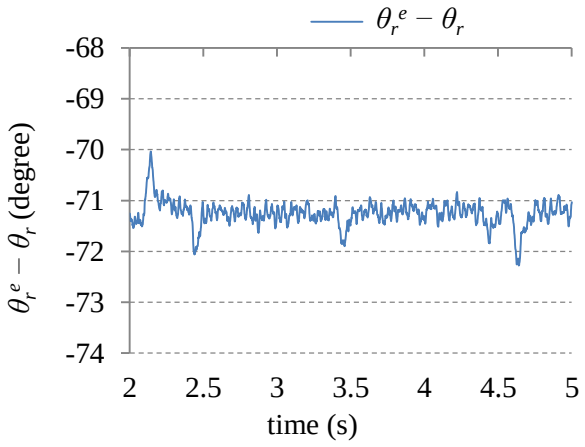

(e) Estimation error of the slip angle

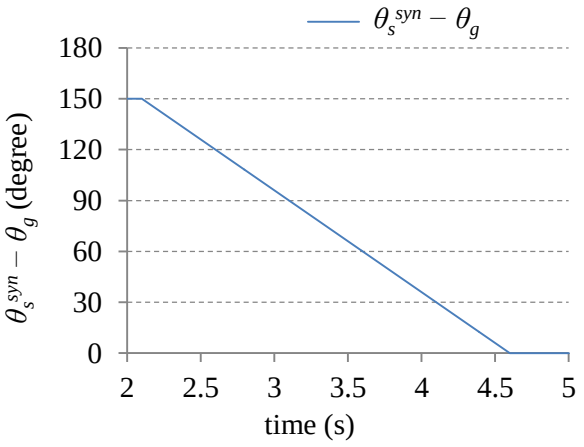

(f) Synchronization and grid angle difference

Fig. 5.35: Simulation results of the conventional direct voltage control for the synchronization with R-L load of R = 200 Ω and L = 0.1 H and ω_m = 1.0 pu.

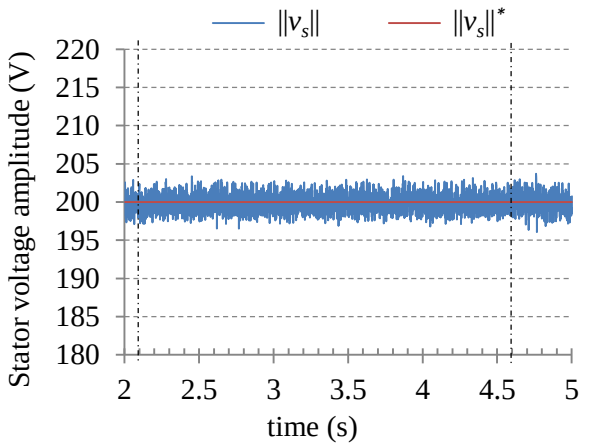

(a) Stator voltage amplitude

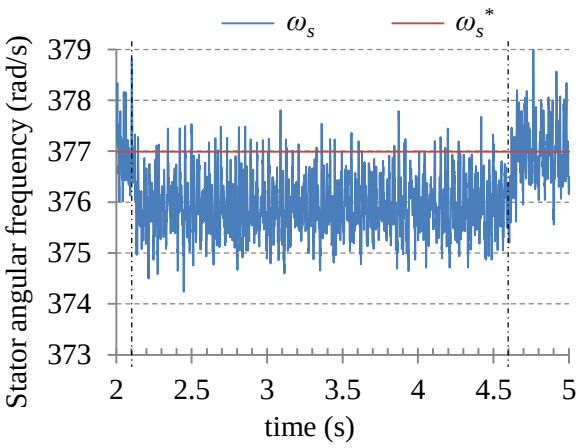

(b) Stator voltage angular frequency

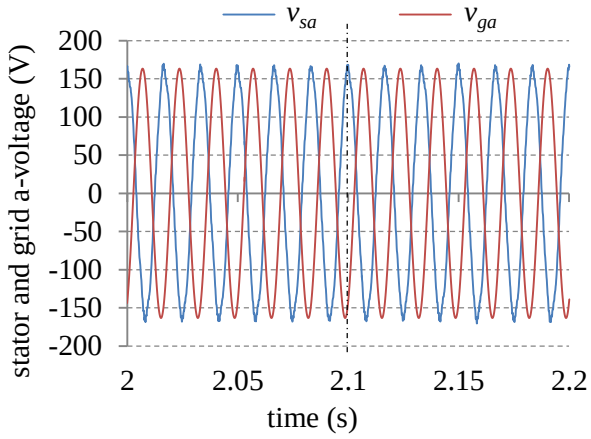

(c) Stator and grid a-voltage at the beginning of synchronization

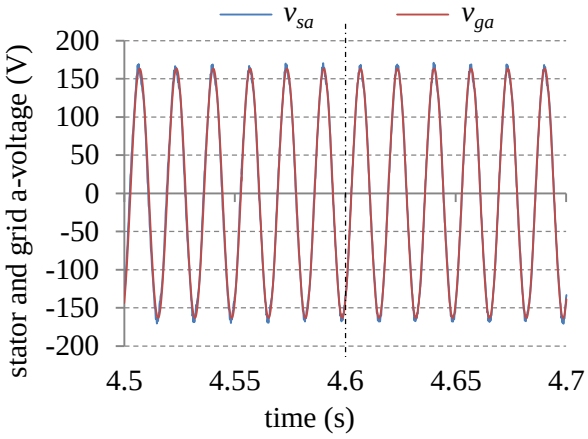

(d) Stator and grid a-voltage at the end of synchronization

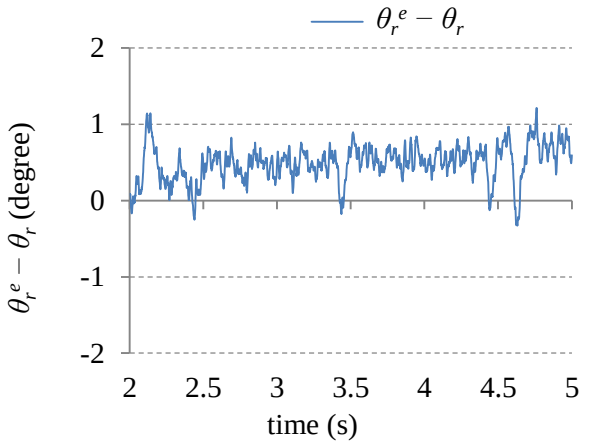

(e) Estimation error of the slip angle

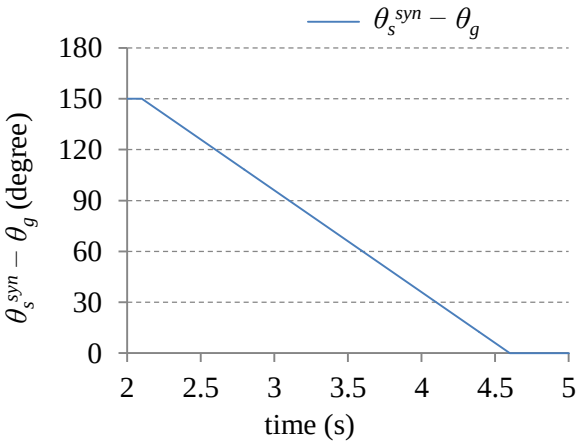

(f) Synchronization and grid angle difference

Fig. 5.36: Simulation results of the modified direct voltage control for the synchronization with R-L load of R = 200 Ω and L = 0.1 H and ω_m = 1.0 pu.

From the results in Fig. 5.33 to Fig. 5.36, both the conventional and the modified direct voltage control successfully synchronize the stator voltage with the grid voltage. During the synchronization mode, the frequency of the stator voltage is slightly varied from the nominal frequency. This variation depends on the initial difference between the angle of the stator and the angle of the grid.

The maximum frequency variation occurs when the initial angle difference is equal to ±180 degrees as in Fig. 5.33 and Fig. 5.34. The average frequency variation, in this case, is equal to 0.2 Hz.

Although the stator and the grid voltage are synchronized in Fig. 5.33 and Fig. 5.35, the conventional method produces a large error in the slip angle; this error will produce inrush currents. On the other hand, the modified method would achieve smooth connection because the modified direct voltage control obtains the slip angle which is approximately equal to the slip angle of grid-connected mode.

C. Connection to the Grid

In the follow tests, the DFIG is connected to the grid directly at the end of the synchronization mode at 4.6 sec, and the control system is instantly changed to the grid-connected mode. During all the following tests, the DFIG speed is fixed at a sub-synchronous speed of 0.8 pu.

First, the connection to the grid under no load condition is investigated. The results with the conventional and the modified direct voltage control are shown in Fig. 5.37 and Fig. 5.38 respectively.

Referring to Fig. 5.37, since the conventional method could not obtain the slip angle, the grid-connected control will have a sudden error in the slip angle of −85 degrees at the instant of connection. Although the stator voltage is synchronized with the grid voltage, this sudden slip angle error produces inrush currents which can be excessive in the case of medium and large DFIGs.

On the other hand, the modified method obtain an estimation of the slip angle and, consequently, the connection is smoother without any inrush current. This is another merit of the modified direct voltage control.

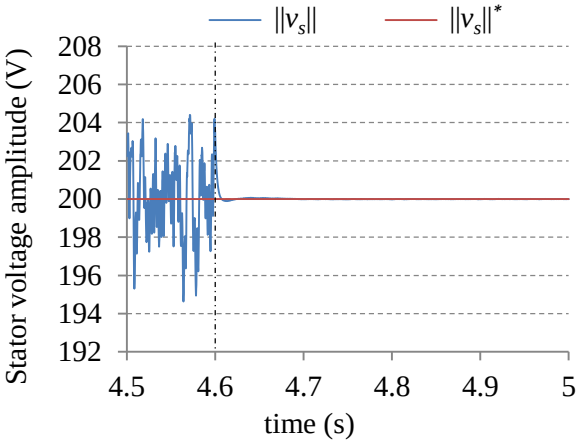

(a) Stator voltage amplitude

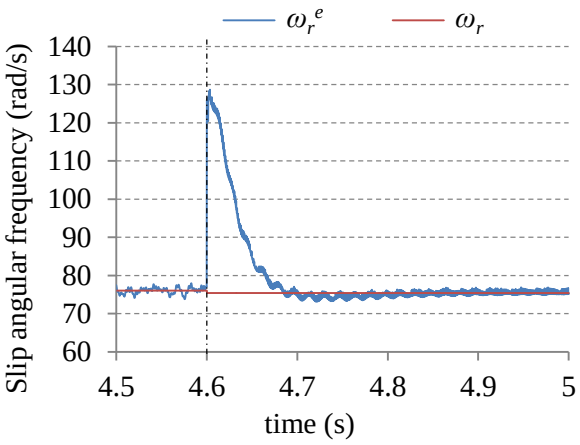

(b) Stator voltage angular frequency

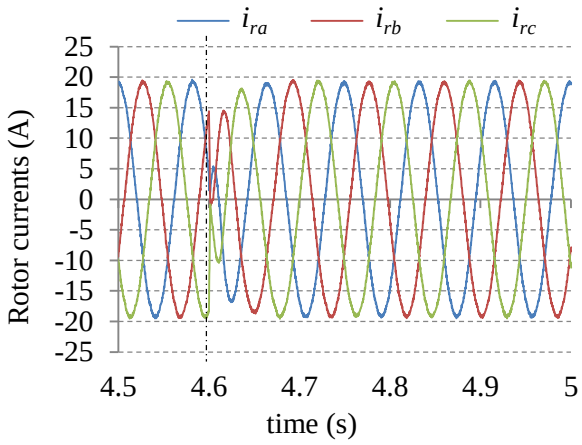

(c) Stator currents

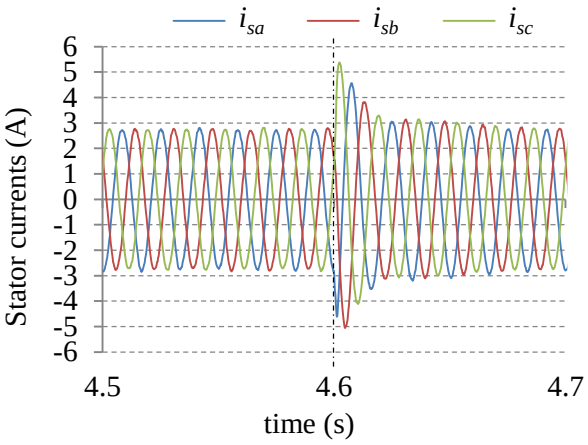

(d) Rotor currents

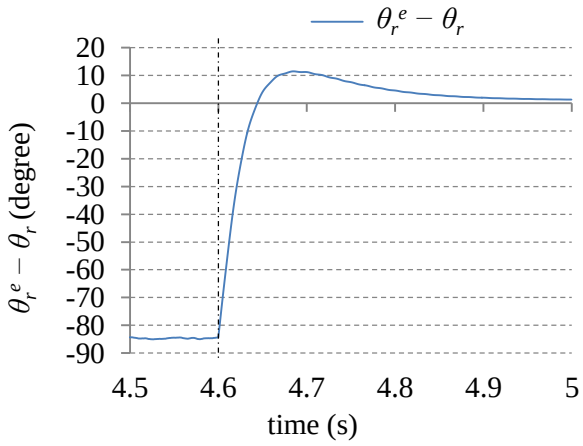

(e) Estimation error of the slip angle

Fig. 5.37: Simulation results for grid connection with the conventional direct voltage control under no load condition with ω_m = 0.8 pu.

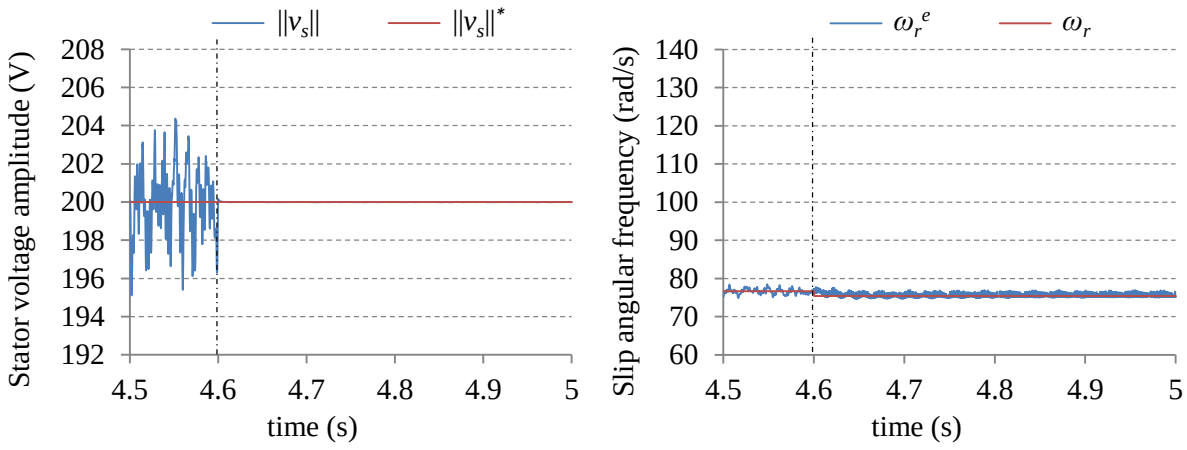

(a) Stator voltage amplitude

(b) Stator voltage angular frequency

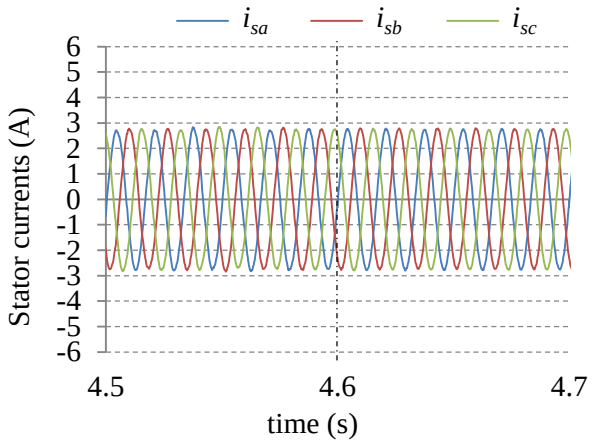

(c) Stator currents

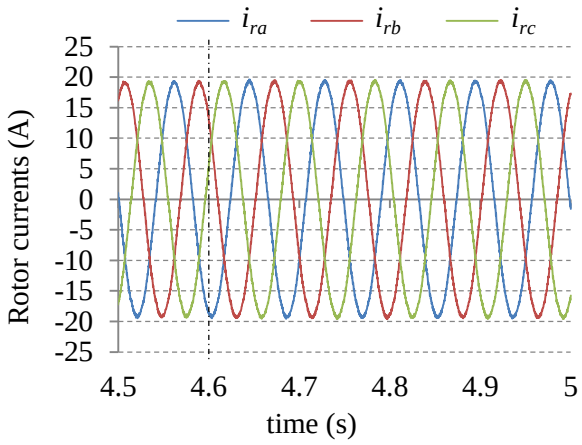

(d) Rotor currents

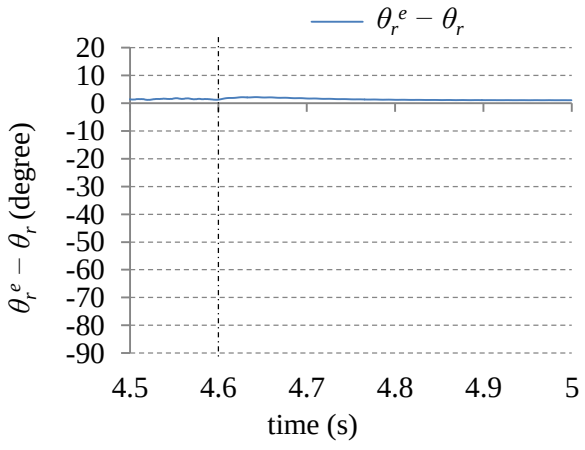

(e) Estimation error of the slip angle

Fig. 5.38: Simulation results for grid connection with the modified direct voltage control under no load condition with ω_m = 0.8 pu.

Second, the connection to the grid with a balanced series R-L load, which is R = 150 Ω and L = 0.1 H, is considered. The load is connected in advance during the stand-alone; that is before the synchronization started. The results with the conventional and the modified method are shown in Fig. 5.39 and Fig. 5.40 respectively.

From Fig. 5.39, the slip angle error at the instant of connection is around −61 degrees, which is smaller than that in Fig. 5.37. This is why, the inrush current in this case is slightly smaller and is damped faster.

From Fig. 5.40, the modified direct voltage control achieves smooth connection to the grid for this load too.

Next, the connection to the grid with a balanced series R-C load, which is R = 80 Ω and C = 60 μF, is considered. This load produces an angle γ_r equal to around −40 degrees, which does not cause instability of the negative-sequence compensation. The results with the conventional and the modified direct voltage control are shown in Fig. 5.41 and Fig. 5.42.

In Fig. 5.41, with this load, the initial slip angle error is smaller than the previous cases; this is why, the inrush current is significantly reduced but still not zero. On the other hand, the proposed method achieves smooth connection regardless of the load.

D. Disconnection from the Grid

In the follow tests, the DFIG is disconnected from the grid at 2 sec, and the control system is instantly changed to the stand-alone mode. During all the following tests, the DFIG speed is fixed at a hyper-synchronous speed of 1.2 pu. To achieve smooth disconnection, the initial reference angle for the stator voltage is equal to stator voltage angle at the instant of disconnection. Similarly, the amplitude, the angle, and xy-components of the rotor current are equal to their value at the instant of disconnection.

First, the active and reactive power references during the grid-connected mode are set equal to their value during the stand-alone mode; this means that the DFIG circuit is exchanging very small current with the grid before disconnection. During the stand-alone and under no load condition, the active and reactive powers are equal to 25 W and −772 VAR respectively. The results for this test with the conventional and the modified direct voltage control are given in Fig. 5.43 and Fig. 5.44 respectively.

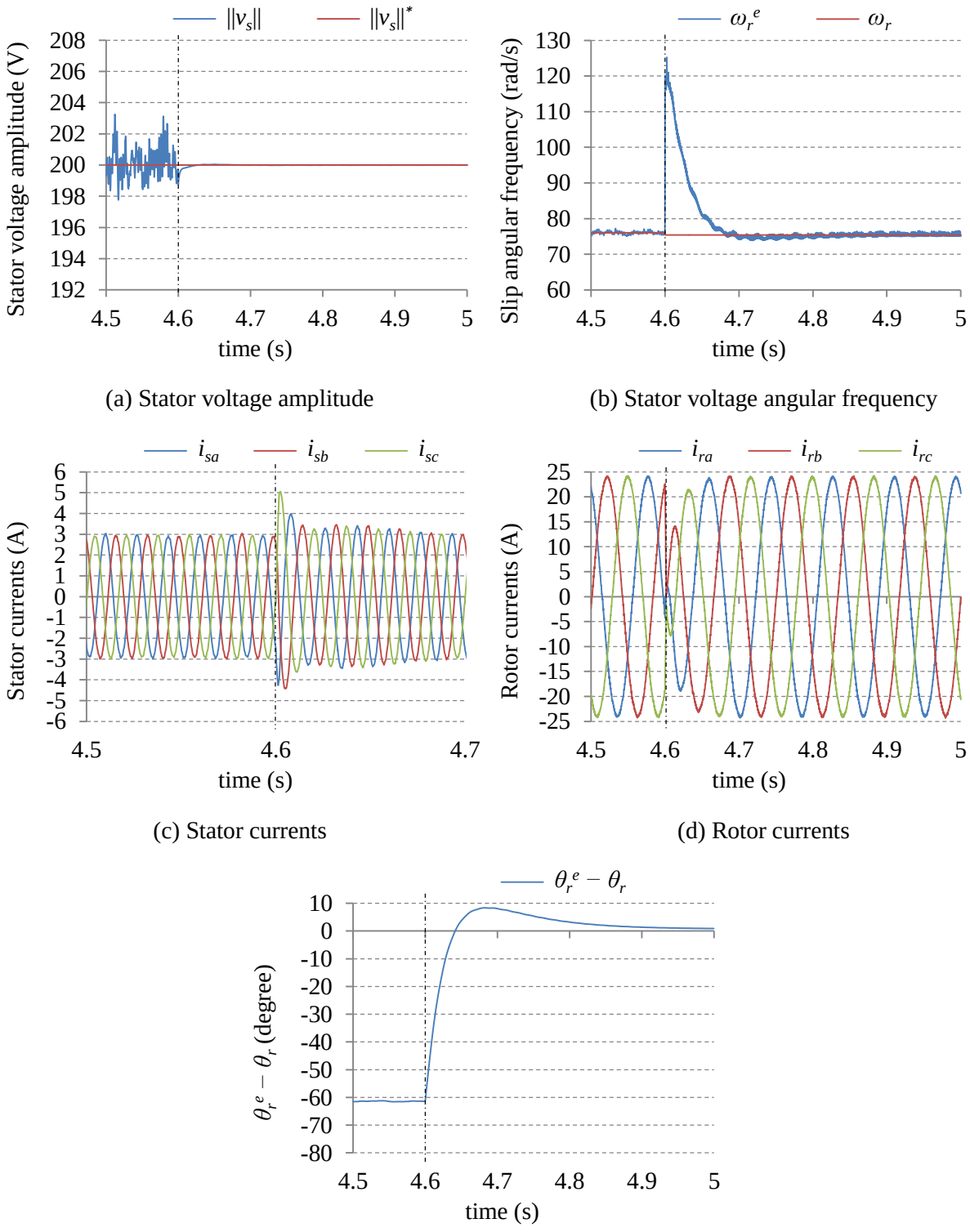

(a) Stator voltage amplitude

(b) Stator voltage angular frequency

(c) Stator currents

(d) Rotor currents

(e) Estimation error of the slip angle

Fig. 5.39: Simulation results for grid connection with the conventional direct voltage control with R-L load of R = 150 Ω and L = 0.1 H and ω_m = 0.8 pu.

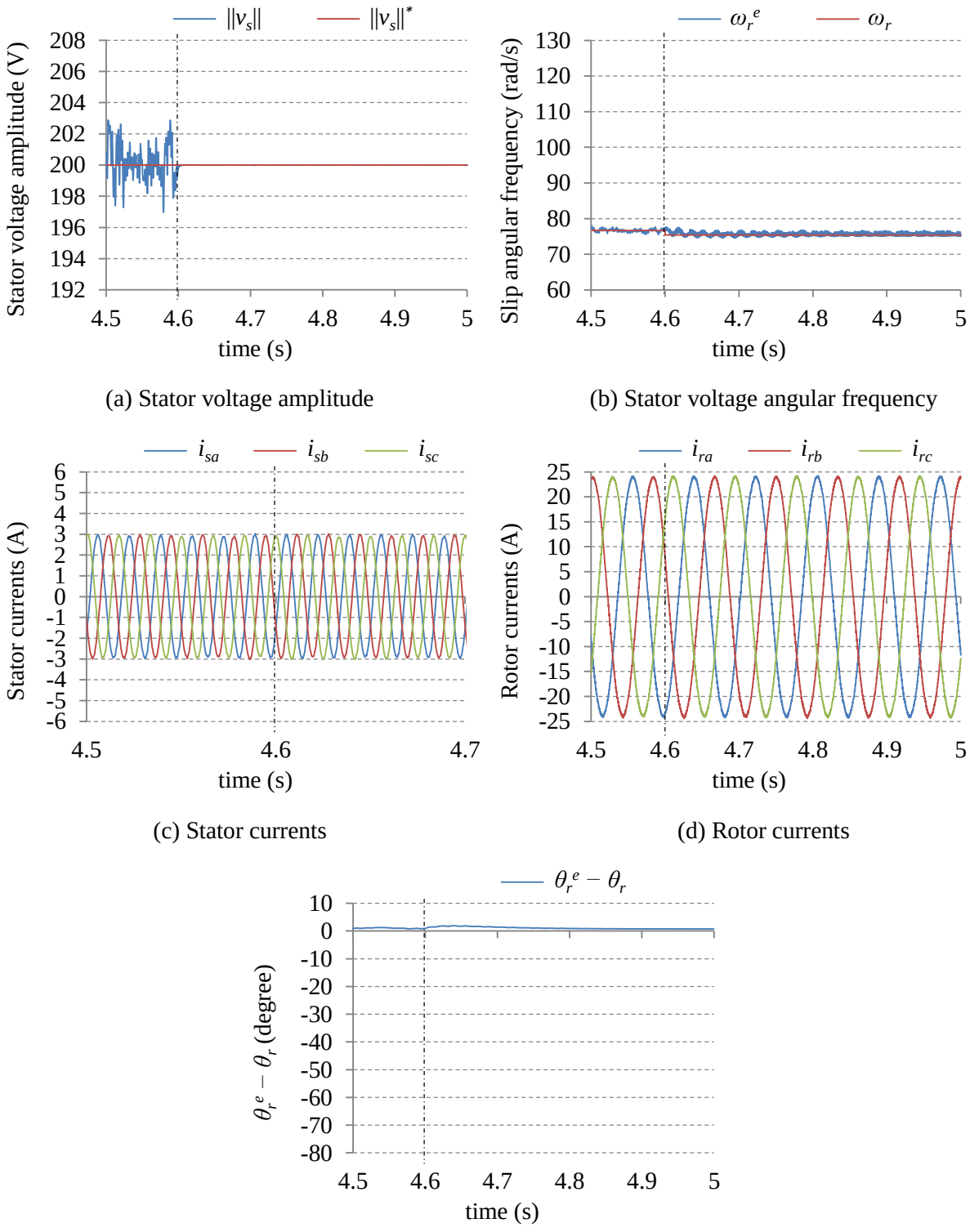

(a) Stator voltage amplitude

(b) Stator voltage angular frequency

(c) Stator currents

(d) Rotor currents

(e) Estimation error of the slip angle

Fig. 5.40: Simulation results for grid connection with the modified direct voltage control with R-L load of R = 150 Ω and L = 0.1 H and ω_m = 0.8 pu.

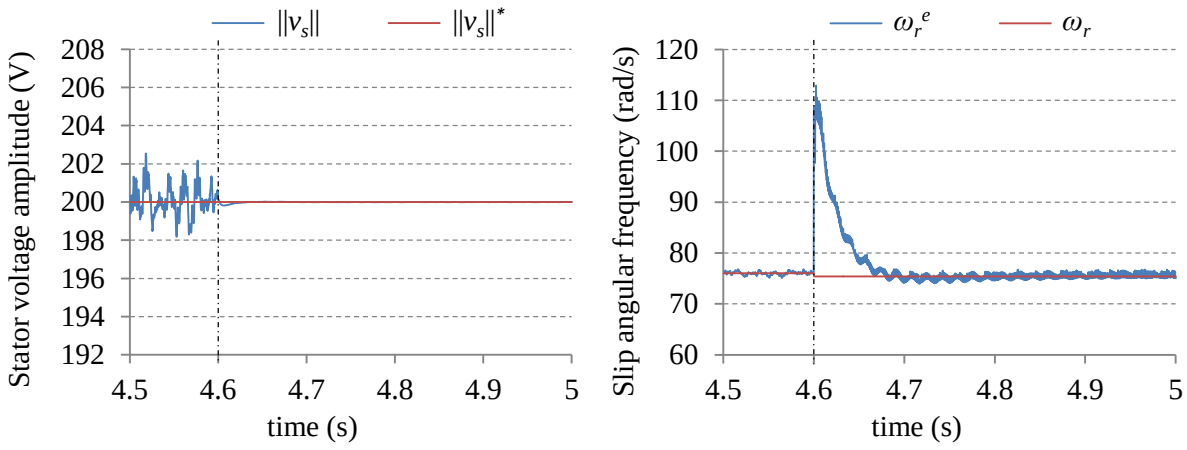

(a) Stator voltage amplitude

(b) Stator voltage angular frequency

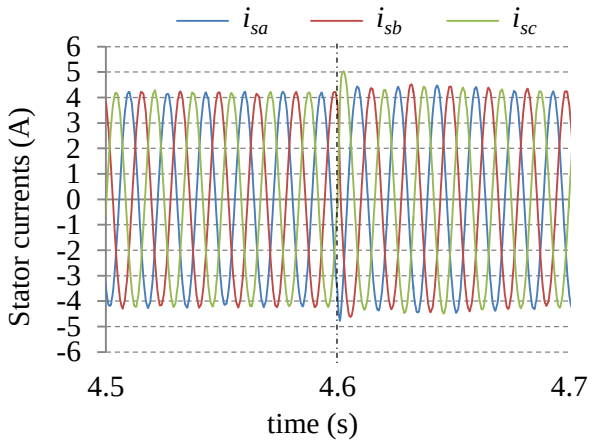

(c) Stator currents

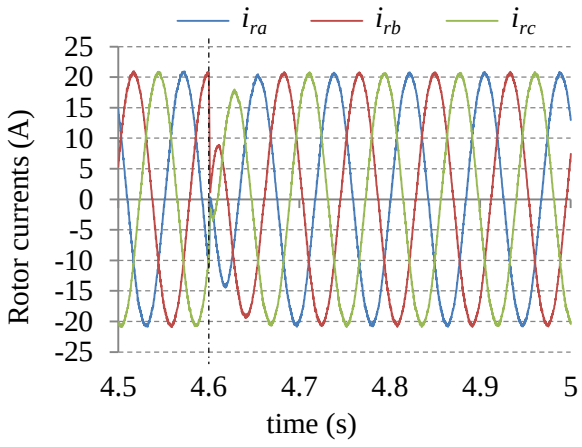

(d) Rotor currents

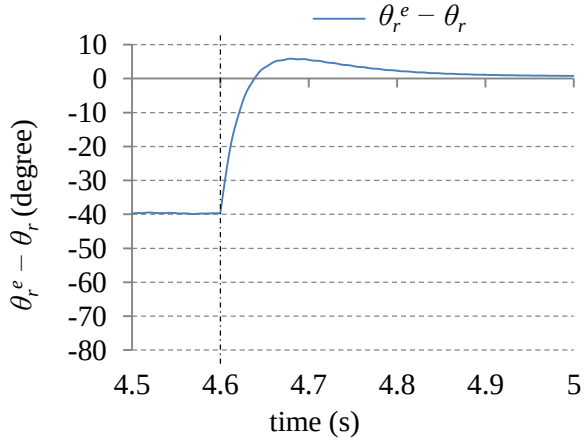

(e) Estimation error of the slip angle

Fig. 5.41: Simulation results for grid connection with the conventional direct voltage control with R-C load of R = 80 Ω and C = 60 µF and ω_m = 0.8 pu.

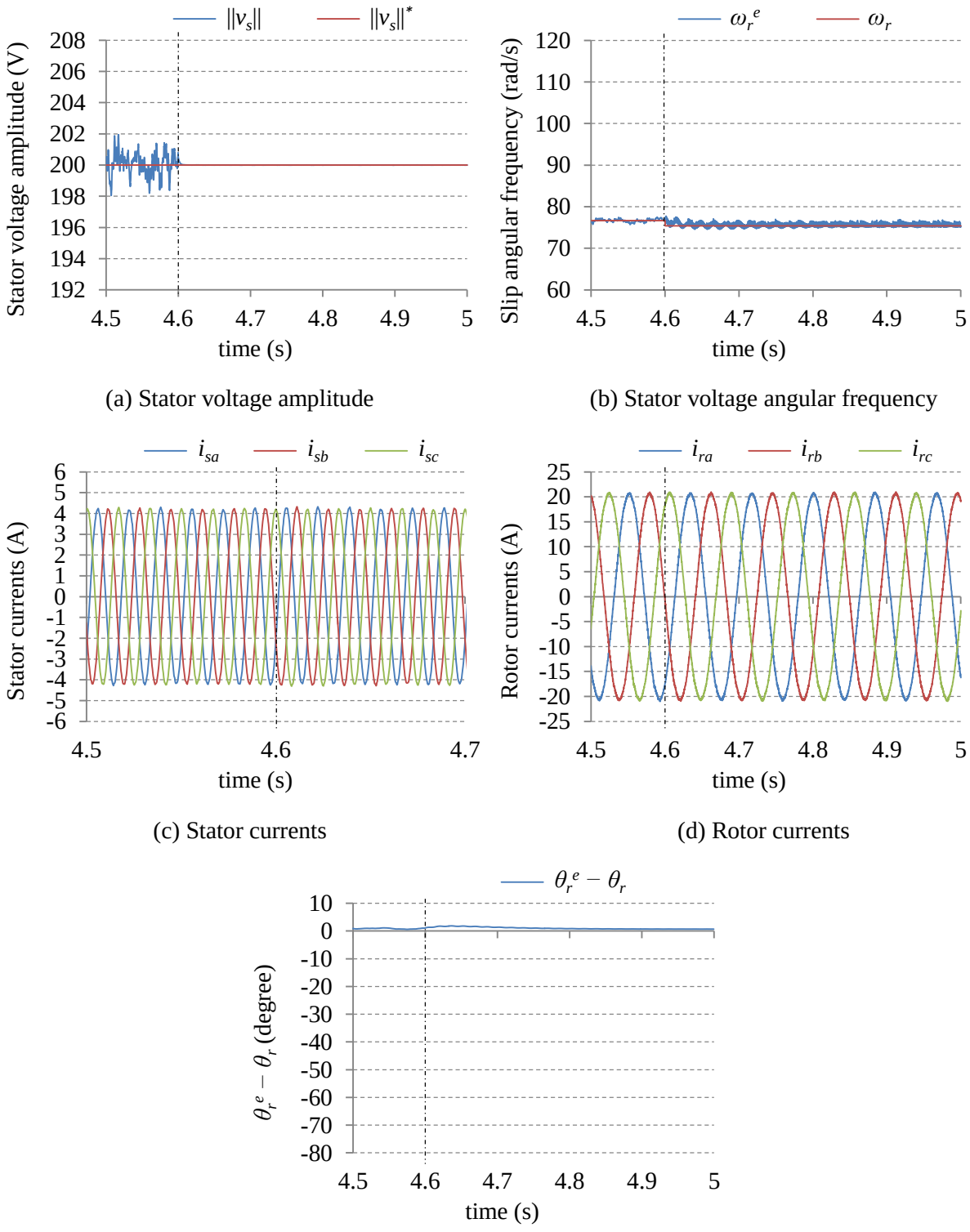

(a) Stator voltage amplitude

(b) Stator voltage angular frequency

(c) Stator currents

(d) Rotor currents

(e) Estimation error of the slip angle

Fig. 5.42: Simulation results for grid connection with the modified direct voltage control with R-C load of R = 80 Ω and C = 60 µF and ω_m = 0.8 pu.

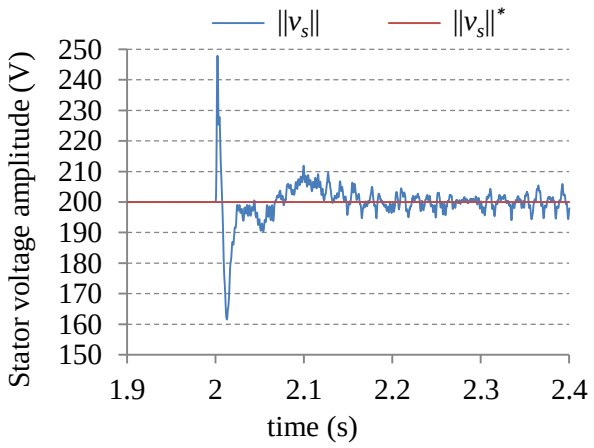

(a) Stator voltage amplitude

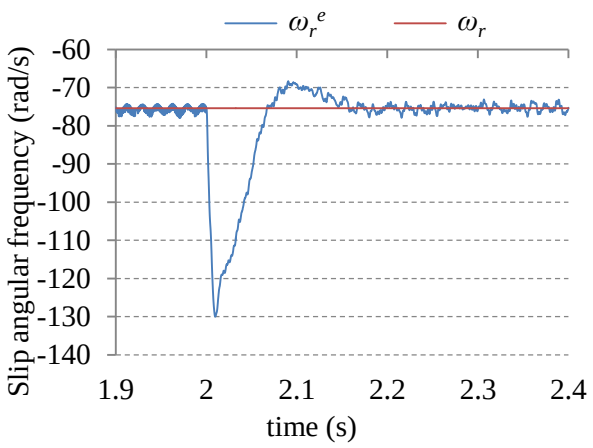

(b) Stator voltage angular frequency

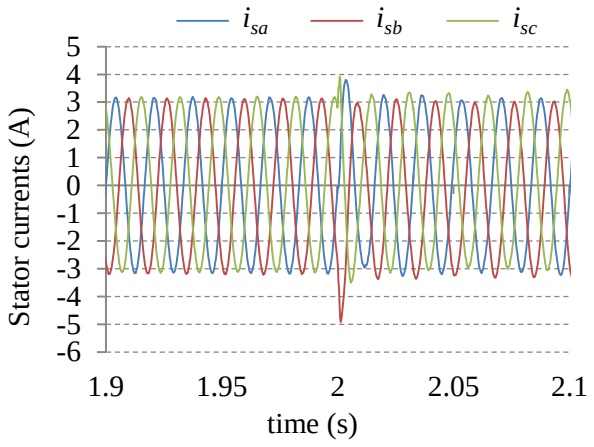

(c) Stator currents

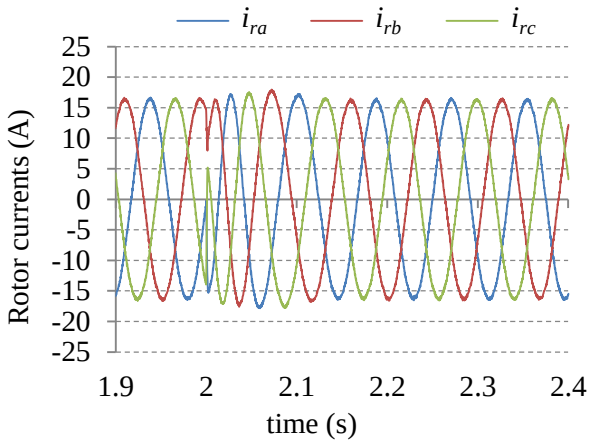

(d) Rotor currents

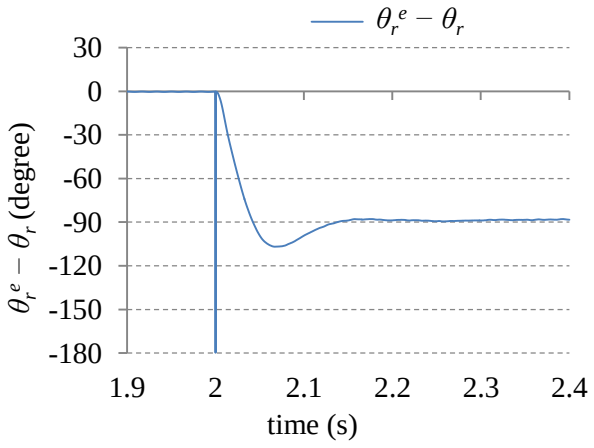

(e) Estimation error of the slip angle

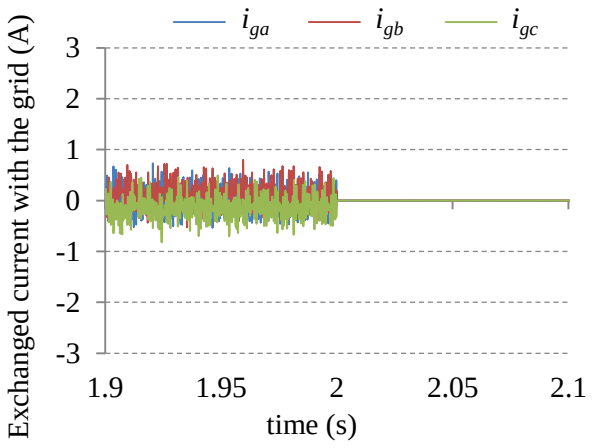

(f) Exchanged current with the grid

Fig. 5.43: Simulation results for disconnection from the grid with the conventional direct voltage control under no load condition with P_s* = 25 W, Q_s* = -772 VAR and ω_m = 1.2 pu.

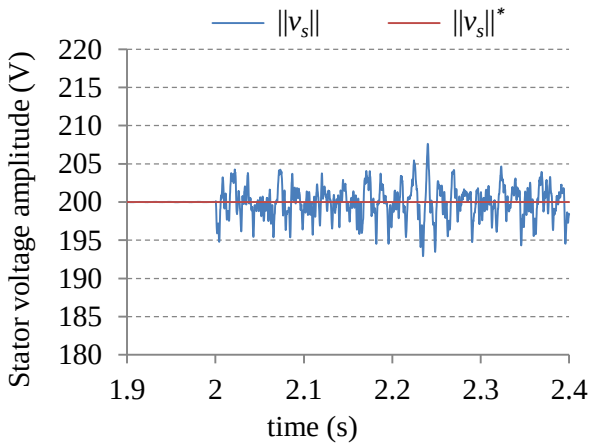

(a) Stator voltage amplitude

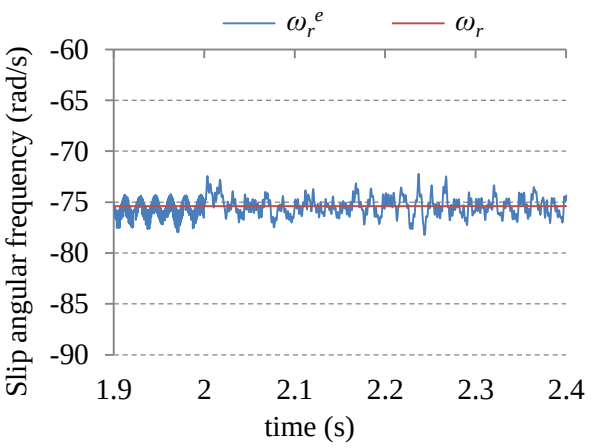

(b) Stator voltage angular frequency

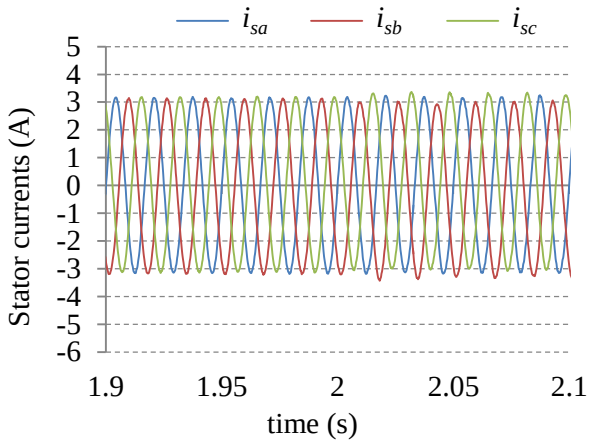

(c) Stator currents

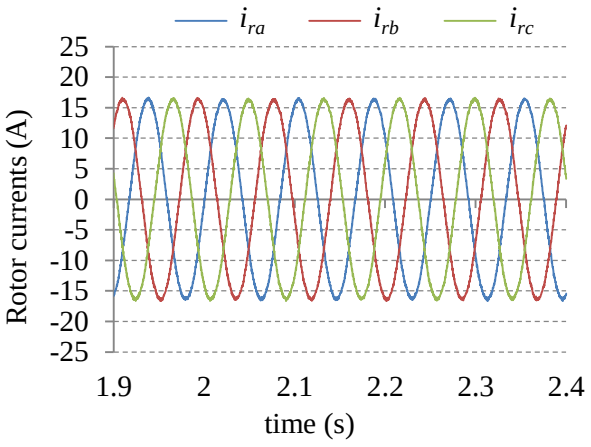

(d) Rotor currents

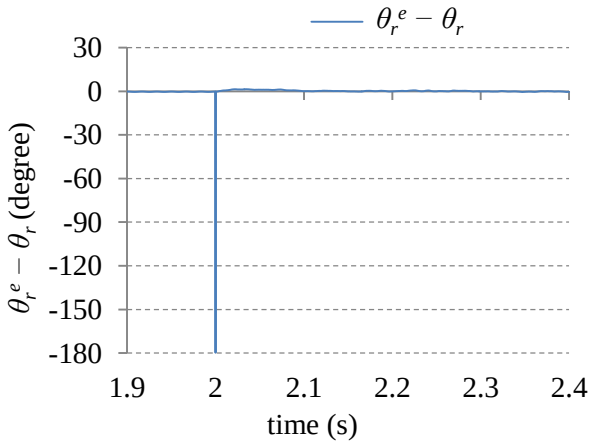

(e) Estimation error of the slip angle

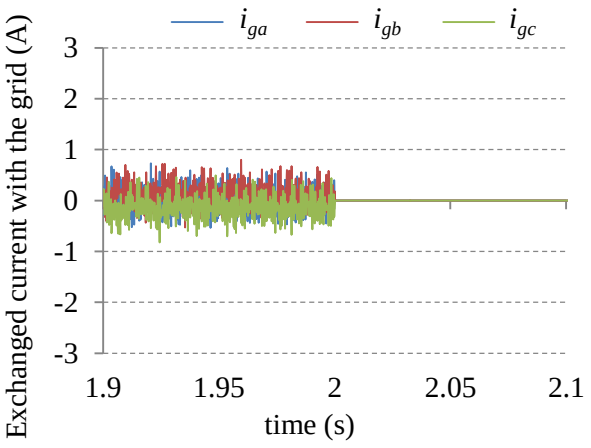

(f) Exchanged current with the grid

Fig. 5.44: Simulation results for disconnection from the grid with the modified direct voltage control under no load condition with P_s* = 25 W, Q_s* = -772 VAR and ω_m = 1.2 pu.

From the results in Fig. 5.43 and Fig. 5.44, the conventional direct voltage control does not achieve smooth disconnection from the grid while the modified direct voltage control does. However, this smooth disconnection requires disconnection with the active and reactive power references equal to their values during the stand-alone mode, which is usually unknown.

In practice, the DFIG is disconnected from the grid after detecting a grid failure, and the active and reactive power references will be different from their value during the stand-alone mode. To investigate this case, the following test is carried out.

In this test, the local load is a resistive load of 100 Ω which was connected earlier during the grid-connected mode. The active and reactive power references during the grid-connected mode are 0 W and −1200 VAR respectively, which are different from their value during the stand-alone mode, 363 W and −772 VAR. The results for this test with the conventional and the modified direct voltage control are shown in Fig. 5.45 and Fig. 5.46 respectively. From these results, the conventional and the modified direct voltage control have similar disconnection performances; there is a transient response of the stator voltage amplitude and frequency after the disconnection. To achieve smooth disconnection, the current exchanged with the grid should be zero at the instant of disconnection which requires additional current sensors at the grid side.

5.3.3 Experimental Results

A. Stand-Alone Mode

First, the variable speed operation is investigated. The DFIG speed was increased from a sub-synchronous speed of 0.8 pu to a hyper-synchronous speed of 1.2 pu within 1 sec. When the DFIG speed reaches the synchronous speed a purely resistive load of 75 Ω is suddenly connected at 0 sec. The results for this test with the modified method are shown in Fig. 5.47.

The direct voltage control is robust against variations in the DFIG speed, and it has a good response for sudden load change.

Second, the steady-state response of the conventional and the modified method are compared under no load condition. The speed during this test is fixed at a sub-synchronous speed of 0.9 pu. The result of the conventional and the modified method are shown in Fig. 5.48 and Fig. 5.49 respectively.

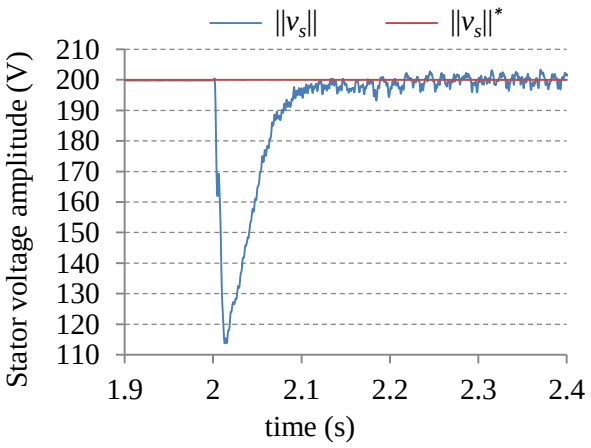

(a) Stator voltage amplitude

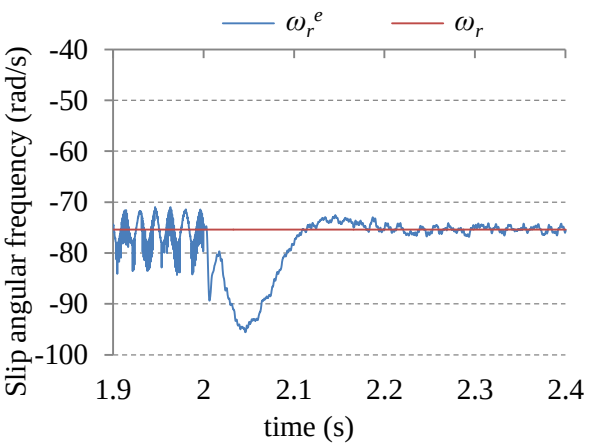

(b) Stator voltage angular frequency

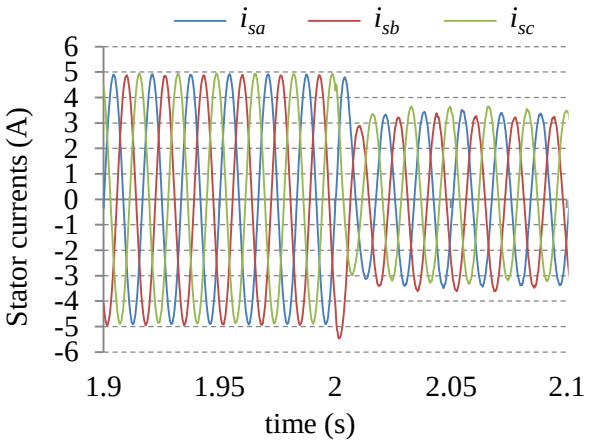

(c) Stator currents

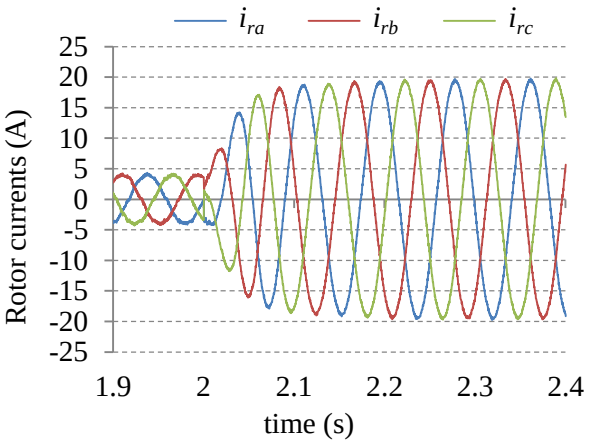

(d) Rotor currents

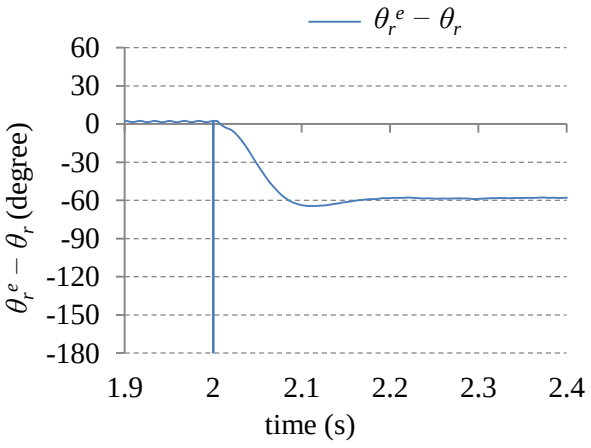

(e) Estimation error of the slip angle

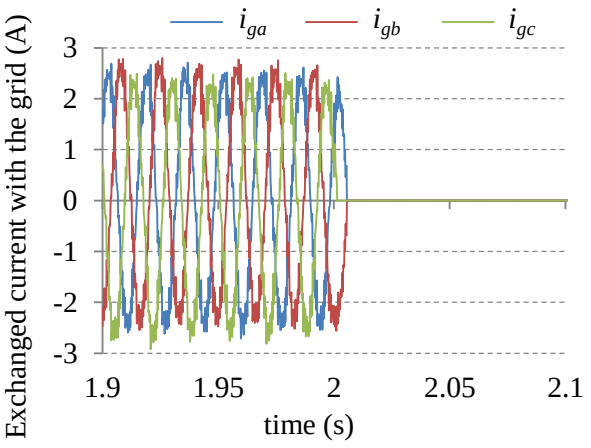

(f) Exchanged current with the grid

Fig. 5.45: Simulation results for disconnection from the grid with the conventional direct voltage control with local load of 100 Ω, P_s* = 0 W, Q_s* = -1200 VAR and ω_m = 1.2 pu.

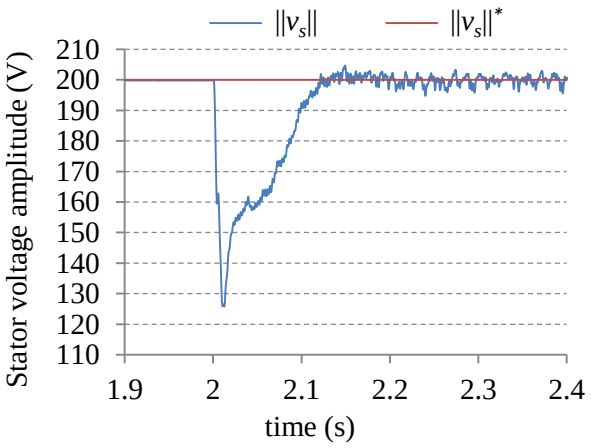

(a) Stator voltage amplitude

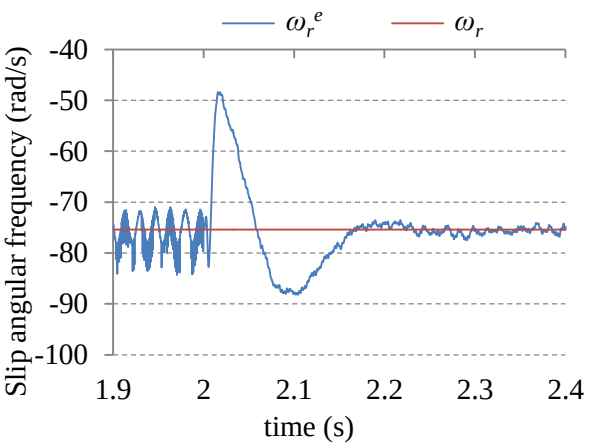

(b) Stator voltage angular frequency

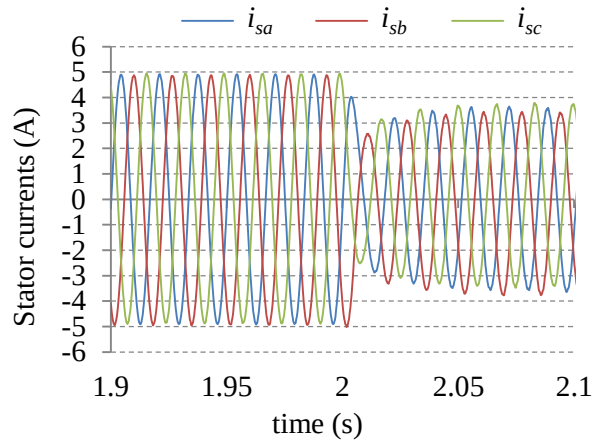

(c) Stator currents

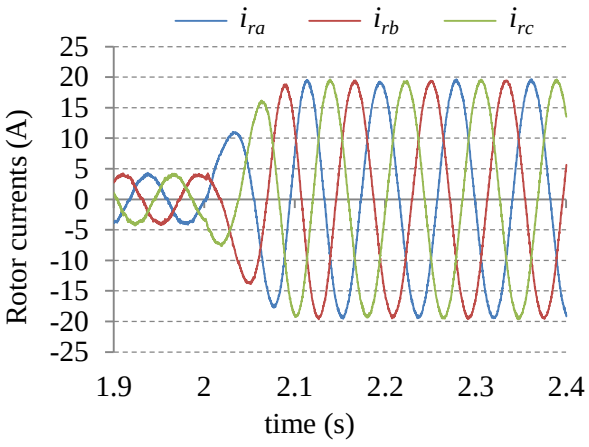

(d) Rotor currents

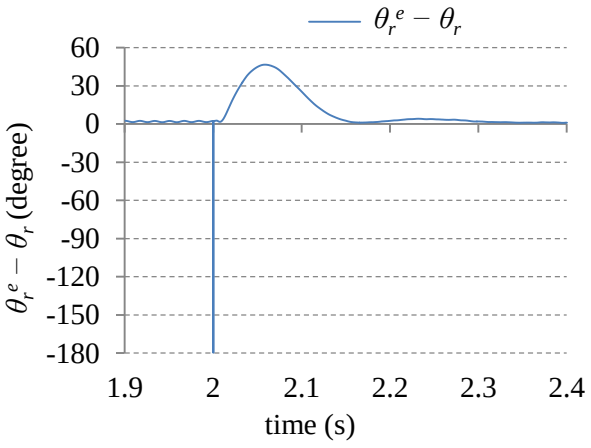

(e) Estimation error of the slip angle

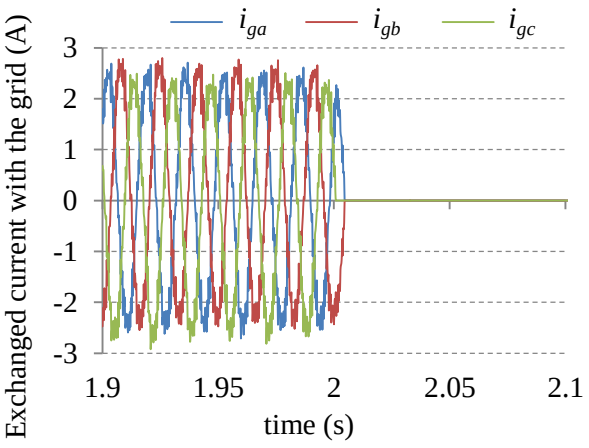

(f) Exchanged current with the grid

Fig. 5.46: Simulation results for disconnection from the grid with the modified direct voltage control with local load of 100 Ω, P_s* = 0 W, Q_s* = -1200 VAR and ω_m = 1.2 pu.

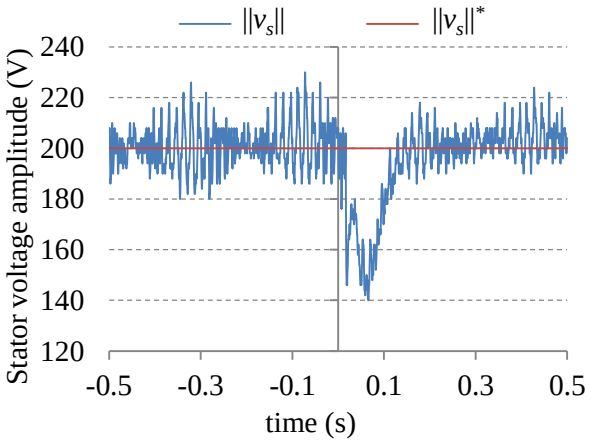

(a) Stator voltage amplitude

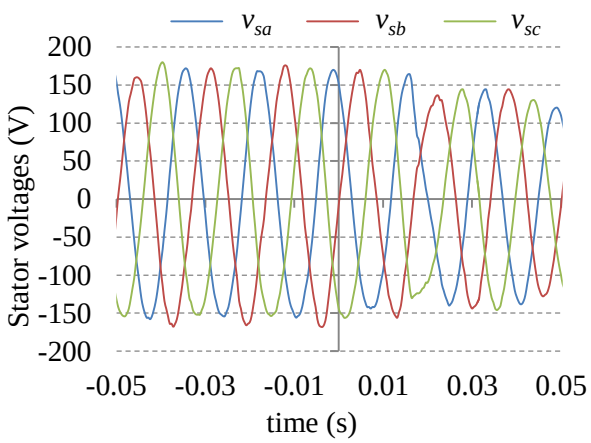

(b) Stator voltages

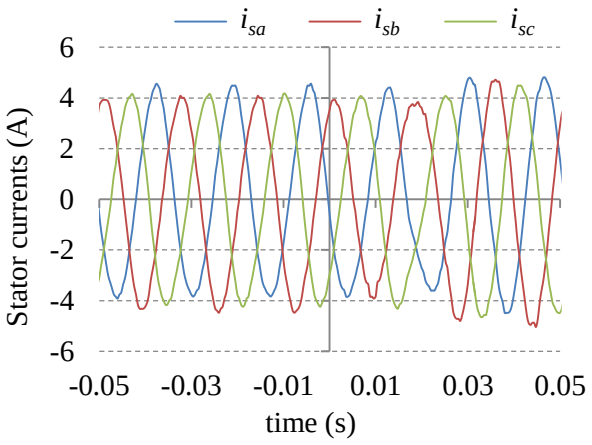

(c) Stator currents

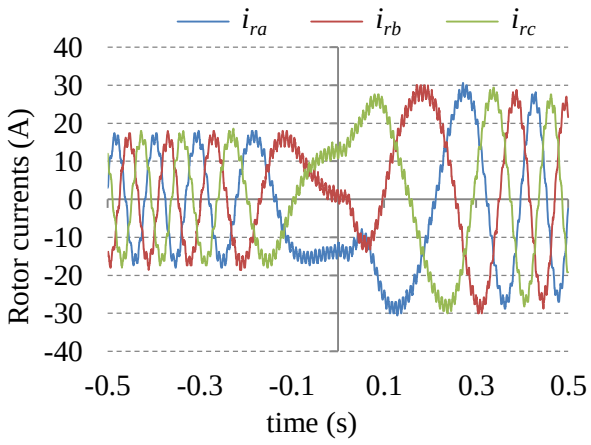

(d) Rotor currents

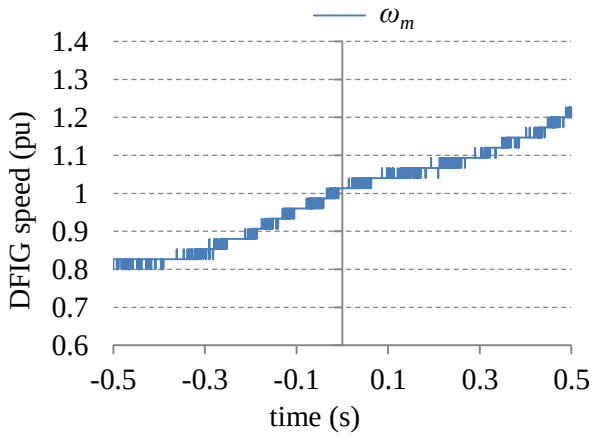

(e) DFIG's speed

Fig. 5.47: Experimental results for variable speed operation with the modified direct voltage control, where a resistive load of 75 Ω is connected at 0 sec.

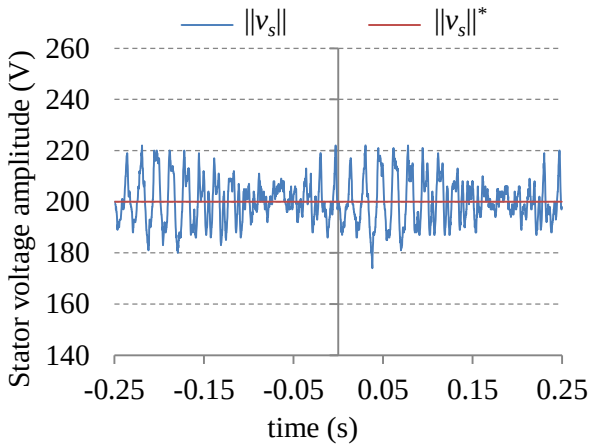

(a) Stator voltage amplitude

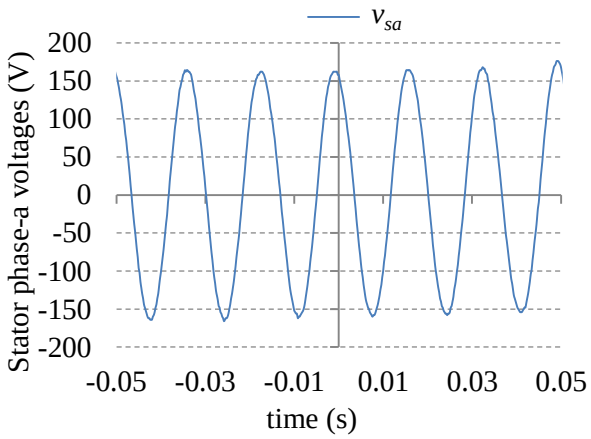

(b) Stator phase-a voltage

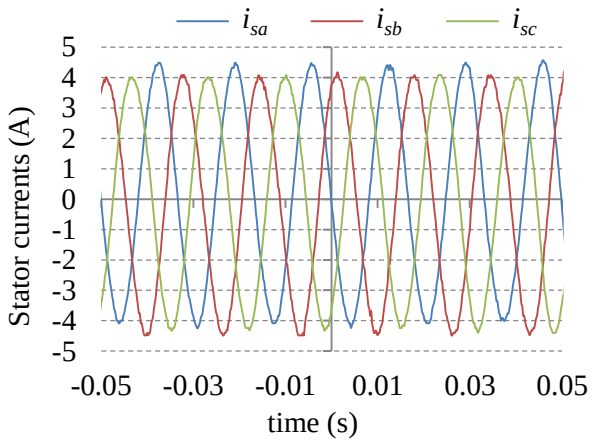

(c) Stator currents

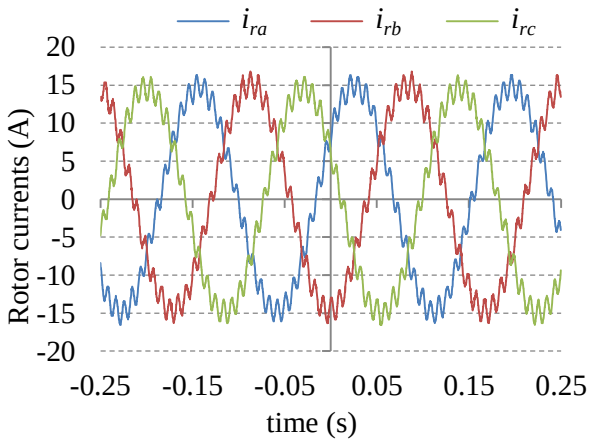

(d) Rotor currents

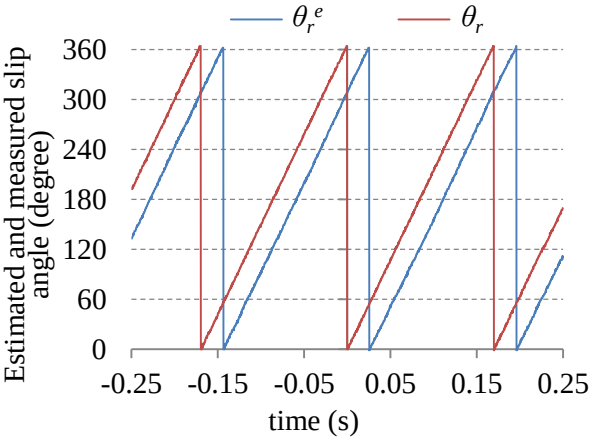

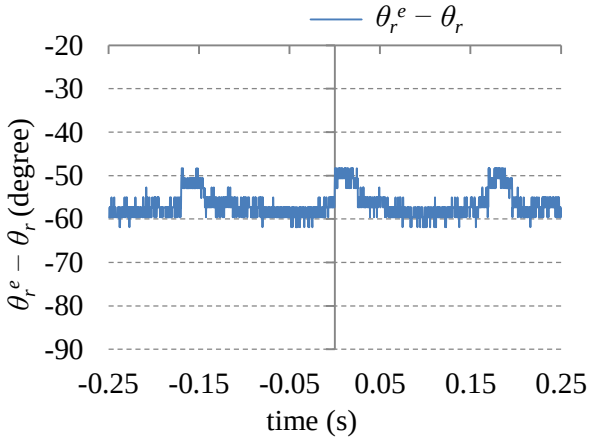

(e) Estimation and measured slip angle

Fig. 5.48: Experimental results for steady-state response of the conventional direct voltage control under no load condition and with and ω_m = 0.9 pu.

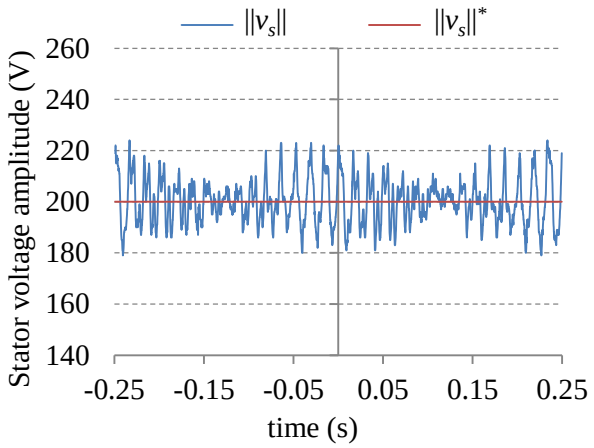

(a) Stator voltage amplitude

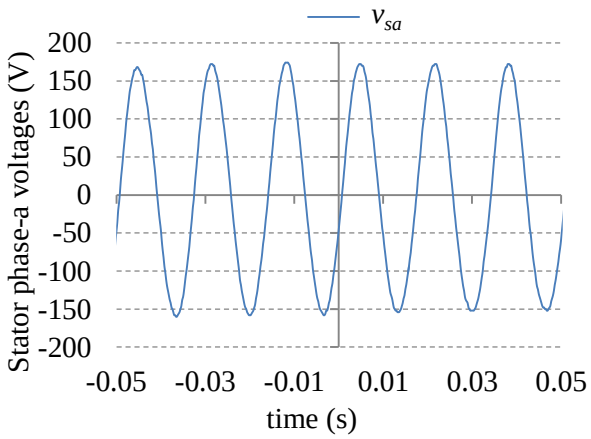

(b) Stator phase-a voltage

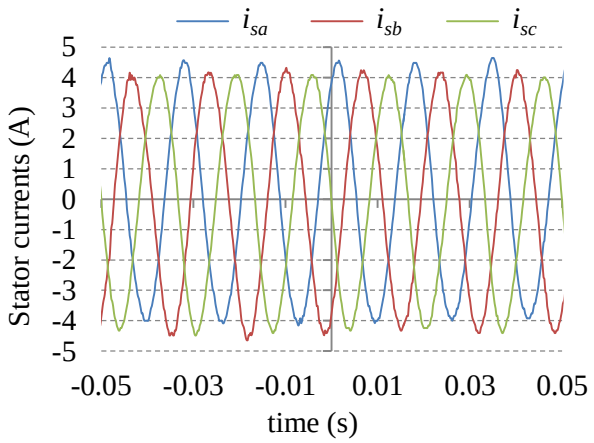

(c) Stator currents

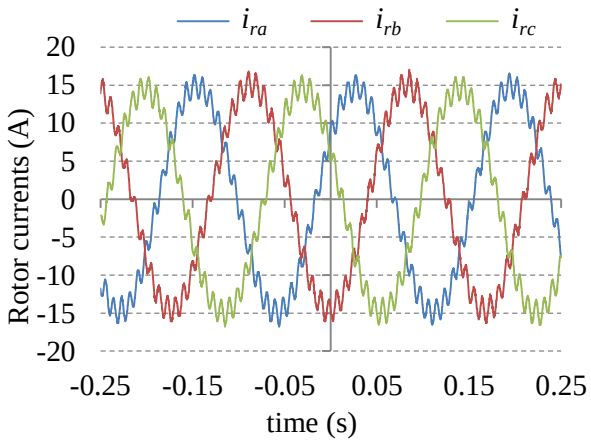

(d) Rotor currents

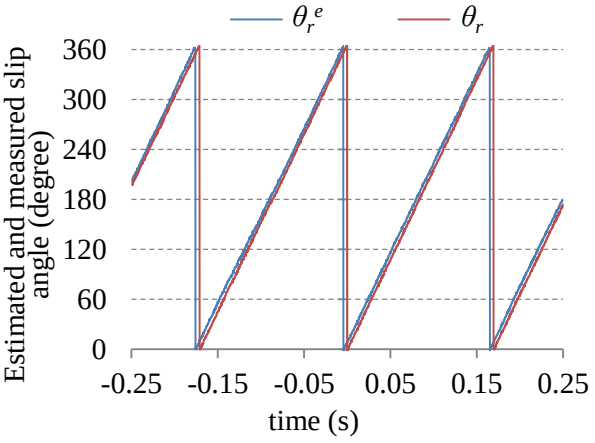

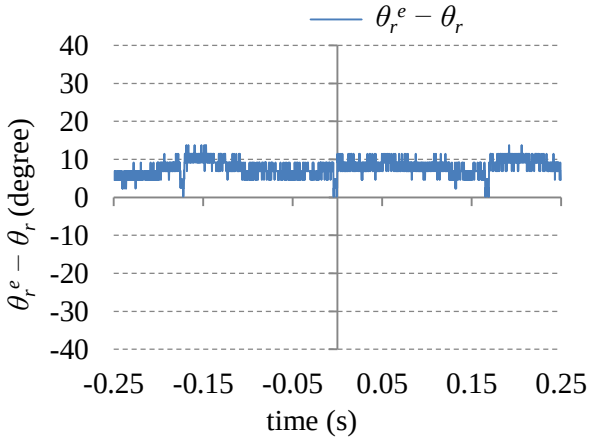

(e) Estimation and measured slip angle

Fig. 5.49: Experimental results for steady-state response of the conventional direct voltage control under no load condition and with and ω_m = 0.9 pu.

Similar to the simulation results, from Fig. 5.48 and Fig. 5.49, although the amplitude and frequency response of both method are similar, the conventional method cannot obtain the slip angle, whereas the modified method obtains a good estimation of the slip angle.

From Fig. 5.49, the estimation error in the experiments is higher than in simulation; this is because the ignored stator winding resistance in the practical DFIG is higher than its standard value which increases the estimation error.

Next the steady-state performance of the negative-sequence compensation control is investigated. First an unbalance series resistive-inductive load, which is given in Table 5.5, is considered. This load produces an angle γ_r equal to around -60 degrees. During this test, the DFIG speed is fixed at a sub-synchronous speed of 0.9 pu.

Table 5.5: Parameters of the experiment's inductive load

	R (Ω)	L (H)
Phase-a	155	0.35
Phase-b	215	0.66
Phase-c	155	0.35

The result for this test with the conventional and the modified method are shown in Fig. 5.50 and Fig. 5.51 respectively. From these results, for an inductive load, the conventional and the modified method have similar response, and the negative-sequence compensation is stable. The problem arises with some capacitive loads which will considered next.

The unbalance series resistive-capacitive load of choice is given in Table 5.6. This load produces an angle γ_r equal to around -15.5 degrees. During this test, the DFIG speed is fixed at a hyper-synchronous speed of 1.1 pu.

Table 5.6: Parameters of the experiment's capacitive load

	R (Ω)	C (μF)
Phase-a	134	19.3
Phase-b	82	19.3
Phase-c	134	19.3

The result for this test with the conventional and the modified method are shown in Fig. 5.52 and Fig. 5.53 respectively.

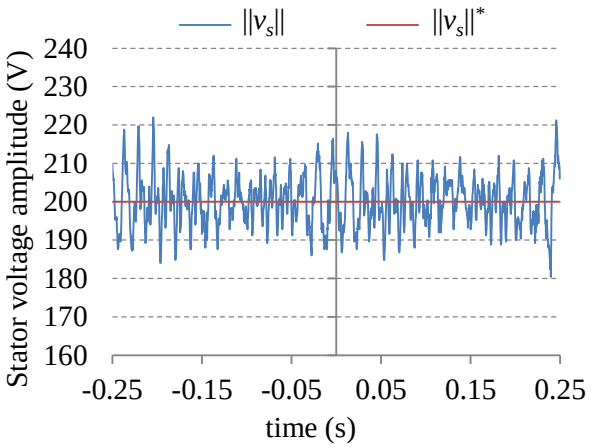

(a) Stator voltage amplitude

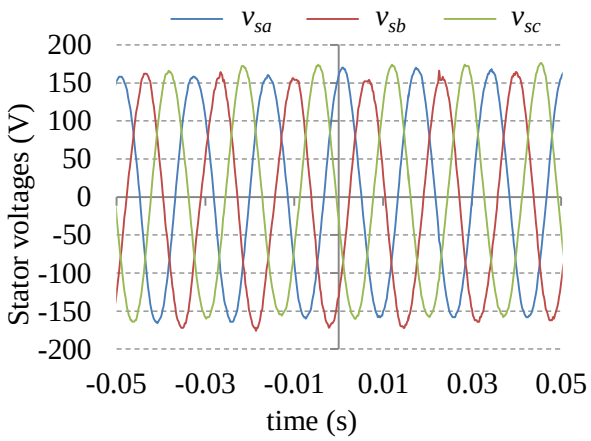

(b) Stator voltages

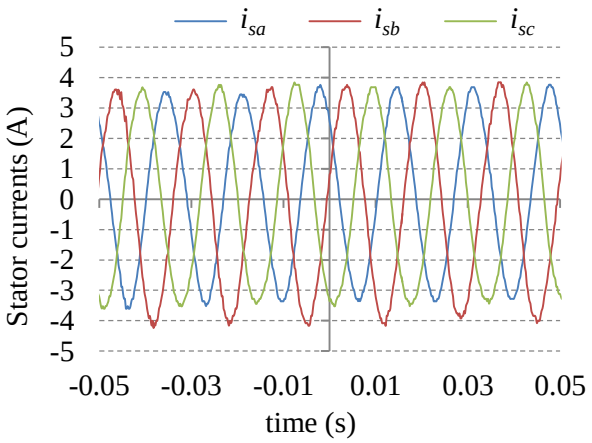

(c) Stator currents

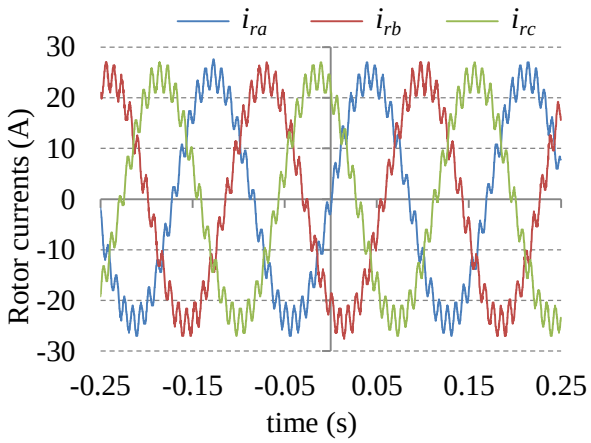

(d) Rotor currents

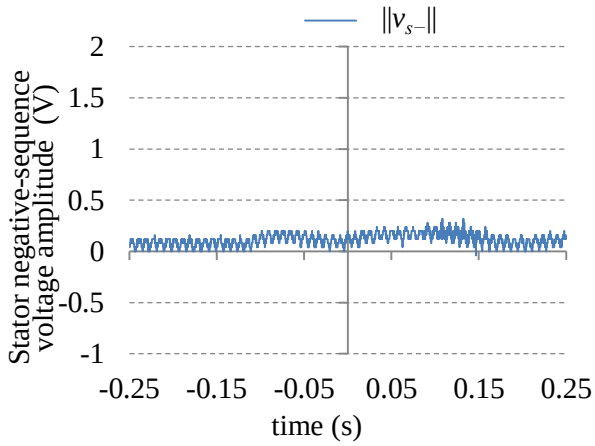

(e) Stator negative-sequence voltage amplitude

Fig. 5.50: Experimental results of the conventional direct voltage control at steady-state with an unbalanced series-resistive-inductive load, and ω_m = 0.9 pu.

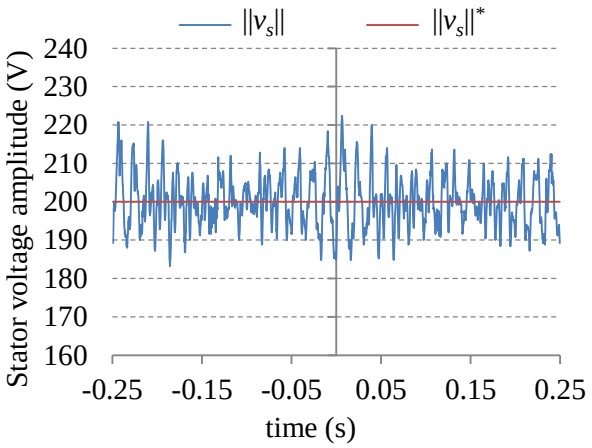

(a) Stator voltage amplitude

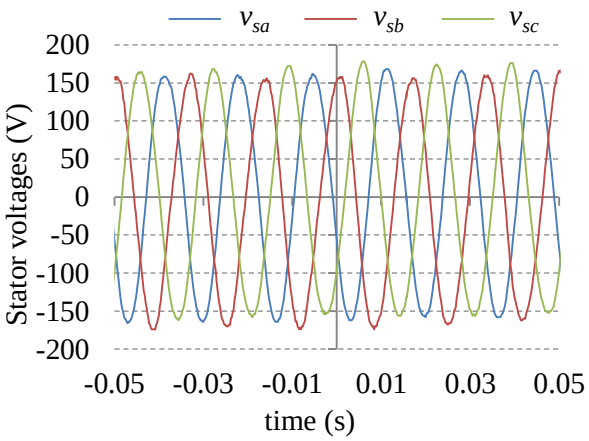

(b) Stator voltages

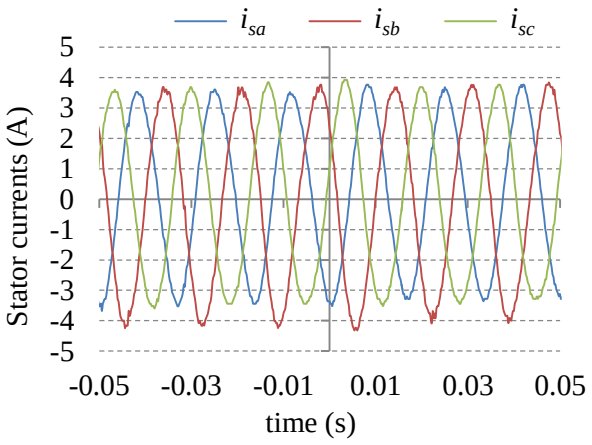

(c) Stator currents

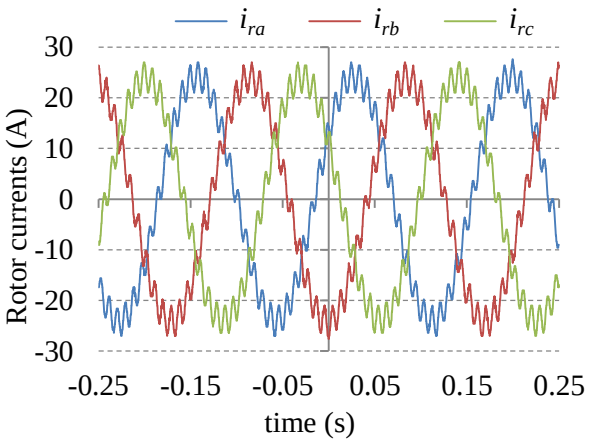

(d) Rotor currents

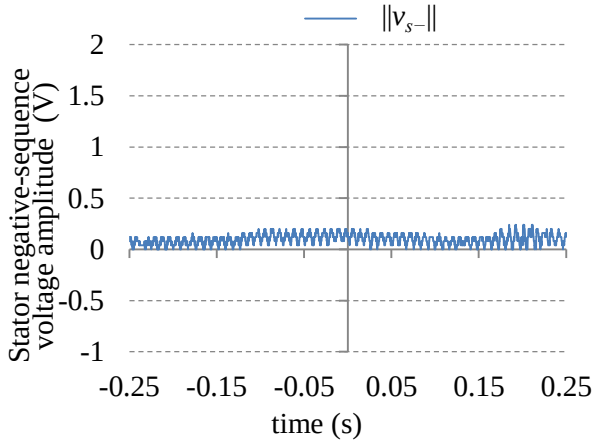

(e) Stator negative-sequence voltage amplitude

Fig. 5.51: Experimental results of the modified direct voltage control at steady-state with an unbalanced series-resistive-inductive load, and ω_m = 0.9 pu.

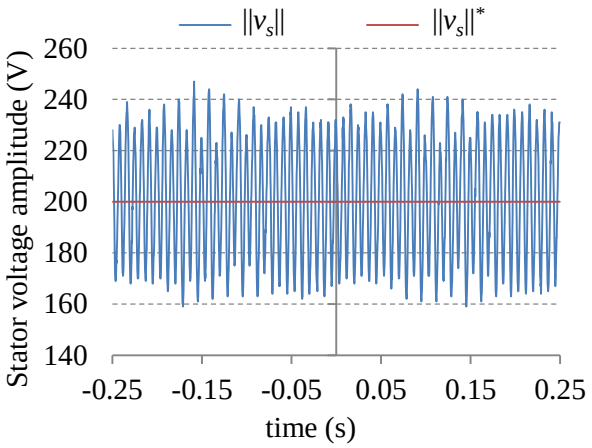

(a) Stator voltage amplitude

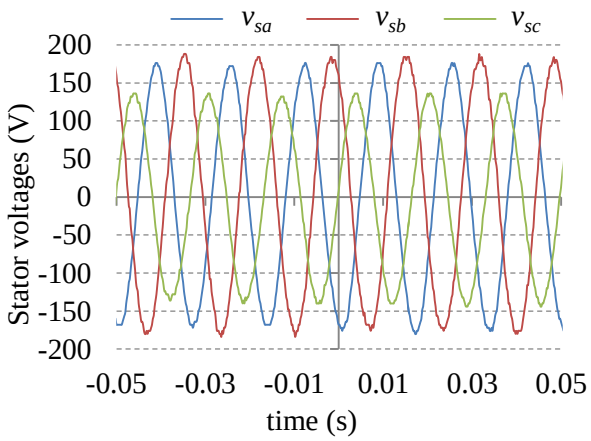

(b) Stator voltages

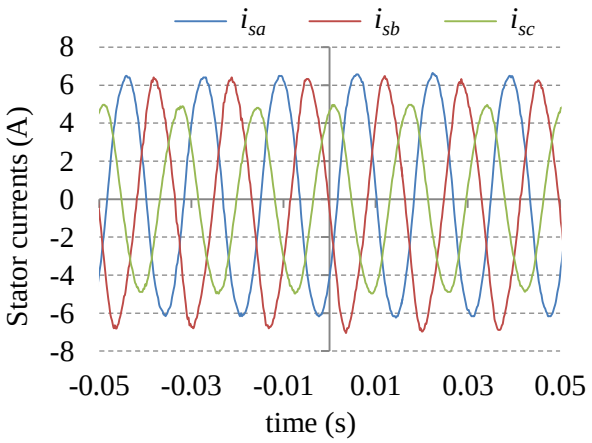

(c) Stator currents

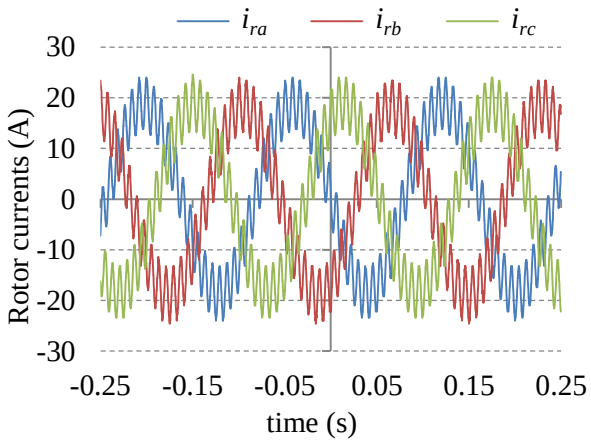

(d) Rotor currents

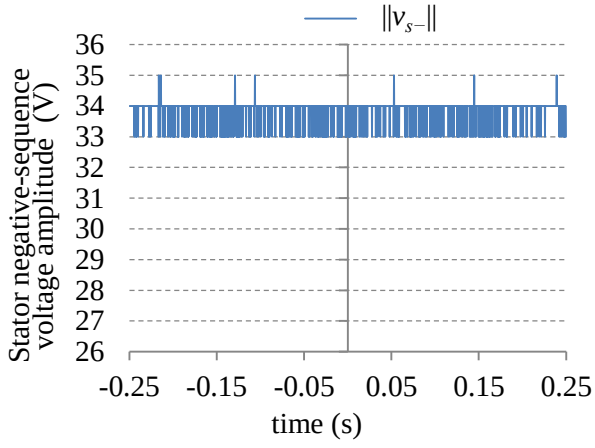

(e) Stator negative-sequence voltage amplitude

Fig. 5.52: Experimental results of the conventional direct voltage control at steady-state with an unbalanced series-resistive-capacitive load, and ω_m = 1.1 pu.

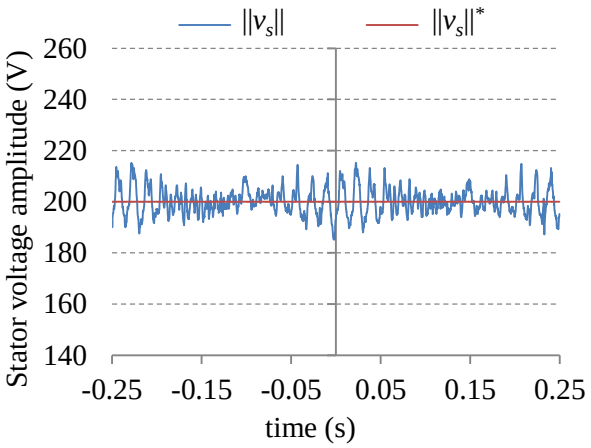

(a) Stator voltage amplitude

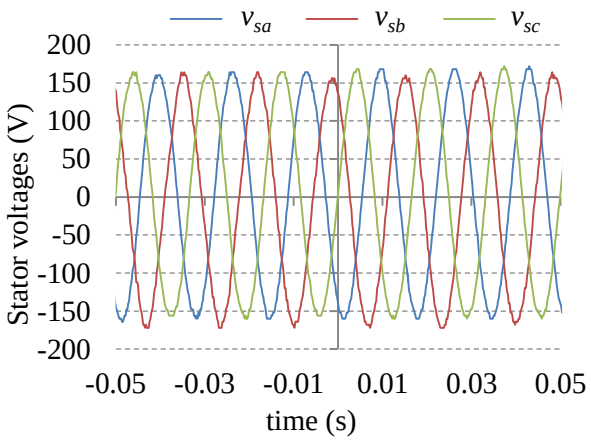

(b) Stator voltages

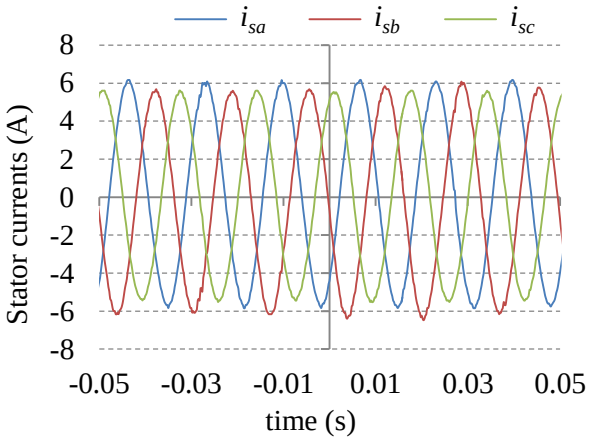

(c) Stator currents

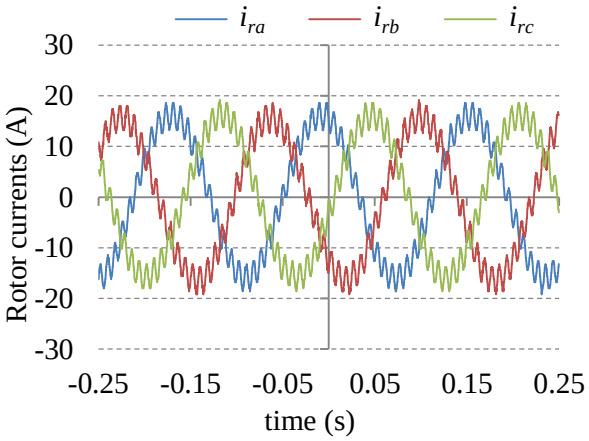

(d) Rotor currents

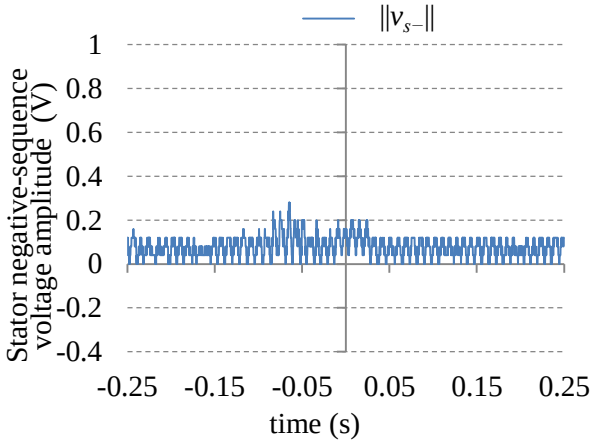

(e) Stator negative-sequence voltage amplitude

Fig. 5.53: Experimental results of the modified direct voltage control at steady-state with an unbalanced series-resistive-capacitive load, and ω_m = 1.1 pu.

From Fig. 5.52, although the amplitude and the angle control of the stator voltage are stable with the conventional direct voltage control, the negative-sequence compensation becomes unstable for this capacitive load. This causes large rotor negative-sequence currents which increase the stator negative-sequence voltage instead of decreasing it.

The stator negative-sequence voltage increases until it reaches a large value of 34 V at steady-state. This stator negative-sequence voltage is limited at this value because the PI controllers of the negative-sequence compensation had reached saturation.

On the other hand, with the modified direct voltage, the negative-sequence compensation is stable and effectively reduces the stator negative-sequence voltage to a very low value of around 0.1 V. It can be concluded that the modified method can support full range of loads because it estimates the slip angle.

B. Connection to the Grid

Unlike the simulation, there is a delay of 1 sec between the end of the synchronization mode and the connection of the DFIG to the grid. The no load condition is considered only because it is the worst case scenario in terms of inrush current.

The DFIG speed is fixed at a sub-synchronous speed of 0.9 pu. The results for grid connection with the conventional method is shown in Fig. 5.54, while the results with the modified method are shown in Fig. 5.55.

From Fig. 5.54, since the conventional method could not obtain the slip angle, the grid-connected control will have a sudden error in the slip angle of −60 degrees at the instant of connection. Although the stator voltage is synchronized with the grid voltage, this sudden slip angle error produces inrush currents which is twice the steady-state stator current.

On the other hand, the modified method obtain an estimation of the slip angle and, consequently, the connection is smoother.

When the DFIG is connected to the grid, the negative-sequence compensation will suddenly change from eliminating the stator negative-sequence voltage to eliminating the stator negative-sequence current. This produces a slow transient response of the rotor negative-sequence current.

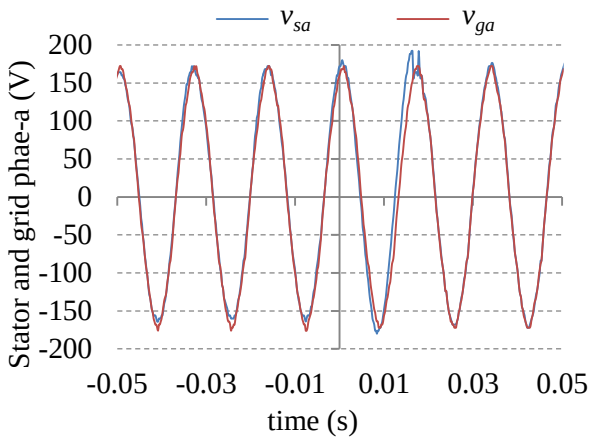

(a) Stator and grid phase-a

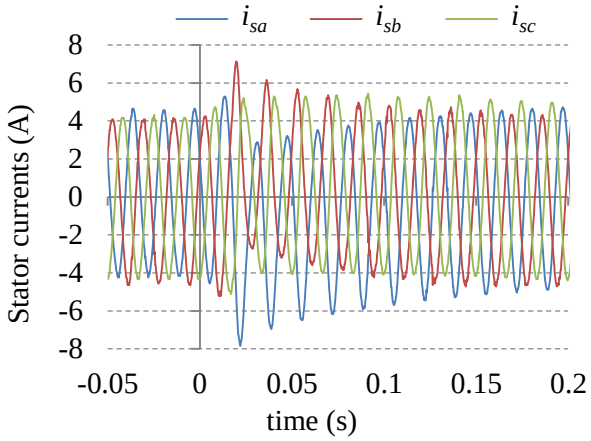

(b) Stator currents

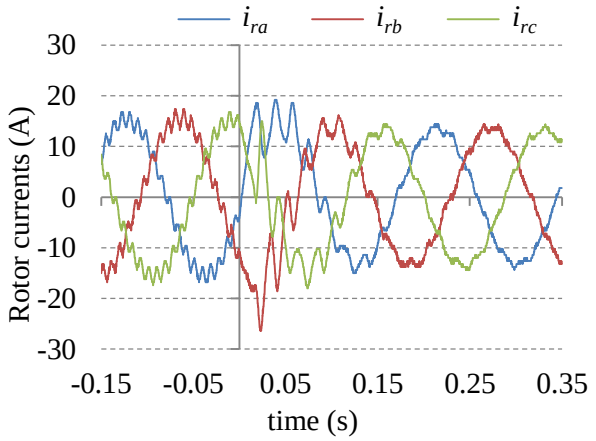

(c) Rotor currents

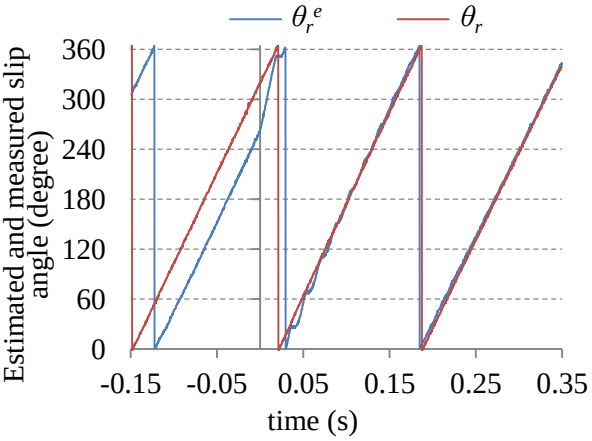

(d) Estimated and measured slip angle

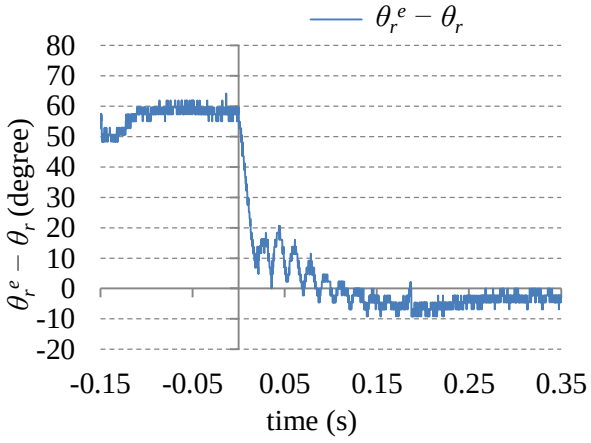

(e) Estimation error of the slip angle

Fig. 5.54: Experimental results for grid connection with the conventional direct voltage control under no load condition with ω_m = 0.9 pu.

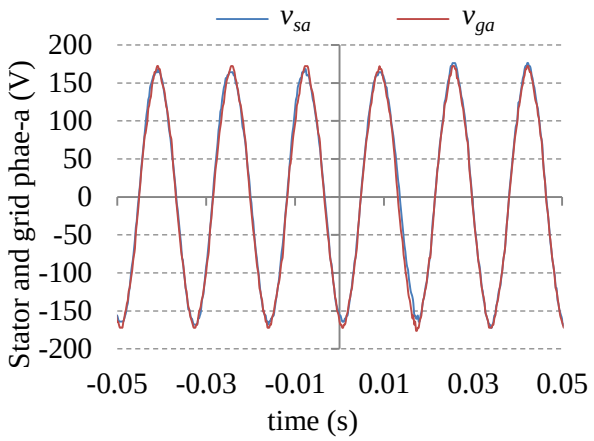

(a) Stator and grid phase-a

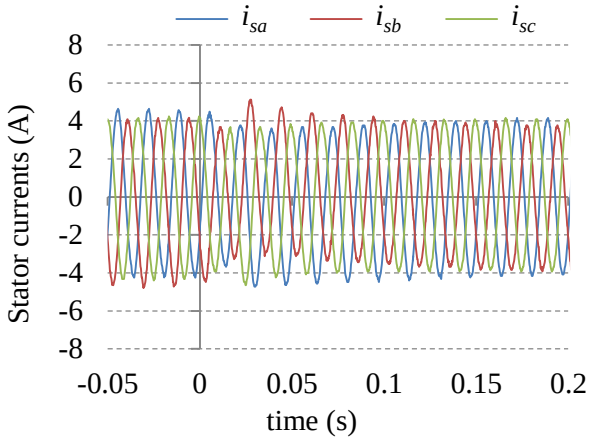

(b) Stator currents

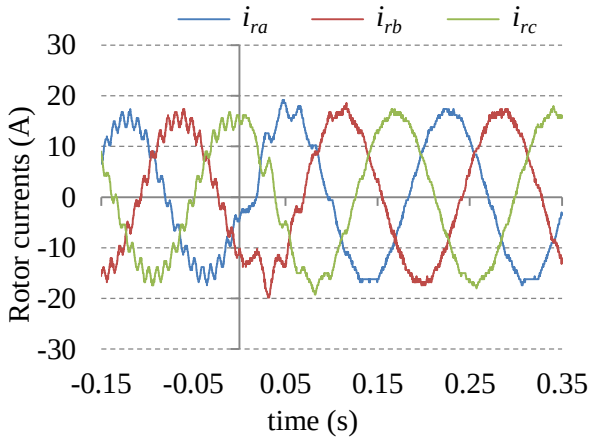

(c) Rotor currents

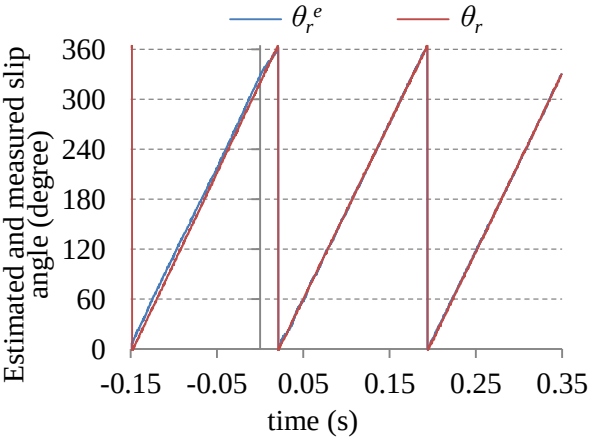

(d) Estimated and measured slip angle

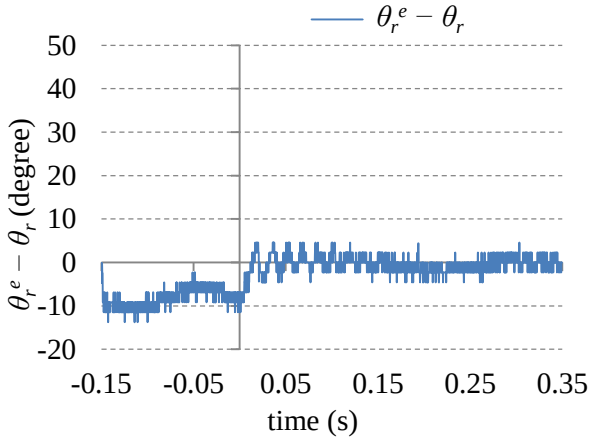

(e) Estimation error of the slip angle

Fig. 5.55: Experimental results for grid connection with the modified direct voltage control under no load condition with ω_m = 0.9 pu.

5.4 Conclusion

This chapter has introduced the analysis and design of a control system, which is based on the direct voltage control, for the stand-alone DFIG. This control can also be used to achieve synchronization with the grid voltage prior to connecting the DFIG to the grid. This chapter has explained the direct voltage control and has demonstrated its limitations which are:

- The conventional direct voltage control cannot obtain the slip angle
- The conventional direct voltage control cannot achieve smooth connection to the grid even with synchronization mode.
- The negative-sequence compensation through RSC cannot be stable for some capacitive load.

To solve these limitation, a new estimator of the rotor current angle in the dq-frame was proposed and introduced to the direct voltage control. This modified direct voltage control has all the advantages of the conventional direct voltage control such as sensorless control and relatively fast dynamics. In addition, the modified direct voltage control overcomes all the limitation of the conventional direct voltage control.

Simulation and experiments were carried out to demonstrate the limitations of the conventional direct voltage control and to compare its performance with the modified direct voltage control.

References

[1] G. Iwanski and W. Koczara, "Sensorless Stand Alone Variable Speed System for Distributed Generation," in *Proc. 35th IEEE Power Electronics Specialists Conf.,* Aachen, Germany, 2004, vol. 3, pp. 1915-1921.

[2] G. Iwanski and W. Koczara, "Sensorless Direct Voltage Control Method for Stand-Alone Slip-Ring Induction Generator," in *Proc. European Conf. Power Electronics and Applications,* Dresden, Germany, 2005, pp. 1-10.

[3] G. Iwanski and W. Koczara, "DFIG-Based Power Generation System with UPS Function for Variable-Speed Applications," *IEEE Trans. Ind. Elect.,* vol. 55, no. 8, pp. 3047-3054, Aug. 2008.

[4] G. Iwanski and W. Koczara, "Positive and Negative Sequence Based Sensorless Control for Stand-Alone Slip-Ring Generator," in *Proc. 12th EPE-PEMC,* Portoroz, Slovenia, 2006, pp. 555-560.

[5] G. Iwanski and W. Koczara, "Sensorless Direct Voltage Control of the Stand-Alone Slip-Ring Induction Generator," *IEEE Trans. Ind. Elect.,* vol. 54, no. 2, pp. 1237-1239, Apr. 2007.

[6] G. Abad, J. López, M. A. Rodríguez, L. Marroyo, and G. Iwanski, *Doubly Fed Induction Machine: Modeling and Control for Wind Energy Generation*. New Jersey: John Wiley, 2011, Chap. 11.

Chapter 6

Conclusion

In this work, control systems for a variable speed doubly-fed induction generator during the stand-alone mode, the grid-connected mode, and the synchronization mode were designed and tested with simulation and experiments.

The control systems duties depends on the current mode of operation. During stand-alone, the control must regulate the frequency and amplitude of the output voltage. During the synchronization mode, the control system must align the stator voltage with the grid voltage to achieve smooth connection to the grid. During grid-connected mode, the control system regulates the generated active and reactive power.

For the grid-connected mode, a new decoupled control was proposed to control the active and reactive power. The proposed decoupled control does not require any DFIG parameter for the online calculation, its performance is independent of the grid voltage amplitude and orientation.

To achieve sensorless control during grid-connected mode, a new slip angle estimator which is based on rotor current estimation, was proposed. The proposed estimator requires the least number of machine parameters compared with model-based estimators; it requires the stator inductance only which can be measured directly at the stator side. Compared with other rotor current-based estimators, the proposed estimator has better implementation which eliminates the need for stator flux and improved the model accuracy.

For the stand-alone mode, the direct voltage control was adopted, and its limitation were investigated. The direct voltage control cannot obtain the slip angle which causes the negative-sequence compensation through RSC to become unstable for some loads. To solve this issue, a new estimator of the rotor current angle is proposed and integrated into the direct voltage control. This estimator enables the direct voltage control to extract the slip angle and to support full range of linear loads.

During the synchronization mode, the direct voltage control can be employed with appropriate frequency and amplitude references. However, the conventional direct voltage control cannot achieve smooth connection to the grid even after voltage synchronization because of the absence of the slip angle. On the other hand, the modified direct voltage control achieves smooth connection regardless of the load.

All these modes of operations have been investigated with simulation and experiments. The results proved the theoretical analysis and supported the proposed control design. The research target, which is designing control systems for the DFIG-based distributed generation systems, was accomplished.

For future work, some points can be addressed: Since the slip angle estimator accuracy strongly depends on the stator inductance accuracy, algorithms for adaptive tuning of the stator inductance can be investigated to increase the robustness of the estimator. During the grid-connected mode, the grid codes require the generation system to continue operation and to support the grid during faults. Therefore, fault-ride-through performance should be addressed.

List of Publications

Journals

1. A. B. Ataji, Y. Miura, T. Ise, and H. Tanaka, “Direct Voltage Control with Slip Angle Estimation to Extend the Range of Supported Asymmetric Loads for Stand-Alone DFIG,” *IEEE Trans. Power Electronics*, vol. 31, no. 2, pp. 1015-1025, Feb. 2016.

2. A. B. Ataji, T. Ise, Y. Miura, and H. Tanaka, “A New Robust Decoupled Control of the Stator Active and Reactive Currents for Grid-Connected Doubly-Fed Induction Generators,” *Energies*, accepted for publication on 03 Mar. 2016.

Conferences with Review

3. A. B. Ataji, Y. Miura, T. Ise, and H. Tanaka, “Machine Parameter Independent Control of a Grid-Connected Variable Speed Doubly-Fed Induction Generator for Gas Engine Generation Systems,” in *2013 IEEE ECCE Asia Downunder Conf.*, Melbourne, Australia, 3-6 June 2013.

4. A. B. Ataji, Y. Miura, T. Ise, H. Tanaka, “Sensorless Direct Voltage Control for Stand-Alone DFIG with Improved Negative-Sequence Voltage Compensation,” in *the 16th European Conf. Power Electronics and Applications*, Lappeenranta, Finland, 26-28 Aug. 2014.

Conferences without Review

5. A. B. Ataji, Y. Miura, and T. Ise, “Sensorless Control of Grid-Connected Doubly-Fed Induction Generator,” in *平成 24 年電気関係学会関西連合大会* (*2012 Kansai-Section Joint Convention of Institutes of Electrical Engineering*), Osaka, Japan, 8-9 Dec. 2012.

6. A. B. Ataji, Y. Miura, T. Ise, and H. Tanaka, “Rotor Position Sensorless Control of a Grid-Connected Variable Speed Doubly-Fed Induction Generator for Gas Engine Generation Systems,” in *電気学会半導体電力変換研究会* (*Technical Meeting on Semiconductor Power Converter*), Kyoto Japan, 25-26 Jan. 2013.